UAB
Universitat Autònoma de Barcelona

ADVERTIMENT. L'accés als continguts d'aquesta tesi queda condicionat a l'acceptació de les condicions d'ús establertes per la següent llicència Creative Commons: 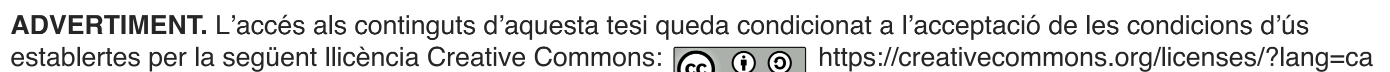 https://creativecommons.org/licenses/?lang=ca

ADVERTENCIA. El acceso a los contenidos de esta tesis queda condicionado a la aceptación de las condiciones de uso establecidas por la siguiente licencia Creative Commons: 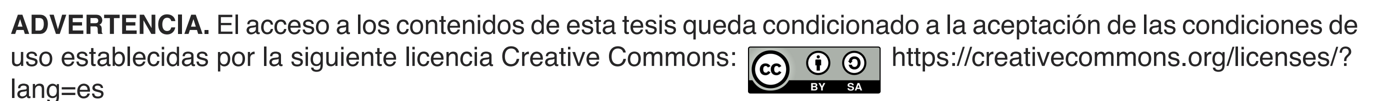 https://creativecommons.org/licenses/?lang=es

WARNING. The access to the contents of this doctoral thesis it is limited to the acceptance of the use conditions set by the following Creative Commons license: 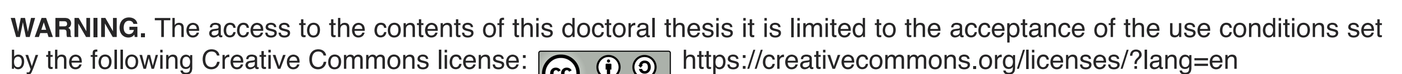 https://creativecommons.org/licenses/?lang=en

Low Gain Avalanche Detectors (LGADs and iLGADs) for High-Energy Physics and Synchrotron Applications

Author:
Albert Doblas Moreno

Supervisors:
Dr. David Flores Gual
Dr. Salvador Hidalgo Villena

Academic Tutor:
Dr. Lluís Font Guiteras

A thesis submitted in fulfillment of the requirements for the degree of

Doctor in Physics

Physics Department
Universitat Autònoma de Barcelona

December, 2022

Declaration of Authorship

This document certifies that the thesis *Low Gain Avalanche Detectors (LGADs and iLGADs) for High-Energy Physics and Synchrotron Applications* has been written by Albert Doblas Moreno under the supervision of Dr. David Flores Gual and Dr. Salvador Hidalgo Villena, to fulfill the requirements to obtain the degree of Doctor in Physics.

Author: Albert Doblas Moreno	*Supervisor:* Dr. David Flores Gual
Supervisor: Dr. Salvador Hidalgo Villena	*Academic Tutor:* Dr. Lluís Font Guiteras

Cerdanyola del Vallès, December 2022

A mis padres.

Acknowledgements

First of all, I would like to thank my supervisors for the opportunity to carry out this doctoral thesis and for their support over the years. I would like to thank Giulio Pellegrini, without him this would not have been possible.

David Quirion, your invaluable help and knowledge have helped me to achieve my goals. Thank you.

Pablo Fajardo and Marie Ruat, thank you for providing your experience and knowledge in the field of X-Ray detectors.

I would like to thank Celeste Fleta for her involvement in the Radiation laboratory, as well as Javier Bravo for his help whenever I needed it.

Xavier Jordà, Miquel Vellheví and David Sánchez, thank you for your willingness and help whenever I needed to use the Power Laboratory.

This thesis would not make sense without the fabrication of the detectors, so the Clean Room of the IMB-CNM has a lot to do with it. There have been many runs and stages we have shared over the years. Thank you all for your dedication, help and patience.

Mar Carulla, thank you for helping me to enter this world.

Carlos Couso, I think you are the person who knows the most about Sentaurus that I have met. Your advice and help have been of great value. Thank you.

I would also like to remember all the people who work in IT: Nieves, Santi, Ramon and Xevi. Néstor, we have a Sant Pancraç pending.

I wanted to thank all the members of the Radiation Group, who at one time or another have supported me. In particular, I wanted to thank Neil Moffat for always being willing to help me in any way he could. Jairo, I am sure that the future of this work is in good hands. Thank you for everything. Maria Manna, we have shared courses, congresses, trips... Thank you very much for your understanding during these years.

I would also like to remember the whole group of Power devices. The few times I stayed for lunch they always welcomed me with open arms.

Albertito, thank you for always bringing a smile to my face. I guess sharing a name and hairstyle has somehow brought us together.

Throughout these years I have shared an office with incredible professionals and, above all, incredible people. Thank you very much for everything. I hope I don't forget anyone: Manu, Víctor, Maria, Bernat, Eric, Naüm, Conrad, Emma.

Finally, I wanted to thank my great friend and confidant. Alberto, more than 10 years of friendship, sharing exams, labs, PowerPoints... and finally a PhD (and coffees).

Apart from being a great person (although not very nice), you are a great professional and friend. Thanks for everything.

Me gustaría acordarme de mis amigos. *Lladres:* aunque vuestra principal ayuda haya sido preguntarme cada fin de semana durante un año y medio cuando terminaba, una parte de este trabajo también es vuestro. Ignasi, gracias por preocuparte tanto por mi durante este tiempo (y siempre).

Resistencia: normalmente de noche, pero siempre dispuestos hacerme desconectar. Gracias por ayudarme a ser más feliz durante estos años (y los que quedan).

Belén, unque nuestros caminos se hayan separado, creo que sería injusto no agradecer todo tu apoyo durante estos años. Gracias por todo.

Por último, quería dar un gracias enorme a mi gran familia, la que pase lo que pase siempre está dispuesta ayudarme de alguna manera u otra. Y sé que el Iaio también me ha ayudado de alguna forma.

David, aunque te hayas leído media página de la tesis, gracias por ser el mejor hermano que podría tener.

Mama, Papa, sé que habéis sufrido más que yo, así que este trabajo es tan vuestro como mío. Gracias por ser mi guía.

UNIVERSITAT AUTÒNOMA DE BARCELONA

Abstract

Universitat Autònoma de Barcelona
Physics Department

Doctor in Physics

Low Gain Avalanche Detectors (LGADs and iLGADs) for High-Energy Physics and Synchrotron Applications

by Albert Doblas Moreno

This thesis presents the development of Low Gain Avalanche Detectors (LGAD) and iLGAD at IMB-CNM (CSIC) for use in High Energy Physics experiments and synchrotron applications.

The Large Hadron Collider (LHC) is at the center of the efforts of the entire particle physics community, as it is the most powerful particle accelerator in the world. It is planned that the LHC will be upgraded (HL-LHC), providing a higher luminosity that will lead to a wider range of data collected in the experiments, thus establishing a new paradigm in high-energy physics. However, particle detectors capable of precisely measuring the trace and time when charged particles pass through the detector are needed.

The development of radiation detectors is not only based on experiments in particle physics, but they are also commonly used in synchrotrons, in which X-Ray beams are used for various applications. In both applications, radiation detectors are subject to highly radioactive environments, so their performance is affected. Therefore, there is a commitment to optimizing the design of these detectors so that they are able to provide optimum performance under these conditions.

This work describes the design, fabrication, and characterization of LGAD detectors for use in the HL-LHC. In addition, other variants such as the Inverse LGAD (iLGAD) or the nLGAD (LGAD with n-type substrates) have been optimized and fabricated to cover a wide range of applications within the charged particle and X-Ray detection.

Contents

Abstract **v**

List of Figures **x**

List of Tables **xvii**

List of Abbreviations **xix**

Introduction **1**

1 Semiconductor Radiation Detectors **4**
1.1 Introduction 4
1.2 Detectors for HEP experiments 6
1.2.1 High-Luminosity LHC 7
Timing detectors and 4D tracking 8
1.3 Detectors for synchrotron radiation 9
1.3.1 European Synchrotron Radiation Facility (ESRF) 10
1.3.2 X-Ray detectors 10
X-Ray interaction with matter 11
1.4 Silicon detectors 12
1.4.1 Charged particles interaction with matter 12
1.4.2 Working principles of silicon detectors 13
1.4.3 PiN diode 14
Current and capacitance characteristics 14
Signal formation 15
ToF measurement 16
1.5 Detectors with intrinsic amplification 17
1.5.1 Avalanche Photo-Diode (APD) 17
1.5.2 Low Gain Avalanche Detector 19
1.6 Segmented detectors 21
1.6.1 Hybrid Pixel Detectors (HPD) 22
1.6.2 High-fill factor LGAD structures 23
Inverse LGAD (iLGAD) 24
AC-LGAD 24
Trench-Isolated LGAD (TI-LGAD) 25
Trench iLGAD 25

1.7 Radiation damage . . . 26
1.7.1 Bulk damage . . . 26
Leakage current . . . 27
Charge collection efficiency . . . 27
Effective doping concentration and depletion voltage . . . 27
Acceptor removal . . . 28
1.7.2 Surface damage . . . 30
1.8 Conclusions . . . 31

2 Development of LGAD sensors for the HL-LHC upgrade 32
2.1 Introduction to the LGAD technology . . . 32
2.1.1 LGAD design . . . 32
2.1.2 LGAD fabrication process . . . 34
2.1.3 LGAD as a timing detector . . . 34
2.1.4 LGAD major challenges . . . 37
2.1.5 AIDA-2020 production . . . 37
2.1.6 Radiation hardness requirements for LGADs . . . 37
CMS Endcap Timing Layer . . . 38
ATLAS High Granularity Timing Detector . . . 38
2.2 Design and optimization of the detectors . . . 39
2.2.1 Multiplication region optimization . . . 39
Deep multiplication implant . . . 41
2.2.2 Periphery optimization . . . 44
2.3 Photolithographic mask designs . . . 45
2.4 Fabrication process . . . 49
2.4.1 Multiplication layer . . . 52
2.4.2 Temporary metal . . . 54
2.4.3 End of the process . . . 54
2.5 Characterization of the AIDAv1 fabrication run . . . 56
2.5.1 On wafer electrical characterization . . . 56
2.5.2 Leakage current issue analysis . . . 59
2.5.3 Characterization on AIDAv1 irradiated samples . . . 60
Electrical characterization . . . 61
Gain and timing measurements . . . 62
2.6 Characterization of the AIDAv2 fabrication . . . 63
2.6.1 Characterization of non-irradiated sensors . . . 63
On wafer electrical characterization . . . 63
Gain measurements . . . 69
2.6.2 Characterization of irradiated sensors . . . 71
Electrical Characterization . . . 71
Acceptor Removal . . . 72
Collected charge and time resolution . . . 73

Mortality in irradiated LGADs 75
2.6.3 Summary of sensor properties 76
Non-irradiated sensors 76
Irradiated sensors 77

3 LGAD sensors for timing applications in 150 mm silicon wafers 79
3.1 Introduction 79
3.2 Design and optimization of the LGAD sensors 80
3.2.1 Multiplication region optimization 80
3.3 Photolithographic mask designs 81
3.4 Fabrication of the LGAD detectors 84
3.4.1 Multiplication layer 84
3.5 Characterization of the LGAD sensors 88
3.5.1 Characterization of non-irradiated sensors 88
Electrical characterization 88
Gain and timing measurements 93
3.5.2 Characterization of irradiated sensors 95
Gain measurements 95
Acceptor removal studies 97
Timing measurements 98
3.5.3 Summary and conclusions 100
Non-irradiated sensors 100
Irradiated sensors 100
3.6 ATLAS-CMS Common Run 100
3.6.1 Optimization of the sensors for the HL-LHC 101
Optimization for irradiated sensors 101
3.6.2 Photolithographic mask designs 103
3.6.3 Fabrication of the sensors 104
3.6.4 Characterization of the LGAD sensors 105
3.6.5 Summary and conclusions 108

4 Inverse LGAD for X-Ray Applications 110
4.1 Introduction 110
4.1.1 First iLGAD generation (iLG1) 110
4.2 Optimization of the iLGAD detectors 112
4.2.1 Periphery optimization for X-Ray applications 112
Multiplication side optimization 112
Ohmic side optimization 113
4.3 Photolithographic mask designs 115
4.4 Fabrication of the iLG2 119
4.4.1 Multiplication layer 121
4.4.2 End of the process 123
4.5 Characterization of the fabricated sensors 124

4.5.1 Electrical characterization . . . 124
Pad LGAD structures . . . 124
Inverse LGAD structures . . . 126
MOS capacitors . . . 128
4.5.2 Gain measurements . . . 130
4.5.3 Irradiated measurements . . . 131
4.6 Summary and conclusions . . . 132

5 Trench iLGAD for 4D Tracking Applications 134
5.1 Introduction . . . 134
5.2 Trench iLGAD design . . . 135
5.2.1 Concept and structure design . . . 135
5.2.2 Periphery optimization . . . 137
5.3 Fabrication of the third iLGAD generation . . . 139
5.3.1 Type of wafer selection . . . 139
Trench iLGAD in Si-Si wafers . . . 139
Trench iLGAD in epitaxial wafers . . . 141
5.3.2 Fabrication process . . . 142
5.4 Photolithographic mask designs . . . 143
5.5 Conclusions and future work . . . 146

6 Development of LGAD sensors in n-type substrates 147
6.1 Introduction . . . 147
6.2 The nLGAD detector . . . 148
6.2.1 Optimization and design of the nLGAD detector . . . 149
Photolithographic mask designs . . . 151
6.2.2 Fabrication process . . . 152
6.2.3 Characterization of the detectors . . . 154
Electrical characterization . . . 154
Gain measurements . . . 156
6.2.4 Conclusions . . . 157
6.3 Proton Low Gain Avalanche Detector (pLGAD) . . . 158
6.3.1 Optimization of the pLGAD sensor . . . 159
Multiplication region optimization . . . 159
Periphery optimization . . . 162
6.3.2 Conclusions . . . 163

Conclusions and Future Work 165

Scientific Contributions 169

Bibliography 171

List of Figures

1.1 ATLAS detector experiment. Extracted from [16]. 6
1.2 CMS detector experiment. Extracted from [17]. 7
1.3 Different configurations of a tracking system with timing capabilities. Adapted from [18] 8
1.4 Sketch of a synchrotron facility. Extracted from [22]. 9
1.5 X-Ray classification by photon energy range and typical detection technologies used. Adapted from [25]. 11
1.6 (a) Mass attenuation coefficient of silicon as a function of the photon energy. (b) Photon absorption length in silicon as a function of the incident energy. Data were taken from [27]. 12
1.7 Band diagram **(a)** before junction and **(b)** at thermal equilibrium. Adapted from [10] 13
1.8 Typical **(a)** Current-voltage and **(b)** Capacitance-voltage graphs in a silicon PiN diode. 15
1.9 Sketch of a PiN detector. 16
1.10 Schematic diagram of a time-tagging detector. Adapted from [30]. . . 17
1.11 Sketch of an APD detector. 18
1.12 Typical I-V and gain characteristics of an APD detector [32] 19
1.13 Sketch of an LGAD detector. 19
1.14 Simulated net doping profile of an LGAD sensor in the multiplication region. 20
1.15 Sketch of (a) pixelated and (b) strip p-type silicon detectors. 21
1.16 Cross-section of a hybrid pixel detector. 23
1.17 Cross section of two neighbors LGAD elements. 23
1.18 (a) LGAD and (b) iLGAD design comparison. 24
1.19 Cross-section of the AC-LGAD 25
1.20 Cross-section of the TI-LGAD 25
1.21 Cross-section of the Trench iLGAD sensor active area. 26
1.22 Depletion voltage and effective doping concentration dependence with the fluence for an n-type detector. Graph taken from [50]. 28
1.23 Doping concentration as a function of the equivalent fluence for a standard LGAD sensor. 29
1.24 Schematic illustration of the formation of a conductive layer at the Si-SiO_2 interface provoked by an ionizing particle. Adapted from [60]. 30

2.1 (a) Doping profiles and electric field at the multiplication region (b) Cross-section of the standard LGAD design 33
2.2 Sketch of a standard LGAD fabrication process. 35
2.3 (a) Cross-section of an LGAD in SOI wafer (b) Cross-section of an LGAD in Si-Si wafer. 36
2.4 Research lines of the AIDA-2020 project. Adapted from [64] 38
2.5 Simulated net active doping concentration for different boron doses of a Si-Si LGAD sensor at the multiplication region. 40
2.6 (a) Breakdown voltage as a function of the multiplication layer dose. (b) C-V simulations for different boron doses for the multiplication layer. (c) Transient simulation (I-t) for an LGAD sensor for different applied voltages (d) Gain simulation for different boron doses. 41
2.7 Simulated boron profiles for different implantation energies. 42
2.8 Simulated profiles of an LGAD using an energy of 400 and 800 keV. . 43
2.9 Simulated electric field of an LGAD using an energy of 400 and 800 keV. 43
2.10 Simulated breakdown voltage for different boron doses using an energy of 400 and 800 keV. 44
2.11 Breakdown voltage as a function of JTE width and the non-gain distance. 45
2.12 Sketch of the mask levels in the mask CNM913. 47
2.13 LGAD designs in the mask CNM913. (a) Pad (b) 2x2 (c) 5x5 (d) 1x4 (e) 2x4 (f) 4x4 (g) 24x4. 48
2.14 Final mask design CNM913 for the AIDA2020 production. 49
2.15 Simulated doping profile in a Si-Si process in high resistivity p-type wafers. 50
2.16 Sketch of the AIDA2020 fabrication process. 51
2.17 Four-probe sheet resistance measurement in n-type wafers. 52
2.18 Sheet resistance map in test wafer for the AIDA2020 production for a dose of $1.8 \cdot 10^{13}$ at/cm^2. 53
2.19 Cross-section of the core region in a 2x2 pixelated LGAD using the temporary metal. 55
2.20 Simulated net active doping concentration after the LGAD fabrication. 55
2.21 Fabricated wafer for the AIDA2020 production. 55
2.22 (a) Picture of the setup in the Radiation Detectors lab at IMB-CNM. Extracted from [41]. (b) Sketch of the measurement procedure to carry out the electrical characterization. 56
2.23 I-V measurements at room temperature for 1.0x1.0 mm^2 pad LGADs using different boron doses in (a) 35 µm and (b) 50 µm thick wafers. . 57
2.24 (a) Breakdown voltage as a function of boron dose for different LGAD pad sensors and (b) I-V measurements in the guard ring of different LGADs. 58
2.25 Current density at room temperature for 2x2 and 5x5 arrays, CMS strips and Pad LGADs for a medium dose and using 35 µm thick wafers. 58

2.26 C-V measurements at room temperature for 1.0x1.0 mm^2 pad PiN and LGAD using 35 µm thick wafers. 59
2.27 TCAD simulations assuming a gap of 0.5 µm between multiplication region and JTE, which induces a high leakage current in the measurement. 60
2.28 Thermographic image of a pad LGAD from AIDAv1 fabrication at 20 and 150 V. 60
2.29 I-V measurements on proton-irradiated LGAD sensors from AIDAv1 fabrication. 61
2.30 C-V measurements on proton-irradiated LGAD sensors from AIDAv1 fabrication. 61
2.31 Gain measurements on proton-irradiated LGAD sensors from AIDAv1 fabrication. 62
2.32 I-V measurement on 1.3x1.3 mm^2 pad LGADs for different IP values (wafer 4) at room temperature. 64
2.33 I-V measurement on 1.3x1.3 mm^2 pad LGADs with IP47 from wafer 2 at -20 ºC. 64
2.34 I-V measurement on 1.0x1.0 mm^2 pad LGADs from different wafers at 20 ºC. 65
2.35 I-V measurements for different IP values (wafer 4) at room temperature for (a) 1.3x1.3 mm^2 and (b) 1.0x1.0 mm^2 2x2 LGADs. 66
2.36 I-V measurements for different IP values (wafer 4) at room temperature for 1.3x1.3 mm^2 5x5 LGADs. 66
2.37 (a) C-V measurements at room temperature for 1.3x1.3 mm2 pad LGADs from different wafers. 67
2.38 Depletion width as a function of voltage for pad LGAD sensors from different wafers. 67
2.39 Doping concentration comparison as a function of depletion width for a pad LGAD sensor, using different techniques. 68
2.40 Sketch of the TCT setup used at IMB-CNM lab. 70
2.41 Gain and collected charge of non-irradiated 1.3x1.3 mm^2 pad LGAD from AIDAv2 run. 70
2.42 Current density at -30 ºC for neutron-irradiated LGADs from AIDAv2 run. 71
2.43 CV measurements at -30 ºC and f=100 Hz for neutron-irradiated LGADs from AIDAv2 run. 72
2.44 Gain layer depletion fraction as a function of neutron fluence. 73
2.45 Collected charge at -30 ºC for 1.3x1.3 mm^2 single pad LGADs from the AIDAv2 run. (b) Required voltage to reach minimum collected charge for CMS and ATLAS timing detectors as a function of neutron fluence [78, 77]. 74

2.46 Time resolution at -30 ºC for 1.3x1.3 mm^2 single pad LGADs from the AIDAv2 run [78, 77]. 74
2.47 Collected charge and time resolution at operational voltage as a function of the fluence for HPK, FBK and CNM neutron-irradiated sensors. Measurements performed in [79]. 75
2.48 SEM image of a $3 \cdot 10^{15}$ n_{eq}/cm^2 neutron-irradiated LGAD that has suffered a local burn in the collector ring. 76

3.1 Simulated doping profiles for the 150 mm thermal process for different boron doses. 80
3.2 Gain simulations at room temperature as a function of the gain layer dose for a 50 µm LGAD. 81
3.3 Final design of the mask CNM869. 82
3.4 LGAD pad designs corresponding to the mask CNM869 with an active area of (a) 3x3 mm^2 and (b) 1x1 mm^2. 83
3.5 Mask level illustration of the mask CNM869 at the multiplication side. 83
3.6 LGAD fabrication process for a 150 mm epitaxial-substrate. 85
3.7 Sheet resistance of the gain layer as a function of boron dose measured in test wafers. 86
3.8 Sheet resistance wafer mapping for 150 mm n-type test wafers. 86
3.9 (a) Image of a produced wafer from the 6LG3 generation. Detailed view (b) at the periphery and (c) at the active region of the sensor. . 88
3.10 (a) I-V and (b) C-V measurements in 3.3x3.3 mm^2 LGADs at 20 ºC in different wafers from 6LG1 fabrication. 89
3.11 I-V measurements at different temperatures and implanted doses in 6LG3 LGADs. 90
3.12 C-V measurements at different implanted doses in 6LG3 LGADs. . . . 91
3.13 I-V wafer mapping at 100 V for the medium dose LGAD wafer from 6LG3. 91
3.14 Depletion width as a function of the applied voltage extracted from the C-V measurement in epitaxial wafers (6LG3). 92
3.15 Simulated doping profile at the epitaxial-handle wafer junction, using the extracted value of the doping concentration. 93
3.16 Gain measurements for the 3.3x3.3 mm^2 LGADs from wafer 3 of the 6LG1. 93
3.17 Gain measurements for different boron doses at room and low temperature for the 3.3x3.3 mm^2 LGADs from 6LG3. 94
3.18 Time resolution as a function of applied voltage for the highest dose from 6LG3. 94
3.19 I-V measurement of neutron-irradiated 1.3x1.3 mm^2 single pad LGADs at -20 ºC from 6LG3. 95

3.20 TCT measurement of neutron-irradiated 1.3x1.3 mm^2 single pad LGADs at -20 ºC. . . . 96
3.21 Sr90 measurement of neutron-irradiated 1.3x1.3 mm^2 single pad LGADs at -20 ºC. . . . 97
3.22 Normalized collected charge as a function of applied bias for neutron-irradiated LGADs. . . . 98
3.23 Gain layer depletion as a function of neutron fluence. . . . 98
3.24 Time resolution as a function of applied bias for neutron-irradiated LGADs measured at IMB-CNM laboratories. . . . 99
3.25 Time resolution as a function of applied bias for neutron-irradiated LGADs measured at IFAE laboratories [78]. . . . 99
3.26 Simulated collected charge as a function of boron dose at -20 ºC for 50 µm epitaxial LGADs. . . . 101
3.27 Simulated doping profiles for carbonated LGAD sensors. . . . 102
3.28 CNM1023 mask design with ATLAS and CMS sensors located at the left and right sides, respectively. . . . 103
3.29 LGAD 2x2 array from the CNM1023 mask. . . . 104
3.30 I-V measurements for different LGAD structures integrated into the ATLAS-CMS Common Run, from wafer 8 (top) and wafer 10 (bottom). [88] . . . 106
3.31 C-V measurements for LGADs integrated into different positions through the wafer, from ATLAS-CMS Common Run [88]. . . . 107
3.32 Acceptor removal constant for different LGAD fabrications. Adapted from [89]. . . . 108

4.1 Cross-section of the first iLGAD generation fabricated at IMB-CNM . . . 111
4.2 Charge distribution measured during a test beam for strip LGAD and iLGAD detectors. . . . 111
4.3 I-V simulation of iLGAD structures with different Nox concentrations. Breakdown voltage is reduced by increasing Nox. . . . 112
4.4 Electric field cut at 0.1 µm along the periphery in the multiplication side at 600 V. . . . 113
4.5 Different configurations of the p^+ diffusions at the ohmic side. Multi-ring structure gives the highest breakdown voltage and this is going to be the final design. . . . 114
4.6 Electric field cut at 0.1 µm along the periphery in the ohmic side at 600 V. . . . 114
4.7 I-V simulation of iLGAD structures with Nox = 1012 cm-2. . . . 115
4.8 Final design of the second iLGAD generation . . . 115
4.9 CNM953 mask levels sketch. . . . 117
4.10 Different iLGAD designs included in the mask CNM953: (a) Medipix3, (b) Strip iLGAD, (c) Pad iLGAD, and (d) 10x10 iLGAD. . . . 118

4.11 Design of the CNM953 mask used in the development of the iLG2. . . 119
4.12 Fabrication process for the iLG2. 120
4.13 Average sheet resistance as a function of the boron dose for two LGAD productions and the iLG2 production. 121
4.14 Sheet resistance wafer map for the medium dose in the iLG2. 122
4.15 Detailed view of the iLGAD periphery after the multiplication diffusion 123
4.16 Images of a fabricated wafer at the multiplication and ohmic sides. . . 123
4.17 Detailed views of the iLGAD at the end of the process. (a) Medipix3 design iLGAD at the ohmic side. (b) Zoom of the 45-µm pixel size. (c) Strip iLGAD at the ohmic side (d) Floating n^+ rings at the multiplication side. 124
4.18 I-V measurement of pad LGAD structures at room temperature. . . . 125
4.19 C-V measurement of pad LGAD structures at room temperature. . . . 125
4.20 Current density at room temperature of each iLGAD design in the non-gain wafer. 126
4.21 I-V at room temperature of each iLGAD design. 127
4.22 I-V measurement of the Medipix3 iLGAD at different temperatures. . 127
4.23 C-V measurement of a MOS capacitor at room temperature and 10 kHz. 128
4.24 Energy band diagram of an ideal MOS structure at thermal equilibrium. 129
4.25 C-V simulation of a MOS capacitor at room temperature and 10 kHz. 130
4.26 Left) Collected charge of the iLGAD sensor and the PiN diode. (Right) Gain of the iLGAD sensor at room temperature using the IR laser. . . 131
4.27 Current density of unirradiated and Φ = 10 MRad irradiated iLGAD samples from the iLG1 and iLG2 runs. There 132

5.1 Simulated I-t curve for 50 and 285 m thick iLGADs at 300 V, obtained from a MIP simulation 135
5.2 Cross-section of the Trench iLGAD sensor. 136
5.3 Simulated breakdown voltage as a function of the trench width and depth. 137
5.4 Simulated breakdown voltage as a function of the distance between the trench and the peripheral ring 138
5.5 Simulated voltage and electric field distribution at the breakdown as a function of the distance between the trench and the peripheral ring. (a) Voltage distribution with 10 µm distance, (b) Voltage distribution without distance, (c) Electric field distribution without distance, and (d) Electric field distribution with a 10 µm distance. 139
5.6 Simulated net doping profiles after the Si-Si bonding process for the Trench iLGAD. 140
5.7 Breakdown voltage as a function of the resistivity of the epitaxial gain layer in Trench iLGAD. 141
5.8 Trench depth as a function of DRIE process duration. 142

5.10 Cross-section of the ohmic side of the CNM1086 mask. 143
5.9 Fabrication steps in the Trench iLGAD (iLG3). 144
5.11 Design of the different structures included in the CNM1086 mask set: (a) Timepix3, (b) TDCPix, (c) UZH-PSI, (d) iStrip, (e) Pad Trench LGAD and (f) 3x3 Trench iLGAD. 145
5.12 Full view of the CNM1086 mask set. 146

6.1 Different charge deposition scenarios using p-type and n-type substrate LGADs. 148
6.2 nLGAD simulated doping profile using a low dose. 150
6.3 (a) C-V and (b) I-V 1D simulations of the nLGAD structure using a low dose. 150
6.4 Breakdown voltage and gain trade-off for the nLGAD device using an IR laser. 151
6.5 (a) Mask used in the development of nLGAD sensors. (b) Pad design of the nLGAD sensor. 152
6.6 Sketch of the nLGAD fabrication process. 153
6.7 I-V measurements of low-dose nLGAD sensors at room temperature. . 154
6.8 C-V measurements of low-dose nLGAD sensors at room temperature. 155
6.9 (a) I-V and (b) C-V measurements of n-type PiN sensors at room temperature. 156
6.10 Gain as a function of the absorption length for nLGAD detectors, using different low-penetrating particle sources [98]. 157
6.11 Cross-section of the pLGAD structure. 159
6.12 Optimised net doping concentration of the $p^+/p/n$ region for a pLGAD sensor. 160
6.13 Electric field distribution along the depth of the multiplication region at 700 V. 160
6.14 Transient simulation of PiN and pLGAD structures biased at 200 V, irradiated with a 15 keV proton. 161
6.15 Breakdown voltage and gain trade-off as a function of the peak doping concentration of the n-type multiplication layer. 162
6.16 Cross-section of the pLGAD design, including the periphery and the active area. 162
6.17 Cross-section of the pLGAD design, including the periphery and the active area. 163
6.18 Cross-section of the pLGAD design, including the periphery and the active area. 163

List of Tables

1.1 Main properties of semiconductor materials at T=300 K 5

2.1 Sensor properties at -25 ºC required for the CMS ETL MIP timing detector. 38
2.2 Sensor properties at -30 ºC required for the HGTD timing detector. . 39
2.3 Mask level description of the mask CNM913. 46
2.4 Parameters of LGADs designed in the mask CNM913. 48
2.5 Sheet resistance and oxide growth for the multiplication layer in the AIDA2020 production for a dose of $1.8 \cdot 10^{13}$ at/cm^2. 53
2.6 Multiplication layer parameters used in the AIDAv1 fabrication. Boron energy is set to 100 keV in all the wafers. 54
2.7 Multiplication layer parameters used in the AIDAv2 fabrication, where all are fabricated in 50 µm thick substrates. 54
2.8 Gain layer depletion voltage values for irradiated sensors, extracted from C-V measurements. 72
2.9 Summary of electrical performance before and after irradiation for the CMS Market Survey. 78
2.10 Summary of electrical performance before and after irradiation for the ATLAS Market Survey. 78

3.1 Mask levels for the mask CNM869 82
3.2 Multiplication layer dose and energy values for the 6LG1 generation. 87
3.3 Multiplication layer dose and energy values for the 6LG3 generation. 87
3.4 Parameters of the devices located in the ATLAS side of the CNM1023 mask. 104
3.5 Parameters of the devices located in the CMS side of the CNM1023 mask. 104
3.6 Boron and carbon doses (at/cm^2 x10^{13}) and DOTs used in the ATLAS-CMS Common Run. 105
3.7 Yield for different LGAD structures integrated into the ATLAS-CMS Common Run. 106
3.8 Acceptor removal constant (10^{-16} cm^2) for carbonated and non-carbonated LGADs from ATLAS-CMS Common Run, using CV and IV measurements [89, 90] 108

4.1 Mask levels for the 12 photolithographic steps in the iLG2 116

4.2 Design parameters of the different iLGAD detectors included in the mask CNM953. 118
4.3 Main characteristics of the wafers used in the production and their description. 119
4.4 Experimental and simulated oxide thickness of the different regions in the detector 123
4.5 Electrical characteristics of the different produced structures in the iLG2 generation. 133

5.1 Boron parameters for the multiplication layer of Si-Si wafers for the iLG3. 140
5.2 Parameters for the handle wafer, multiplication layer, and active substrate in the epitaxial Trench iLGAD. 141
5.3 Ohmic side mask level description of the CNM1086 mask set 143
5.4 Design parameters of the different pixelated structures included in the CNM1086 mask set. 145

List of Abbreviations

AIDA	**A**dvanced **E**uropean **I**nfrastucture for **D**etectors at **A**ccelerators
ALICE	**A** **L**arge **I**on **C**ollider **E**xperiment
APD	**A**valanche **P**hoto-**D**iode
ASIC	**A**pplication-**S**pecific **I**ntegrated **C**ircuit
ATLAS	**A** **T**oroidal **L**HC **A**pparatu**S**
BNL	**B**rookhaven **N**ational **L**aboratory
CCE	**C**harge **C**ollection **E**fficiency
CERN	**E**uropean **C**ouncil for **N**uclear **R**esearch
CMS	**C**ompact **M**uon **S**olenoid
CNM	**N**ational **M**icroelectronics **C**entre
CSIC	**C**onsejo **S**uperior de **I**nvestigaciones **C**ientíficas
CT-PPS	**C**MS **T**OTEM **P**roton **P**osition **S**pectrometer
ESRF	**E**uropean **S**yncrotron **R**adiation **F**acility
ETL	**E**ndcap **T**iming **L**ayer
FBK	**F**ondazione **B**runo **K**essler
HEP	**H**igh **E**nergy **P**hysics
HGTD	**H**igh **G**ranularity **T**iming **D**etector
HL-LHC	**H**igh-**L**uminosity **L**arge **H**adron **C**ollider
HPD	**H**ybrid **P**ixel **D**etector
HPK	**H**amamatsu **P**hotonics
IMB-CNM	**I**nstitute of **M**icroelectronics of **B**arcelona
INFN	**I**talian **I**nstitute for **N**uclear **P**hysics
IP	**I**nter-**P**ad
JTE	**J**unction **E**xtension **T**ermination
LGAD	**L**ow **G**ain **A**valanche **D**etector
LHC	**L**arge **H**adron **C**ollider
LHCb	**L**arge **H**adron **C**ollider **b**eauty experiment
LINAC	**Lin**ear **Ac**celerator
MCP	**M**icro**c**hannel **P**lates
MIP	**M**inimum **I**onizing **P**article
NIEL	**N**on-**I**onising **E**nergy **L**oss
PKA	**P**rimary **K**nock-on **A**tom
PMT	**P**hoto**m**ultiplier **T**ubes
SDR	**S**emiconductor **R**adiation **D**etectors
SIMS	**S**econd **M**ass **I**on **S**pectrometer

SMU	**S**ource **U**nit **M**easurement
SOI	**S**ilicon-**O**n-**I**nsulator
SRP	**S**preading **R**esistance **P**rofiling
TCAD	**T**echnological **C**omputer **A**ided **D**esign
ToF	**T**ime **of** **F**light
WBG	**W**ide **B**and **G**ap

Introduction

In the last years, the use of semiconductor radiation detectors has been widely studied for high-energy physics (HEP). The technological development in this field has been centred on the Large Hadron Collider (LHC), the world's largest and most powerful particle accelerator with a circumference of 27 km, which has been the place where the particle physics community has been studying physical phenomena and the origin of the universe for years. The High-Luminosity LHC (HL-LHC) promises to improve the performance of the already mentioned LHC by providing it with a much higher luminosity ($\sim$ 3000 fb^{-1}), i.e. a higher number of interactions, which will result in a much larger capacity to generate experiments, and in turn, collect more data.

The development of radiation detectors plays a crucial role in particle accelerators since they need to offer specific efficiency in detecting the trajectory and timing of particles crossing the detector. In that sense, new sensors are being developed to enhance their performance using novel structures and materials, in order to be used in the HL-LHC. The main added problem in the use of detectors for HEP experiments is the degradation of their capability when exposed to high levels of radiation. Therefore, their development in this field also includes a specific study to improve their performance under high radiation levels. Many projects are established to develop detectors for the HL-LHC. For instance, the RD50 project aims to develop radiation hard semiconductor devices for very high luminosity colliders.

In addition to their use for HEP applications, radiation sensors have been used in other radiation sources such as synchrotrons, where X-Rays are used to study the properties of various materials. Therefore, it is important to use radiation devices capable of detecting X-rays of different energies to cover a wide range of applications. However, in the same way as in particle accelerators, X-Ray irradiation induces radiation damage which makes it necessary to optimise the design and technological characteristics of the sensors. The use of radiation detectors for X-Rays opens up the possibility of their use in medical and health applications. In addition, the possibility to detect different types of radiation provides a wide range of applications for these devices.

The Institute of Microelectronics of Barcelona (IMB-CNM), which is the Barcelona headquarters of the National Microelectronics Centre (CNM, CSIC), has developed several technologies in the field of radiation sensors in recent years. Within the framework of the RD50 project, the IMB-CNM has produced LGAD (Low Gain Avalanche Detectors) and 3D detectors for use in the ATLAS and CMS experiments, which will

be modified and improved for the HL-LHC. The development of LGADs has been extended to several manufacturers and research centres due to their characteristics like an intrinsic amplification of the signal and their application in the field of particle physics. The technological parameters, as well as their design, have been studied and developed in recent years at IMB-CNM in order to present a better performance. The fill-factor problem is a crucial design challenge where signal amplification is lost in a certain area of the sensor. In order to overcome the fill-factor problem, which entails the fabrication of sensors with an amplification independent of the incident position, some structures have been fabricated on behalf the LGAD technology. The inverted LGAD (iLGAD) and the AC-LGAD have been proposed by IMB-CNM in order to meet the specifications of a 100% fill-factor.

This thesis presents the latest advances in the development of LGAD and iLGAD detectors for use in various applications. Mainly, this development focuses on the improvement of the detectors for use as timing detectors in the ATLAS and CMS detectors and as X-Ray detectors. Thus, this work presents the various technological challenges encountered during the development of radiation detectors, such as the optimisation of the termination of the sensors, the use of different wafer sizes and the need to optimise the sensor design to obtain a performance according to the final application. The detectors have been designed under TCAD (Technological Computer Aided Design) simulations, manufactured in the IMB-CNM clean room and characterised in the specialised laboratories of the IMB-CNM and in several laboratories within the RD50 collaboration.

- **The first chapter** presents the state of the art of radiation detectors, as well as an introduction to the different types of LGAD detector structures.
- **The second chapter** focuses on the development of thin detectors for use as timing detectors in the ATLAS and CMS experiments. This chapter covers the entire detector development process, including design, fabrication and a comprehensive characterisation of the sensors (non-irradiated and irradiated).
- **The third chapter** presents the challenge of developing LGAD timing detectors on 150 mm wafers. Here, the technological optimisation process to achieve similar performance to that previously obtained on 100 mm wafers is shown. In addition, the fabrication process and the characterisation of the detectors before and after irradiation are detailed.
- **The fourth chapter** shows the development of iLGADs for use as X-Ray detectors. The sensor termination has been optimised to achieve enhanced performance under the effects of X-Ray irradiation. The fabrication process of these sensors is also detailed, as well as the electrical characterisation before and after being irradiated with X-Rays, to assess whether the optimisation of the design has been successful.

- **The fifth chapter** is devoted to the development of a new design for the iLGAD. In this case, a trench termination is presented to improve performance and reduce the manufacturing processes discussed in the previous chapter. The entire design optimisation development and a first manufacturing proposal for the detector are presented in this work.

- **In the sixth chapter**, a further variant based on the LGAD is presented. In this case, we have developed an LGAD with an n-type substrate (nLGAD). The chapter details the technological optimisation process to achieve a functional LGAD with a different substrate to the one used in the previous fabrications. The fabrication and first experimental results are presented. In this way, the new Proton LGAD (pLGAD) design is detailed, which promises to detect very low-penetration particles in silicon such as low-energy protons. The design and optimisation of the sensor, which is based on the nLGAD, is highlighted.

Chapter 1

Semiconductor Radiation Detectors

An extended review of semiconductor radiation detectors is described in this chapter. It includes the use of detectors for high-energy physics and synchrotron applications, the basic working principles of silicon detectors, the description of detectors with intrinsic gain and segmented sensors. Finally, a review of radiation damage in radiation detectors is given.

1.1 Introduction

Semiconductors are considered one of the main materials to detect radiation due to their unique properties, like fast charge collection and the possibility to fabricate very small structures ($\sim$ nm). Compared to gas detectors, in semiconductor radiation detectors (SRDs) the required energy to produce a signal is lower (3.6 eV in silicon compared to 30 eV in gas). Furthermore, semiconductors are commonly used in the microelectronics industry, and they take benefit from the knowledge acquired in this field with semiconductor materials. The choice of semiconductors as detectors is also made due to the simplicity of the integration of the detector with the electronics.

Silicon (Si) is the main material used in microelectronics and, therefore, silicon detectors have been widely used as radiation detectors among other materials. Germanium (Ge) is another elemental semiconductor that is also used in microelectronics, as well as silicon-germanium (SiGe). Semiconductor compounds such as gallium arsenide (GaAs) or cadmium telluride (CdTe) have been also considered radiation detectors, especially for X-Ray and gamma detection [1]. Wide bandgap semiconductors (WBG) like silicon carbide (SiC) and gallium nitride (GaN) are commonly used in the power devices field [2] and they are considered as detectors due to their better electrical and thermal properties than elemental semiconductors [3, 4, 5, 6, 7]. SiC sensors are considered owing to their better radiation hardness and low leakage current than silicon, which gives SiC an outstanding material for harsh radiation fluences. For instance, 4H-SiC PiN detectors have been successfully fabricated and characterized for timing applications [4]. GaN devices are specially studied for X-Ray and α-particles detection. Nevertheless, the lack of commercialization of high-quality substrates and

the difficulty to produce p-type substrates prevents GaN sensors to be considered in large-scale productions. In addition, diamond is also considered to detect radiation due to their greater mobility of holes and electrons and the ability to sustain a higher breakdown voltage than silicon. Nevertheless, the signal generated by a particle is smaller and it is more expensive due to the necessity of a high-purity substrate and the lack of large-scale growth techniques [8]. Despite the improved performance of WBG materials, silicon has been chosen over these materials due to their better integration with microelectronics fabrication, the availability of Si in nature, and the ability to fabricate very complex structures. Moreover, for large-scale productions, silicon presents a lower operative cost.

Table 1.1 shows the main properties of some of these materials at T=300 K [9, 10, 11]. The first property described in the table is the density of the material, which is directly related to the energy lost per unit length. Therefore, materials with a higher density can provide sufficient signal to detect particles in thin detectors, as is the case for CdTe, which is used to detect X-Rays that in silicon detectors need a much larger thickness [12]. Another property to take into account is the E_g value, since the lower it is, the higher the number of charge carriers per unit energy loss. In this sense, Ge was used in the first detectors for particle physics [13]. However, such a low E_g requires an operating temperature of 77 K, which complicates the functionality of the detector. It is important to mention that the mobility of both electrons and holes plays a crucial role in particle detection since higher mobility implies faster charge collection (10 ns in Si). Finally, the e-h pair creation energy gives us a measure of the threshold energy to operate the detector. In this case, the diamond would need much higher energy than silicon, for example.

	Si	**Ge**	**GaAs**	**CdTe**	**4H-SiC**	**Diamond**
Density (g/cm^3)	2.39	5.32	5.3	6	3.2	3.2
E_g (eV)	1.11	0.66	1.4	1.4	3.26	5.4
μ_e(cm^2 V^{-1} s^{-1})	1350	3900	<8500	1000	750	1900
μ_h (cm^2 V^{-1} s^{-1})	500	1900	<400	-	100	1600
e-h creation (eV)	3.6	2.96	4.3	4.4-4.7	7.8	13

Table 1.1: Main properties of semiconductor materials at T=300 K

The main application of SRDs is their use in high-energy physics (HEP) experiments, which involve the collision of light particles such as electrons, protons or positrons accelerated to energies of the order of GeV or TeV. Because of these collisions, many of particles are generated, the properties of which are the object of study. Moreover, SDRs are widely used in synchrotron facilities, where high-energy electrons produce X-Rays at different energies to provide techniques to learn about the structure and behavior of matter at the molecular and atomic levels. SRDs are also present in

life science and health applications [14, 15], like radiography and radiation therapy, taking advantage of their use as X-Ray detectors.

The main problem related to SRDs is the radiation damage produced in the detectors when they are used in harsh environments. Depending on the type of radiation, the detector is subjected to different damage. For instance, the irradiation of high-energy particles implies bulk damage, while X-Rays produce damage at the surface of the sensor. This radiation affects the performance of the detector, diminishing its operability, and, as a result, the difficulty to use them in a radiation environment. HEP facilities, like the Large Hadron Collider (LHC), will require in the future extreme radiation fluences, and, therefore, new materials like WBG semiconductors and novel structures have been studied in recent years in order to find solutions to increase the radiation hardness of semiconductor radiation detectors.

1.2 Detectors for HEP experiments

Understanding the elementary particles that are the fundamental constituent of the matter is the main goal of HEP. In this respect, CERN has played a very important role by setting up the LHC in 2008, which is the world's largest (27 km in circumference) and most powerful particle accelerator.

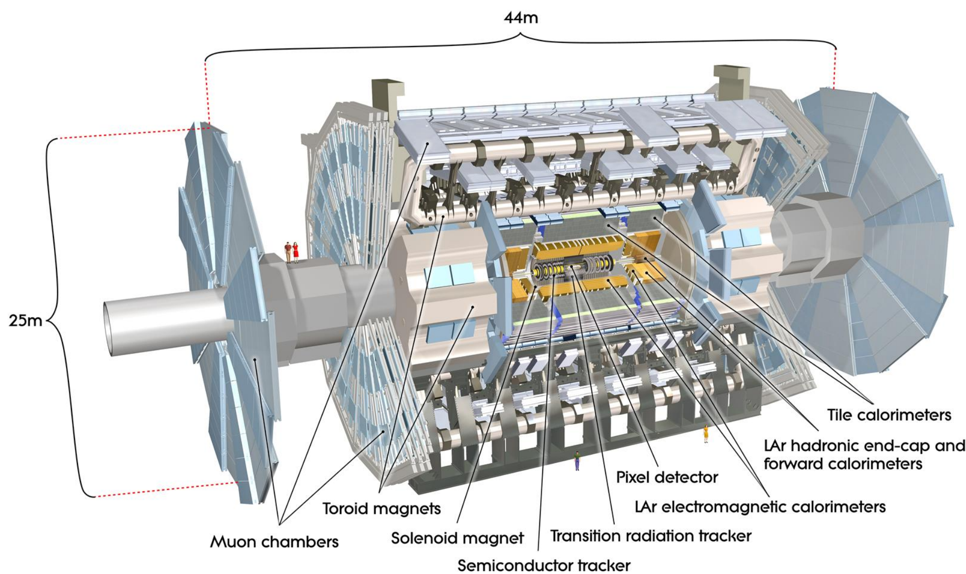

Figure 1.1: ATLAS detector experiment. Extracted from [16].

The beams of the LHC were made to collide at four points around the LHC, where there are four particle detectors: ATLAS (A Toroidal LHC ApparatuS), CMS (Compact Muon Solenoid), ALICE (A Large Ion Collider Experiment) and LHCb (Large Hadron Collider beauty experiment). ATLAS experiment investigates the search for the Higgs boson, extra dimensions, and dark matter. ATLAS detector is depicted in figure 1.1. The CMS experiment covers a similar range of physics experiments as

ATLAS. However, they use a different technical approach. The design of the magnets is different and the technical staff works independently, in order to find the best solution following a different path. ALICE studies the physics of strongly interacting matter at extreme energy density, where a phase of matter called quark-gluon plasma forms. This experiment is designed to recreate the conditions that existed in the universe just after the Big Bang. Finally, LHCb investigates the differences between matter and antimatter, by studying the “beauty quark” [16]. No detector can detect all the particles and provide all the necessary measurements in a HEP experiment. Therefore, the detectors built in the LHC are made with a different types of detectors, creating different layers. For instance, in figure 1.2 one can see a transverse slice through the CMS detector.

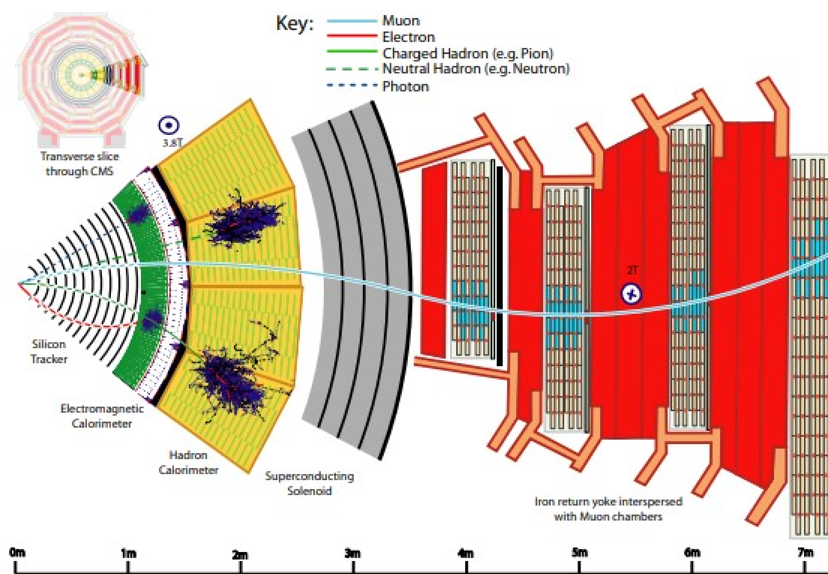

Figure 1.2: CMS detector experiment. Extracted from [17].

In a detector, there should be four types of detectors:

- **Tracking detectors.** They provide a precise measurement of the track and momentum of the charged particles, which are subjected to magnetic fields.
- **Vertex detectors.** These are the innermost tracking detectors, which can determine the direction of the particle in order to find its origin.
- **Calorimeters.** These detectors measure the energy of photons, electrons, and hadrons through absorption.
- **Muon detectors.** Used to identify and measure with precision the momentum of muons outside the magnet.

1.2.1 High-Luminosity LHC

The HL-LHC is a project that aims to improve the performance of the LHC by increasing the luminosity by a factor of 10. The luminosity of the accelerator is

proportional to the number of collisions occurring in a certain time range, which results in more data and experiments. This implies an advance in the study and discovery of new phenomena and particles. However, this advance in luminosity leads to much higher radiation exposure, causing the detectors to be affected. In addition, the pile-up effect, which is the number of collisions per bunch crossing, is being increased in the HL-LHC. Therefore, both ATLAS and CMS experiments are being revamped to cope with the new requirements. Specifically, the High Granularity Timing Detector (HGTD) and the Endcap Timing Layer (ETL) of the ATLAS and CMS experiments, respectively, are being updated using appropriate timing detectors with a low time resolution.

Timing detectors and 4D tracking

There is widespread interest in the particle physics industry in measuring the temporal information of charged particles since it is used to identify them using the Time-of-Flight (ToF). The standard ToF schemes are usually large since there is a necessity to have long distances between the production and detection points. For this reason, fine granularity sensors like silicon-based diodes, Cherenkov gas detectors, or scintillators have been investigated to obtain a fast ToF [18]. Timing detectors able to provide temporal resolutions of 10-30 ps, can be used to reduce the expected high pile-up effect in the HL-LHC since they are able to measure the arrival time of each track with high precision.

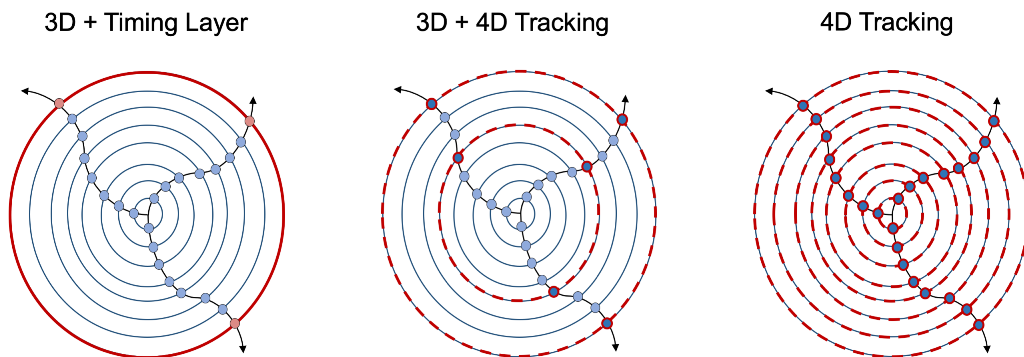

Figure 1.3: Different configurations of a tracking system with timing capabilities. Adapted from [18]

SDRs can be subjected to segmentation in order to measure the track of the particles with higher precision. In this sense, striped (2D) and pixelated (3D) electrodes are used as tracking detectors due to their low-resolution measurement of the trace of charged particles. Nevertheless, the use of silicon detectors for the HL-LHC must combine low tracking and timing resolutions, which introduces the concept of 4D tracking, where a detector exhibits high precision in tracing the particle's trajectory and at the same time a very low time resolution. Figure 1.3 shows different 3D tracking systems that are able to provide timing information. The first configuration is the most feasible since it only requires a timing layer added to the 3D detection

system, which is composed of some stacked tracking layers. This system will collect the timing information at the first timing layer (red dots) without having spatial information. On the contrary, in the next tracking layers, the spatial information will be recognized (blue dots). The second possible configuration combines both 3D and 4D tracking capabilities, where one or more 4D tracking layers are added to the detector. Then, both time and spatial information of any particle crossing the 4D tracking layer are received by the detector (blue-red dots). Therefore, this configuration shows 4D tracking capability only in a few layers, since the rest are standard 3D tracking layers. Finally, the last possible construction is the development of a full 4D tracking system, where all the layers are able to provide 4D information. Nevertheless, the development of this system is very challenging. For some applications, the intermediate configuration can be enough since does not require such low temporal and spatial resolutions.

For the ATLAS and CMS timing detectors updates, the Low Gain Avalanche Detectors (LGAD) have been proposed thanks to their ability to be segmented and achieve low temporal resolutions [19, 20]. In addition, these sensors are being optimized to enhance their timing performance and their tracking capabilities using LGAD-based designs [21, 18].

1.3 Detectors for synchrotron radiation

A synchrotron is a huge installation that produces light with outstanding properties and it is based on a circular accelerator of charged particles (electrons). It is well established that charged particles that are accelerated produce electromagnetic radiation. As electrons are reflected through powerful magnetic fields, a synchrotron can produce extremely brilliant light, which wavelength ranges from the X-Rays to infrared light.

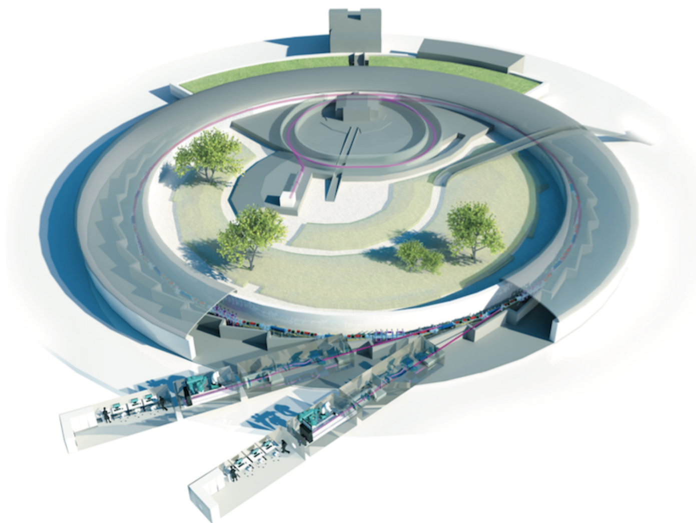

Figure 1.4: Sketch of a synchrotron facility. Extracted from [22].

The photon flux can be up to 10^{14} photons/second with a range of energies between 0.1-150 keV which leads to different applications. Nevertheless, this huge flux can lead to radiation-induced detectors. Therefore, X-Ray detectors have been developed in recent years to cope with these requirements. Figure 1.4 shows a sketch of a synchrotron. Electrons are generated in the LINAC (LINear ACcelerator) and, afterward, the electron beam is transferred into the Booster synchrotron where it is accelerated up to almost the speed of light. These electrons are injected into a storage ring, which is maintained at very low pressure (10^{-9} mbar) since it is mandatory to avoid the electrons from colliding with residual molecules and thus deflecting their trajectory. Surrounding the storage ring, some laboratories are placed in order to study the light emitted by the electrons, which are called beamlines. Here, the light is studied depending on the knowledge area or the final application [22, 23].

1.3.1 European Synchrotron Radiation Facility (ESRF)

The European Synchrotron Radiation Facility (ESRF) is in Grenoble, France. It is one of the most cutting-edge X-Ray sources in Europe. The operational energies of the ESRF range from 10-120 keV. The ESRF-EBS (Extremely Brilliant Source) is an upgrade during 2015-2022 for the ESRF [24], which will bring a high-energy light synchrotron source. The new X-ray source will open a huge variety of groundbreaking research techniques and will cover a wide range of applications such as health, biology, climate, energy and sustainable economy, materials and innovative industry, world cultural heritage and earth sciences, and planetary research. ESRF has developed a project for the development of novel 2D detectors during 2016-2022, which has two main schemes:

- Research and development of new 2D detectors:
  - Noise-free small pixel detectors.
  - Large format detectors for high-energy diffraction.
- Technology programs:
  - High-Z and advanced semiconductor sensors, structured and high-resolution scintillators for imaging detectors.
  - Advanced control and data acquisition.
  - Energy dispersive detection technology.

For this reason, there is a huge interest to develop X-Ray detectors to cover all the schemes proposed in this project.

1.3.2 X-Ray detectors

Since synchrotrons use X-Rays, specific detectors must be fabricated to detect them. Figure 1.5 shows the classification of X-Rays as a function of the photon energy range

and the typical technology used, where semiconductor-based detectors are used for direct detection of X-Rays. An incident X-Ray creates electron-hole pairs in the active volume of the detector, leading to a detectable signal.

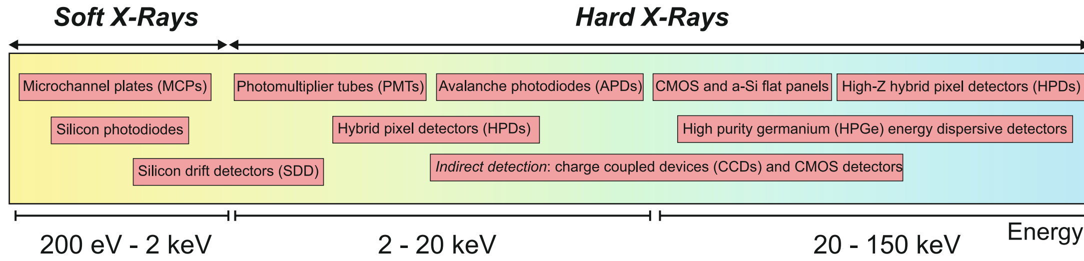

Figure 1.5: X-Ray classification by photon energy range and typical detection technologies used. Adapted from [25].

The operation can be explained by using the basic PiN detector, where is desired to have a high-resistivity substrate to deplete the substrate. APDs (Avalanche Photo-Diode) and HPDs (Hybrid Pixel Detectors) are used for hard X-Rays with medium energy. All of them are going to be fully described in the following chapters. On the other hand, scintillators are used for the indirect detection of X-Rays. Scintillation is the phenomenon where light is emitted when radiation is absorbed in a certain material. X-Rays go through a scintillating material and an image sensor collects the emitted light, which can be converted to a detectable signal. MCPs (Microchannel Plates) and PMTs (Photomultiplier Tubes) are common scintillator detectors used for low-medium X-Ray detection.

X-Ray interaction with matter

The interaction between X-Rays and matter is crucial to understanding how an X-Ray detector works. Lambert-Beer law states that the intensity of a photon decreases exponentially with the thickness of the material and depends on the incident photon energy [26]. Equation 1.1 shows this dependence.

$$I(x) = I_0 \exp\left(-\mu E x\right) \tag{1.1}$$

Where µ is the attenuation coefficient and depends on the material. The mass attenuation coefficient is defined as the attenuation coefficient µ per density unit. Figure 1.6(a) shows the behavior of the mass attenuation coefficient of Si as a function of the incident photon energy. As can be observed, photoelectric absorption is the dominant contribution until 50 keV.

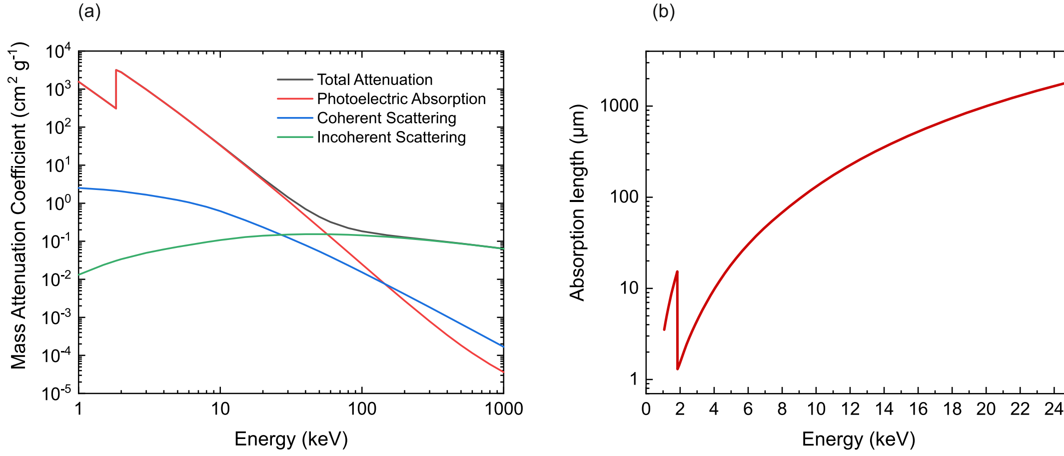

Figure 1.6: (a) Mass attenuation coefficient of silicon as a function of the photon energy. (b) Photon absorption length in silicon as a function of the incident energy. Data were taken from [27].

Figure 1.6(b) shows the photon absorption length in Si as a function of the energy. Depending on the application (i.e., the photon energy), the detector should have a thickness according to these characteristics. Silicon detectors are limited up to 25 keV since the active substrate must be higher than 1 mm for higher energies. The photoelectric absorption efficiency with 500 µm thickness falls to a 20% at 25 keV [28]. For this reason, silicon-based detectors are not the best option for high-energy X-Rays. Therefore, other semiconductors like Cd(Zn)Te or GaAs are under investigation due to their higher density than silicon. The attenuation coefficient in these compounds is much bigger than in Si, providing detectors to be used for high-energy X-Rays applications. Moreover, thin substrates of high-Z semiconductors are suitable for lower energy ranges.

1.4 Silicon detectors

Silicon detectors have been widely used for HEP and X-Ray applications and they have evolved to reach optimal performance for each field. In this section, the basic principles of silicon detectors are depicted, using the PiN diode as a reference.

1.4.1 Charged particles interaction with matter

The charge deposited by a particle passing through a detector is directly related to the energy of the particle, so it is essential to understand the interaction between charged particles and the substrate of a detector. In this way, it is possible to determine the energy of charged particles. Charged particles deliver part of their energy through elastic collisions with electrons. The rate of ionization loss ($-dE/dx$) of a charged particle in the matter is modeled with the Bethe-Bloch formula [11].

$$-\frac{dE}{dx} = Kz^2\frac{Z}{A}\frac{1}{\beta^2}\left(\ln\frac{2m_e c^2\gamma^2\beta^2 T_{max}}{I^2} - \beta^2 - \frac{\delta}{2}\right) \tag{1.2}$$

where $K = 4\pi N_A r_e^2 m_e c^2$= 0.307 MeV cm^2, z is the charge of the particle, Z and A are the atomic and mass numbers, respectively, $m_e c^2$ is the electron rest mass energy (511 keV), β is the velocity of the particle in speed light units, γ is the Lorentz factor ($1/\sqrt{1-\beta^2}$), I is the mean excitation energy (137 eV), δ and C are the density and shell corrections and, finally, T_{max} is the maximum energy transfer in a single collision. Because of equation 1.2, the energy loss of charged particles depends on the velocity of the incident particle. Since the maximum energy loss is reached for low and high-velocity particles, medium-velocity particles deliver the minimum energy loss rate. These particles are the so-called minimum ionizing particles (MIP), which are very useful in the characterization of detectors since their energy loss in silicon is well known.

1.4.2 Working principles of silicon detectors

The basic structure of a silicon detector is the p-n junction diode, which is typically used as a rectifier, for switching and other electronic applications. One can understand the basics of electronics through this structure. A junction of an n-type and a p-type doped semiconductor composes the diode. Figure 1.7(a) shows the band diagram for two separated n and p semiconductors, where the Fermi level (E_F) for the p-type is just over the valence band since there is a lack of electrons and, on the contrary, the E_F for the n-type is underneath the conduction band. Figure 1.7(b) shows the band diagram when the junction occurs at thermal equilibrium.

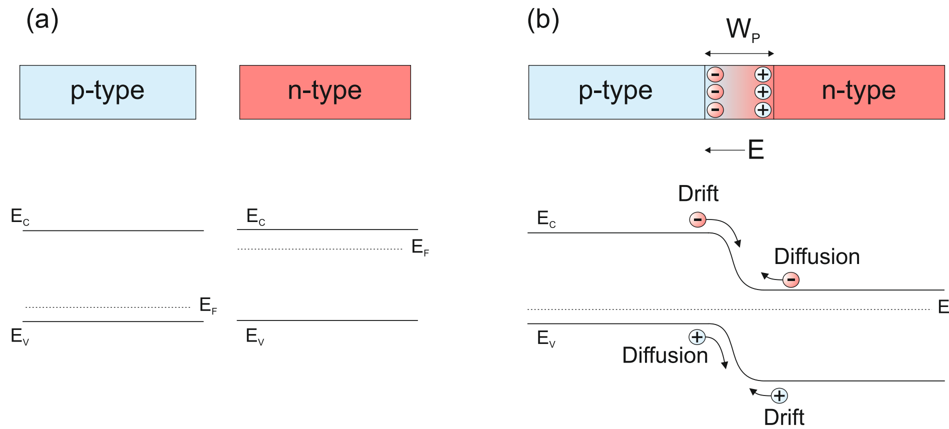

Figure 1.7: Band diagram **(a)** before junction and **(b)** at thermal equilibrium. Adapted from [10]

There is a carrier concentration diffusion due to a large carrier concentration gradient. Holes diffuse from the p-type to the n-type and electrons from the n-type to the p-type. Since holes are mobile and acceptor ions are fixed, some negative acceptor ions (N_A) near the junction are left uncompensated. On the other hand, positive donor ions (N_D) are uncompensated as electrons leave the n-type material. Consequently, a negative space charge is created at the p-type and a positive at the n-type leading to a gradient of space charge, which creates an electric field between both semiconductors. This electric field goes from the n-type toward the p-type. Therefore, holes are drifted

from the n to the p, and, on the contrary, electrons are drifted from the p towards the n.

1.4.3 PiN diode

Based on the p-n junction, the PiN diode is the standard silicon sensor used for particle detection and it is going to be used to describe the main characteristics of silicon sensors. It is based on the junction of three semiconductors: one p-type doped, one very low doped which can be p-type or n-type, and one n-type doped semiconductor, thus leaving a highly resistive material between the p-n junction described above.

Current and capacitance characteristics

PiN diodes are operated with a reverse voltage, in order to have a wider spatial region of charge. Because there are no moving charges on the substrate, any charge created by a charged particle passing through the bulk of the detector can be detected. By applying an inverse voltage, the spatial region of charge (W) can be calculated by solving Poisson's equation assuming an abrupt junction between the two semiconductors:

$$W = \sqrt{\frac{2\epsilon_s}{qN_B}(V_{bi} - V)} \tag{1.3}$$

Where the built-in potential (V_{bi}) is the electrostatic potential difference between the p and n regions in thermal equilibrium and N_B is the bulk doping concentration, which corresponds to the highly resistive semiconductor. Taking equation 1.3 into account, by decreasing the substrate doping concentration, the detector's space charge is increased. The detector's depletion width is related to the depletion capacitance by:

$$C = A\frac{\epsilon_s}{W} \tag{1.4}$$

Their unit is the Faraday (F) and it can be also written as capacitance per unit area (C_j). Equation 1.4 can be re-written as a function of N_B and C_j:

$$\frac{1}{C_j^2} = \frac{2(V_{bi} - V)}{q\epsilon_s N_B} \tag{1.5}$$

One can use equation 1.5 to calculate the doping concentration of the bulk with the capacitance. Capacitance-voltage measurements are widely used to determine the depletion voltage of the diode and can be useful to determine the doping concentration by representing 1.5 versus the applied voltage. N_B can be calculated by applying a linear fit, extracting N_B from the slope of the curve. Drawing two tangent lines at the two different slopes, full depletion voltage (V_{FD}) is calculated from their intersection. Since a detector must work in full depletion, V_{FD} is the minimum voltage at which the detector can be operational. On the other hand, in order to know the maximum voltage at which the detector is operational, breakdown voltage (V_{BD}) is defined. In forward conduction, the current flows rapidly before one volt (0.7 in

Si). On the contrary, in reverse conduction, the current is very low (< 1nA) until it reaches the V_{BD} and the current starts to flow fast. Current-voltage measurements are commonly used to determine V_{BD} by applying a reverse bias. V_{BD} differs from different semiconductor materials and technological parameters used to fabricate the detector. In standard silicon PiN detectors, it can reach a thousand volts. Fig 1.8(a) shows the typical current-voltage in reverse and forward conduction. Fig 1.8(b) shows a $1/C^2$-voltage measurement, which is explained how V_{FD} is calculated. When the diode is under depletion, the capacitance is decreasing until it reaches the minimum capacitance value.

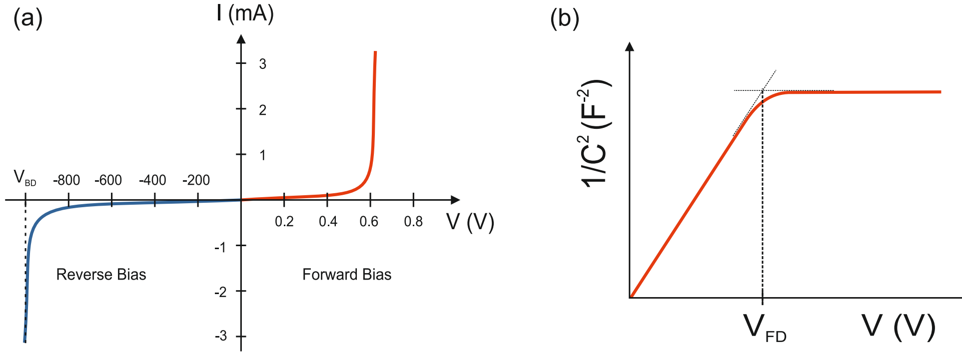

Figure 1.8: Typical **(a)** Current-voltage and **(b)** Capacitance-voltage graphs in a silicon PiN diode.

Signal formation

Fig 1.9 shows an illustration of a PiN detector working in full depletion mode. A particle is crossing the detector and generates electron-hole pairs in the high-resistivity silicon. An electric field is generated allowing a drift of the carriers toward the electrodes. Drift velocity is directly related to the electric field by:

$$\vec{v}_{e,h} = \mu_{e,h}\,\vec{E} \tag{1.6}$$

where $\mu_{e,h}$ is the mobility of electrons and holes, respectively. As electrons have higher mobility in silicon than holes (see table 1.1), their velocity is higher. Nevertheless, this relation is no longer linear at high electric fields [10], and velocity is saturated at a given electric field, reaching the saturation velocity. The Schockley-Ramo theorem [29] states that the charge (Q) and the current (i) that are induced by a moving point (x_0) with a charge q are given by:

$$Q = -q\;\varphi(\vec{x_0}) \tag{1.7}$$

$$i = \frac{dQ}{dt} = -q\left(\frac{\partial\varphi}{\partial x_0}\frac{dx_0}{dt} + \frac{\partial\varphi}{\partial y_0}\frac{dy_0}{dt} + \frac{\partial\varphi}{\partial z_0}\frac{dz_0}{dt}\right) = q\vec{v}\cdot\vec{E_\varphi} \tag{1.8}$$

where φ is the weighting potential and $\vec{E_\varphi}$ is the weighting field. They are related as $\vec{E_\varphi} = \nabla\varphi$. The weighting field is obtained by setting one electrode to one and the

others to zero and it only depends on the geometry of the electrodes. Nevertheless, the direction and the velocity of the charge are determined by the electric field.

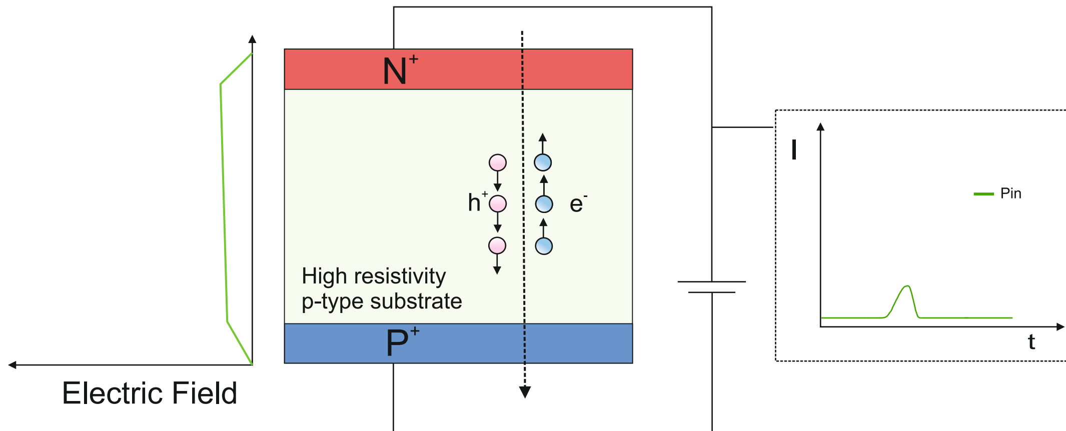

Figure 1.9: Sketch of a PiN detector.

ToF measurement

Time resolution can be altered by each step in the readout process and any effect that changes the shape of the signal. It can be expressed as the sum of different parameters [30] :

$$\sigma_t^2 = \sigma_{Timewalk}^2 + \sigma_{Landaunoise}^2 + \sigma_{Distortion}^2 + \sigma_{Jitter}^2 + \sigma_{TDC}^2 \tag{1.9}$$

- $\sigma_{Timewalk}$: Variation in the time of arrival produced by a different signal amplitude.
- $\sigma_{Landaunoise}$: Non-uniform energy deposition (by the incident particle) leads to irregularities in the signal shape.
- $\sigma_{Distortion}$: As seen in equation 1.8, induced current by a charge carrier is proportional to drift velocity and weighting field. A non-saturated drift velocity and non-uniform weighting field results in signal distortion.
- σ_{Jitter} :This parameter refers to electronic noise.
- σ_{TDC}: Uncertainty of the TDC bin.

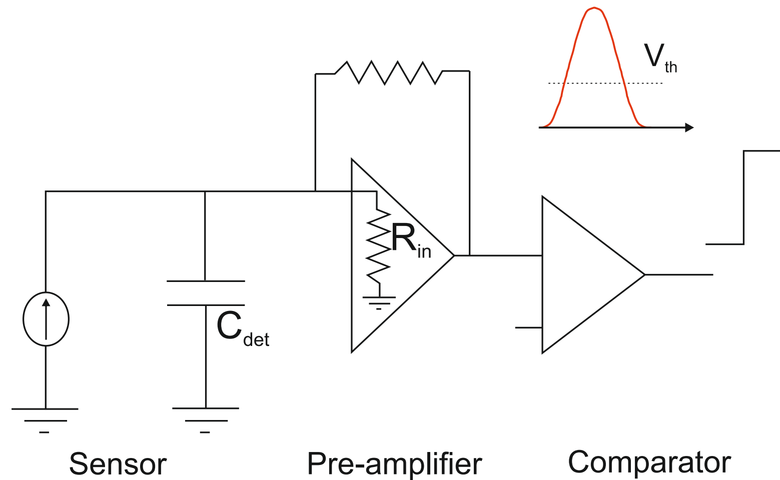

Figure 1.10: Schematic diagram of a time-tagging detector. Adapted from [30].

1.5 Detectors with intrinsic amplification

One advantage of SRD over gas detectors is a low energy required to produce a measurable signal which provides low noise electronics. However, an amplification of the signal is required due to a low signal. Detectors with an intrinsic amplification were proposed to amplify the signal reducing the amplification required by external electronic devices, which can rise the noise of the measurement.

1.5.1 Avalanche Photo-Diode (APD)

Avalanche Photo-Diode (APD) is one of the better-known diodes with intrinsic amplification, where a region with high electric field is created under the readout diffusion. Based on the forenamed PiN detector, a p-type layer (gain layer) is diffused underneath the n-type electrode, thus creating a high electric field in the p-n junction. Electrons collected by the n^+ electrode will pass through this region, and, in turn, these electrons are accelerated and then they create more electron-hole pairs that create themselves more electron-hole pairs. This mechanism is known as multiplication [11].

Figure 1.11 shows an illustration of an APD, the electric field across the thickness of the detector, and the signal obtained compared to that of a PiN diode. Thanks to the electric field peak at the n^+/p junction, an amplification of the particle signal can be achieved. Since the electric field depends on the sensor doping profiles, the thickness and peak of both diffusions are two critical parameters when making detectors with amplification. A trade-off between electrical performance and desired gain must be taken into account.

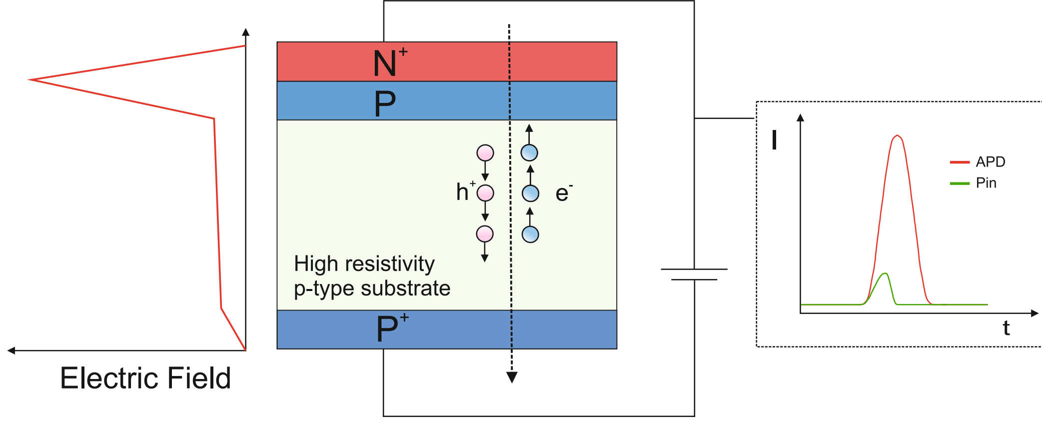

Figure 1.11: Sketch of an APD detector.

The charge collected by the detector can be determined by its relation to intensity and time by:

$$I = \frac{dQ}{dt} \Rightarrow Q = \int_{t_0}^{t_f} I \ dt \tag{1.10}$$

To quantify the signal amplification, the gain is defined as

$$G = \frac{Q_{AD}}{Q_{PiN}} \tag{1.11}$$

where Q_{AD} is the charge generated in an avalanche detector and Q_{PiN} is the charge generated in a PiN detector. As depicted in figure 1.12, an APD can operate in two different modes, depending on the applied voltage. The gain layer starts to deplete until the detector reaches the depletion gain layer voltage ($\mathrm{V_{GL}}$), where the substrate is under depletion until full voltage depletion ($\mathrm{V_{FD}}$) is applied. Applying a higher voltage than $\mathrm{V_{FD}}$, the APD has a low and linear gain value until the detector reaches $\mathrm{V_{BD}}$ and enters in Geiger mode, reaching high gain values. Typically, this linear behavior is observed during a low-voltage regime.

For HEP and X-Ray applications, it is usual to use APDs in linear mode to avoid injecting excessive noise into the measurement. Since the linear mode operation of an APD is reduced to a few volts, Low Gain Avalanche Detectors (LGADs) have been proposed due to their lower gain. These sensors are going to be fully described in the following sections.

In the high-energy physics community, it is common to express the gain of avalanche detectors as a charge collection (in fC). In this case, Q_{AD} is compared to the charge generated by a MIP particle. In [31], the energy loss of MIP particles is studied as a function of silicon substrate thickness. Knowing the thickness of the substrate used in an avalanche detector and its charge, the gain can be expressed in terms of the charge collected by the electrode in fC.

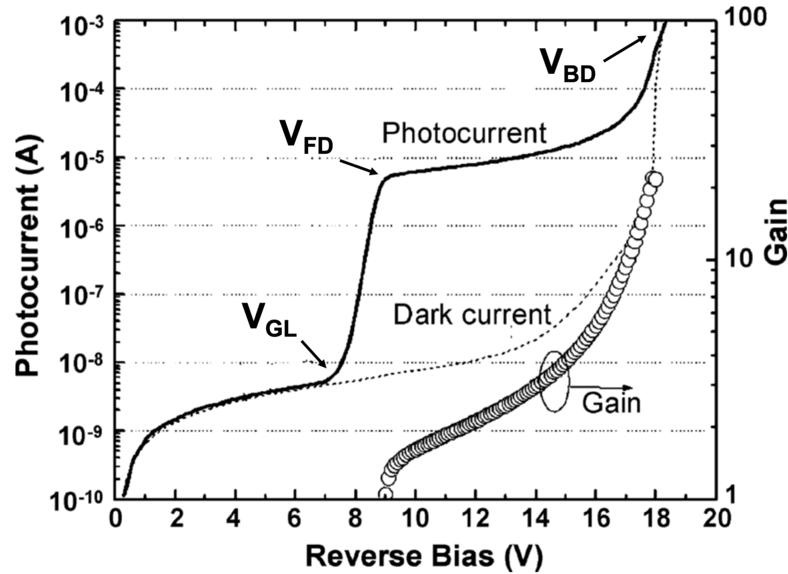

Figure 1.12: Typical I-V and gain characteristics of an APD detector [32]

1.5.2 Low Gain Avalanche Detector

Based on the APD concept, the Low Gain Avalanche Detector (LGAD) uses a p-type diffusion, called multiplication layer, less doped than an APD, which provides the sensor to prevent the signal to be over the dynamic range of the readout electronics [33]. Furthermore, LGADs can be operated in a wider voltage regime since there is an increase of V_{BD} caused by the lower electric field due to the low-doped multiplication layer. In addition, LGADs substrates can be thinned maintaining the performance as standard thick substrates, which can be useful for timing applications, where thin substrates ($\sim$ 50 µm) are required.

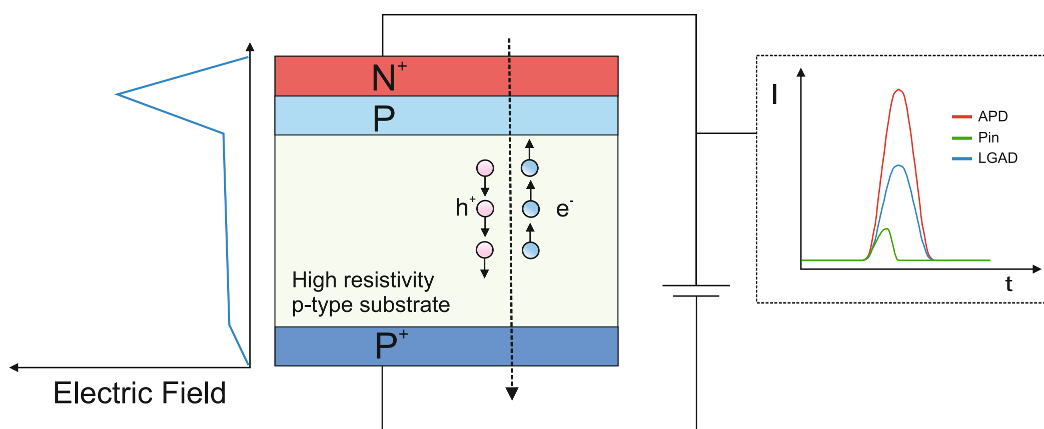

Figure 1.13: Sketch of an LGAD detector.

Figure 1.13 shows a sketch of an LGAD, the electric field distribution along the depth of the diode, and the signal compared with a PiN and an APD. As we can observe, the peak is lower than the APD and this provokes that the signal (and therefore the

charge) is lower. However, the charge collected is enough to achieve the desired signal amplification.

Collecting charge from a particle induces a certain noise in the measurement, caused by different mechanisms which are not related to the signal generation. We expect to have low noise in comparison with the signal amplitude. The relation between both is the so-called signal-to-noise ratio (S/N), which results low in LGADs. Therefore, we can achieve enough gain to amplify the signal without increasing the noise. Furthermore, it allows a finer segmentation since it presents a lower electric field, rather than the APD.

The same way as in the APD, energy, and dose of the boron implantation for the multiplication layer formation are the most important parameters. Small changes can lead to huge modifications in the gain and the breakdown voltage of the devices. Therefore, the doping profile must be optimized to reach the optimal gain. Figure 1.14 shows the simulated profile at the multiplication region for a standard LGAD fabricated at IMB-CNM. The peak value and the depth of the boron profile must be tuned since the gain will depend on the total charge. As already stated, there is a high sensitivity with the technological parameters and a trade-off between gain and voltage breakdown must be defined, depending on the final application.

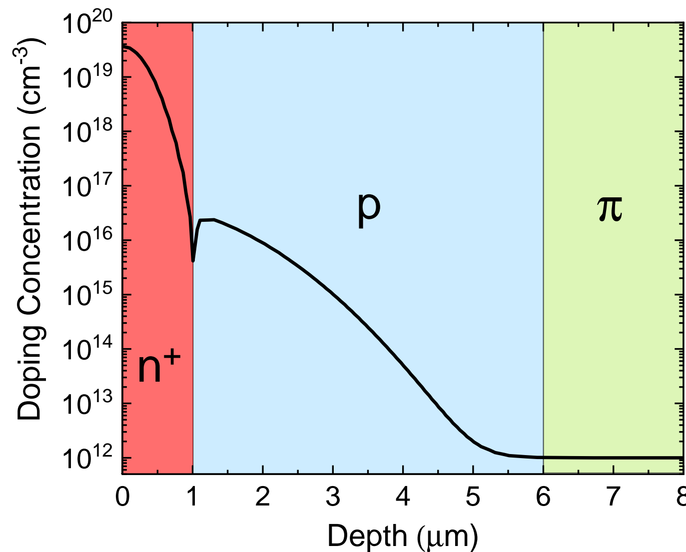

Figure 1.14: Simulated net doping profile of an LGAD sensor in the multiplication region.

In the last years, different profiles have been studied to enhance the performance of LGADs. In this sense, high-energy (deeper) with the lowest dose (lower peak) LGADs have been produced, maintaining a suitable charge (gain) while lowering the electric field peak. Having a wider and lower electric field distribution entails achieving a better uniformity of the multiplication layer peak over the wafer. In addition, this

profile has also been tuned and studied to withstand highly radioactive environments by enriching the multiplication layer with carbon [34].

LGAD was first successfully fabricated and characterized by IMB-CNM. These sensors have been widely studied in recent years for high-energy physics experiments [35, 36]. The following chapters are going to describe the last development of LGAD sensors developed in IMB-CNM for timing applications.

1.6 Segmented detectors

We are able to determine the energy of a charged particle traversing a detector since it is related to the deposited charge. Nevertheless, by using the design in figure 1.9, one cannot determine in which position of the detector the particle is going through, thus different designs have been studied in order to know the position and the energy simultaneously.

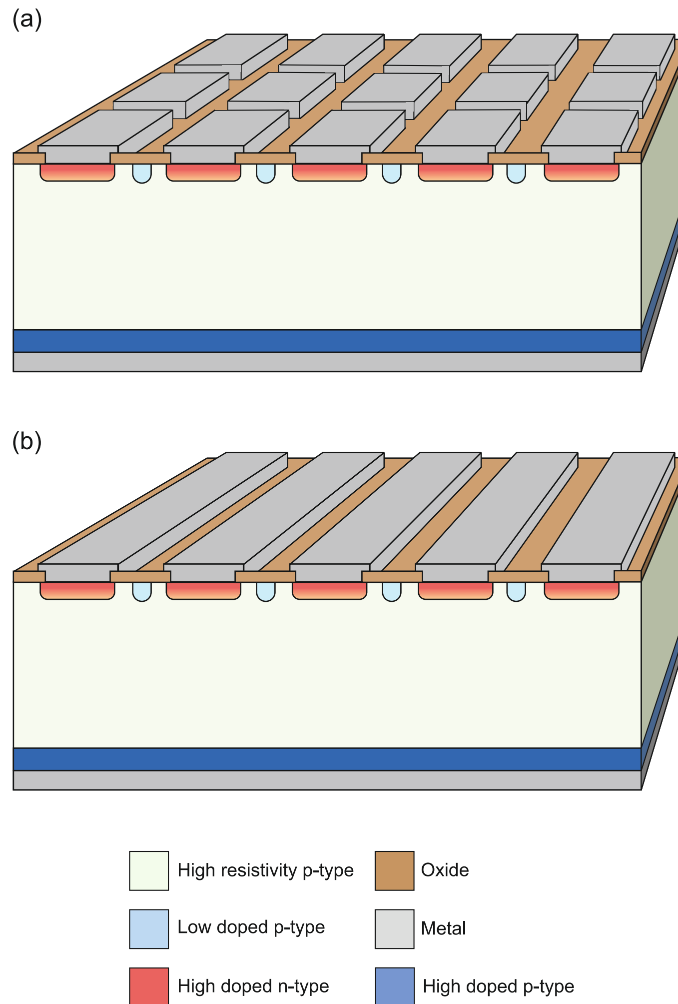

Figure 1.15: Sketch of (a) pixelated and (b) strip p-type silicon detectors.

One way to determine simultaneously the energy and position of a particle is by segmenting into strips (2D) or pixels (3D) the electrode that is acting as a collector. Therefore, by collecting the individual charge of each strip (or pixel), we are able to determine its position. Figure 1.15 shows a sketch of (a) pixelated and (b) strip detectors. In our case, as we were using a p-type PiN detector, the n-type diffusion is segmented.

Pixelated detectors can provide better performance than strip detectors since a high density of points can be achieved by segmenting the electrode. There is an important value in segmented diodes which is the pitch, which is defined as the distance between the centers of two adjacent electrodes (strip or pixel). The position resolution (σ_x) that a detector can achieve is directly related to the pitch by [11]:

$$\sigma_x = \frac{p}{\sqrt{12}} \tag{1.12}$$

Therefore, with low pitch distance, we can achieve very high position resolutions. Due to the advancements in photolithographic processing, nowadays very low pitch (< 60 µm) can be fabricated, which leads to a position resolution of ~ 15 µm. Silicon-based segmented detectors have been studied as tracking detectors, in order to measure the track of a particle going through the detector taking benefit of their high position resolution.

1.6.1 Hybrid Pixel Detectors (HPD)

HEP and X-Ray detection demands the use of big-area ($\sim$ cm^2), and, in this respect, hybrid pixel detectors (HPD) show great potential. These detectors consist of a connection between a segmented detector and an external readout chip (ASIC), where each pixel has a corresponding pixel on the readout chip. This hybridization allows a full area coverage and the possibility to optimize the sensor according to the desired application. One of the most widely used ASIC designs in the industry is the Medipix3 [37], which uses a 55 µm pitch (45 µm pixel width) and a 256x256 pixel array, giving the chip a high density of read points. The connection between the readout chip and the detector is made by solder bumps that are deposited on top of the detector pixels. Figure 1.16 shows a cross-section of an HPD, where it can be clearly seen how the pixel detector is connected by the solder bumps to the readout chip.

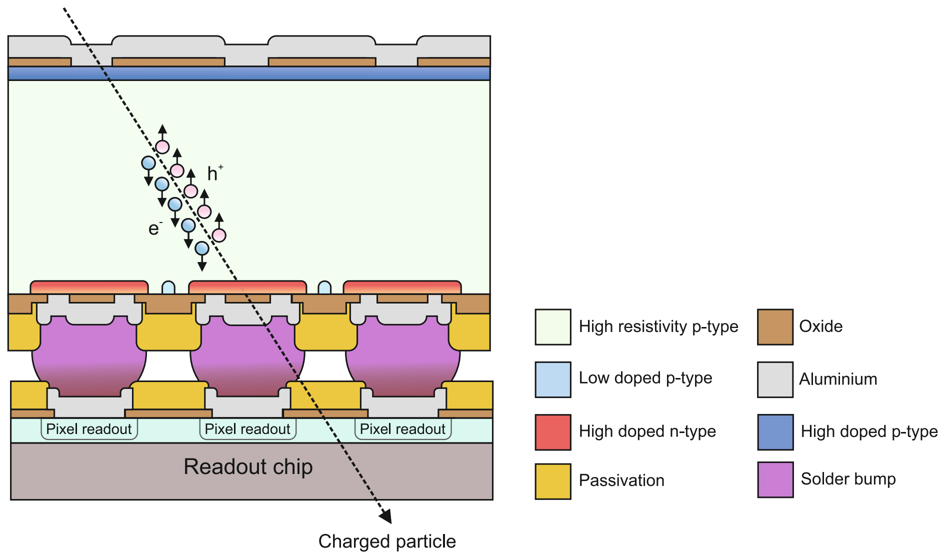

Figure 1.16: Cross-section of a hybrid pixel detector.

1.6.2 High-fill factor LGAD structures

In the same way as a PiN detector, LGADs can be subject to a fine segmentation of their electrodes. Figure 1.17 shows the cross-section of a pixelated LGAD into two neighbor elements and the expected gain across the device. Between both LGAD elements, there is an area of no gain, where the particles do not show amplification. In this sense, the fill factor is defined as the ratio between the gain area and the total area of the device. This factor is increased by decreasing the non-gain area between pixels. Nevertheless, planar sensors must be optimized to reach a trade-off between detector performance and this no-gain area.

Therefore, in order to increase the fill factor and thus the detection area in segmented LGADs, different structures have been reported in recent years, which are described in detail below.

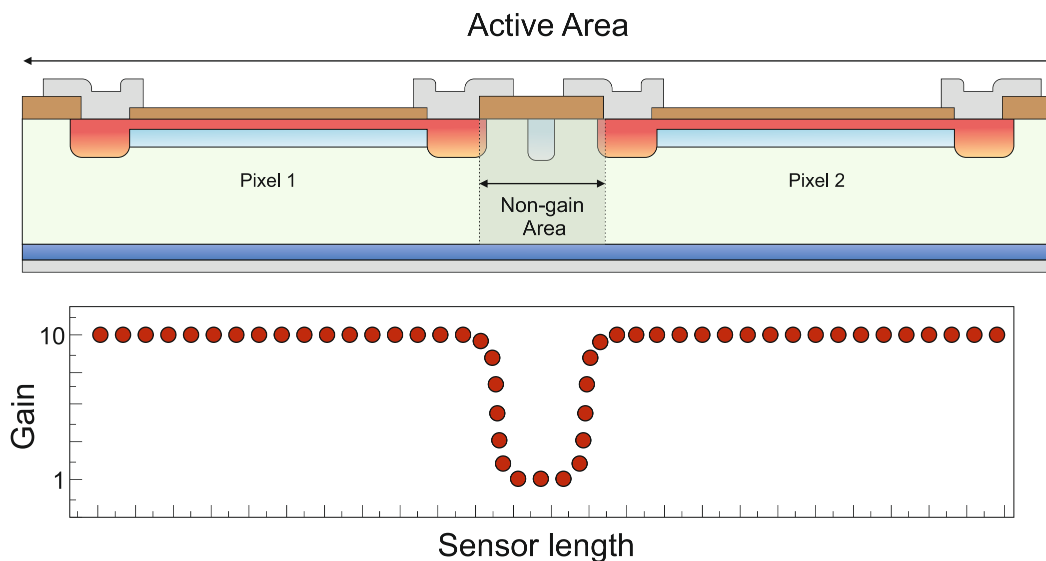

Figure 1.17: Cross section of two neighbors LGAD elements.

Inverse LGAD (iLGAD)

The inverse LGAD (iLGAD) sensor was first proposed by IMB-CNM [38, 39]. In this case, the segmentation is made at the ohmic contact, allowing a continuous unsegmented multiplication. Therefore, the charge collected by any charged particle crossing through the detector will be multiplied, whatever it is the incident point. Consequently, the fill factor of this structure is by definition 100%. Figure 1.18 shows the comparison between LGAD and iLGAD technologies. It is important to mention that collection is made by holes in the iLGAD since segmentation is done in the p^+ electrodes and this entails a slower timing performance in thick substrates due to the lower mobility of holes. Micro-strip iLGADs were successfully characterized showing a continuous gain making them suitable for tracking applications [40]. Next chapters will explain the development of different iLGAD technologies at IMB-CNM.

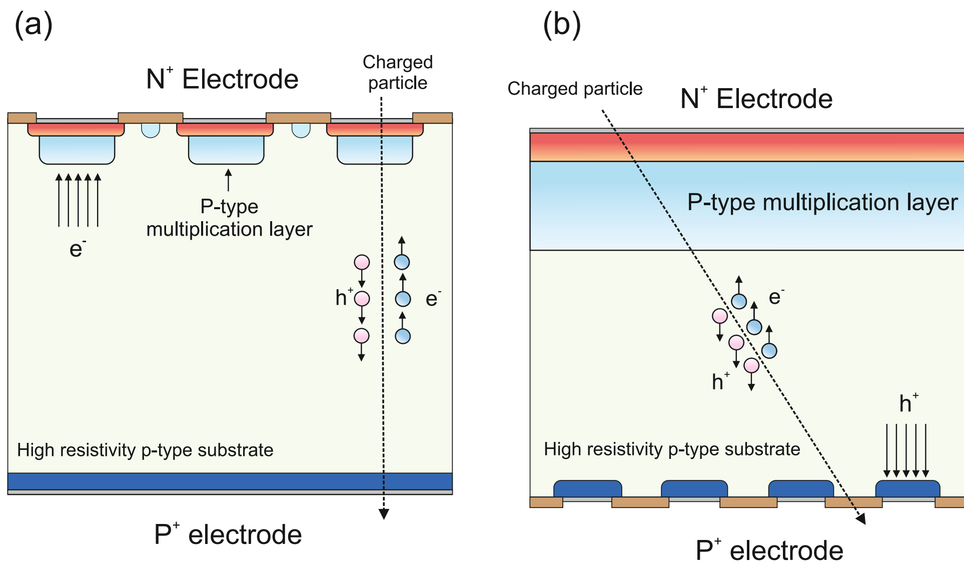

Figure 1.18: (a) LGAD and (b) iLGAD design comparison.

AC-LGAD

AC-LGAD is another sensor that is able to provide a fill factor of 100%. Figure 1.19 shows a scheme of the sensor. Based on the LGAD, here there is an AC-coupled readout through a dielectric and a n^+ resistive implant. Therefore, the n^+/p region is unsegmented while the segmentation is done at the AC-strips/pixels, allowing the device for the desired 100% fill factor. In these sensors, is very important to control the doping concentration of the resistivity n^+ layer and the dielectric thickness, as well as the multiplication layer. AC-LGADs were first successfully fabricated by IMB-CNM [41]. In addition, these sensors have been produced and tested by the Brookhaven National Laboratory (BNL) [42, 43] and the Fondazione Bruno Kessler (FBK) in collaboration with the Italian National Institute for Nuclear Physics (INFN) [44]

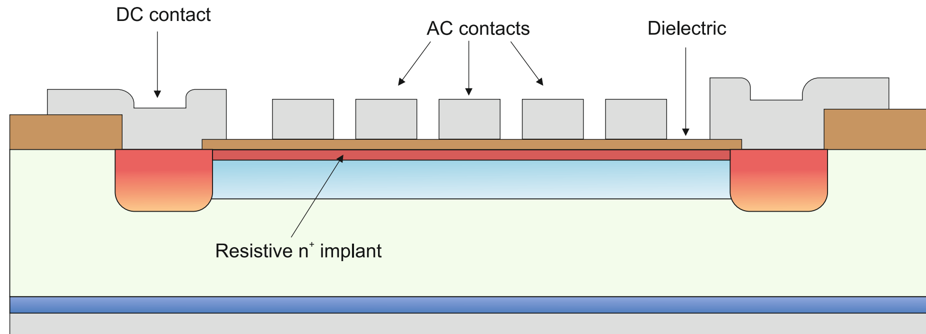

Figure 1.19: Cross-section of the AC-LGAD

Trench-Isolated LGAD (TI-LGAD)

In order to fabricate an LGAD reducing the non-gain area but maintaining a similar sensor design, the trench-isolated LGAD (TI-LGAD) has been proposed by FBK [45]. Figure 1.20 shows the design between pixels of this sensor. Here, a vertical trench isolates the pixels shrinking the non-gain area until up to 6 µm. Despite this design does not exhibit a 100% fill factor, it uses an existing technology used in CMOS (for instance, in silicon photomultipliers) and the electronics is the same that in standard LGAD sensors.

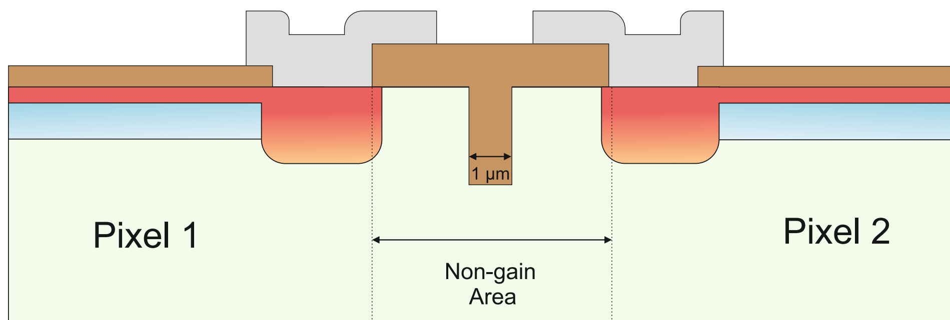

Figure 1.20: Cross-section of the TI-LGAD

Trench iLGAD

Based on the iLGAD, the Trench iLGAD sensor has been proposed by IMB-CNM [46], where an iLGAD is built on thin substrates ($\sim$ 50 µm) to be used for timing applications. Thus, this design exploits the main benefits of thin pixelated LGADs providing a 100 % fill factor and using trenches to isolate the active area of the sensor to reduce the fabrication steps. Figure 1.21 shows a cross-section of the Trench iLGAD sensor, where a low resistivity handle wafer supports the p-type multiplication layer and the thin high resistivity p-type substrate. P-type electrodes are diffused and activated on top of the device allowing the unsegmented multiplication at the bottom. Trenches arrive until the handle wafer properly isolates the active area. Chapter 5 is devoted to describing the whole optimization and fabrication of the Trench iLGAD.

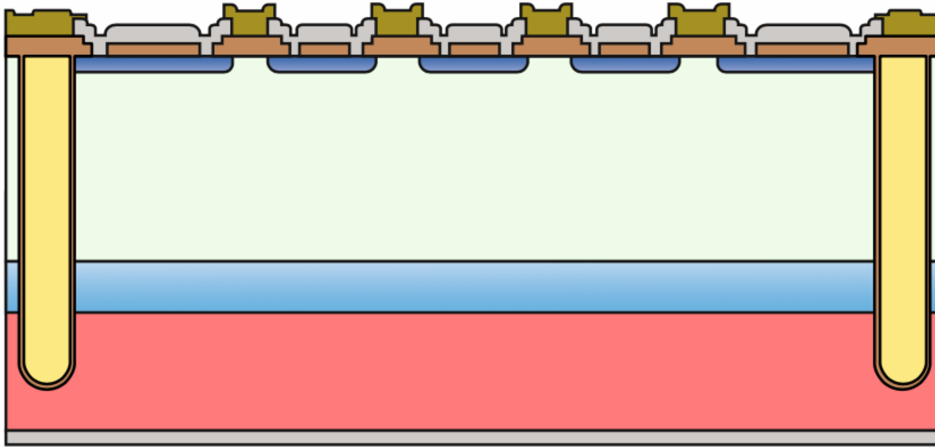

Figure 1.21: Cross-section of the Trench iLGAD sensor active area.

1.7 Radiation damage

Radiation detectors must be operated in harsh radiation environments, which lead to high radiation fluences, which diminish the performance of the detectors up to the point of they can be useless. Radiation damage can be distinguished into two types: ionization and displacement damage, depending on the type of radiation. Ionization does not damage the bulk of the detector, while it can create fixed charges in the insulating material and at the interface between the substrate and the insulating material. Therefore, ionization causes damage to the surface of the detector. On the other hand, displacement does not cause damage at the surface but it can damage the bulk of the detector, leading to an alteration of its properties [47].

1.7.1 Bulk damage

Bulk damage is the main damage mechanism in HEP experiments. In order to study the damage produced by different particles with different energies, the NIEL (Non-Ionising Energy Loss) was established. Under this hypothesis, radiation damage is scaled with a reference value set for 1 MeV neutrons. Therefore, irradiation studies scale the fluence used in the experiments to 1 MeV neutron fluence. High energetic particles like hadrons, leptons and photons provoke displacement damage in the bulk of the silicon detector. It is caused by displacing a *primary knock-on atom* (PKA) out of its lattice site. This displacement leads to a silicon interstitial and a leftover vacancy, which is defined as a Frenkel pair [48]. Some of these Frenkel pairs will be recombined, while the remaining pairs can migrate through the lattice reacting with other impurities in the bulk and producing point defects. Consequently, the properties of the sensors are altered [49]. The next subsections are going to describe the main effects due to bulk damage in silicon sensors.

Leakage current

There is an increase of the current in irradiated sensors due to the existence of defects close to the middle of the bandgap, which is charge carrier generation centers. The increase in current is proportional with to the 1 MeV equivalent fluence (Φ_{eq}) by:

$$\Delta I = I_{bulk}(\Phi_{eq}) - I_{bulk}(0) = \alpha \Phi_{eq} V \tag{1.13}$$

where α is the current-related damage factor and V the depleted volume.

Charge collection efficiency

Charge carriers travel through the detector as they are collected on the electrodes. In irradiated detectors, some of them can become trapped in a defect level by losing charge and thus reducing the detector signal. The probability of trapped charge increases with the presence of defects, which are greater in a high fluence environment. Consequently, charge collection efficiency (CCE) is decreased in irradiated detectors. This effect can be described assuming that the charge depends only on the transport time [50] and is related to the effective trapping time (τ_{eff}):

$$Q(t) = Q(0) \exp \frac{-t}{\tau_{eff}} \tag{1.14}$$

$$\frac{1}{\tau_{eff}} = \frac{1}{\tau_{eff}} + \beta \Phi_{eq} \sim \beta \Phi_{eq} \tag{1.15}$$

where β is the effective trapping damage constant. The effective carrier lifetime before irradiation ($\tau_{eff}(0)$) can be neglected in standard silicon. Therefore, τ_{eff} decreases linearly with fluence. Nevertheless, some studies have been carried out to demonstrate that this linear relation is not always present in high-radiation environments [30].

Effective doping concentration and depletion voltage

The defects induced by radiation lead to a change in the effective doping concentration (N_{eff}) of the sensor. Therefore, depletion voltage is also modified since it is directly related to N_{eff} by:

$$V_d = \frac{q|N_{eff}|d^2}{2\epsilon\epsilon_0} \tag{1.16}$$

where d is the thickness of the sensor, q is the elementary charge, ϵ_0 is the vacuum permittivity and ϵ is the relative permittivity of silicon.

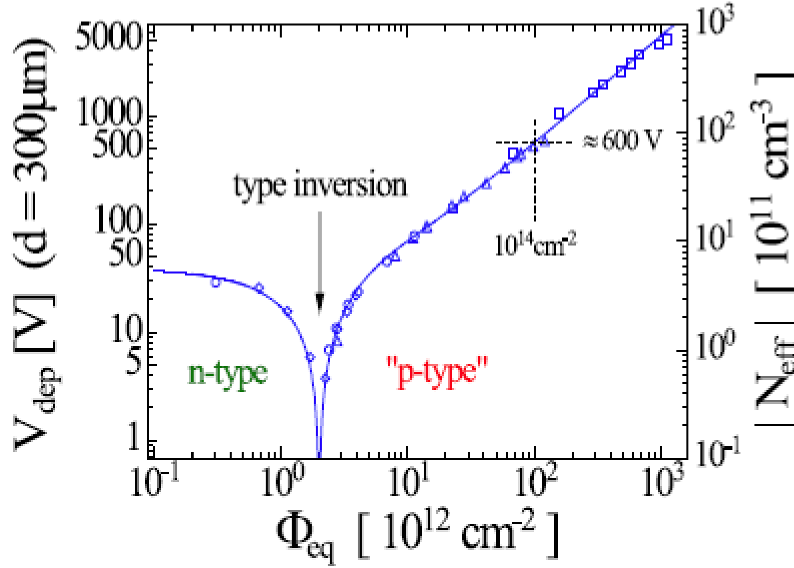

Figure 1.22: Depletion voltage and effective doping concentration dependence with the fluence for an n-type detector. Graph taken from [50].

Figure 1.22 shows the dependence of the effective doping concentration for an n-type detector with the fluence. It is clear that before irradiation, the detector has a high resistivity in the order of $\sim 10^{11}$cm^3. Nevertheless, due to radiation, there is a formation of a negative space charge, which compensates for the positive space charge of the initial substrate until it reaches very low values (almost intrinsic silicon). This phenomenon is the so-called inversion since the space charge sign is inverted from n-type to p-type. For a fluence higher than the inversion point the space charges become even more negative, reaching huge values for the depletion voltage. The sensor would not be operative for very high fluences since the depletion voltage is higher than the breakdown voltage of the detector. In high resistivity p-types substrates, the space charge remains negative and no inversion is expected. Therefore, detectors for HEP are usually built in high resistivity p-type substrates.

Acceptor removal

Acceptor removal states that electrically active shallow acceptors are transformed into defect complexes that do not have the initial properties. This can be also applied into donors. Effective doping concentration depicted in the previous subsection can be described by acceptor/donor removal and acceptor creation by [30]:

$$N_{eff} = N_{D_0} e^{-C_D \Phi_{eq}} - N_{A_0} e^{-C_A \Phi_{eq}} - g_{eff} \Phi_{eq} \qquad (1.17)$$

where $N_{D_0,A_0}$are the doping concentrations before irradiation, $c_{D,A}$ are the donor and acceptor coefficients, and $g_{eff} = 0.02$ cm^{-1} is the coefficient of proportionality between new acceptor defects and the fluence.

The reduction of acceptor atoms due to irradiation is a crucial effect in LGADs. Previous sections explain the importance of the multiplication layer in LGADs. This effect deactivates the acceptor-doped implant provoking a reduction in the gain. This reduction has been reported for neutron irradiations [51] and for charged hadrons [36]. Acceptor removal is empirically modeled [30] by the equation:

$$N_A(\Phi_{eq}) = N_A(0)e^{-c_A \Phi_{eq}} \tag{1.18}$$

where c_A is a constant that depends on the acceptor concentration and on the type of irradiation.

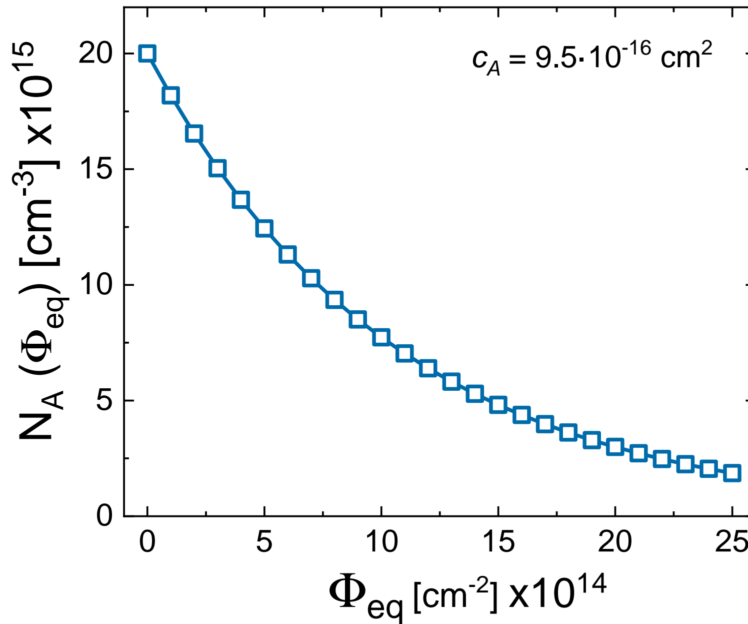

Figure 1.23: Doping concentration as a function of the equivalent fluence for a standard LGAD sensor.

Figure 1.23 shows this relationship in a standard LGAD sensor assuming a doping concentration peak of $2 \cdot 10^{16}$ cm^{-3} before irradiation and a constant value of $9.5 \cdot 10^{-16}$ cm^2 [36]. As one can observe, the peak is reduced by a 12% achieving a value of $2.5 \cdot 10^{15}$ cm^{-3} at $\Phi_{eq} = 2.5 \cdot 10^{15}$ cm^{-2}. This means that at this fluence the gain is almost removed. Therefore, in order to use LGADs in harsh radiation environments, this boron peak must be increased. Nevertheless, the trade-off between V_{BD} and gain must be conserved before irradiation. There is a huge commitment in the HEP community to better understand this effect and to mitigate it. Some studies report that boron multiplication layers enriched with carbon have better radiation resistance [53]. Moreover, other materials like gallium have been tested as a gain layer to be more radiation-resistant than boron [34, 52]. Higher radiation-resistant materials, like SiC, are proposed as a substrate [53, 54]. However, these studies are under investigation to help LGADs to support high radiation fluences.

1.7.2 Surface damage

As aforementioned, surface damage is caused by ionization. Synchrotron radiation sources use X-Rays as ionizing particles. For silicon detectors, the expected operational energy is below 25 keV. Therefore, only surface damage is expected in silicon detectors used for synchrotron radiation [55]. Usually, n-type silicon is used for X-Ray irradiations since the substrate is not inverted. Consequently, detectors must be designed taking into account the surface damage caused by X-Rays. A lot of work has been developed in recent years in order to optimize the design and the technological parameters of the detectors to make them suitable for X-Ray irradiation [56, 57, 58, 59].

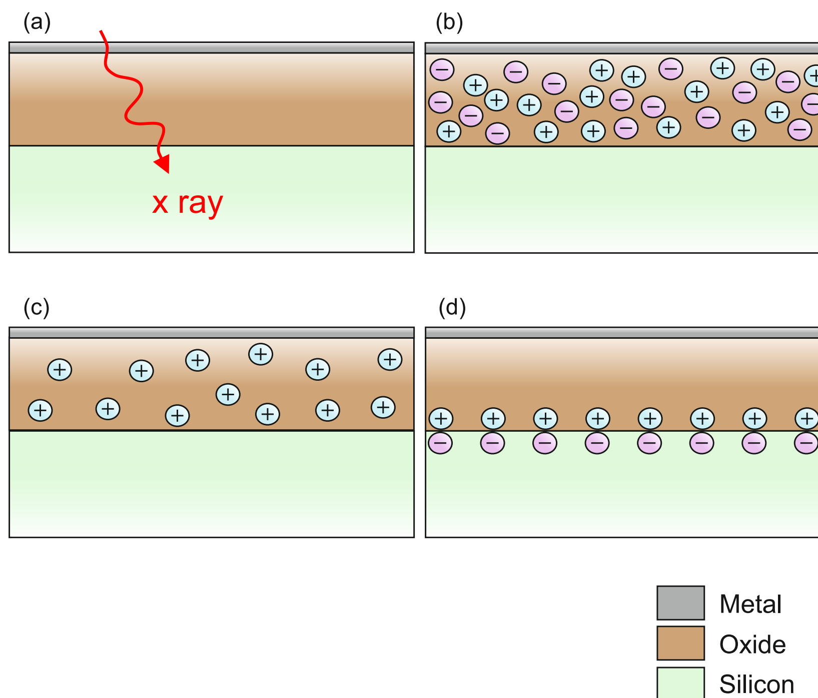

Figure 1.24: Schematic illustration of the formation of a conductive layer at the Si-SiO_2 interface provoked by an ionizing particle. Adapted from [60].

The process of surface damage provoked by an X-Ray is depicted in figure 1.24. When an X-Ray crosses the device (a), electron-hole pairs are created (b). Since electrons have high mobility inside the SiO_2, most of them will be recombined, contrary to holes. Therefore, holes can be trapped in the oxide (c). This presence will result in an attraction of electrons at the interface, creating a conductive layer (d). This conductive layer can lead to several problems in segmented detectors, creating electric field peaks at the edges of the diffusions and, consequently, diminishing the electrical performance of the detector.

1.8 Conclusions

This chapter has shown the state of the art of radiation detectors for HEP experiments and X-Ray applications. Through this development, the main silicon-based sensors have been introduced, summarising their properties based on the PiN detector. Intrinsically amplified detectors such as APDs and LGADs, as well as segmented detectors, have been described. Then, novel solutions proposed to develop LGAD technology with a high fill factor value have been presented. Finally, the main radiation damage in detectors, depending on the radioactive source, are described.

This chapter contains the basic information for the development of LGAD and iLGAD detectors at IMB-CNM for use in HEP and X-Ray detection applications. The next chapters will describe the development of thin LGADs for their use as timing detectors in the HL-LHC. In addition, iLGADs have been designed and produced to detect X-Rays thanks to a new termination, which has been optimized taking into account the surface damage present during X-Ray irradiations. Furthermore, the development of a thin iLGAD optimized for timing applications is presented in this thesis. Finally, the design and optimization procedure of an LGAD based on n-type substrates to detect low-penetration particles is fully described.

Chapter 2

Development of LGAD sensors for the HL-LHC upgrade

In this chapter is going to be exhaustively described the whole development of LGADs for their use in the future HL-LHC. It covers the optimization by using TCAD tools, the mask design, and the fabrication of the sensors. In addition, it is presented an extensive characterization of the fabricated LGADs, including electrical and gain measurements before and after irradiations.

2.1 Introduction to the LGAD technology

During the last few years, the RD50 collaboration has been involved in the development of radiation sensors for the HL-LHC upgrade. Since their first appearance, LGADs have been widely studied due to their unique properties and, in this framework, the IMB-CNM has developed LGAD productions to be used in the ATLAS and CMS experiments [33, 38, 61].

2.1.1 LGAD design

Figure 2.1(a) shows a sketch of the typical doping profiles in an LGAD detector and the electric field in this region. Multiplication region is composed by the $n^+/p/\pi/p^+$ structure, creating a high electric field peak at the n^+/p junction, where an appropriate optimization is crucial to reach the desired performance of the sensor. Figure 2.1(b) shows a cross-section of an LGAD sensor. Here, the multiplication region and the periphery of the sensor are exposed.

The peripheral region of the LGAD was optimized to support high breakdown voltages and avoid a high leakage current [62] and it consists of different edge termination strategies. Although dopants diffuse towards silicon vertically, some lateral diffusion is expected, which creates a curvature at the end of the diffusion. This curvature entails a higher electric field than the one created in the main junction. Because this behavior is inherent to the diffusion process, the only way to remove it is to extend the multiplication layer diffusion until the edges of the sensor. Nevertheless, this solution presents some disadvantages, like a high leakage current injection, since the edges of the sensor are usually subject to dicing processes that can induce defects.

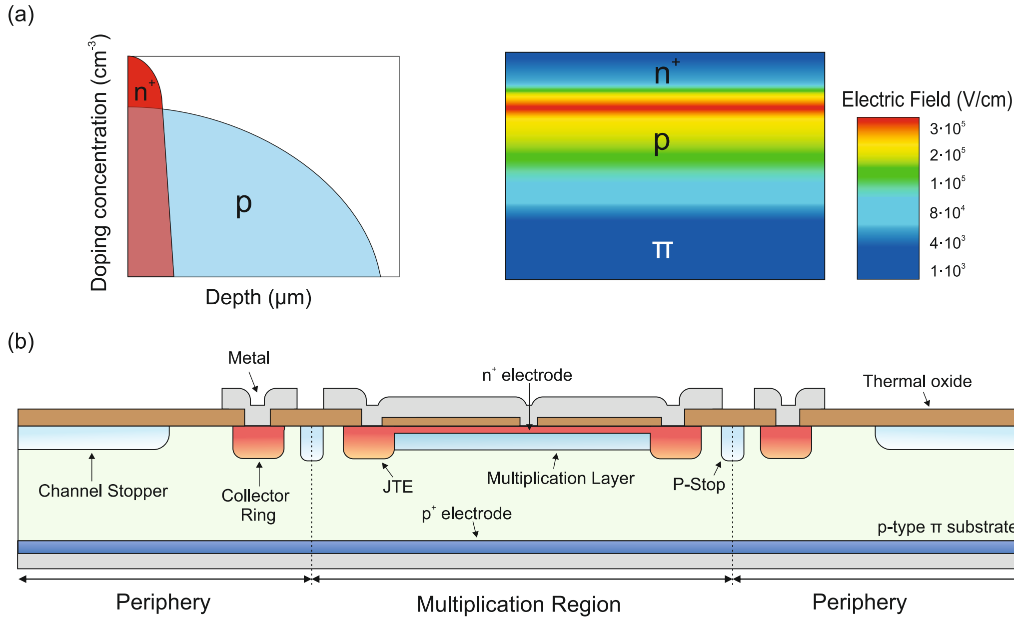

Figure 2.1: (a) Doping profiles and electric field at the multiplication region (b) Cross-section of the standard LGAD design

Some edge termination techniques used in typical power devices are described in [62], where the Junction Termination Extension (JTE) is the most commonly used in LGAD sensors. Here, the charge is added by implanting an n-type region at the edge of the main junction, which can be adjusted with the ion implant dose and energy in order to provide better uniformity. Thus, a planar surface is achieved by providing a similar V_{BD}. In addition, the JTE leads to the fabrication of a high number of small sensors per wafer, since the width needed can be reduced to tens of microns. The effectiveness of the JTE is enhanced by adding a field plate, which is a metal extension over the field oxide that overhangs the JTE in order to reduce the electric field value at the well outer curvature area. By using the field plate, the electric field peak is moved towards the oxide, which is able to support higher electric fields than silicon. Furthermore, a collector ring is diffused with the same technological characteristics as the JTE, in order to collect the peripheral current created by defects at the edge of the sensor.

As already stated in chapter 1, X-Rays induce a high concentration of charges in the oxide. Commonly, during standard semiconductor fabrications, some charges are created in the oxide, leading to a concentration of electrons at the Si-SiO_2 interface, in the same way as X-Rays. Nevertheless, during the fabrication, this concentration is much lower than during X-Ray irradiations, although it has to be taken into consideration since the electron conductive layer is going to shortcut both JTE and collector ring diffusions. Therefore, a p-stop diffusion is placed between both n-type diffusions to avoid this effect. In addition, by increasing the applied bias, depletion width increases both laterally and vertically, leading that depletion reaching the edge of the detector and inducing a high current injection to the multiplication region. To

mitigate this effect, a p-type channel stopper diffusion is located at the edges of the sensor. The optimization of the edge termination in LGAD sensors is fully described in [63].

2.1.2 LGAD fabrication process

LGADs were first fabricated in 285 µm thick substrates. Their development is fully described in [63]. They were fabricated in p-type high resistivity (> 10 k$\Omega \cdot$cm) wafers. The fabrication of LGAD sensors consists of seven major steps:

1. P-stop diffusion
2. JTE diffusion
3. Multiplication layer
4. N^+ and P^+ diffusions
5. Contact opening
6. Metallization (Multiplication and back-side)
7. Passivation

A summary of the LGAD fabrication process is depicted in figure 2.2. Before the fabrication, a field oxide is grown to avoid contamination during the next steps. P-stop, JTE, multiplication layer, and contact diffusions follow the same procedure. First, a photolithographic step is developed to assure the implantation is done in the desired region. The species (B or P) are implanted through a screen oxide (365 Å) and then are activated and diffused by a thermal step, which has been optimized for each diffusion. Then, after a photolithographic step, the contacts are opened for subsequent metal deposition, which is etched after an additional photolithographic step. Finally, a passivation layer, which consists of a bi-layer of oxide and nitride, is deposited on the detector to avoid contamination after the fabrication. This passivation layer is selectively etched to assure electrical contact. During the process, some characterizations are carried out to control it, such as oxide measurements and microscopic images. Usually, the whole fabrication process of an LGAD consists of between 70 to 90 steps, which entails 4 to 6 months spent.

2.1.3 LGAD as a timing detector

As aforementioned described, there is a necessity to reduce the active thickness of the detectors to improve the time resolution. In this sense, IMB-CNM has developed thin LGADs (~ 50 µm) using SOI (silicon on insulator) and Si-Si (silicon-silicon) wafers. Figure 2.3 shows a sketch both designs. For the LGAD integrated on SOI wafers, the first step is to define a p^+ layer on the surface of the wafer that will be act as an active layer. Then, a buried oxide of 1 mm is grown on the p^+ side and the active

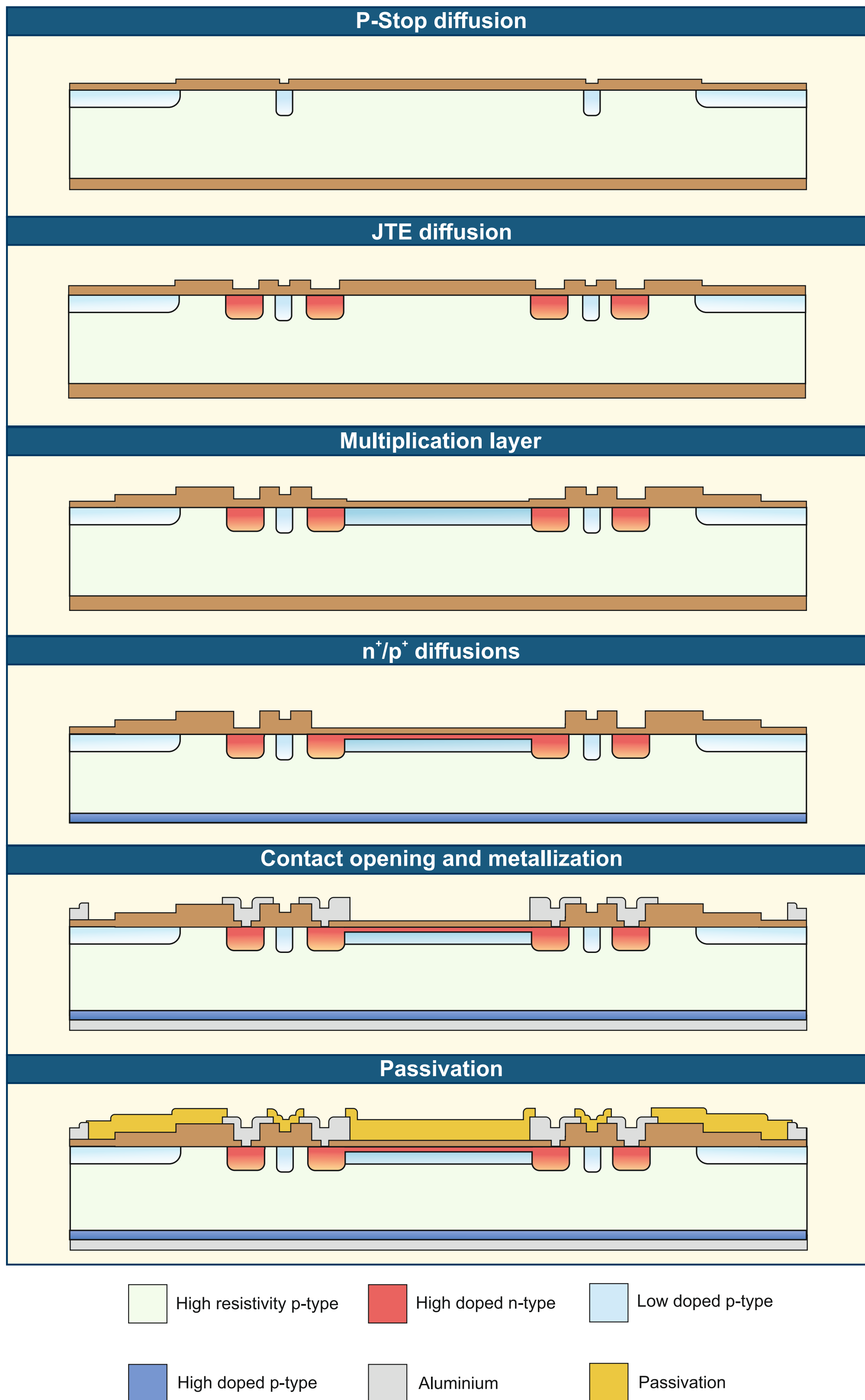

Figure 2.2: Sketch of a standard LGAD fabrication process.

wafer is bonded to another thick wafer, which is the handle wafer. After this process, the active wafer is thinned to 50 µm and the fabrication process starts. Using SOI wafers, after the LGAD fabrication on the active side, at the end of the process the silicon of the handle wafer is etched in specific areas in order to facilitate the electrical contact to the buried p^+ layer to define the cathode/anode contact of the detector. Then, metal is deposited on the whole handle wafer surface to assure it reaches the p^+ electrode (Figure 2.3(a)). This technological approach has been optimized for the use of LGADs in the CMS TOTEM Proton Position Spectrometer (CT-PPS) [41].

Another configuration of thin LGAD is the use of Si-Si wafers, depicted in figure 2.3(b). In this case, a low-resistivity p-type handle wafer (thick) is bonded through a thermal process to a high-resistivity p-type active wafer, which is again thinned to 50 µm. This handle wafer act as a p^+ electrode and no etching is necessary with these wafers. The use of Si-Si is simpler for the fabrication of LGADs since it needs less fabrication steps. Nevertheless, there is a diffusion of dopants from the low-resistivity wafer to the high-resistivity wafer, which has to be taken into account. This structure has been optimized and developed to be used in the ATLAS HGTD [61].

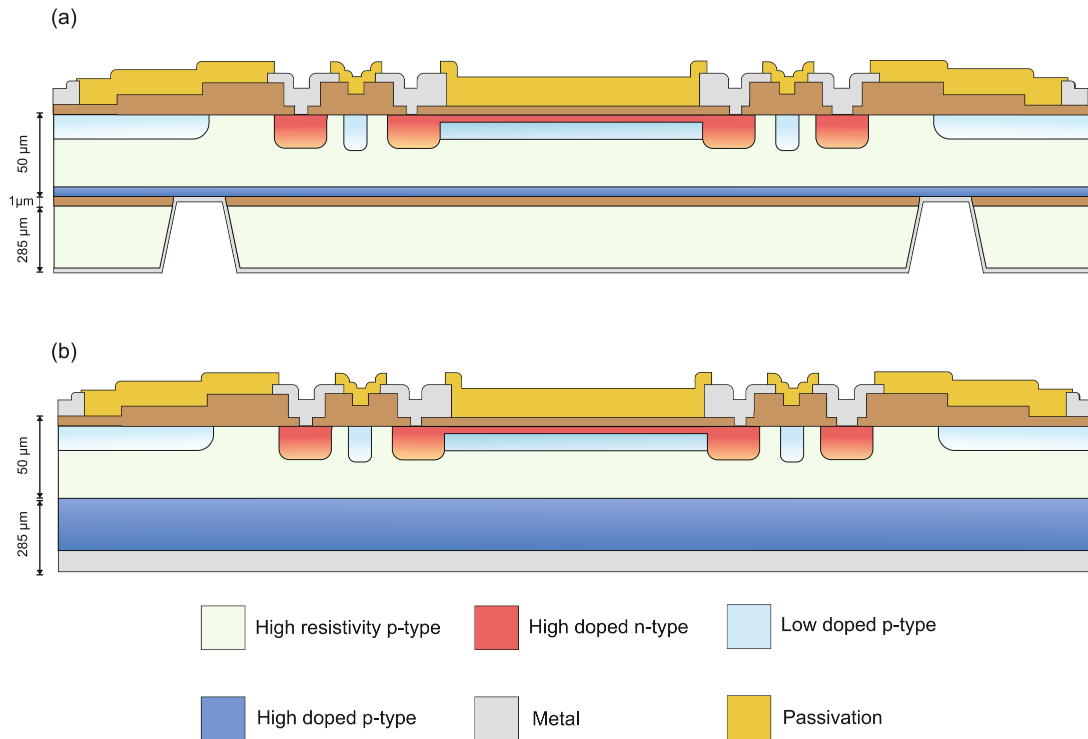

Figure 2.3: (a) Cross-section of an LGAD in SOI wafer (b) Cross-section of an LGAD in Si-Si wafer.

2.1.4 LGAD major challenges

The use of LGADs as a particle detector is contingent on meeting four main challenges.

1. **Safe operating range.** The detector must work over full depletion voltage and below breakdown voltage while maintaining a trade-off between the desired gain and a safe operating voltage.

2. **Radiation hardness.** Since LGADs are proposed for the HL-LHC, they are going to be subjected to a harsh radiation environment, which leads to a degradation in the detector performances. In this sense, new materials have been proposed to build the multiplication layer [52, 53, 54]. For instance, some studies reported an increase in radiation hardness by enriching the multiplication layer with carbon [34].

3. **Yield.** Pixelated high-area LGADs ($\sim$ cm^2) have been designed for ATLAS and CMS experiments. As already stated, the resistivity of the gain layer is a crucial parameter in the performance of LGADs. Small changes in the resistivity may lead to non-uniformities in the gain that can lead to a premature breakdown voltage.

4. **Fill factor.** Pixelated detectors present a non-gain area in which particles are not multiplied. In this sense, the principal LGAD manufacturers have developed novel structures like iLGADs, AC-LGAD, TI-LGAD, or Trench iLGAD to achieve a 100% fill factor [38, 39, 40, 41, 42, 43, 44, 45].

The development of LGADs is based on these constraints.

2.1.5 AIDA-2020 production

IMB-CNM has developed LGAD sensors on behalf of the AIDA-2020 (Advanced European Infrastructure for Detectors at Accelerators) project [64]. It is a project where research institutions, universities, and technological centers are working together to develop detector technologies with European research infrastructures. Figure 2.4 shows a scheme of the main research lines of the project, which aims to push detector technologies beyond state-of-the-art. In this sense, at IMB-CNM we have developed pixelated thin LGAD sensors to meet the requirements of the AIDA-2020 project.

2.1.6 Radiation hardness requirements for LGADs

One of the research lines in the AIDA-2020 project is developing radiation hardness detectors, which is also one of the main challenges in LGADs. In this sense, IMB-CNM has been developing LGAD sensors for HEP experiments such as the LHC. As already described in chapter 1, the HL-LHC is going to surpass the performance of the existing LHC providing a higher luminosity which will entail higher radiation damage in the detectors. Thus, ATLAS and CMS are willing to use pixelated LGADs in their timing layers that must accomplish specific requirements [19, 20]

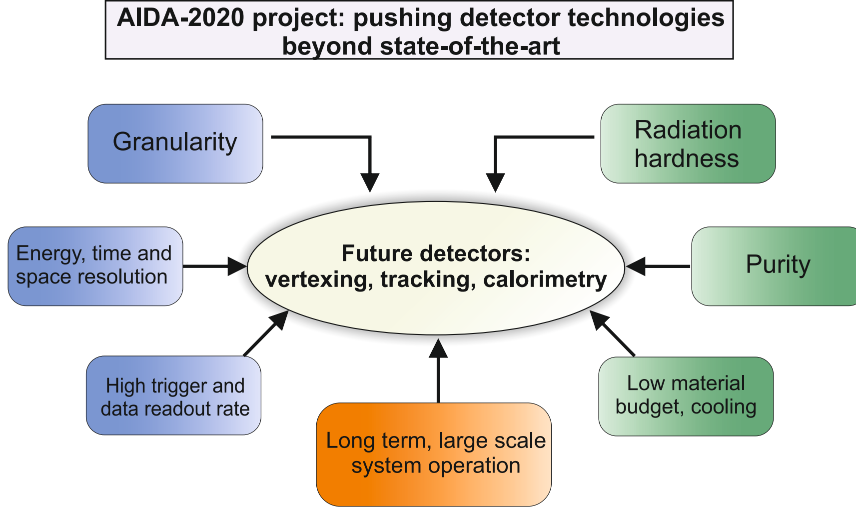

Figure 2.4: Research lines of the AIDA-2020 project. Adapted from [64]

CMS Endcap Timing Layer

Table 2.1 shows the main sensor properties for the ETL upgrade. The working temperature is expected to be at -25 ºC and they must work between a fluence of 1.0-1.5 $\cdot 10^{15}$ n_{eq}/cm^2. CMS expects to use 39000 LGADs, where 32000 are going to be located at the low-fluence level and 7000 at the highest fluence level. V (8fC) is defined as the voltage where the detector is able to collect a charge of (8 ± 2) fC. The maximum operating voltage is 600 V for 50 µm detectors.

Un-irradiated		**Irradiated (1-1.5 $\cdot 10^{15}$ n_{eq}/cm^2)**	
V_{FD}	<50 V	V(8 fC)/D	<12 V/µm
V_{BD}	130-250 V	V_{BD}	>V(8 fC) + 30 V
σ at V(8 fC)	<50 ps	σ at V(8 fC)	<50 ps
I_{leak}	1 µA	I_{leak}	<1 mA
CC/MIP at V(8 fC)	8 ± 2 fC	CC/MIP at V(8 fC)	8 ± 2 fC

Table 2.1: Sensor properties at -25 ºC required for the CMS ETL MIP timing detector.

ATLAS High Granularity Timing Detector

The properties required for ATLAS to use LGADs in the HGTD are illustrated in table 2.2. In this case, detectors are expected to work at -30 ºC and under a fluence up to 2.5 $\cdot 10^{15}$ n_{eq}/cm^2. The expected collected charge for each pad is 4 fC, while time resolution must be under 70 ps. Although it was initially intended to use a voltage of 800 V [19], in the end, this value has been reduced to 600 V due to premature mortality observed in irradiated LGADs [65, 66, 49].

	Un-irradiated	**Irradiated ($2.5 \cdot 10^{15}$ n_{eq}/cm^2)**
V_{GL}	60 V	
V_{FD}	$<V_{GL}$ + 90 V	
V_{BD}	$(V_{BD} - V_{GL})/D > 0.7V/\mu m$ $V_{BD} > V_{FD} + 30V$	
V_{op}	600 V	
I_{leak}	2 µA/cm^2	<5 µA
CC (V_{op})	>15 fC	4 fC
$\sigma(V_{op})$	35 ps	<70 ps

Table 2.2: Sensor properties at -30 ºC required for the HGTD timing detector.

At IMB-CNM, we have developed LGAD sensors in order to cope with both requirements. In the following sections, the whole development of the sensors is going to be described, as well as a full characterization to study the availability of the LGAD technology for the HL-LHC upgrade. Moreover, we propose novel strategies in order to enhance the performance of the detectors.

2.2 Design and optimization of the detectors

This production takes benefit of previous thin LGAD designs. The multiplication region has to be optimized to meet the first LGAD challenge which is to have a safe operability range. In this sense, we have used Technological Computer-Aided Design (TCAD) tools (Synopsys Sentaurus [67]) in order to tune the multiplication layer to assure a low linear gain. Furthermore, the periphery of the detectors needs to be studied to reach the optimum technological parameters.

2.2.1 Multiplication region optimization

First, we performed a technological simulation of the multiplication region. We have followed the same technological steps as the fabrication for different boron doses of the gain layer. Figure 2.5 shows the simulated net active doping concentration profiles for each structure. As one can observe, the differences in the peak value for the multiplication region are not so evident (in these simulations, the multiplication layer has been diffused at 1150 ºC for 90 minutes). Despite there being no big differences in the boron peak, the electrical performance is heavily decreased. In this sense, we carried out I-V and C-V simulations in each structure to see the differences in terms of breakdown voltage and depletion of the gain layer.

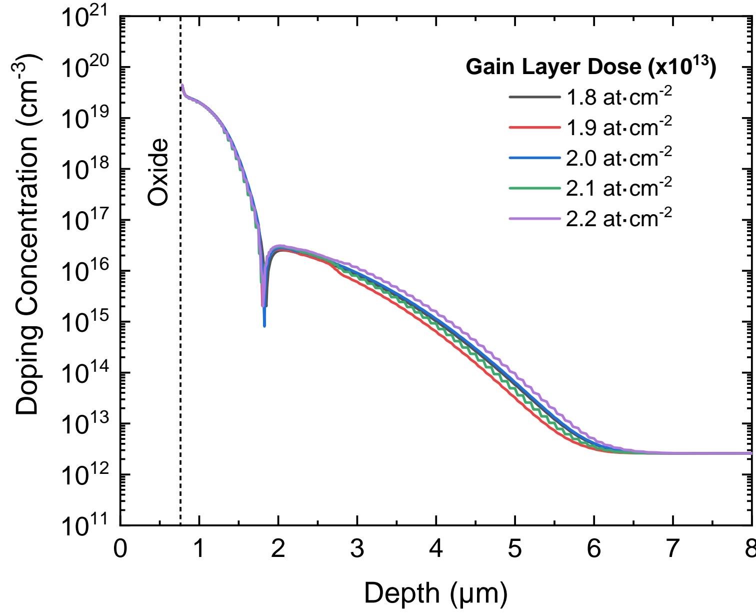

Figure 2.5: Simulated net active doping concentration for different boron doses of a Si-Si LGAD sensor at the multiplication region.

Figure 2.6(a) shows the breakdown voltage as a function of the boron doping of the multiplication layer, where there is an almost linear behavior between breakdown and boron doping concentration. Figure 2.6(b) shows the C-V simulation for each boron dose and one can observe how depletion of the gain layer increases with the dose, as expected. Since we are using a 50 μm high resistivity active substrate, full depletion voltage is achieved a few volts after the gain layer depletion. Finally, we performed gain simulations. First, a MIP goes through the sensor at a given time (in this case 1 ns), and then the current is evaluated in a certain amount of time (5-10 ns). Therefore, we are able to obtain the I-t simulated curve of the sensor, as depicted in figure 2.6(c) with a dose of $1.8{\cdot}10^{13}$ cm^{-2}. Then, this procedure is repeated with a PiN diode and thus the gain is calculated by dividing the charge of each structure, which is calculated with the integral of the I-t curve. The area, and therefore the charge, is increasing with voltage applied, contrary to in a PiN diode, where the charge remains the same after full depletion voltage. Figure 2.6(d) shows the gain for different boron doses. As we expected, the gain increases with the dose and it has a linear shape in the lowest doses.

Our goal is to manufacture a detector with a gain between 10-20 in order to work in linear mode during a high voltage regime and, in this sense, doses of 1.8, 1.9, and 2.0 are suitable for this technology. On the other hand, a dose of 2.1 presents a linear and suitable gain with the issue of low voltage capability. Finally, the highest dose makes the sensor almost unusable before irradiation with a very high gain. We have to take into consideration that this is a 1D simulation; therefore, the values for breakdown voltage will decrease in a real sensor.

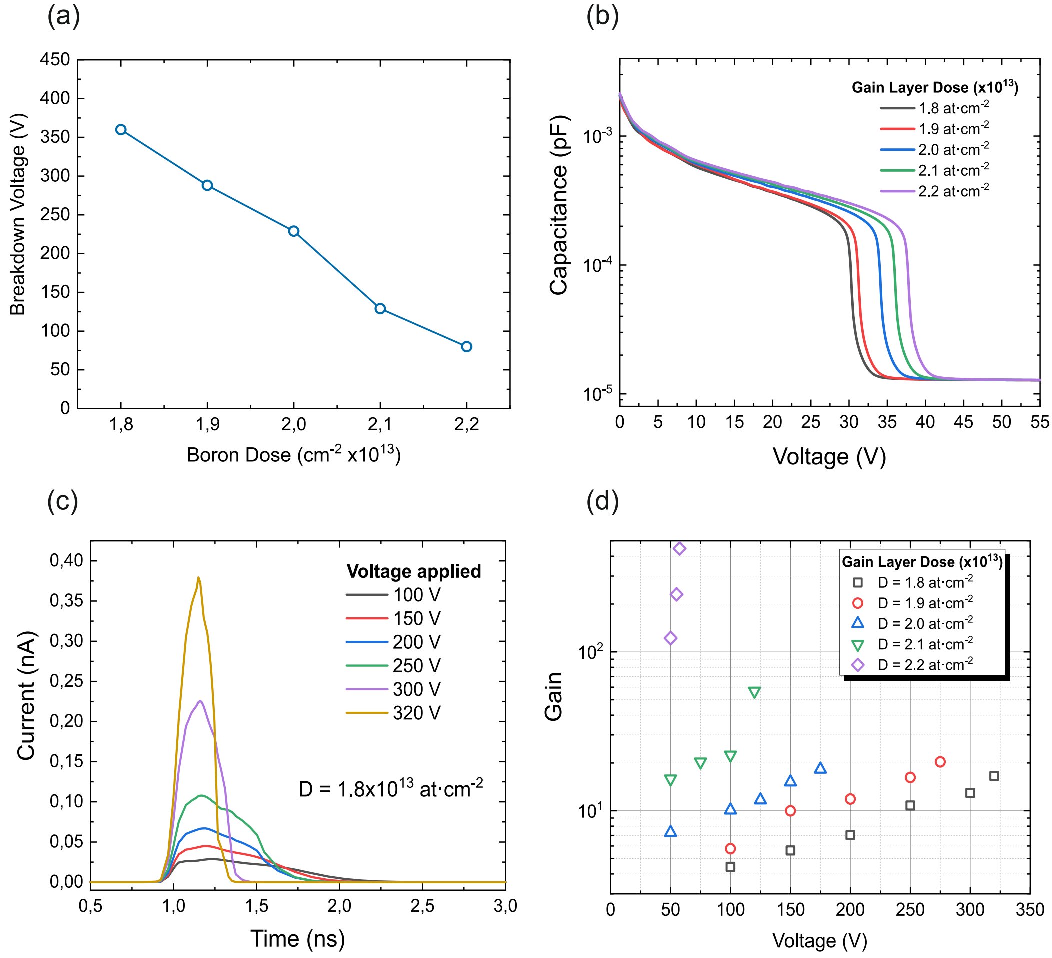

Figure 2.6: (a) Breakdown voltage as a function of the multiplication layer dose. (b) C-V simulations for different boron doses for the multiplication layer. (c) Transient simulation (I-t) for an LGAD sensor for different applied voltages (d) Gain simulation for different boron doses.

Deep multiplication implant

We have optimized the LGADs using the standard multiplication region profiles. Nevertheless, different solutions have been envisaged in the last years to assure better performance of the sensor [30, 68]. The non-uniformity of the gain layer is one of the major concerns when fabricating LGAD sensors due to several technological factors. The main parameters directly involved in the gain layer formation are the boron implantation dose, the implantation energy, and the temperature of the drive-in step. A non-uniform temperature may lead to several changes in the gain layer. A different growth for the screening oxide, for instance, can lead to a different implantation dose/energy. However, the most important parameter is the temperature of the drive-in processes after the multiplication layer implantation, which extends to some hours. If very high implantation energy is available, the gain layer could be directly created

without being diffused for a long time, just an impurity activation thermal step would be necessary.

Figure 2.7 shows the simulated boron profiles as a function of depth for different energy implantation with a fixed Boron implantation dose. As it can be inferred, boron diffusions up to ~ 5 µm can be obtained without a drive-in step, with a low-energy n^+ implantation, in order to maintain the boron concentration peak far from the n^+/p junction. This strategy will allow the structure to have a lower (but wider) electric field peak. In this sense, two different structures with the same n^+ implantation at 40 keV have been simulated, implanting the boron of the gain layer at 400 and 800 keV.

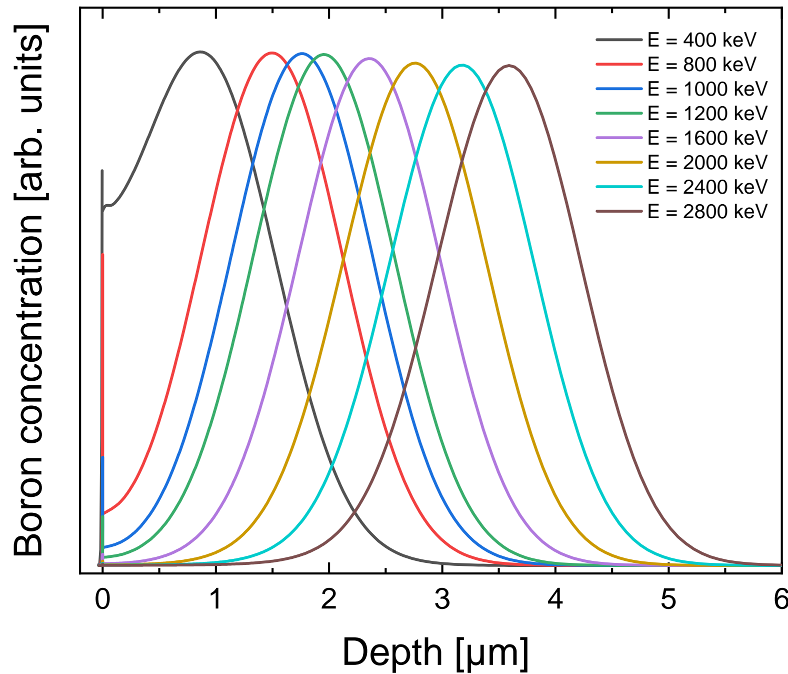

Figure 2.7: Simulated boron profiles for different implantation energies.

As energy increases, the boron implantation dose must be decreased in order to reach a similar electrical performance. A final rapid thermal annealing (RTA) during 30 seconds at 700 ºC is added in the simulation to activate the dopants. Figure 2.8 shows the doping profiles of both structures and figure 2.9 shows the electric field distribution over the thickness of the sensor, which is wider with a lower peak in the case of LGAD sensors implanted at 800 keV. Nevertheless, the electric performance of both sensors is similar. Figure 2.10 shows the breakdown voltage of both structures, exhibiting a linear relation with the Boron implanted dose, which is optimized for each structure. Therefore, in terms of electrical performance, there is no difference between structures. A higher uniformity should be expected with this strategy. The uncertainty related to the gain layer is only devoted to the implantation parameters, such as the dose and energy of the n^+ and gain layer since thermal uncertainty has been removed.

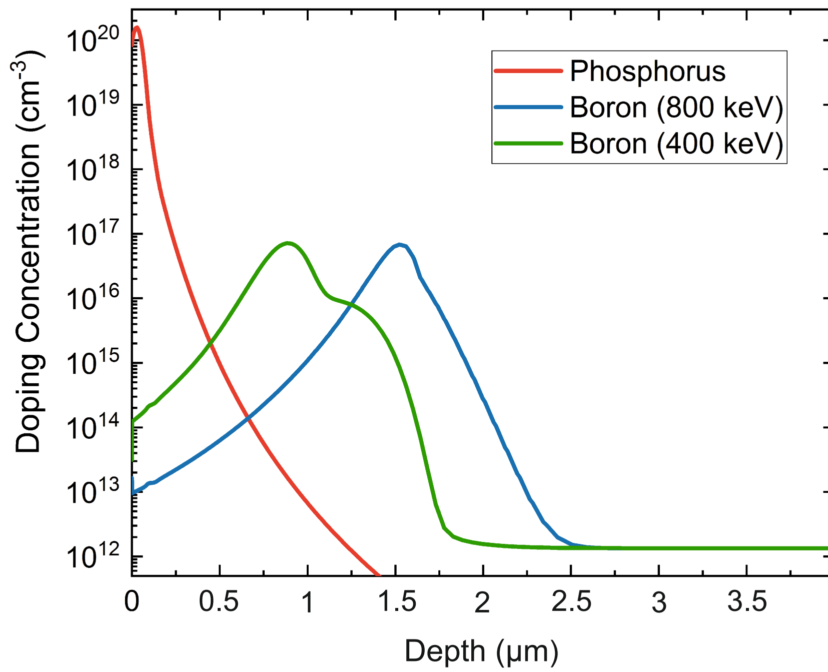

Figure 2.8: Simulated profiles of an LGAD using an energy of 400 and 800 keV.

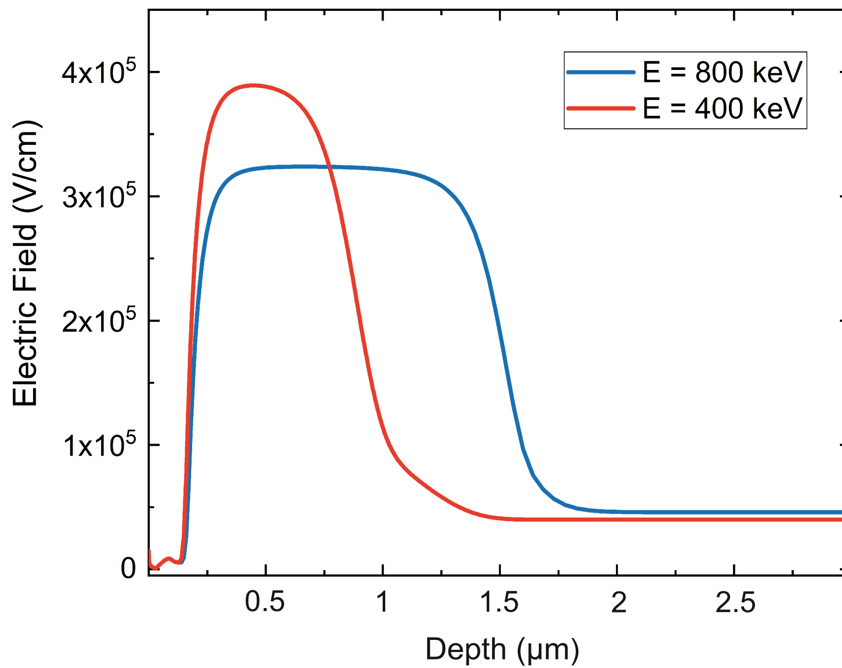

Figure 2.9: Simulated electric field of an LGAD using an energy of 400 and 800 keV.

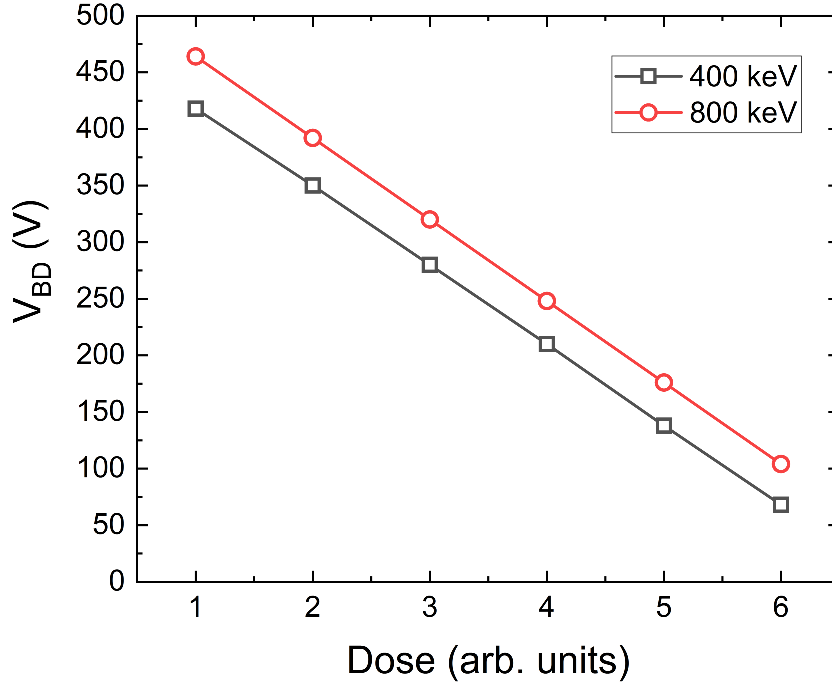

Figure 2.10: Simulated breakdown voltage for different boron doses using an energy of 400 and 800 keV.

2.2.2 Periphery optimization

LGAD design consists not only of multiplication optimization but also the optimization of the periphery. As aforementioned, the periphery design has been previously optimized in [62]. Nevertheless, in this production, we aim to design LGAD sensors with the lowest fill factor achievable and design big-area pixelated sensors. We define inter-pad distance (IP) as the distance between two pixelated multiplication layers. A 100% fill factor is achieved with an IP of 0 µm, which is not possible using a pixelated LGAD structure, and, obviously, the fill factor decreases with IP. Therefore, we must optimize the IP value in order to integrate LGADs with a specific electrical performance minimizing its value.

JTE is diffused at the edge of the gain layer and a p-stop diffusion is diffused at the middle of both pixels. In our design, the distance between the JTE and the p-stop remains always the same while the width of the JTE is changing and the gain layer is diffused 3 µm inside the JTE. Therefore, the lowest the JTE width, the lowest the IP distance. Another design solution to increase breakdown voltage is to widen the distance between JTE diffusions which entails a decrease in the fill factor. Therefore, we must find a trade-off between design parameters and the electrical performance of the sensor.

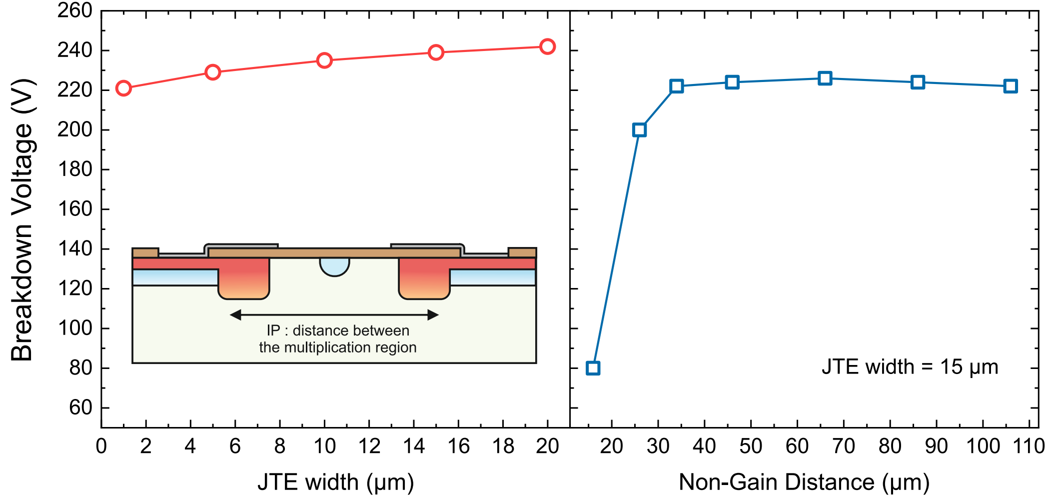

Figure 2.11: Breakdown voltage as a function of JTE width and the non-gain distance.

Figure 2.11 shows the breakdown voltage as a function of the JTE width and the non-gain distance, where, as expected, it increases with the JTE width. Nevertheless, we do not observe a high change in electrical performance. As the gain layer is diffused 3 µm inside the JTE, we consider a minimum width of 5 µm for the JTE. We have used three different IP distances: 37, 47, and 57, which correspond to a JTE width of 5, 10, and 15 µm, respectively. The electrical performance is increased by a larger non-gain distance, where reaches saturation at $\sim 30\ \mu$m. Hence, the use of a higher non-gain distance is not optimal since gain area will be lost. In this sense, a JTE width higher than 15 μm is not needed since there is no much benefit in terms of breakdown voltage.

There is an additional constraint in the interpad design, which is the *Pop-Corn* noise, where micro-discharges appear at a certain voltage. This does not prevent the detector from continuing to operate, but the associated noise increases, worsening the measurement [69]. *Pop-Corn* noise is generated through the n-type conducting layer created under the oxide, which with the p-stop creates a p-n punch-through design. For this reason, two ways can be envisaged to solve this problem: lowering the p-stop doping concentration or widening the distance between p-stop and JTE diffusions. The first option may lead to a loss in sensor performance, and therefore a trade-off must be considered. The voltage supported by a punch-through diode increases with junction width [10], thus a widened IP distance implies better behavior of the sensor. Nevertheless, a higher IP distance leads to a lower fill factor.

2.3 Photolithographic mask designs

We have designed a photolithographic masks set according to the TCAD simulations and the challenge to develop high-area LGAD sensors. The mask "CNM913" has nine levels that correspond to the different photolithographic steps for fabrication. Table

2.3 shows each level with their description and alignment. These are the standard structures for an LGAD design that have been previously described. In addition, we have designed an extra level for the metallization of the ohmic side, which is used to allow future laser measurements.

The final mask level is the temporary metal, where a metal layer is deposited on the active area and the rings of the sensor, in order to short-cut all the pixelated pads. Using this approach, we can bias all the pads at the same voltage by only contacting one pad facilitating the electrical characterization of the sensors, especially the higher area detectors. Nevertheless, by using this procedure, we are not going to be able to determine the current level of each individual pad. Figure 2.12 shows a cross-section of the multiplication side for the AIDA2020 design where each mask level is depicted to show an illustration of the mask. Metallization levels (Metl and Metl2) are in blue to illustrate they are negative levels.

Mask level	Level description	Alignment
Pstop	P-Stop Diffusion	Flat
JTE	JTE Diffusion	P-Stop
Mult	Multiplication Layer	JTE
Nplus	N+ Diffusion	Mult
Cont	Contact Opening	Nplus
Metl	Metallization	Nplus
BMetl	Metallization	Metal
Pass	Passivation	Metal
Metl2	Temporary Metal	Metal

Table 2.3: Mask level description of the mask CNM913.

Table 2.4 shows the main LGAD designs used in the mask. We included pad sensors with different multiplication areas to test the technology and to facilitate the characterization. Furthermore, pixelated 2x2 LGADs have been also considered. In this case, these sensors are useful to study the benefits of pixelating detectors without increasing the complexity of the measurement. Finally, in order to study the yield, we have implemented 5x5 LGADs, which consist of 25 pixels with a total area of 8x8 mm^2.

All these sensors, except the 5x5 LGADs, have different multiplication areas, as depicted in table 2.4. There are PiN diodes designed to test the leakage current and the charge collected in order to use it as a reference for the gain measurements. In all the devices there is an opening in the multiplication side metal to let the laser penetrate in the gain measurements, in a similar way as in the ohmic side. As well as the standard square-pixelated LGADs, we have designed rectangular-pixelated LGAD sensors, to compare both designs' electrical performances, including different rectangular-pixel number devices in order to study their influence on the yield value.

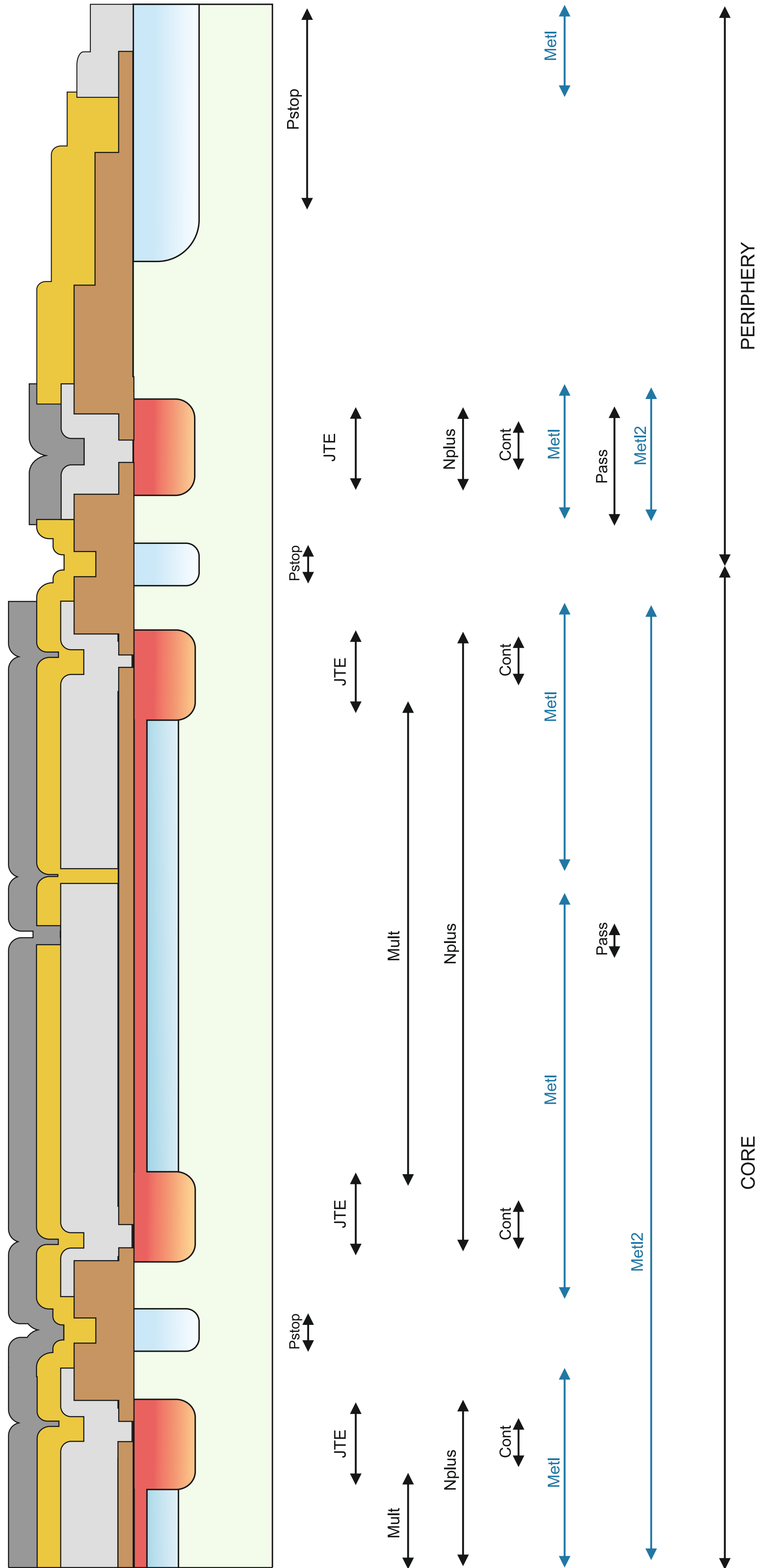

Figure 2.12: Sketch of the mask levels in the mask CNM913.

Here, the detectors are made of different columns of four pixels LGADs and are going to be used to perform inter-pad studies. Contrary to the square-pixelated LGADs, there is an opening in the metal between two strips, in order to evaluate the non-gain area. Figure 2.13 shows the designs of each sensor presented in table 2.4. Figure 2.13 shows the final mask design including all the structures that have been aforementioned described.

LGAD design	Pad area (mm^2)	Total area (mm^2)	JTE width (µm)
Pad	1x1; 1.3x1.3	2.3x2.3; 2.5x2.5	5; 10; 15
2x2	1x1; 1.3x1.3	3.4x3.4 ; 3.8x3.8	5; 10; 15
5x5	1.3x1.3	8x8	5; 10; 15
1x4	0.96x2.96	1.48x12.41	5; 10; 15
2x4	0.96x2.96	2.48x12.41	5; 10; 15
4x4	0.96x2.96	4.48x12.41	5; 10; 15
24x4	0.96x2.96	24.51x12.41	5; 10; 15

Table 2.4: Parameters of LGADs designed in the mask CNM913.

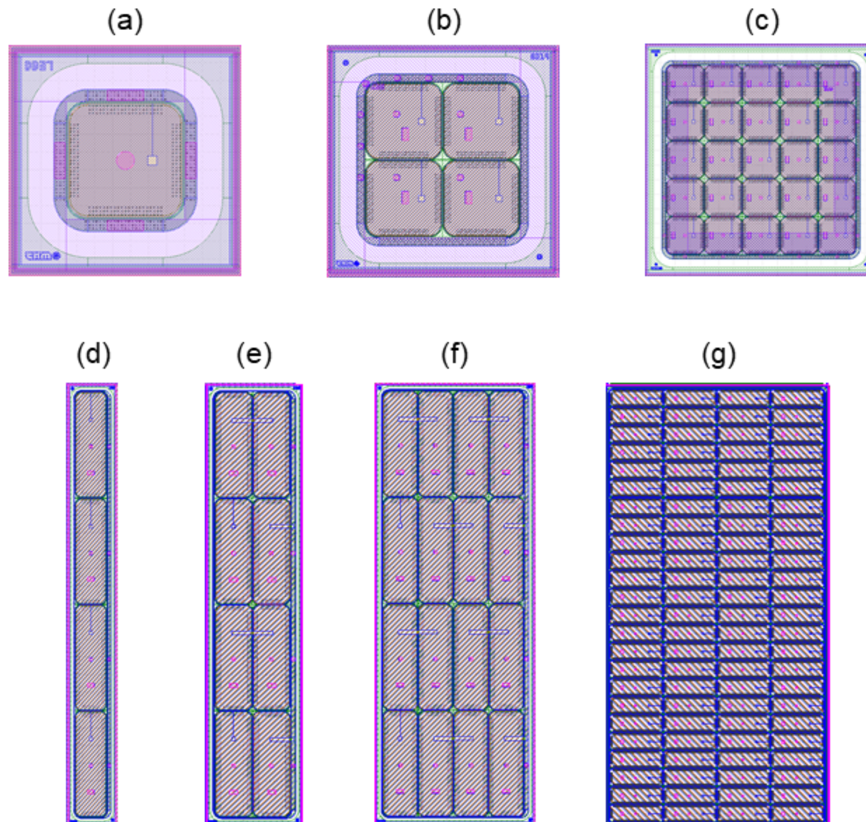

Figure 2.13: LGAD designs in the mask CNM913. (a) Pad (b) 2x2 (c) 5x5 (d) 1x4 (e) 2x4 (f) 4x4 (g) 24x4.

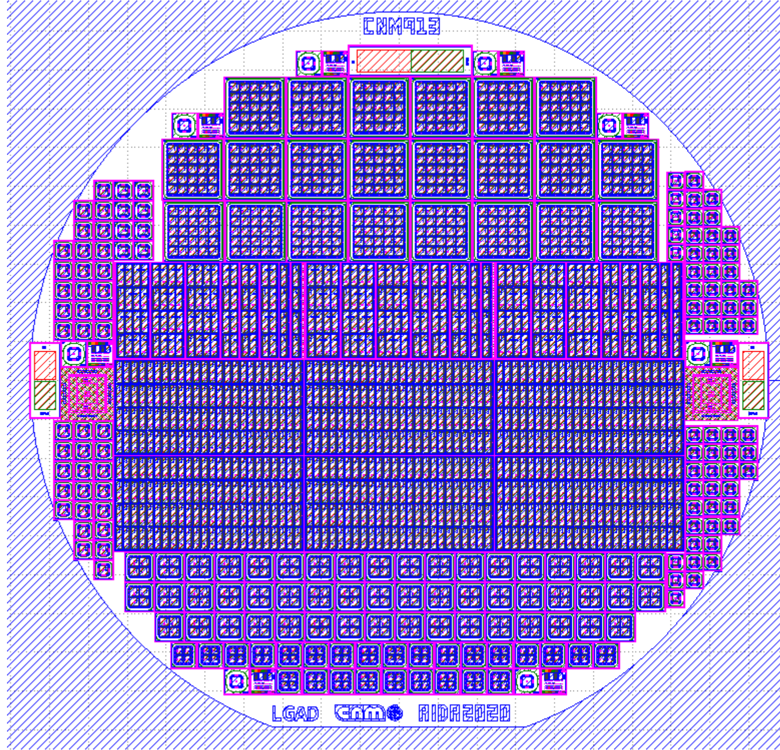

Figure 2.14: Final mask design CNM913 for the AIDA2020 production.

2.4 Fabrication process

In the framework of the AIDA2020 project, we have fabricated two runs of LGAD sensors (AIDAv1 and AIDAv2) with identical fabrication processes, according to the technological simulations and using the described mask set. We have used high-resistivity (>10 kΩ·cm) Si-Si p-type wafers with a low-resistivity p-type wafer acting as a handle wafer. For the AIDAv1 fabrication, we used both 35 and 50 ± 5 µm thick wafers, while for the AIDAv2 we only used 50 µm thick wafers. The reason for not including 35 µm thick wafers in the second fabrication is the fact that they do not demonstrate better performance for timing applications, as we are going to prove in later sections.

Figure 2.15 shows the simulated boron profile after the Si-Si bonding process where the thermal budget consists of oxidation of 1200 ºC during 30 minutes using 50 µm thick wafers. As one can observe, boron is diffused from the low to the high resistivity wafer up to 5 µm, approximately. Therefore, the active thickness of the process wafer can be diminished by 4-5 µm. Moreover, the wafers will suffer more thermal processes due to the dopants diffusions and, therefore, this value can be increased at the end of the fabrication. As described in the first section, the process consists of seven photolithographic steps. Figure 2.16 shows the whole fabrication process for the AIDA2020 production, illustrated with a pad LGAD. The process is the same as described in figure 2.2, but in this case, we have used the aforementioned

Si-Si wafers. The process consists of 77 steps, including the nine photolithographic steps. LGADs have been already fabricated in IMB-CNM in Si-Si wafers and their full description can be found in [41].

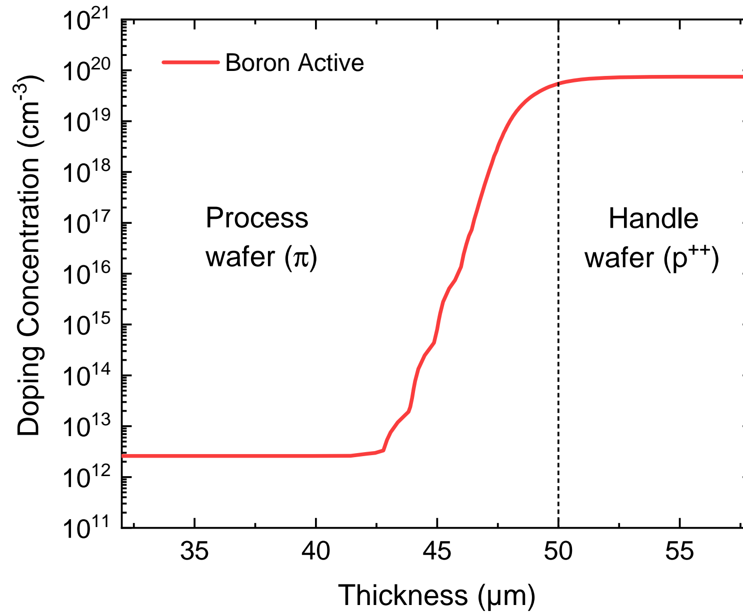

Figure 2.15: Simulated doping profile in a Si-Si process in high resistivity p-type wafers.

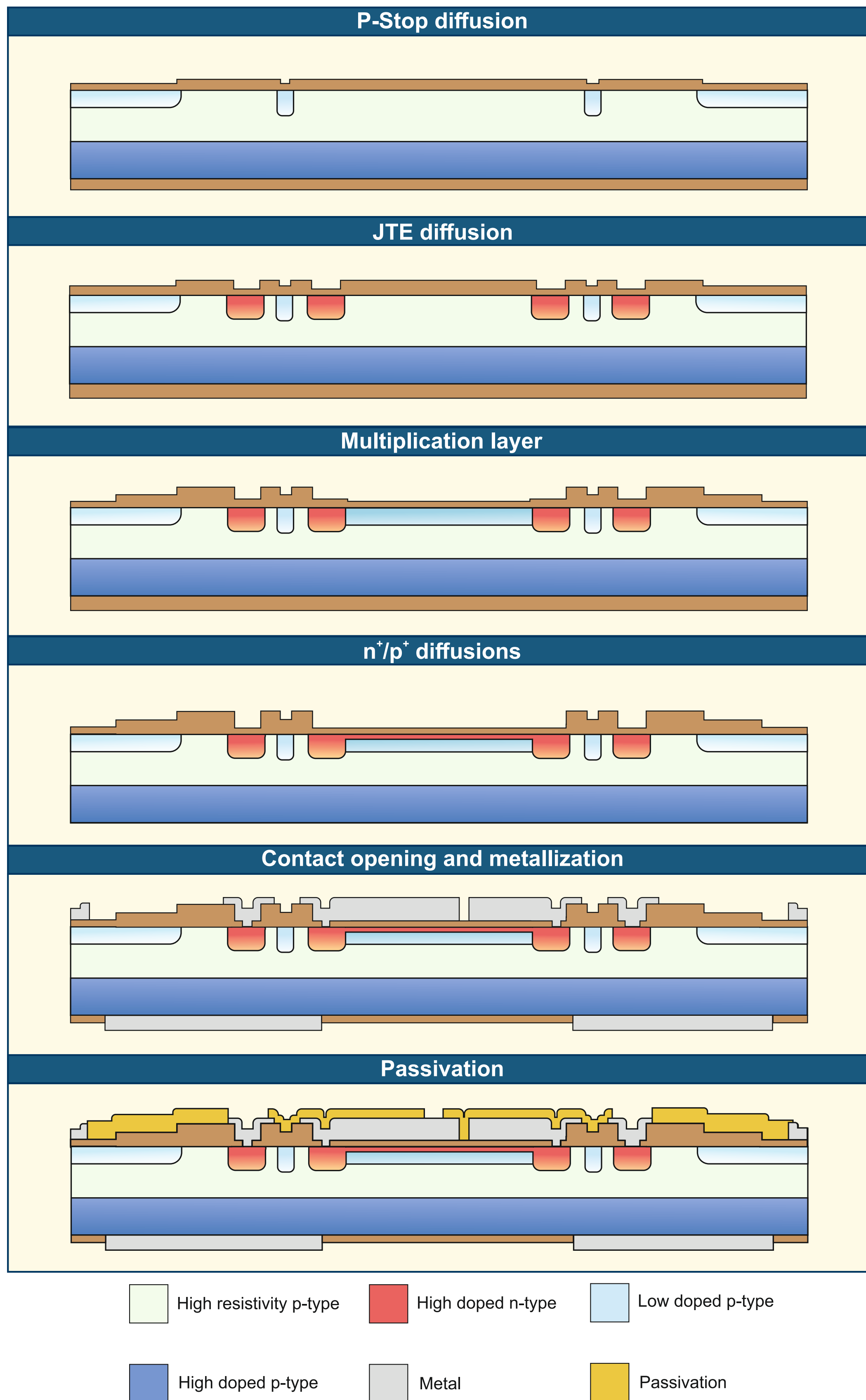

Figure 2.16: Sketch of the AIDA2020 fabrication process.

2.4.1 Multiplication layer

The most important parameter during LGAD fabrication is the multiplication layer since there is a huge necessity to control its doping concentration. Thus, we use test wafers to extract information about it. These test wafers are n-type doped and they suffer the exact same steps as the process wafers. After the thermal diffusion of boron, the oxide is removed from the test wafers and then a four-probe measurement is carried out to extract the sheet resistance of the boron diffusion at 49 different points along the wafer. Figure 2.17 shows the mechanism of extracting the sheet resistance in test wafers.

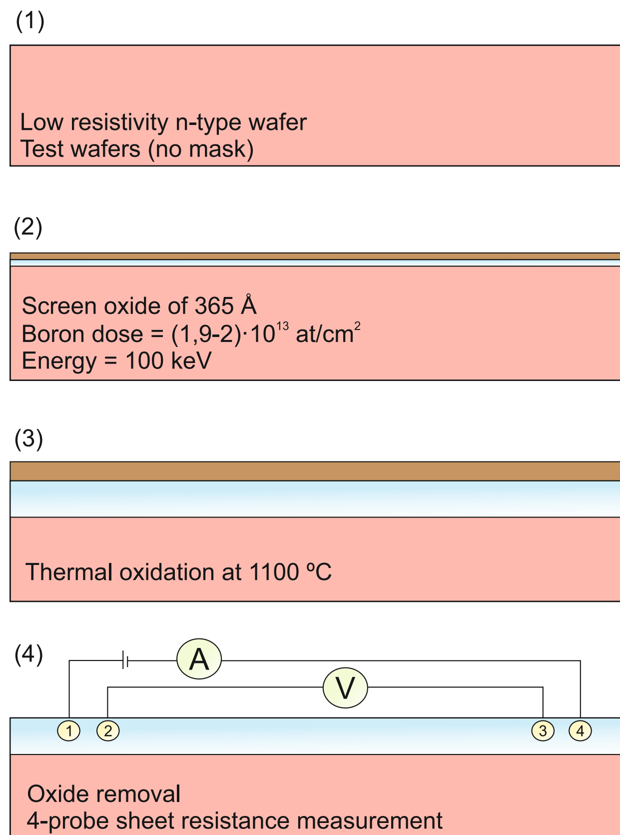

Figure 2.17: Four-probe sheet resistance measurement in n-type wafers.

This procedure is carried out as well with technological simulations to compare the results achieved. Table 2.5 shows the sheet resistance results, which are the average values of the 49 measurements in the wafer, and the oxide growth during the annealing of the two test wafers used in this fabrication, as well as the simulated values. There is a high consistency in the sheet resistance values between test wafers and simulation. Nevertheless, there is a high non-uniformity in the oxide growth, which can result in non-uniformity resistivity along the wafer.

Wafer	Sheet resistance (Ω/sq)	Oxide growth (Å)
Test wafer 1	2864 ± 45	4884 ± 256
Test wafer 2	2895 ± 51	
Simulation	2800	5410

Table 2.5: Sheet resistance and oxide growth for the multiplication layer in the AIDA2020 production for a dose of $1.8 \cdot 10^{13}$ at/cm^2.

Figure 2.18 shows the wafer map for the sheet resistance in a test wafer. There is a non-uniformity in the sheet resistance that can result in a different gain along the wafer and difficulty to produce high-area detectors. It is clear that the non-uniformity goes from left to right, which means that detectors fabricated at the right should have higher gain (and lower breakdown voltage) since the boron peak is higher.

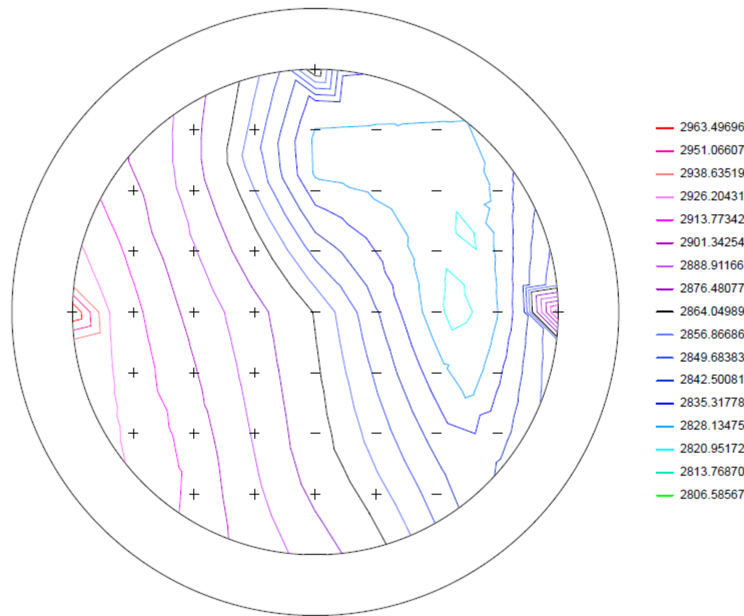

Figure 2.18: Sheet resistance map in test wafer for the AIDA2020 production for a dose of $1.8 \cdot 10^{13}$ at/cm^2.

Tables 2.6 and 2.7 shows the main characteristics for the multiplication layer parameters for both the AIDAv1 and AIDAv2 fabrications, respectively. It is important to emphasize that AIDAv1 fabrication uses a higher set of parameters for the multiplication layer dose, while AIDAv2 only uses one value.

Wafer	Thickness (µm)	Dose (at/cm^2)
1	35 µm	PiN
2, 3		$1.75 \cdot 10^{13}$
4, 5		$1.8 \cdot 10^{13}$
6, 7		$1.9 \cdot 10^{13}$
8, 9	50 µm	$1.75 \cdot 10^{13}$
10,11		$1.8 \cdot 10^{13}$
12		$1.85 \cdot 10^{13}$
13, 14		$1.9 \cdot 10^{13}$

Table 2.6: Multiplication layer parameters used in the AIDAv1 fabrication. Boron energy is set to 100 keV in all the wafers.

Wafer	Dose (at/cm^2)	Energy (keV)
1-4	$1.8 \cdot 10^{13}$	100

Table 2.7: Multiplication layer parameters used in the AIDAv2 fabrication, where all are fabricated in 50 µm thick substrates.

2.4.2 Temporary metal

At the end of the process, a second metal layer is deposited on the previously processed passivation and metal. As aforementioned, temporary metal is used for an easier electrical characterization in high-area pixelated detectors since results difficulty contacting all the pads at the same voltage. Figure 2.19 shows a cross-section of a 2x2 pixelated LGAD with the temporary metal. As can be observed, temporary metal is in contact with the metal and then all pads are electrically contacted at the same voltage. After this process, electrical tests are performed on the wafers to test the main pixelated structures and extract the main characteristics.

2.4.3 End of the process

The final step in the development of AIDA2020 sensors is the removal of temporary metal. After the testing of pixelated structures, wafers are back in the clean room to remove the temporary metal and the process is finished. Figure 2.20 shows the simulated net doping profile after the whole process. Finally, there is a diffusion of $\sim$ 10 µm from the handle wafer to the active wafer, which can lead to a thinner detector. This may cause a higher gain (and lower breakdown voltage) due to the higher electric field peak when shrinking the depleted substrate of the sensor. Figure 2.21 shows an image of a fabricated wafer corresponding to the AIDA2020 production.

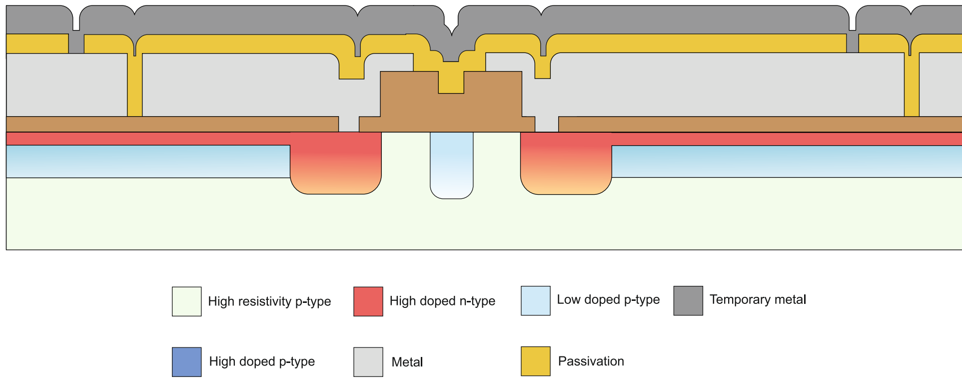

Figure 2.19: Cross-section of the core region in a 2x2 pixelated LGAD using the temporary metal.

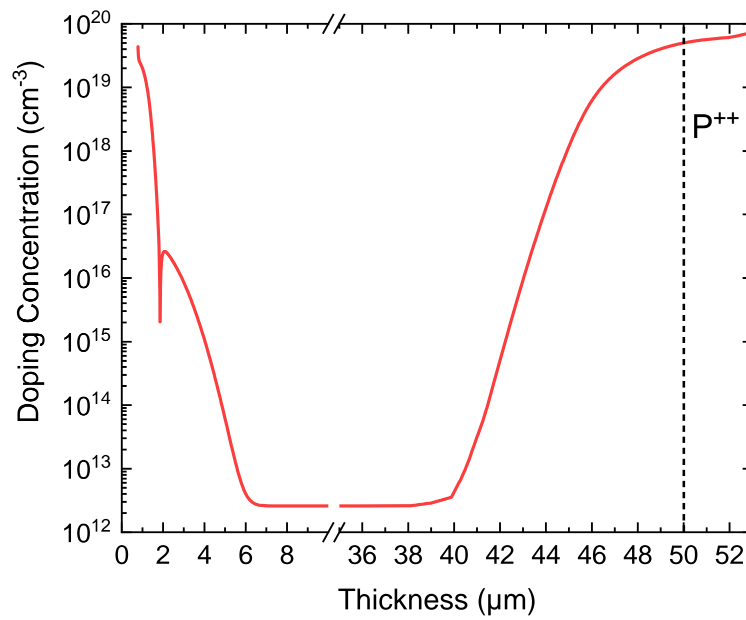

Figure 2.20: Simulated net active doping concentration after the LGAD fabrication.

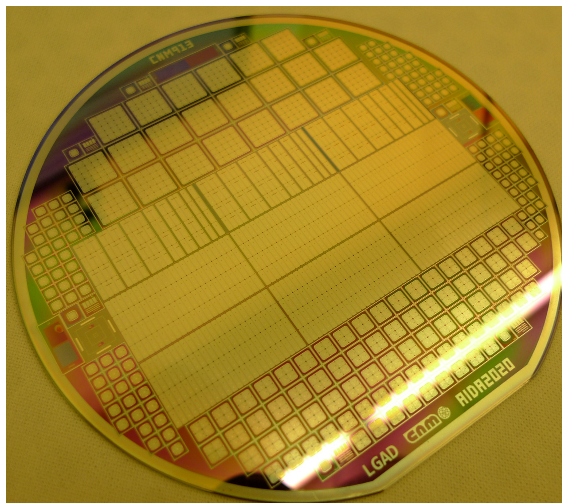

Figure 2.21: Fabricated wafer for the AIDA2020 production.

2.5 Characterization of the AIDAv1 fabrication run

On-wafer electrical characterizations have been carried out in wafers with temporary metal from the AIDAv1 fabrication run, as well as gain and irradiation measurements on diced sensors [ref].

2.5.1 On wafer electrical characterization

Figure 2.22 shows the setup used for the electrical characterization and its full description can be found in [41].

(a)

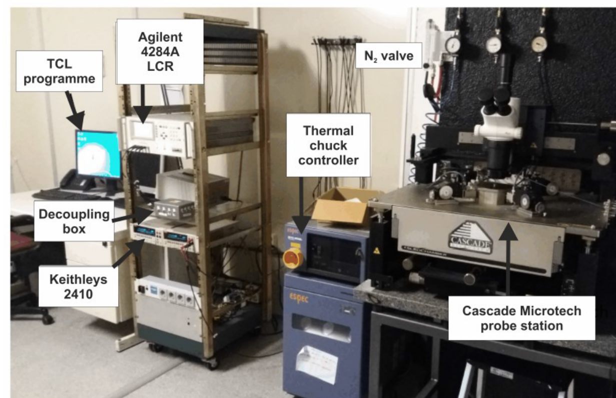

(b)

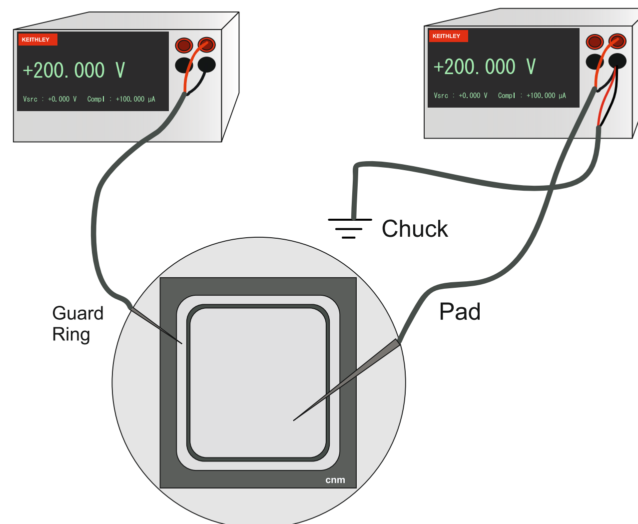

Figure 2.22: (a) Picture of the setup in the Radiation Detectors lab at IMB-CNM. Extracted from [41]. (b) Sketch of the measurement procedure to carry out the electrical characterization.

The measurements have been carried out using a probe station and the procedure or LGADs (and PiNs) with a collector ring is depicted in figure 2.22(b). Voltage is applied to the probes (positive for reverse bias) and each probe is connected to a different (interconnected) Source-Measure Unit (SMUs, Keithley 2410). The ohmic

side of the detector is in contact with the chuck of the probe station, which is at the ground and can be thermally controlled. For C-V measurements, the probes are not directly connected to the SMUs. In this case, the connection is performed through a decoupling box, which is connected to an LCR meter.

First, we characterized the wafers with the temporary metal, in order to test the pixelated structures. Figure 2.23 shows the I-V measurements at room temperature for different boron doses and wafer thicknesses, for 1.0x1.0 mm^2 sensors. On the one hand, higher boron doses entail higher leakage currents and lower breakdown voltage, as anticipated. On the other hand, the breakdown voltage is higher for thicker wafers since the electric field peak at the multiplication region will be higher in thinner sensors at the same working voltage. Nevertheless, the lowest breakdown voltage achieved is $\sim$ 100 V, which may entail a suitable gain-breakdown voltage trade-off. The leakage current at room temperature is clearly too high to operate these sensors in these conditions and later subsections will be focused to understand this behavior.

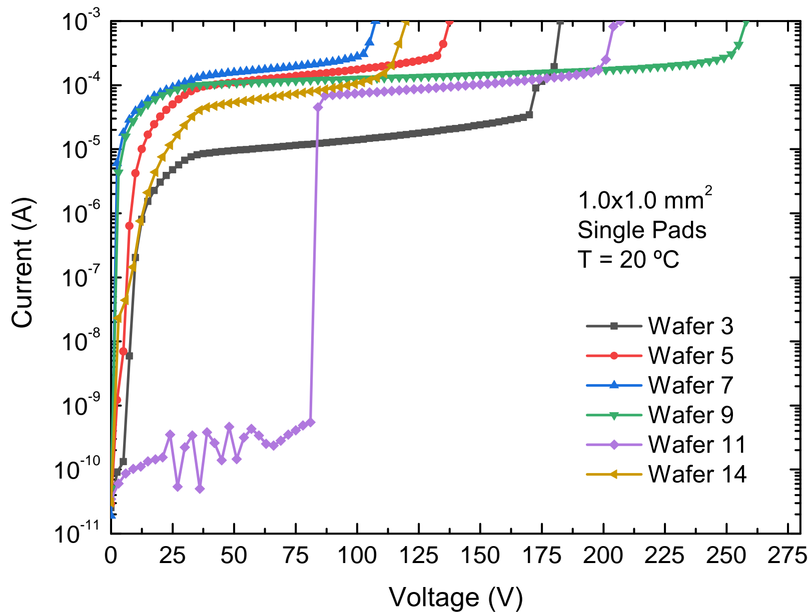

Figure 2.23: I-V measurements at room temperature for 1.0x1.0 mm^2 pad LGADs using different boron doses in (a) 35 µm and (b) 50 µm thick wafers.

The dependence between breakdown voltage and boron dose is depicted in figure 2.24(a). As we observed in the I-V measurements, there is a high reduction of breakdown voltage for thinner substrates due to the higher electric field, and, moreover, this reduction applies to higher doses.

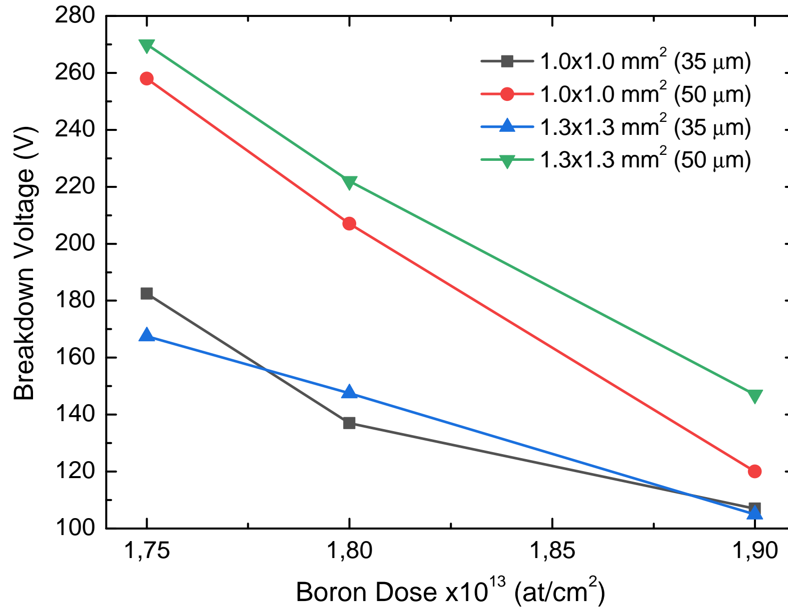

Figure 2.24: (a) Breakdown voltage as a function of boron dose for different LGAD pad sensors and (b) I-V measurements in the guard ring of different LGADs.

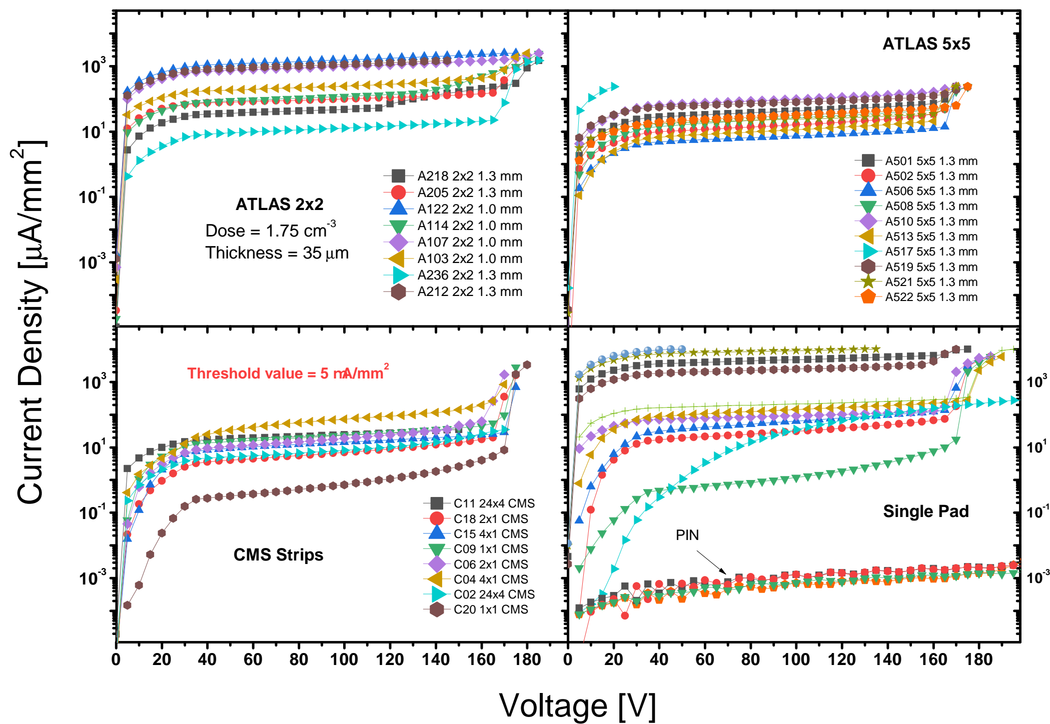

Figure 2.25: Current density at room temperature for 2x2 and 5x5 arrays, CMS strips and Pad LGADs for a medium dose and using 35 µm thick wafers.

Since wafers have temporary metal, we can measure pixelated structures. Figure 2.25 shows the current density measurement for 2x2 and 5x5 arrays, CMS strips, and Pad LGADs for a medium dose and using 35 µm thick wafers at room temperature. Sensors must not overcome the threshold limit of 5 $\mu A/mm^2$, but only PiN sensors

are able to get reasonable leakage current values. There is a high uniformity in terms of current density for all the pixelated structures. Nevertheless, pad LGADs show a higher dispersion which may be caused by the disposition of these sensors in the wafer, because they are distributed throughout all it.
The high leakage current observed in all the LGADs measured from AIDAv1 fabrication may be caused by a higher boron implant than expected. Nevertheless, this should also imply a high reduction of breakdown voltage. In order to discard this hypothesis, we performed C-V measurements on pad LGAD sensors. Figure 2.26 shows the C-V measurements for a PiN and an LGAD sensor from wafer 2. Gain layer depletion occurs at 40 V, which is the expected value for these sensors. Therefore, the high leakage current is not explained by a higher boron dose since V_{BD} and V_{GL} are within the expected parameters.

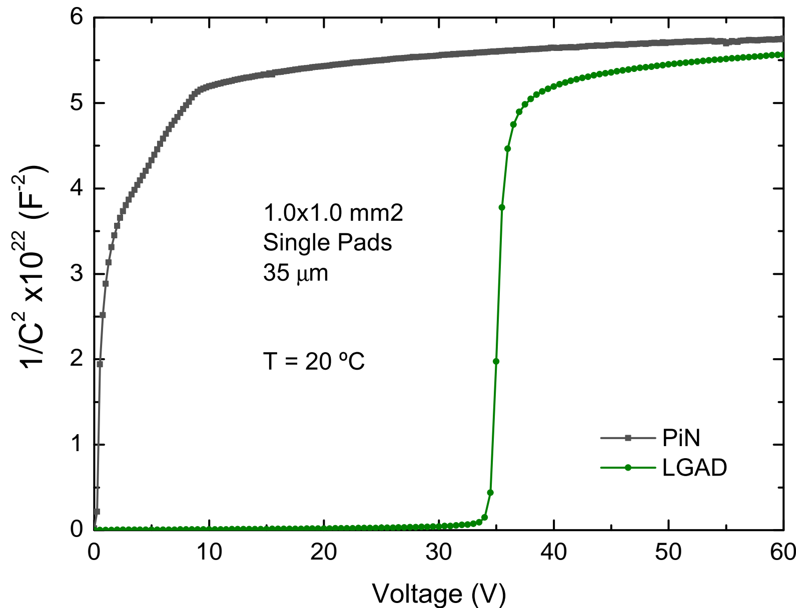

Figure 2.26: C-V measurements at room temperature for 1.0x1.0 mm^2 pad PiN and LGAD using 35 µm thick wafers.

2.5.2 Leakage current issue analysis

We attribute the formation of the multiplication layer to the high leakage current observed in the characterization of LGADs. We have used TCAD tools to study this behavior and solve it for future LGAD developments. In standard LGAD designs, the n^+ is diffused on the multiplication layer until the end of the JTE. In the first AIDA design, we proposed that the n^+ overlaps 5 µm the JTE diffusion, which should be sufficient to contact it. Nevertheless, due to misalignments during the photolithography process, a gap between the multiplication layer and the JTE may occur, inducing a p-type resistor between them. Figure 2.27 shows the TCAD simulation assuming a gap of 0.5 µm between the multiplication region and JTE, which induces a high leakage current in the I-V measurement. The simulated current density is compared

with the proper overhang of the n^+ over the JTE, which gives an eight times lower leakage current, thus solving the leakage current issue.

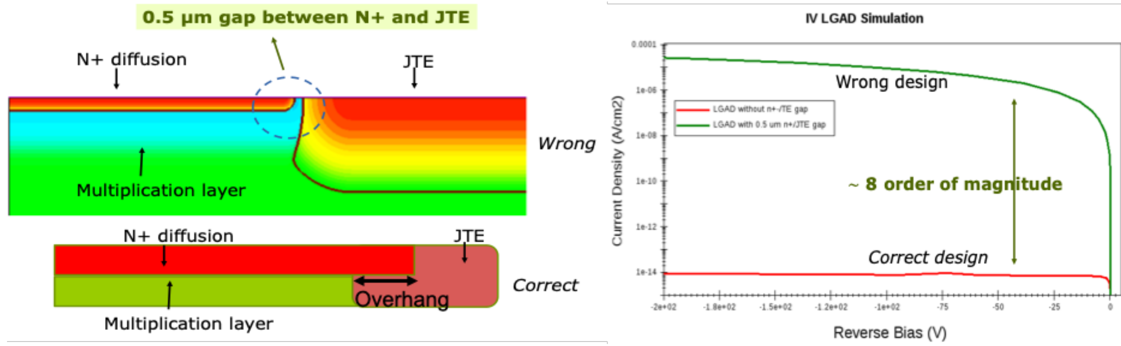

Figure 2.27: TCAD simulations assuming a gap of 0.5 µm between multiplication region and JTE, which induces a high leakage current in the measurement.

To assure the leakage current issue is coming from the multiplication periphery, we performed thermographic measurements on pad LGADs, as observed in figure 2.28. High-current points are observed between the multiplication region and the JTE, which increase their number and intensity by applying a higher voltage.

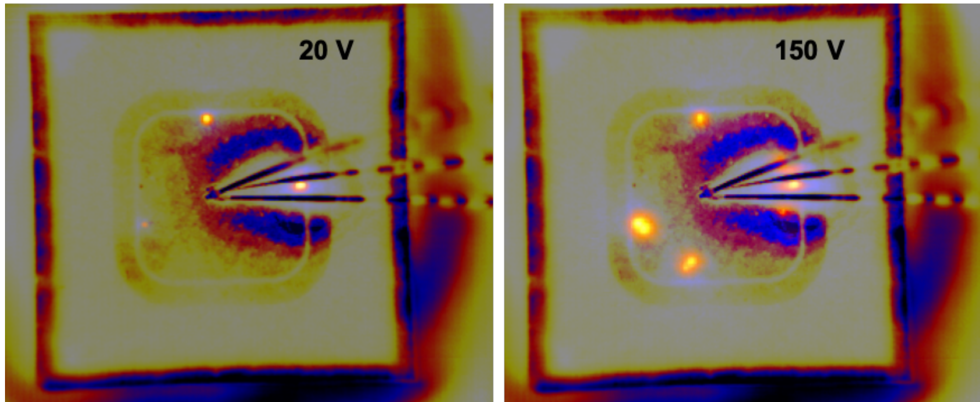

Figure 2.28: Thermographic image of a pad LGAD from AIDAv1 fabrication at 20 and 150 V.

In conclusion, the leakage current issue has been spotted and corrected using a wider overhang between n^+ and JTE. As we shall see below, AIDAv2 fabrication run has used the corrected design, showing an excellent leakage current.

2.5.3 Characterization on AIDAv1 irradiated samples

Selected sensors (1.3x1.3 mm^2) from wafers 5 and 11, which corresponds to a dose of $1.8 \cdot 10^{13}$ cm^{-2} and thicknesses of 35 and 50 µm, respectively, have been tested before and after proton irradiation [70].

Electrical characterization

I-V and C-V measurements have been performed on proton-irradiated sensors at -20 ºC, as shown in figures 2.29 and 2.30. Leakage current decreases with fluence, contrary to previous LGAD fabrications, thus irradiations minimize the high leakage currents observed before irradiation. We found the source of this high leakage current in the gap between n^+ and JTE that creates a p-type resistor, in which doping is reduced with fluence, as observed in acceptor removal studies on previous LGAD fabrications. Therefore, leakage current decreases with fluence since the multiplication layer (and thus gain) is reduced at higher fluences.

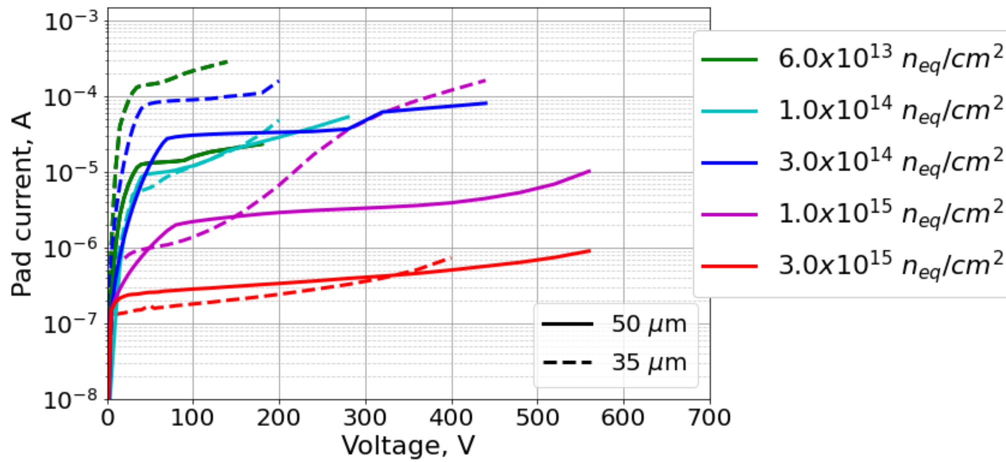

Figure 2.29: I-V measurements on proton-irradiated LGAD sensors from AIDAv1 fabrication.

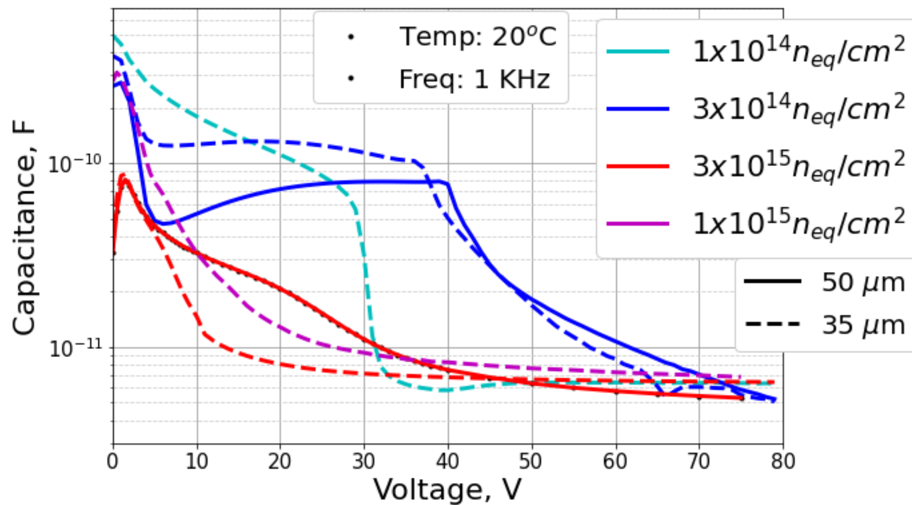

Figure 2.30: C-V measurements on proton-irradiated LGAD sensors from AIDAv1 fabrication.

Figure 2.30 shows the C-V measurements, where V_{GL} is expected to be extracted for future acceptor removal studies. A reduction of V_{GL} should be observed in accordance with the doping concentration of the multiplication layer reduction. Nevertheless,

for some fluences we observe an increase of V_{GL} and further investigations must be addressed to understand this problem [71]. The high leakage current values preclude a thorough investigation of these C-V measurements.

Gain and timing measurements

In addition to the electrical characterization, gain measurements with an IR laser at -20 ºC on non-irradiated and irradiated sensors have been performed, which are shown in figure 2.31. As expected, the gain is heavily decreased with fluence, reaching almost non-gain behavior in 50 µm wafers at $1 \cdot 10^{15}$ n_{eq}/cm^2 fluence. The 35 µm wafers give better results in terms of gain, which is related to the higher electric field at the same voltage due to the thinner depleted substrates.

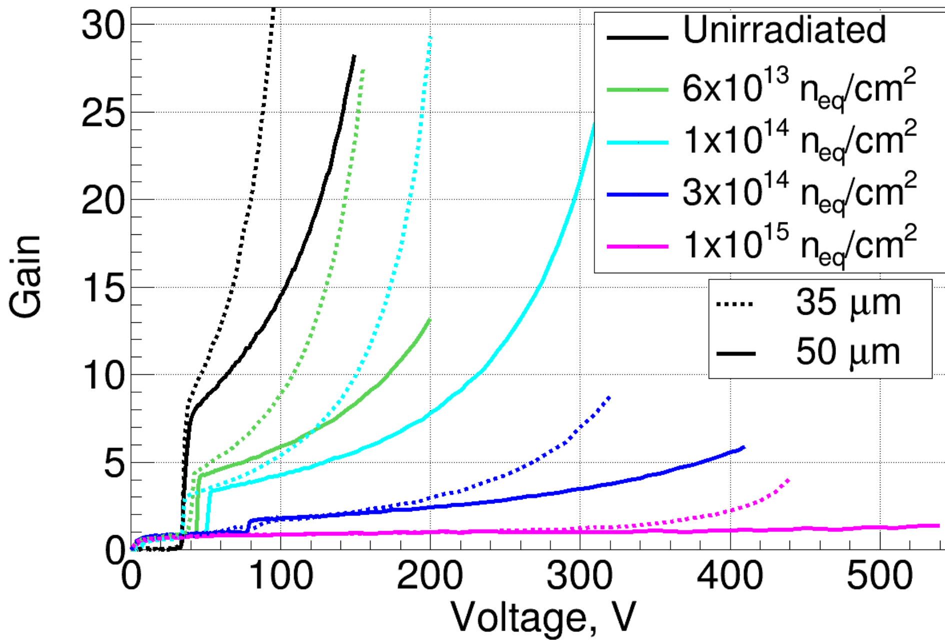

Figure 2.31: Gain measurements on proton-irradiated LGAD sensors from AIDAv1 fabrication.

Furthermore, timing studies have been done in these sensors, where rise time, slew rate, noise, and signal-to-noise ratio have been evaluated [70]. This study reports a better performance of 35 µm thick LGADs in terms of timing due to the lower degradation after proton irradiation. However, the signal-to-noise ratio is lower in thinner substrates which leads to a better jitter in 50 µm wafers. Thus, the use of 35 µm substrates is not fully justified due to the better gain performance since this can be achieved by increasing the doping concentration of the gain layer, for instance. For this reason, AIDAv2 LGADs have been fabricated with 50 µm wafers.

2.6 Characterization of the AIDAv2 fabrication

After the characterization of the AIDAv1 sensors, the photolithographic mask design for the n^+ diffusion has been corrected and used in the AIDAv2 fabrication. The main steps followed in the characterization of LGAD sensors from AIDAv2 fabrication are described below.

1. On wafer electrical characterization (I-V and C-V) at room and low temperature.
2. Wafer dicing process and selection of best-performance sensors.
3. Individual electrical characterization (I-V and C-V) at room and low temperature and gain measurements (laser and Sr90).
4. Irradiation of best sensors at different fluences.
5. Characterization (electrical and gain) in irradiated sensors.

The following subsections describe in detail each step.

2.6.1 Characterization of non-irradiated sensors

On wafer electrical characterization

We have carried out an electrical characterization of the four fabricated wafers. Typical current-voltage (I-V) and capacitance-voltage (C-V) measurements show the desired characteristics of the detector like breakdown voltage, leakage current, depletion of the gain layer, and full depletion of the detector.

The first measurements have been carried out in pad detectors. Figure 2.32 shows the I-V curves for different 1.3x1.3 mm^2 pad LGADs at room temperature for different IP values. The leakage current of the sensors is at $\sim$ 100 pA level and some thermal fluctuations are observed since it is the lowest regime of the setup. The highest IP value has the highest breakdown voltage (115 V), as expected. Nevertheless, it is difficult to clarify the huge difference between 47 and 57 IP values. For the lowest IP value, the maximum breakdown voltage is 90 V. Despite the tendency of breakdown voltage anticipated by simulation, the breakdown voltage is lower than expected. By simulation, this breakdown voltage is attributed to a higher gain layer dose ($\sim$2.15x10^{13}cm^{-3}).

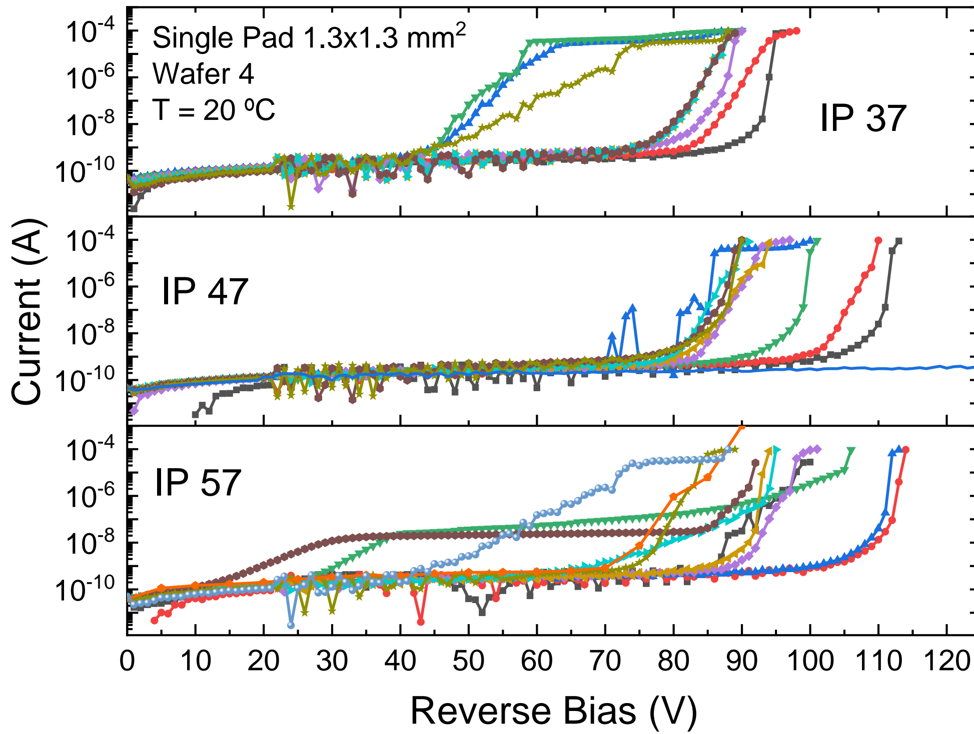

Figure 2.32: I-V measurement on 1.3x1.3 mm^2 pad LGADs for different IP values (wafer 4) at room temperature.

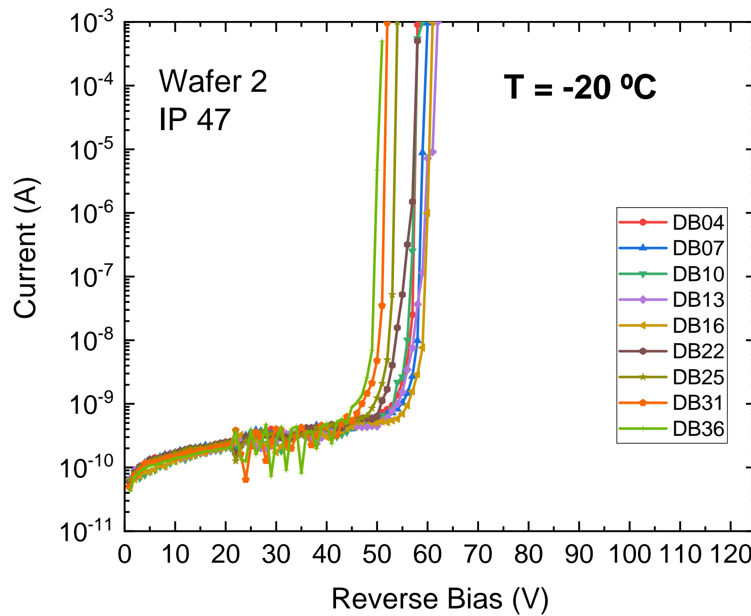

Figure 2.33: I-V measurement on 1.3x1.3 mm^2 pad LGADs with IP47 from wafer 2 at -20 ºC.

We performed low-temperature measurements since it is the conditions for radiation detectors, as shown in figure 2.33. In this case, the breakdown voltage is reduced to 60 V and, therefore, we expect to have a low operation regime. We attribute this effect to the fact that the ionization coefficient is higher at low temperatures [72, 73].

We observe a dispersion in terms of breakdown voltage due to the non-uniform gain layer. As shown in the sheet resistance measurements, there is a huge non-uniformity between the left and right of the wafer. Pad LGADs with an area of 1.3x1.3 mm^2 are located at the left of the wafer and, on the other hand, 1.0x1.0 mm^2 LGADs can be found at the right side of the wafers. Therefore, we expect a lower breakdown voltage in small pad LGADs. Figure 2.34 shows the I-V curves for the 1.0x1.0 mm^2 pad LGADs. As expected, the breakdown voltage is reduced up to 40 V, which makes the detectors almost unusable before irradiation.

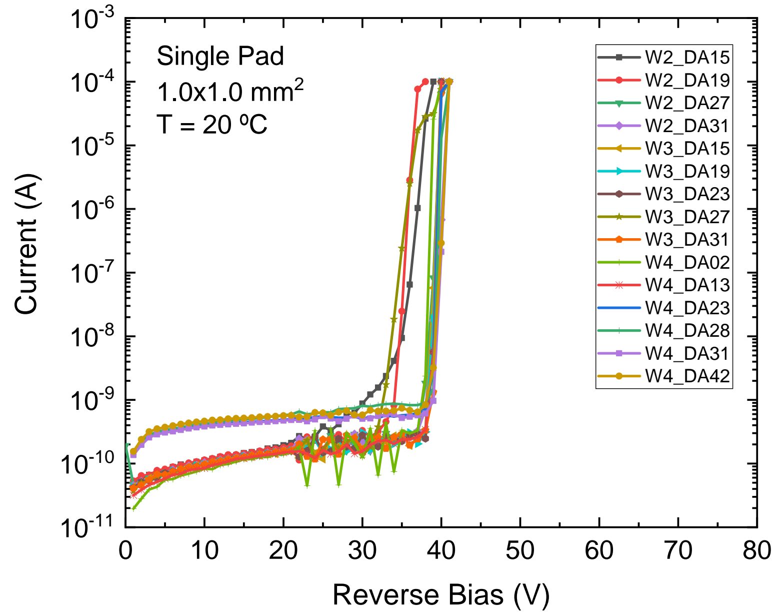

Figure 2.34: I-V measurement on 1.0x1.0 mm^2 pad LGADs from different wafers at 20 ºC.

Using the temporary metal one can measure with the same procedure as the pixelated sensors, where the probe contacts one pad that is connected to all the pixelated electrodes of the sensor. However, we cannot evaluate individually each pad, and, therefore, if one pad has a lower breakdown voltage, the measurement will show this result. Although big pixelated structures are located at the center of the wafer, each IP value has sensors in both areas of the wafer. Figure 2.35 shows the I-V curves at room temperature of 2x2 pixelated LGADs, where, in spite of the higher area, leakage current remains at very low values ($\sim$ 0.1-1 nA). There is a high dispersion in terms of breakdown voltage due to the non-uniform gain layer that results in more relevance than IP values. For instance, in figure 2.35(a), an IP value of 47 presents a higher breakdown voltage. Black-square sensor is located in the left area of the wafer, while the blue-triangle sensor is located in the right area. Even though the higher dispersion, we have devices that can be used before irradiation since the leakage current is very low and some of them reach breakdown voltages up to 80-90 V.

Furthermore, we performed I-V measurements on 5x5 pixelated LGADs, as can be

seen in figure 2.36. Here, the low breakdown voltage is achieved due to the non-uniform gain layer. Nevertheless, we report a very low leakage current in some detectors. In order to fabricate big-area detectors, the gain should be lower to avoid this effect of breakdown voltage reduction.

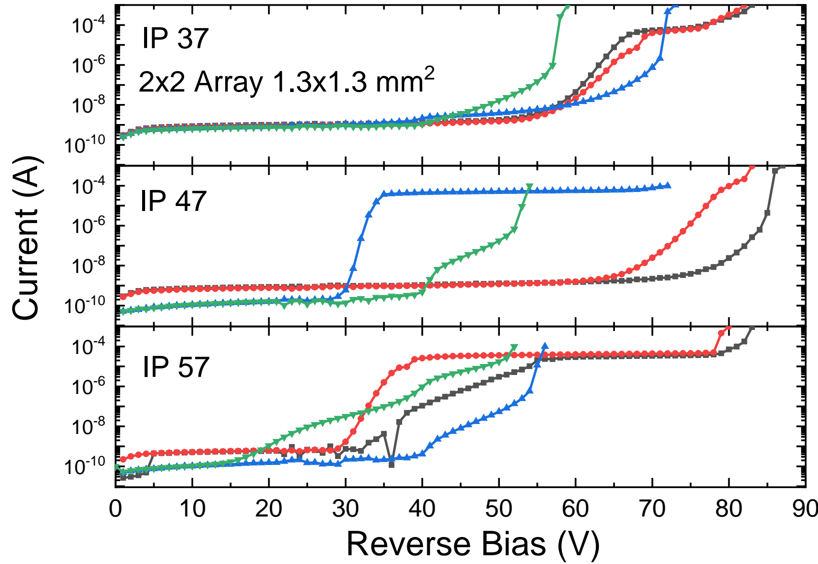

Figure 2.35: I-V measurements for different IP values (wafer 4) at room temperature for (a) 1.3x1.3 mm^2 and (b) 1.0x1.0 mm^2 2x2 LGADs.

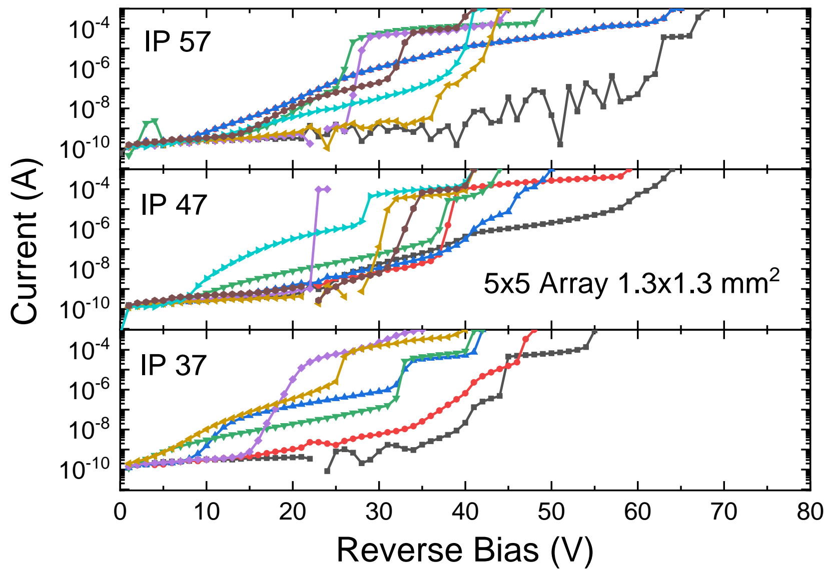

Figure 2.36: I-V measurements for different IP values (wafer 4) at room temperature for 1.3x1.3 mm^2 5x5 LGADs.

C-V measurements have been carried out to extract the gain layer voltage depletion and the full depletion voltage of the sensors. Figure 2.37 shows the C-V measurement on 1.3x1.3 mm^2 pad LGADs for different wafers. Gain layer depletion occurs at 40 V, which is higher than expected. This value can be correlated with the breakdown voltage since we assume the gain layer to have a higher doping concentration than

expected. Again, this value corresponds to a higher dose of $\sim 2.15\text{x}10^{13}$ cm^{-2} and it matches with the observed in the I-V curves. Even if depletion occurs at a higher voltage, there is a high uniformity with pad LGADs between wafers, and full depletion voltage is achieved at 42 V.

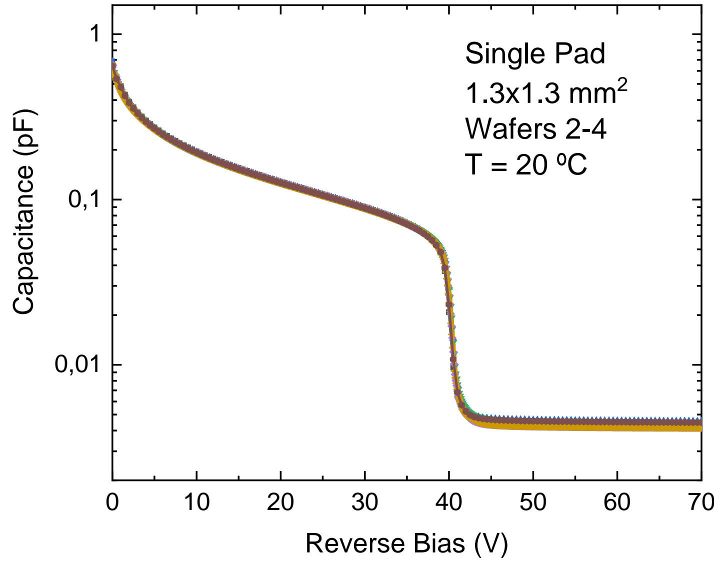

Figure 2.37: (a) C-V measurements at room temperature for 1.3x1.3 mm2 pad LGADs from different wafers.

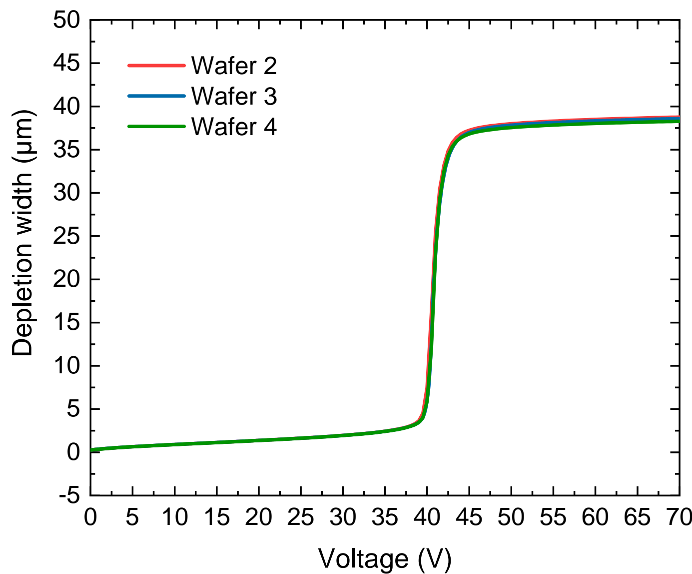

Figure 2.38: Depletion width as a function of voltage for pad LGAD sensors from different wafers.

With C-V measurements, one can extract information about the sensor. Applying a linear fit to the $1/C^2$-V graph, we found a substrate doping concentration of $\sim 2 \cdot 10^{13}$ cm^{-3}. Moreover, depletion width can be calculated by its relation with capacitance. Figure 2.1 shows the depletion width as a function of the applied bias where at 40 V, after gain layer depletion, the sensor starts to deplete until a maximum of 38 µm. This

value agrees with the simulations and demonstrates that the low-resistivity handle wafer is diffusing into the active high-resistivity wafer about 10 µm. Moreover, doping concentration can be extracted by looking at the variation of the inverse square of capacitance with the applied voltage [11]:

$$N_D = \frac{2}{q\epsilon_0\epsilon_{Si}A^2}\left(\frac{\partial(1/C^2)}{\partial V}\right)^{-1} \tag{2.1}$$

Figure 2.38 shows the extracted doping concentration as a function of depletion width. Multiplication layer peak is found at $\sim 1.8 \cdot 10^{16}$ cm^{-3}, which is lower than the simulated and is inconsistent with the lower breakdown voltage obtained by experimental measurements. Nevertheless, some studies report that the peak concentration found by C-V measurement is lower than the measured experimentally [74]. Equation 2.1 supposes that the structure is a one-side abrupt junction. However, in a fabricated LGAD sensor, the depletion region is not ideal due to the JTE and collector ring diffusions. Therefore, profiles extracted from the CV can be used for a qualitative study. Also, Second Mass Ion Spectrometer (SIMS) or Spreading Resistance Profiling (SRP) techniques could extract experimentally the profiles of an LGAD with higher precision, but, as we can see in Figure 2.39, different techniques provide different values for the doping profile. The SIMS measurement is more accurate in calculating the peak, rather than the depth. In this sense, both simulations and C-V measurements show a similar boron peak as in the SIMS measurement. On the other hand, with the SPR the accuracy of the depth is higher, which we compare with C-Vs and simulations, giving a similar result. In conclusion, we must combine all the methods to understand the doping profiles of the fabricated LGAD and it should be used to qualitatively understand the most important parameters of the sensor.

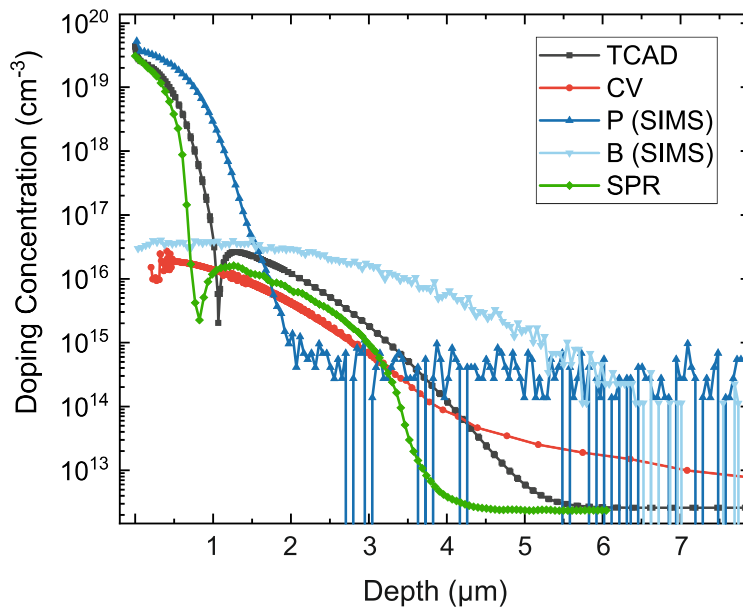

Figure 2.39: Doping concentration comparison as a function of depletion width for a pad LGAD sensor, using different techniques.

Gain measurements

Gain studies have been performed at the IMB-CNM Radiation Detectors lab. To carry out the characterization, the transient current technique (TCT) has been used [75]. This technique is based on the current induced by the movement of charge carriers inside a detector, which is illuminated by picosecond laser pulses, generating the charge carriers. Light has a different absorption in silicon depending the wavelength, and, therefore, by changing the wavelength of the laser, is possible to vary the penetration depth. This allows for performing different studies in silicon detectors.

For instance, an infrared (IR) laser, which has a wavelength of 1064 nm, penetrates about 1 mm in silicon. Thus, for our LGAD samples, an IR laser will penetrate the whole thickness of the sensor and is used to reply to a MIP going through the detector. Blue laser (448 nm) is able to penetrate less than one micron inside silicon; therefore, it is used to study the induced signal when charge carriers are generated at the surface of the detector. This method is used to reproduce low penetrating particle irradiations.

LGADs have been widely characterized by TCT measurements. Some techniques have been used apart from the standard TCT, like edge-TCT which consists in illuminating the detector from the edge with an IR laser. By using this method, the electric field can be extracted, which is a very important parameter in LGAD sensors, especially in irradiated detectors [47].

Figure 2.40(a) shows a sketch of the TCT measurement. LGAD sensors are wire-bonded to a printed circuit board (PCB). LGAD must be over full depletion to assure only charge carriers created by the pulsed laser are collected by the electrodes. The signal formed by the sensor goes through an amplifier and pulses are measured and analyzed by an oscilloscope. Figure 2.40(b) shows the TCT setup used in the IMB-CNM Radiation Detectors Laboratory.

Figure 2.41 shows the gain and collected charge for an LGAD sensor from the AIDAv2 run at room temperature. Until 40 V there is no gain since the sensor is not fully depleted. Then, we observe a gain between 10-40 before 70 V. We expected to have a lower gain before the fabrication, as we can observe in the gain plot devoted to the TCAD simulations (figure 2.6(d)). Nevertheless, based on the electrical performance of the sensor, we presumed that this gain would be higher than expected.

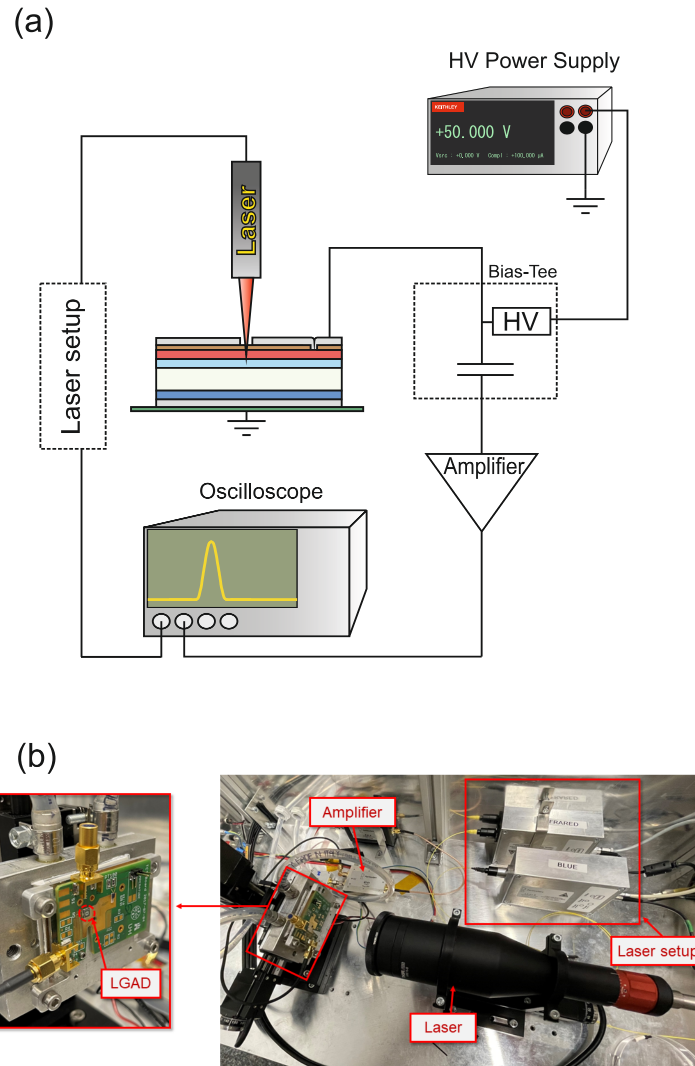

Figure 2.40: Sketch of the TCT setup used at IMB-CNM lab.

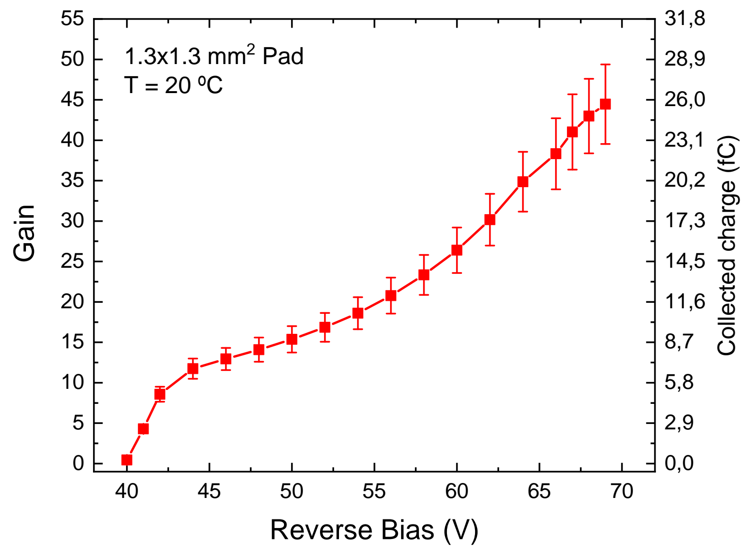

Figure 2.41: Gain and collected charge of non-irradiated 1.3x1.3 mm^2 pad LGAD from AIDAv2 run.

2.6.2 Characterization of irradiated sensors

Electrical Characterization

Pad sensors have been irradiated with neutrons with different fluences up to $2.5 \cdot 10^{15}$ n_{eq}/cm^2. Figure 2.42 shows the current density (J) as a function of reverse bias for these sensors at -30 ºC. Before irradiation, the sensor is under breakdown a few volts after depletion, as we expected from the previous measurements. Nevertheless, breakdown voltage increases (up to 675 V) with fluence and this may entail a reduction of the gain. AIDAv2 sensors provide leakage current densities lower than the HGTD requirement (125 µA/cm²) and it overcomes the threshold only when the device is almost under breakdown. Therefore, in terms of leakage current, the AIDAv2 sensors are suitable to be used in high-radiation environments.

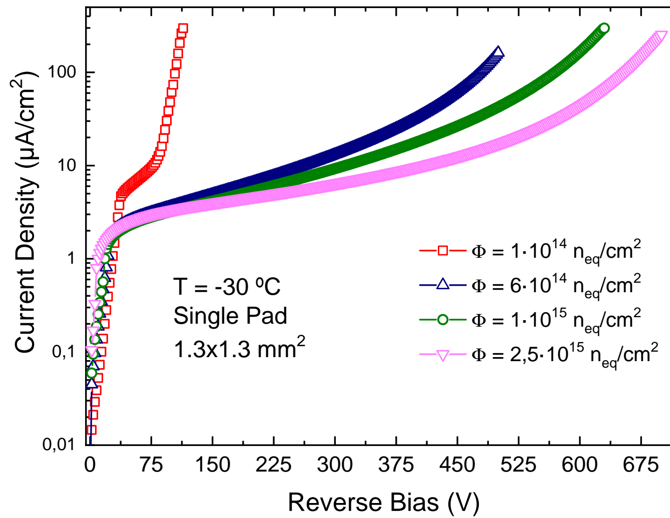

Figure 2.42: Current density at -30 ºC for neutron-irradiated LGADs from AIDAv2 run.

We have carried out C-V measurements to test gain layer depletion voltage. On one hand, we expect to have a lower V_{GL} as fluence increases due to gain reduction and, on the other hand, we assume a higher V_{FD} due to negative space charge formation in the bulk of the sensor. Figure 2.43 shows the C-V measurements of pad LGAD sensors with three different fluences at -30 ºC and at 100 Hz. There are marked in the graph points where the gain layer is fully depleted. As expected, the higher the gain, the lower the voltage depletion. Table 2.8 shows the depletion gain layer at a given fluence extracted from the C-V measurements. In non-irradiated sensors, after depletion of the gain layer, V_{FD} is achieved in a few volts. Nevertheless, irradiated sensors need more voltage as fluence increases to deplete the substrate, reaching values of more than 50 V for the highest irradiated sensor.

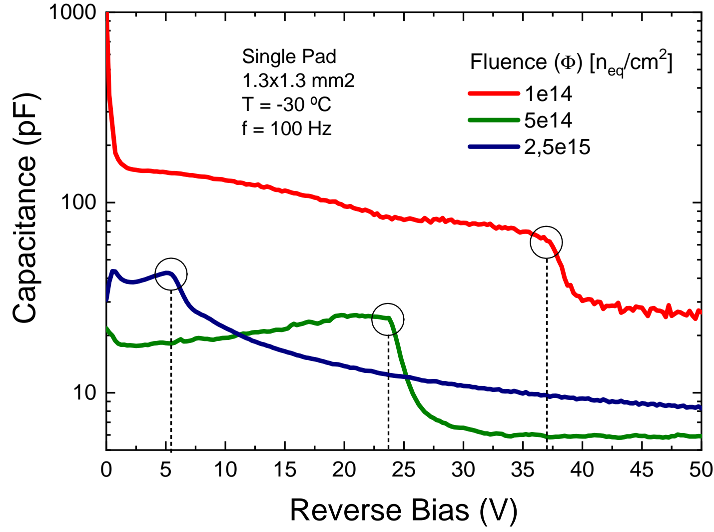

Figure 2.43: CV measurements at -30 ºC and f=100 Hz for neutron-irradiated LGADs from AIDAv2 run.

Gain layer depletion voltage (V)		
Φ=$1 \cdot 10^{14}$ $\mathrm{n_{eq}/cm^2}$	Φ =$5 \cdot 10^{14}$ $\mathrm{n_{eq}/cm^2}$	Φ = $2.5 \cdot 10^{15}$ $\mathrm{n_{eq}/cm^2}$
36.75	23.5	5.25

Table 2.8: Gain layer depletion voltage values for irradiated sensors, extracted from C-V measurements.

Acceptor Removal

From the C-V results, we can study the boron acceptor removal phenomenon, which is crucial in the development of LGADs in harsh irradiation environments. Figure 2.44 shows the gain layer depletion fraction as a function of the fluence. At $2.5 \cdot 10^{15}$ $\mathrm{n_{eq}/cm^2}$, which is the target for ATLAS, we report a V_{GL} fraction of $\sim$ 16,5 %, which entails that gain will be extremely reduced. Equation 1.18 fits empirically this behavior and we extract a value of $c_A = 10.7 \cdot 10^{-16}$ $\mathrm{cm^2}$, which agrees on other studies on neutron-irradiated LGADs [51]. Therefore, the gain will be heavily suppressed after harsh irradiations, and optimization of the gain layer must be envisaged to mitigate this effect. In this sense, the carbon-enriched multiplication layer has been proposed to reduce c_A [34], and thus improve the performance of the sensor at higher fluences.

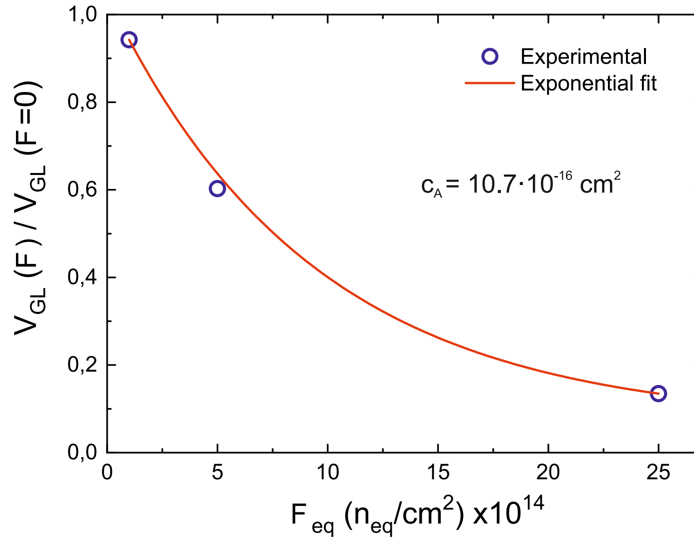

Figure 2.44: Gain layer depletion fraction as a function of neutron fluence.

Collected charge and time resolution

Irradiated sensors have been characterized using a beta setup (Sr90), which is located at IFAE (Institut de Física d'Altes Energies) lab [76, 77, 78]. Collected charge and time resolution have been measured for neutron-irradiated single pad LGADs at -30 ºC. Figure 2.45(a) shows the collected charge of the neutron-irradiated LGADs at -30 ºC. As expected, collected charge decreases with fluence. The unirradiated sample has a low breakdown voltage (46 V) which induces a high collected charge and a low operation voltage range. Sensors can meet the CMS requirements in the lowest fluence regime ($1 \cdot 10^{15}$ n_{eq}/cm^2) below 600 V. On the contrary, the 4 fC required by ATLAS are achieved at 661 V (at $2.5 \cdot 10^{15}$ n_{eq}/cm^2). The maximum charge collected at the highest fluence is 8 fC. Nevertheless, at this voltage, the sensor is almost under breakdown and it cannot be operative.

In addition, time resolution has been measured under the same conditions. Figure 2.46 shows the time resolution as a function of the fluence for the same LGAD sensors. Before irradiation, the sensor cannot be operated at more than 46 V despite it reaching the desired 50 ps. After irradiation, the time resolution is below CMS and ATLAS limits at any fluence point. At $1 \cdot 10^{15}$ n_{eq}/cm^2, the sensor is able to achieve values under 25 ps. Moreover, at $2.5 \cdot 10^{15}$ n_{eq}/cm^2 it can reach 33 ps before the breakdown, but the operational voltage is limited to >600 V. These excellent timing resolution results can be attributed to a high gain and the active thickness reduction due to the Si-Si wafers.

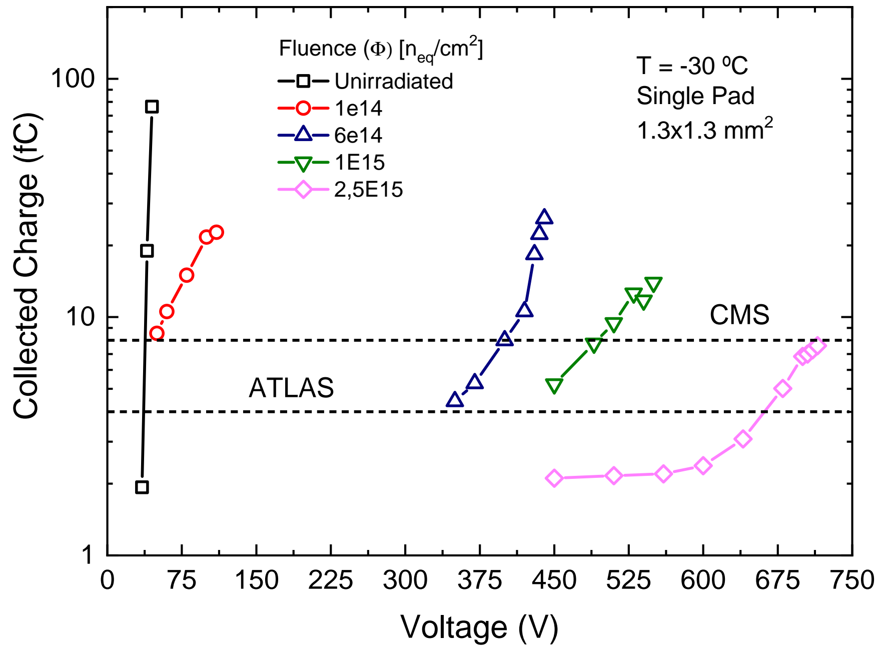

Figure 2.45: Collected charge at -30 ºC for 1.3x1.3 mm^2 single pad LGADs from the AIDAv2 run. (b) Required voltage to reach minimum collected charge for CMS and ATLAS timing detectors as a function of neutron fluence [78, 77].

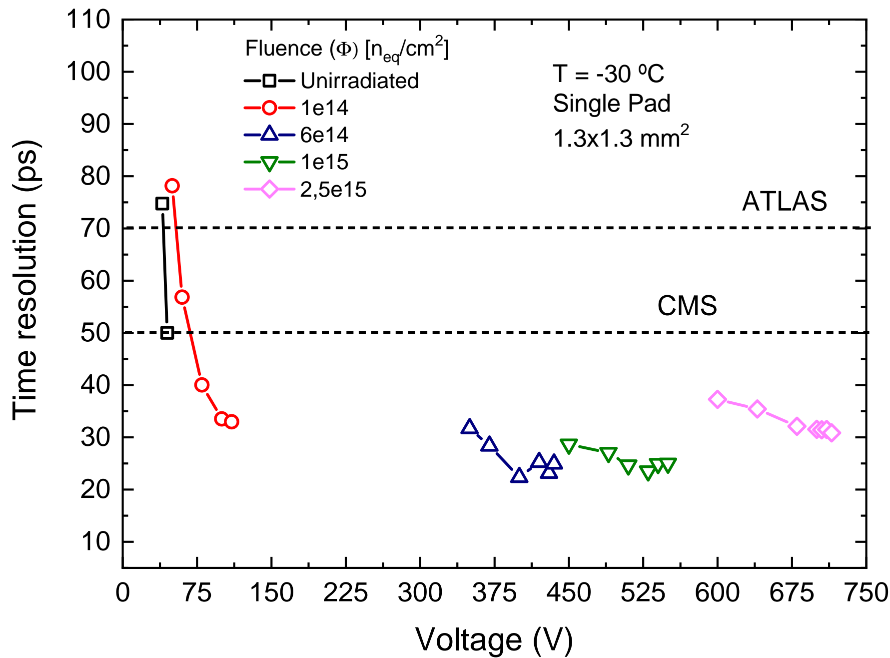

Figure 2.46: Time resolution at -30 ºC for 1.3x1.3 mm^2 single pad LGADs from the AIDAv2 run [78, 77].

AIDAv2 LGAD sensors have been measured at SCIPP (Santa Cruz Institute for Particle Physics) laboratories [79] on behalf of the ATLAS experiment. In this case, only one LGAD from AIDAv2 is measured at $2.5 \cdot 10^{15}$ n_{eq}/cm^2, with an operational voltage of $\sim$ 700 V. In this lab, HPK [80] and FBK [81] neutron-irradiated sensors

have been measured at the same time with the CNM sensor in order to compare different LGAD technologies. Figure 2.47(a) shows the collected charge at the operational voltage as a function of the fluence, where the HPK sensor reaches 6 fC, while FBK and CNM sensors achieve 4 fC. Figure 2.47(b) shows the time resolution at the operational voltage as a function of the fluence, where all LGAD sensors are able to reach a time resolution below ATLAS requirements. At $2.5 \cdot 10^{15}$ n_{eq}/cm^2, LGAD sensor from the AIDAv2 run has the lowest time resolution ($\sim$ 40 ps). The charge collected and time resolution measured at SCIPP is in agreement with the results obtained at IFAE.

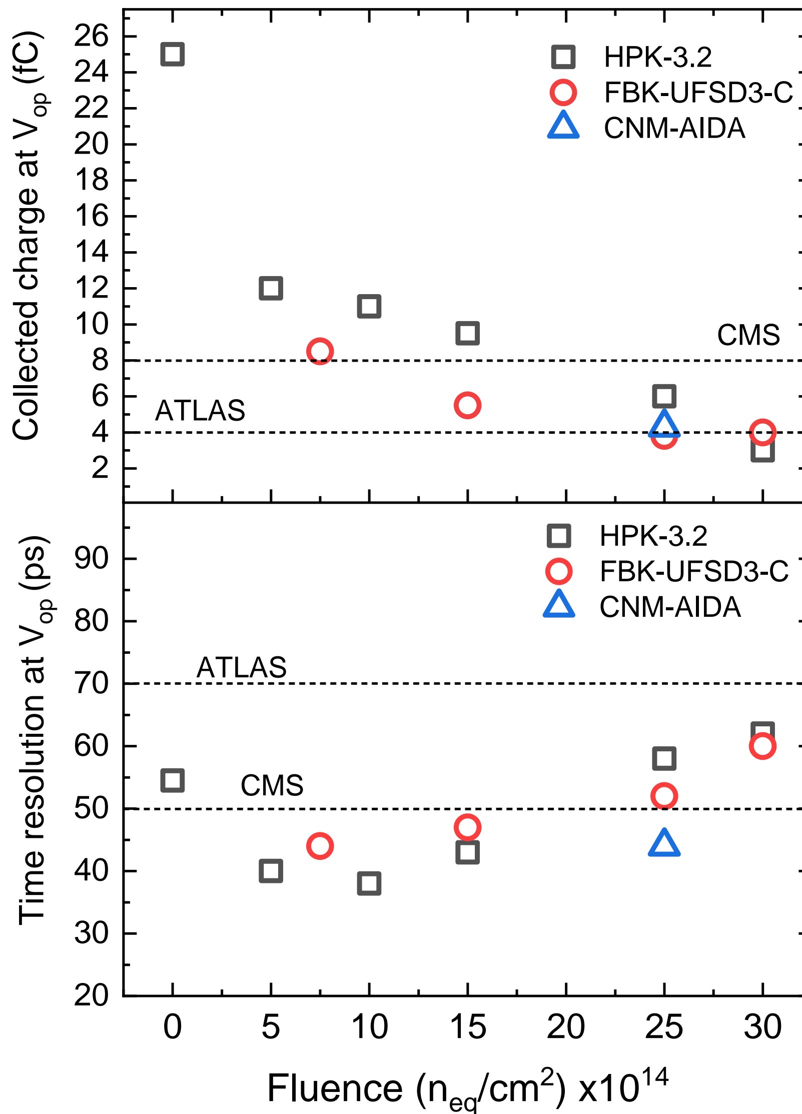

Figure 2.47: Collected charge and time resolution at operational voltage as a function of the fluence for HPK, FBK and CNM neutron-irradiated sensors. Measurements performed in [79].

Mortality in irradiated LGADs

As already stated, applied reverse bias in irradiated LGAD sensors is limited up to 600 V (in 50 µm) in CMS and ATLAS timing detectors. These constraints have been

considered due to premature mortality in high-irradiated LGADs observed in some studies [65, 66], where local burns appear in the pad or in the collector ring (if it is contacted) in the presence of a high electric field. This process is known as Single Event Burnout (SEB) and appears more frequently in test beams where sensors are irradiated, on the contrary, it is less common to observe this effect when measuring in a laboratory. The difference between the irradiation in a test beam or in a laboratory using, for instance, an Sr90 source, is the amount of deposited charge in the sample. The maximum energy for an Sr90 is 2.3 MeV, while in a test beam it can be up to tens of MeV. Therefore, this amount of deposited charge during a test beam may cause conditions that lead to a premature breakdown.

Even if there is no clear answer to this effect, the main hypothesis is that there is an electric field collapse due to a high concentration of free charges [78]. Figure 2.48 shows a Scanning Electron Microscope (SEM) image of a neutron-irradiated LGAD ($3 \cdot 10^{15}$ n_{eq}/cm^2) from a previous fabricated run at IMB-CNM. There is a huge hole in the sensor which causes these sensors cannot to be operative anymore. To avoid this problem we must operate the LGADs at voltages lower than 600 V [82].

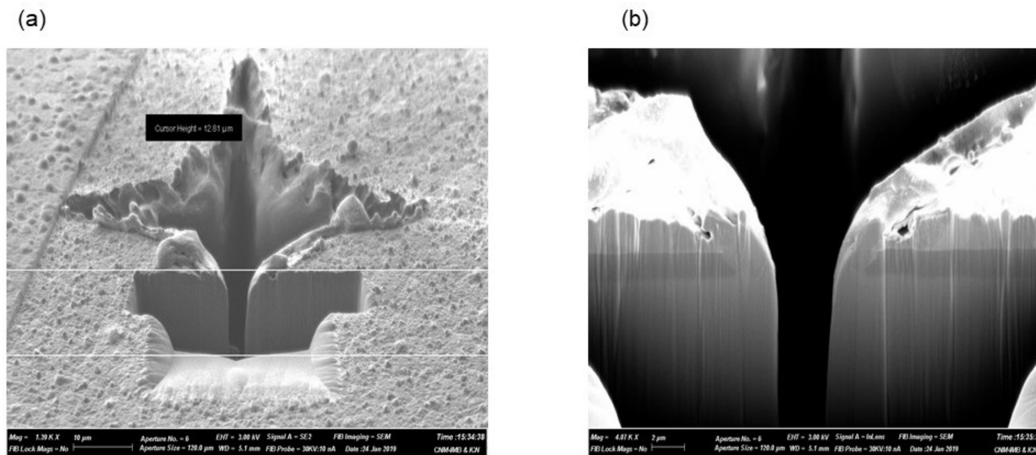

Figure 2.48: SEM image of a $3 \cdot 10^{15}$ n_{eq}/cm^2 neutron-irradiated LGAD that has suffered a local burn in the collector ring.

2.6.3 Summary of sensor properties

After a full characterization of the fabricated sensors, in this section, a summary of the performance before and after irradiation is described.

Non-irradiated sensors

The electrical testing in LGADs before irradiation shows an excellent leakage current both in pad sensors, whatever their size. In terms of breakdown voltage, the values obtained are in general lower than expected. Pad LGADs (1.3x1.3 mm^2) provide maximum values from 90 (IP 37) to 115 V (IP 47 and 57) and this value decreases to a maximum of 60 V at -20 ºC. Small pad LGADs show a maximum breakdown

voltage of 40 V, which is related to their location in the wafer, where a higher doping concentration has been extracted.

Pixelated LGADs (2x2 and 5x5) show an excellent result in leakage current, with some dispersion in the case of 5x5 arrays due to their higher area and the subsequent non-uniform gain layer. There is a high dispersion in terms of breakdown voltage for the 2x2 LGADs which makes it difficult to correlate the performance with the IP values. Nevertheless, some detectors are able to provide similar performance as pad LGADs. On the contrary, only a few 5x5 arrays surpass the 60 V threshold, so performance in high-area sensors must be improved to fabricate big-area LGADs. This may be possible lowering the boron peak, which will result in the worst performance after irradiation. Therefore, engineering analysis in the formation of the gain layer must be envisaged to overcome this problem. The use of a deeper implant could be the solution to mitigate this effect and obtain a more uniform gain layer [30, 68].

C-V measurements show there is a high consistency between fabricated wafers in terms of gain layer depletion, which is situated at 40 V. Due to the high resistivity and thin substrate, the sensor is fully depleted just a few volts after the gain layer. The depletion width is calculated using the C-V measurements showing a value lower than 40 µm due to the diffusion of boron dopants from the low-resistivity handle wafer to the active substrate. This lower depletion width may entail a higher electric field than expected.

Finally, TCT measurements at room temperature reveal a gain between 10-40 V before 70 V, which is increased at lower temperatures. Therefore, we observed a higher gain than expected by simulations but in line with the electrical characterization parameters, such as breakdown and gain layer depletion.

Irradiated sensors

This characterization has been performed on single-pad LGADs. The desired sensors to be used in the timing detectors must be 15x15 or 16x16 pads. In order to study if these samples can be candidates to be used in the future ATLAS and CMS timing detectors, we have compared their performance with the Market Survey design properties. It is important to mention that the CMS Market Survey provides the sensor properties at -25 ºC and we have performed the measurements at -20 ºC before irradiation and -30 ºC after irradiation.

Table 2.9 shows the sensor properties of the LGAD sensors from the AIDAv2 production according to the CMS Market Survey requirements. For un-irradiated sensors, all the requirements are accomplished, except the desired breakdown voltage. As explained in the characterization section, the breakdown voltage of the detectors at low temperatures is lower than expected. Full depletion voltage is achieved at 42 V, which is lower than the 50 V required. Therefore, the operational voltage region is only of 13 V. Leakage current, time resolution, and collected charge requirements are

achieved. For irradiated (at $1 \cdot 10^{15}$ n_{eq}/cm^2) sensors, all the requirements have been accomplished. V(8 fC) is reached at 496 V, which gives a relation with the active thickness of ∼ 10 V/µm. Furthermore, the breakdown voltage is ∼ 100 V over the operational value. The time resolution of the sensors is excellent, providing values under the desired 50 ps in all the fluence and voltage regimes. The charge collected of 8 fC is reached up to $1.5 \cdot 10^{15}$ n_{eq}/cm^2. Finally, the leakage current after irradiation at the operational voltage is 90 µA/cm^2, which is lower than the expected value (< 1 mA in a 15x15 mm^2 sensor). In conclusion, AIDAv2 single pad sensors accomplish the Market Survey sensor requirements except for the breakdown voltage before irradiation.

Un-irradiated		**Irradiated (1-1.5 $\cdot$ 10^{15} n_{eq}/cm^2)**	
V_{FD}	42 V	V(8 fC)/D	10 V/µm
V_{BD}	55 V	V_{BD}	592 V
σ at V(8 fC)	50 ps	σ at V(8 fC)	26 ps
I_{leak}	0.01 µA/cm^2	I_{leak}	90 µA/cm^2
CC/MIP at V(8 fC)	8 fC	CC/MIP at V(8 fC)	8 fC

Table 2.9: Summary of electrical performance before and after irradiation for the CMS Market Survey.

Table 2.10 shows these requirements at -30 ºC. In the same way, as in the CMS requirements, the main problem related to these sensors is the low breakdown voltage. The gain layer and full depletion voltages meet the requirements, as well as the leakage current. The sensors reached a collected charge of 76 fC and a time resolution of 50 ps. After a neutron-irradiation of $2.5 \cdot 10^{15}$ n_{eq}/cm^2, breakdown and gain layer depletion voltages meet the requirements. Nevertheless, the required 4 fC are achieved at 661 V, which is higher than the maximum operating voltage allowed by ATLAS. At 600 V, time resolution has an excellent value of 40 ps, which is far away from the required 70 ps, and leakage current density is ∼ 30 µA/cm^2, which is below the required.

Un-irradiated		**Irradiated (2.5 $\cdot$ 10^{15} n_{eq}/cm^2)**	
V_{GL}	38 V	V_{GL}	5.25 V
V_{FD}	42 V	V_{op}	661 V
V_{BD}	46 V	V_{BD}	714 V
I_{leak} (V_{op})	0.01 µA/cm^2	I_{leak} (V_{op})	125 µA/cm^2
CC (V_{op})	76 fC	CC (V_{op})	4 fC
σ (V_{op})	50 ps	σ (V_{op})	<70 ps

Table 2.10: Summary of electrical performance before and after irradiation for the ATLAS Market Survey.

Chapter 3

LGAD sensors for timing applications in 150 mm silicon wafers

The microelectronics industry is moving towards even larger silicon wafers, in order to optimize the fabrication of chips. In this sense, the IMB-CNM clean room equipment is being renewed in order to cope with this transition. In this chapter, the development of LGAD sensors for timing applications in 150 mm silicon wafers is going to be fully described, including the optimization of the sensors for this technology, the fabrication, and the subsequent characterization before and after irradiation. In addition, it is described a new development in timing LGADs and novel strategies to enhance their performance.

3.1 Introduction

The development of LGADs at IMB-CNM in 150 mm technology is described in this chapter. Large-area semiconductor foundries for CMOS technology use 200 and 300-mm wafers in fully automated lines to maximize the throughput and minimize the waste of silicon. In this framework, wafer manufacturers are producing fewer and fewer 100 mm wafers. Therefore, the IMB-CNM clean room has to transfer all the individual technology steps to 150 mm wafer capability, replacing old machines and furnaces, with the subsequent fitting of the new equipment to the desired technical requirements. The LGAD process technology needs also to be transferred to 150 mm wafers, overcoming the inherent challenges.

The first step is to be able to produce LGADs for the HL-LHC upgrade in 150 mm wafers, starting with pad designs, the simplest LGAD layout. LGADs to be used in the ATLAS and CMS timing detectors have to be fabricated in thin ($\sim$ 50 µm) active layer wafers. However, in the basic LGAD generation in 150 mm technology (labeled as 6LG0), thick wafers have been used (300 µm) for the sake of comparison with the well-established LGAD technology on 100 mm wafers. This LGAD fabrication has to be understood as a seed for future LGAD productions in 150 mm wafers and has been used to calibrate the LGAD technology. With this production, we

obtained basic information about the optimal multiplication layer parameters, and we performed electrical tests to assure that the development of LGADs in 150 mm can be envisaged. Then, the first generation of thin LGADs in 150 mm technology (labeled as 6LG1) is oriented to the fabrication of detectors for timing applications, using SOI wafers with an active layer in the range of 50 µm [41]. A second generation (6LG2) of thin LGAD will use silicon on silicon bonded wafers (Si-Si), and a third generation (6LG3) will use epitaxial silicon wafers where a high-resistivity p-type epitaxy, 55-µm thick, is grown over a low-resistivity wafer.

The next sections describe the design and fabrication of thin LGADs in 150 mm wafers. In addition, the 6LG1 and 6LG3 are fully characterized, including irradiation measurements on the 6LG3 sensors.

3.2 Design and optimization of the LGAD sensors

3.2.1 Multiplication region optimization

The main parameter in LGADs is the multiplication layer and is strongly dependent on the total thermal budget. In the 100 mm technology, the drive-in process was performed at 1150 ºC, but the maximum allowable temperature in 150 mm furnaces is 1100 ºC. Therefore, the drive-in process has been adapted to obtain the desired doping profile. Figure 3.1 shows the simulated doping profiles for the 150 mm technology using different boron doses, where a small difference is observed between them. However, as already seen in previous fabrications, these small changes may lead to a different performance of the sensor.

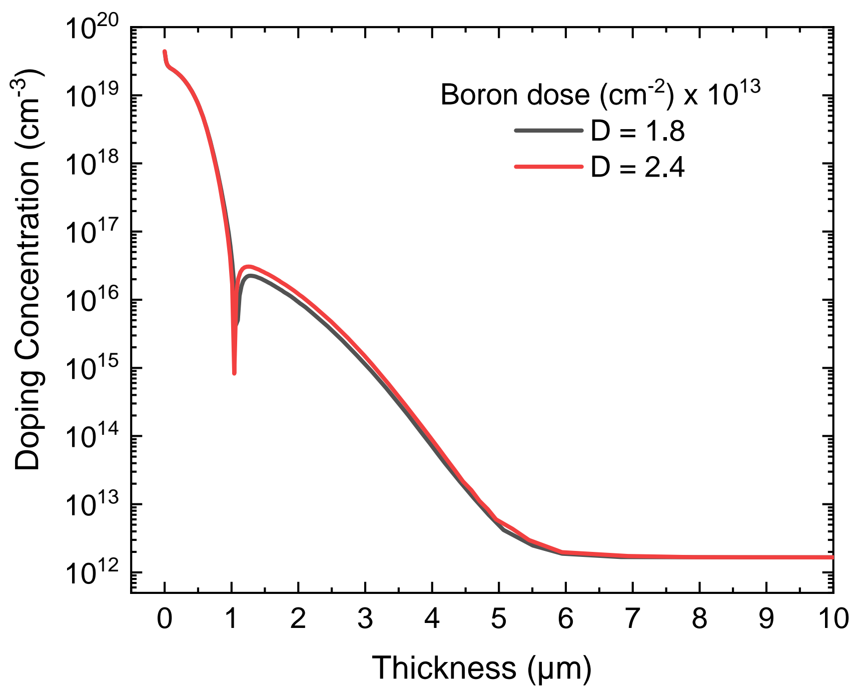

Figure 3.1: Simulated doping profiles for the 150 mm thermal process for different boron doses.

However, it was observed in the AIDA2020 production (100 mm wafers) that small changes in technological parameters lead to several non-uniformities in electrical performance. For this reason, TCAD simulations have been carried out in order to study the electrical performance of the sensor in 150 mm technology. In the performed simulations, the standard high-resistivity values for the substrate and an active thickness of 50 µm have been used. Figure 3.2 shows the gain simulations as a function of the boron dose, where it can be seen that differences in the doping profiles can cause huge variations in the gain of the sensor. Therefore, the thermal process must be as uniform as possible. Simulations can be optimized once the C-V measurements are done on the fabricated LGAD sensors. In this sense, the first LGADs in 150 mm technology for timing measurements will be used as a reference for future LGADs addressed to the HL-LHC. The target is to fabricate a standard LGAD sensor able to be operable in a large range of voltage by showing a low linear gain. Therefore, the boron implantation dose values will be in the range of $1.8 - 2.0 \cdot 10^{13}$ cm^{-2}.

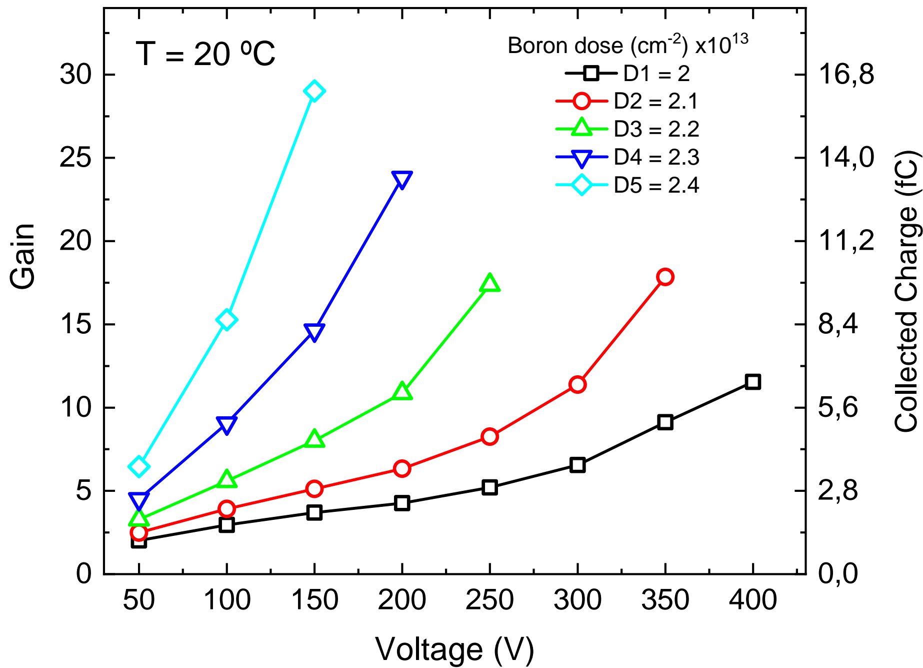

Figure 3.2: Gain simulations at room temperature as a function of the gain layer dose for a 50 µm LGAD.

3.3 Photolithographic mask designs

As aforementioned, pad LGAD designs are used to test the 150 mm process technology before introducing pixelated designs. Table 3.1 describes the different levels of the CNM869 mask at the multiplication side for all the LGAD generations in 150 mm wafers and figure 3.5 shows the geometrical dimensions of each mask level at the multiplication side of the sensor.

Metal is removed at the center of the sensor in order to facilitate the laser illumination during testing, and to avoid reflection. In addition, the ohmic side has a

dedicated metal level for each type of wafer, where standard thick 300 µm, Si-Si, and epitaxial wafers use a net-shape metal in the ohmic side to perform back-side laser measurements.

Mask level	**Level description**	**Alignment**
Pstop	P-stop Diffusion	Flat
JTE	JTE Diffusion	P-stop
Mult	Multiplication Layer	JTE
Nplus	N^+ Diffusion	Mult
Cont	Contact Opening	Nplus
Metl	Metallization	Nplus
Pass	Passivation	Metal

Table 3.1: Mask levels for the mask CNM869

On the other hand, in SOI wafers the supported silicon wafer is etched in four quadrants to facilitate the metal to reach the p^+ electrode, thus enabling electrical contact in the active substrate. Hence, a dedicated mask level is needed for these wafers.

Figure 3.3 shows the final design of the CNM869 mask, and Figure 3.4(a) shows the LGAD pad designs with an active area of 3.3x3.3 mm^2. In addition, there are 18 pad LGADs with an active area of 1.3x1.3 mm^2 (Figure 3.4(b)). Moreover, PiN detectors have been also included in the mask in order to test the reliability of the technology and perform gain measurements.

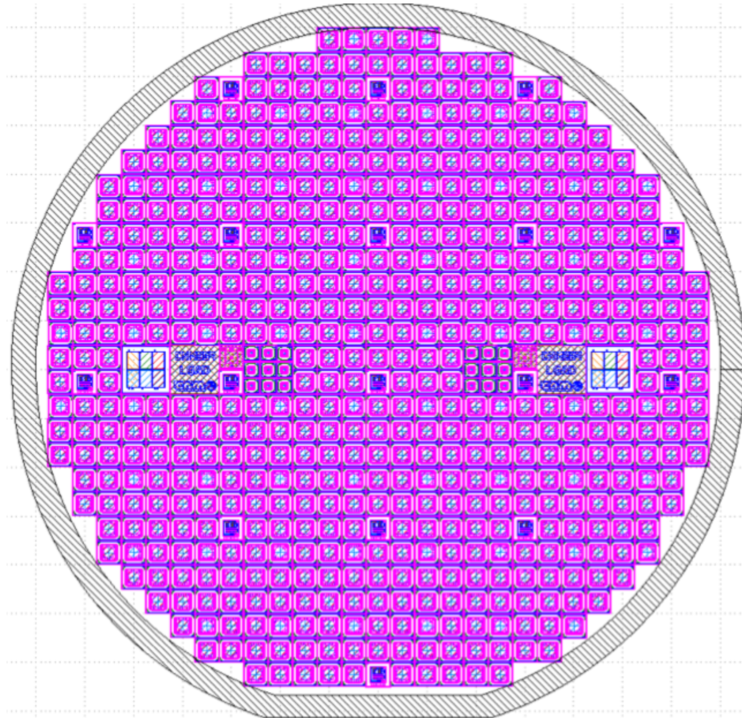

Figure 3.3: Final design of the mask CNM869.

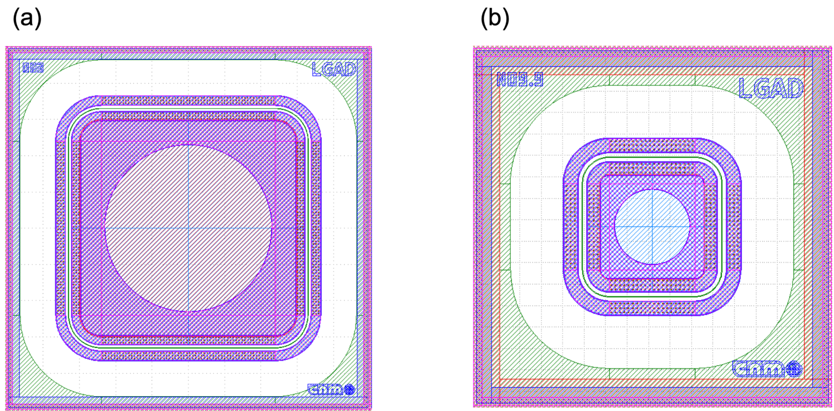

Figure 3.4: LGAD pad designs corresponding to the mask CNM869 with an active area of (a) 3x3 mm^2 and (b) 1x1 mm^2.

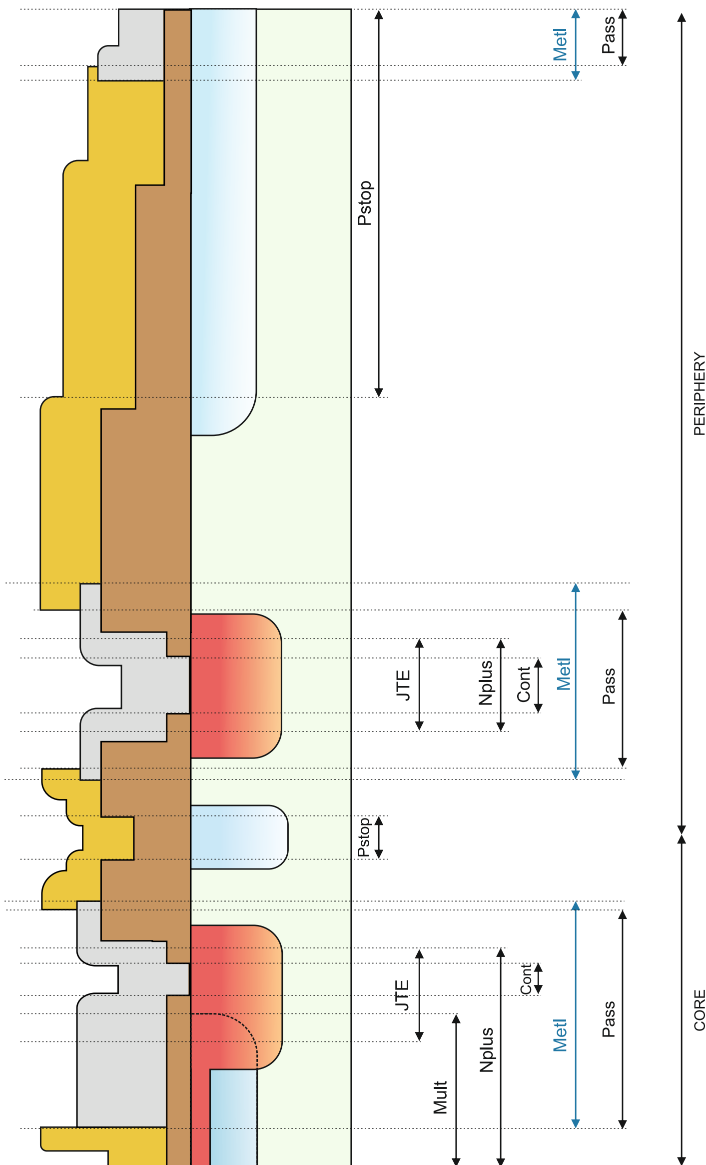

Figure 3.5: Mask level illustration of the mask CNM869 at the multiplication side.

3.4 Fabrication of the LGAD detectors

LGADs of the 6LG0 generation have been fabricated in high-resistivity (6-12 $k\Omega \cdot cm$) p-type 150 mm wafers with a thickness of 300 ± 10 µm. LGADs of the 6LG1 generation have been fabricated in 150 mm high-resistivity (< 5 $k\Omega \cdot cm$) 50/300 ± 1/11 µm SOI wafers. Finally, LGADs of the 6LG3 generation have been fabricated in epitaxial wafers. In this case, an epitaxial high-resistivity (> 200 $\Omega \cdot cm$) substrate of 55 ± 5 µm is grown over a low resistivity (0.01-1 $\Omega \cdot cm$) 525 ± 25 µm handle wafer. The description of the fabrication of LGADs in 150 mm technology is based on the 6LG3 generation, since the use of epitaxial substrates for LGADs has not yet been described. The development of LGADs in SOI and thick wafers are already explained in previous sections, where the main difference between 100 and 150 mm technological process is the drive-in of the multiplication layer.

Figure 3.6 shows the fabrication sequence of LGADs in epitaxial wafers. The process is the same as in the case of Si-Si wafers since there is a high-resistivity active substrate over a low-resistivity handle wafer. Nevertheless, as learned in the AIDA2020 production, a boron diffusion from the low to the high-resistivity wafer can occur, although a lower diffusion in epitaxial wafers is expected since the epitaxial substrate has a higher doping concentration. The exact value for the epitaxial resistivity is not known but it will be calculated through the C-V measurements. Using this value, we can simulate and predict the doping profiles of an LGAD with epitaxial wafers (see section 3.5.1).

3.4.1 Multiplication layer

The drive-in process of the multiplication layer is different for the new generation of LGADs in 150 mm technology. It consists of wet oxidation at 1100 ºC for 20 minutes and subsequent dry oxidation at 1100 ºC for 3 hours. A wide range of boron implantation doses has been used for the gain layer formation to test the gain layer by measuring the sheet resistance.

Figure 3.7 shows the sheet resistance values as a function of the boron dose. Sheet resistance measures the resistivity of the implanted layer at the surface. Therefore, the sheet resistance of the 150 mm process cannot be directly compared with the measured values in the AIDA2020 production, although the obtained values must be similar. The oxide thickness after the multiplication layer drive-in varies between 5140 to 5555 Å, which leads to a high non-uniformity. In the 150 mm technology, the non-uniformity of the gain layer is higher than in 100 mm wafers, increasing the complexity to obtain suitable large-area sensors.

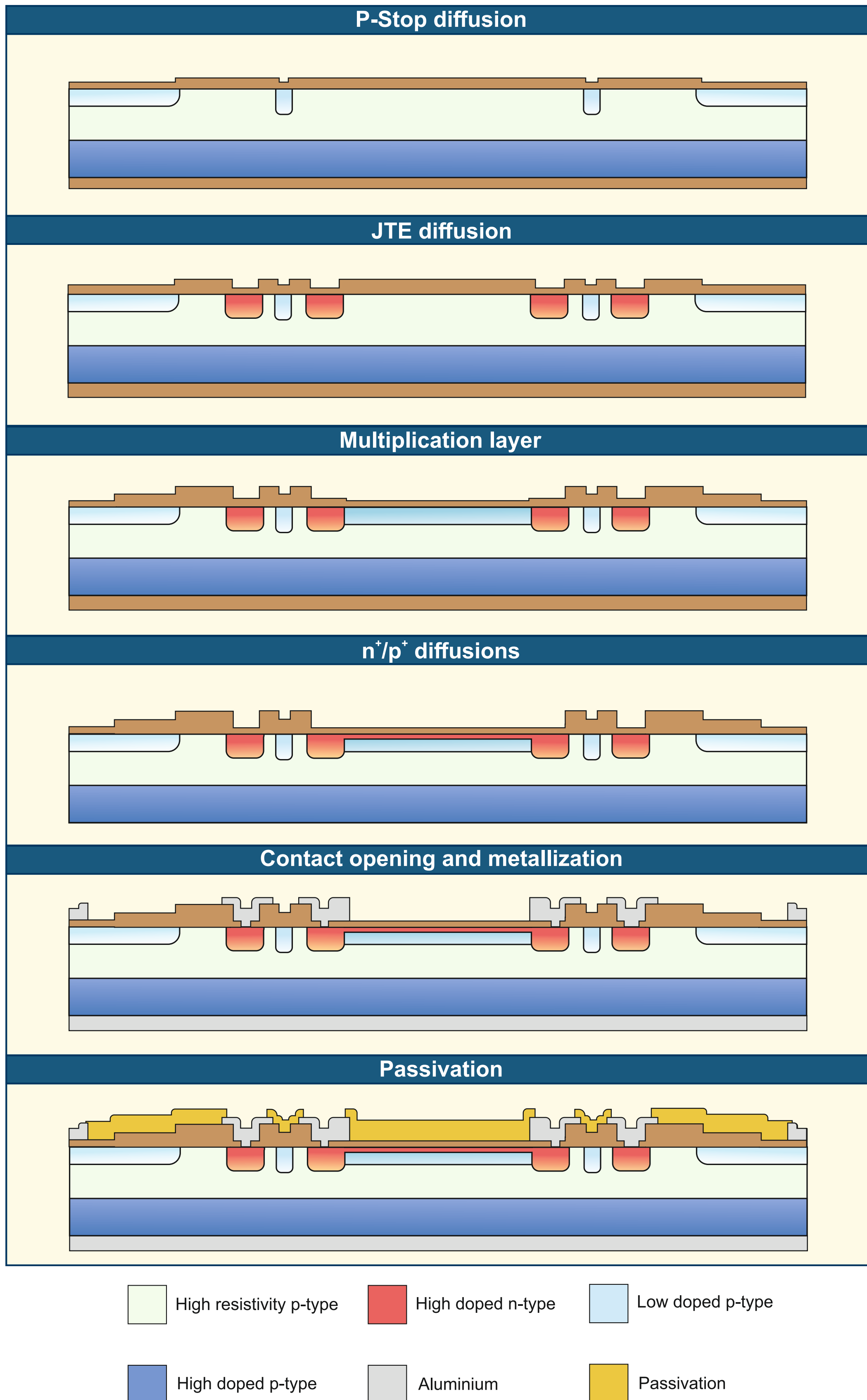

Figure 3.6: LGAD fabrication process for a 150 mm epitaxial-substrate.

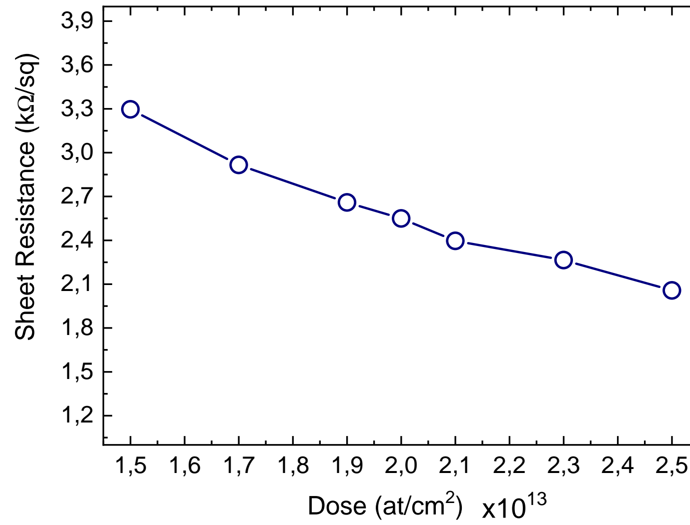

Figure 3.7: Sheet resistance of the gain layer as a function of boron dose measured in test wafers.

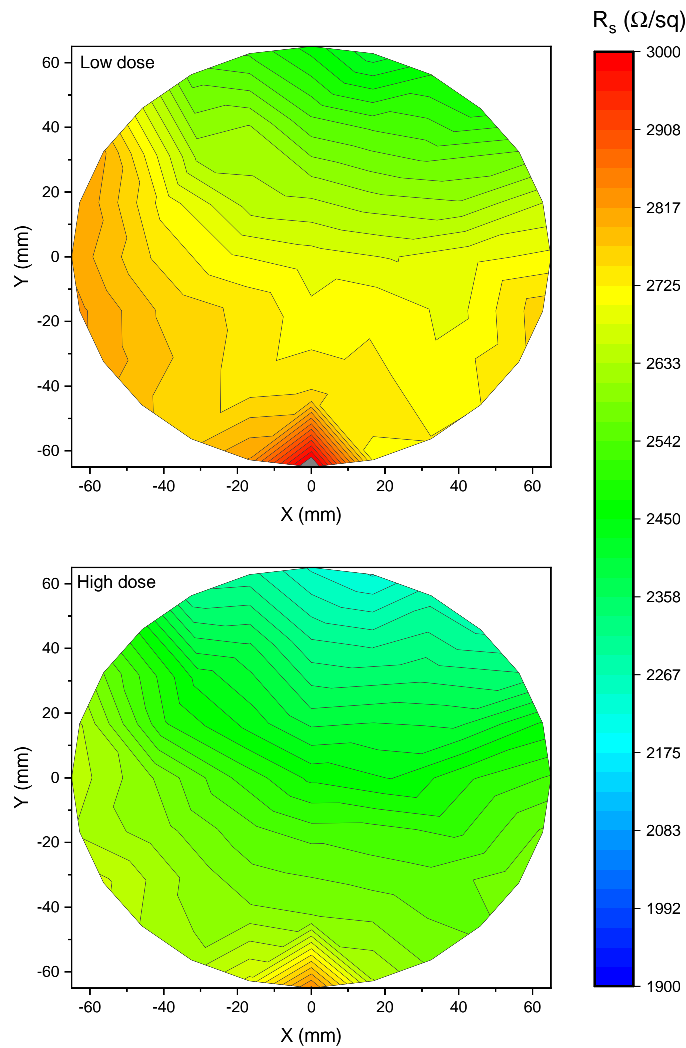

Figure 3.8: Sheet resistance wafer mapping for 150 mm n-type test wafers.

Figure 3.8 shows wafer mappings of two sheet resistance measurements done with different boron doses in n-type test wafers. By simulation, values in the range of 2500 Ω/sq were expected. As we can observe, there is a huge dispersion in terms of resistivity with a dose of $1.9 \cdot 10^{13}$ cm^{-2}. According to the measured data, it is not possible to develop large-area LGADs, since a difference of 400 Ω/sq leads to a huge difference in the electrical performance of the sensor. The wafer corresponding to a boron dose of $1.9 \cdot 10^{13}$ cm^{-2} seems to be more uniform. Nevertheless, we need to use a different method to fabricate the gain layer has to be developed in order to have better uniformity.

Tables 3.2 and 3.3 show the multiplication values for boron dose and energy used in 6LG1 and 6LG3 generations, respectively. In 6LG3 one wafer has been processed skipping the multiplication layer in order to test the technology and a similar behavior between wafers is expected.

Wafer	**Dose (at/cm^2)**	**Energy (keV)**	**Comments**
1	$1.8 \cdot 10^{13}$	100	Low dose - Low Energy
2	$1.9 \cdot 10^{13}$	100	Medium dose - Low Energy
3	$2.0 \cdot 10^{13}$	100	High dose - Low Energy
4	$1.9 \cdot 10^{13}$	120	Medium dose - Medium Energy
5	$2.0 \cdot 10^{13}$	120	High dose - Medium Energy
6	$1.8 \cdot 10^{13}$	150	Low dose - High Energy
7	$1.9 \cdot 10^{13}$	150	Medium dose - High Energy

Table 3.2: Multiplication layer dose and energy values for the 6LG1 generation.

Wafer	**Dose (at/cm^2)**	**Energy (keV)**	**Comments**
1	-	-	PIN
2	$1.9 \cdot 10^{13}$	100	Low dose
3	$1.95 \cdot 10^{13}$	100	Medium dose
4	$2.0 \cdot 10^{13}$	100	High dose

Table 3.3: Multiplication layer dose and energy values for the 6LG3 generation.

Figures 3.9a, 3.9b and 3.9c show images of a finished wafer and detailed views of the periphery and active region of LGAD fabricated sensors, respectively. It can be seen the collector ring, the contact window and the passivation at the middle of the sensor.

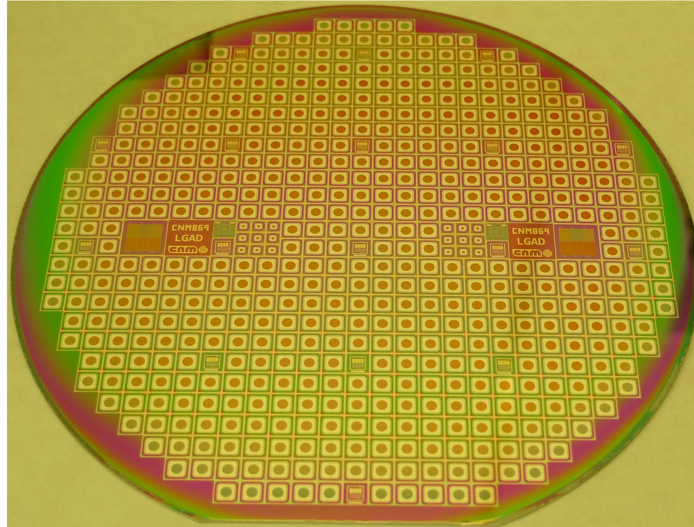

(a)

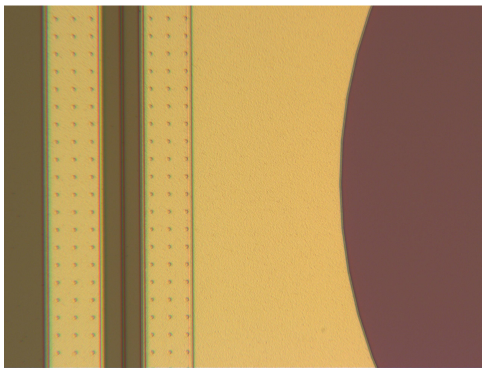

(b)

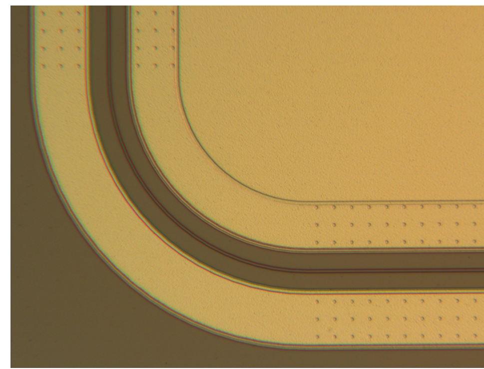

(c)

Figure 3.9: (a) Image of a produced wafer from the 6LG3 generation. Detailed view (b) at the periphery and (c) at the active region of the sensor.

3.5 Characterization of the LGAD sensors

3.5.1 Characterization of non-irradiated sensors

Electrical characterization

Fabricated LGAD sensors from 6LG1 and 6LG3 have been electrically characterized in the IMB-CNM labs to determine their operative range by means of I-V and C-V measurements.

Figure 3.10 shows the IV and CV measurements for different wafers at room temperature, for 3.3x3.3 mm^2 LGADs from 6LG1. Breakdown voltage is reduced from 400 V to 40 V by increasing dose and energy, and leakage current remains at low values (1-10 nA). The use of high energy will not be considered for future developments due to the low breakdown voltage achieved and, therefore, 6LG3 LGADs use only low-energy boron implants. The relationship of breakdown voltage and the increase of gain layer doping is reflected in C-V measurements, where V_{GL} increases with dose

and energy. The sensor with high energy boron dopant cannot be measured due to its premature breakdown, which is lower than its V_{GL}.

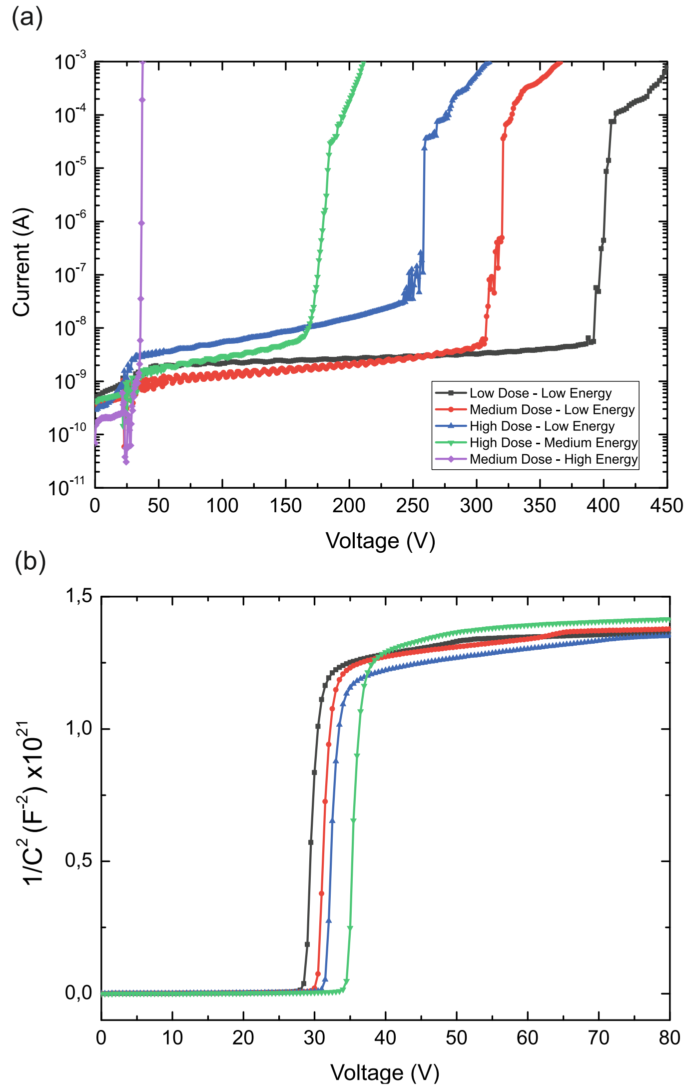

Figure 3.10: (a) I-V and (b) C-V measurements in 3.3x3.3 mm^2 LGADs at 20 ºC in different wafers from 6LG1 fabrication.

The results using LGADs from 6LG1 can be compared with the ones in 6LG3, where the only difference is the use of epitaxial wafers and the low-energy boron implant. Figure 3.11 shows the I-V for the 3.3x3.3 mm^2 LGAD sensors at room and low temperature for each boron dose. From these measurements, it can be inferred that breakdown voltage is reduced with dose and temperature, as expected. Leakage current is lower than 1 nA at low temperatures, while it reaches a maximum of 4 nA at room temperature for the highest dose. Taking into account the 3.3x3.3 mm^2 area, the measured leakage current is an excellent result.

LGADs from 6LG3 are able to support higher V_{BD} in comparison with the ones from 6LG1 and there is lower dispersion in the leakage current. Therefore, in terms of electrical behavior, the use of epitaxial wafers may imply a benefit over SOI wafers. However, further characterizations must be considered to conclude this hypothesis.

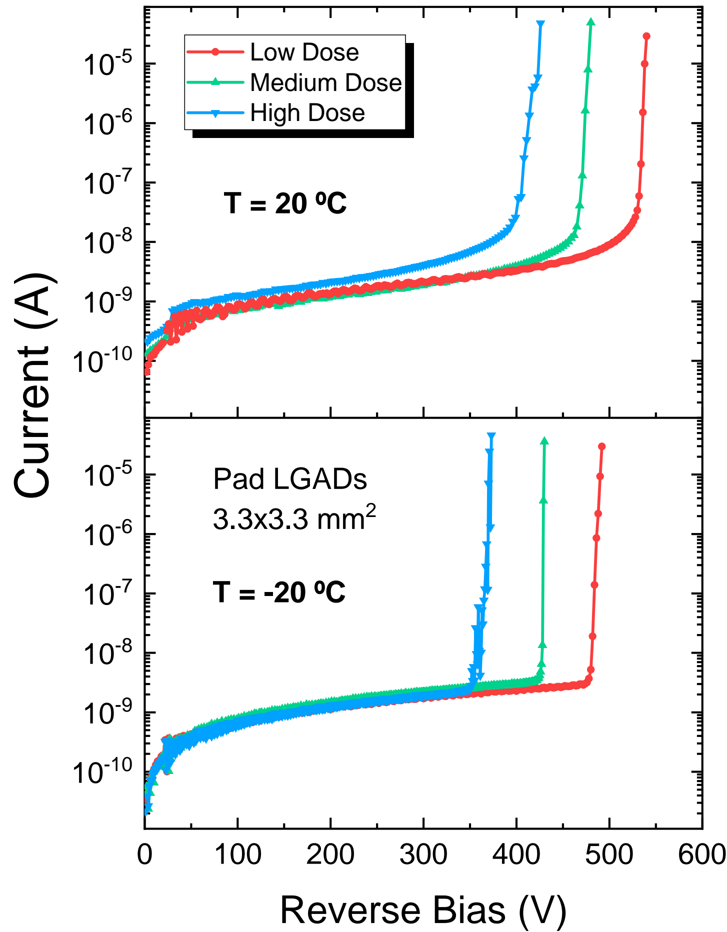

Figure 3.11: I-V measurements at different temperatures and implanted doses in 6LG3 LGADs.

Figure 3.12 shows the C-V measurements at room temperature for each boron dose. As it can be observed, the depletion of the multiplication layer takes place at a higher voltage for the highest dose (∼ 30 V) and full depletion voltage is achieved at 34 V. Therefore, the 6LG3 LGAD sensors exhibit a high operative voltage with low leakage current. These values are similar to the ones obtained using 6LG1 LGADs, thus we expect to have a similar gain with a higher operative regime due to the higher V_{BD}.

Automated I-V measurements have also been performed to determine the yield of the wafers above the gain layer depletion when the device is operative. Figure 3.13 shows the I-V wafer map for medium boron dose wafer from 6LG3 at room temperature, where 531 devices, including PiN diodes, are measured. The yield is defined as the working LGAD sensors divided by the total number of fabricated LGAD sensors. In this case, 358 LGAD sensors exhibit a leakage current lower than 1 µA, which is the upper limit of the operative range, leading to a yield in the range of 76 %.

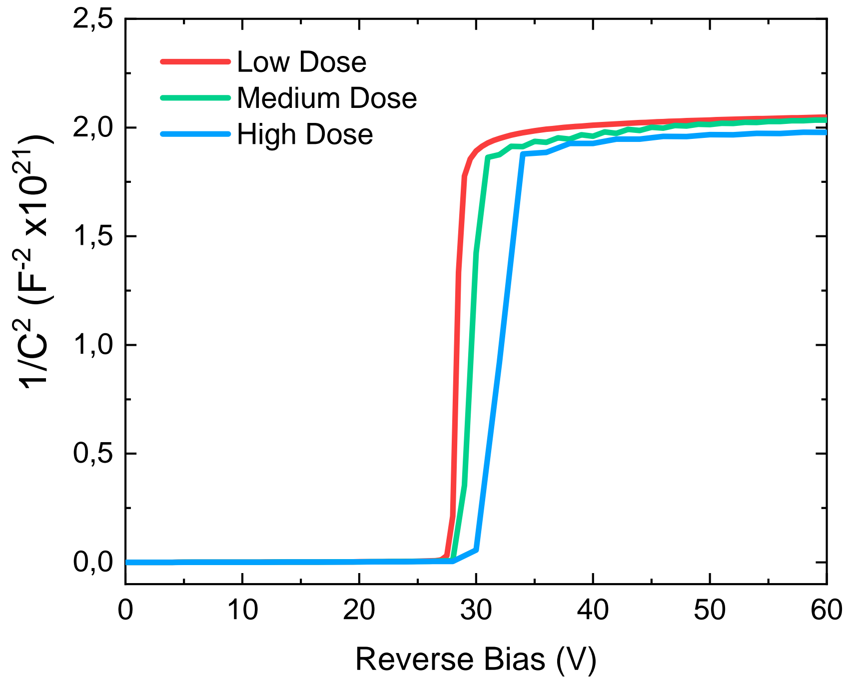

Figure 3.12: C-V measurements at different implanted doses in 6LG3 LGADs.

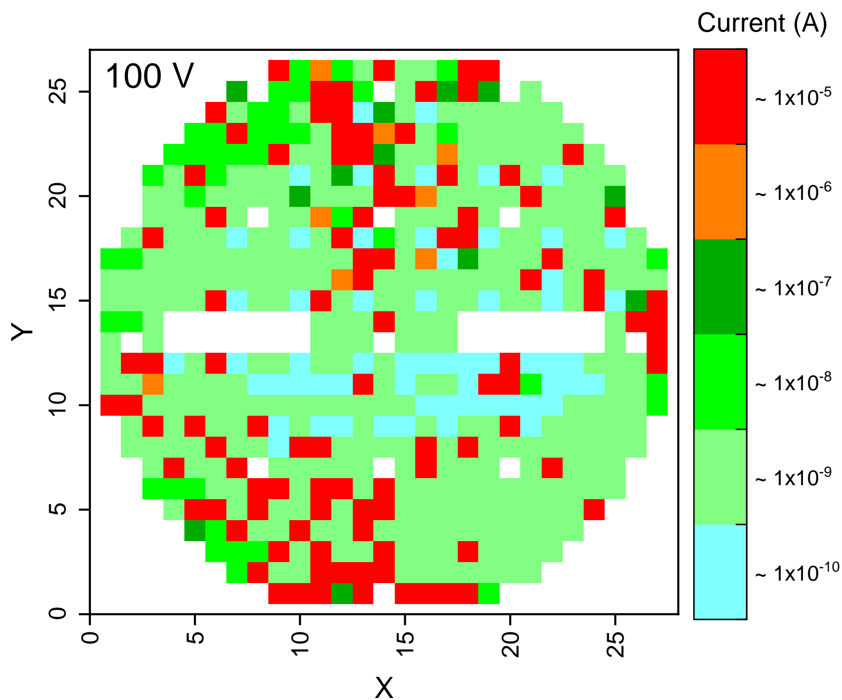

Figure 3.13: I-V wafer mapping at 100 V for the medium dose LGAD wafer from 6LG3.

One of the disadvantages of using epitaxial wafers is the difficulty to produce a high-resistivity substrate with the desired doping value for the active thickness. Assuming that high dispersion is present on the high resistivity values, C-V measurements have been used to experimentally determine the doping concentration and epitaxial

thickness by plotting $1/C^2$-V (the doping concentration corresponds to the slope of the curve). The experimental doping concentration has been found to be $1.7 \cdot 10^{10}$ cm^{-3}, lower than the target and in accordance with the fast decrease in the C-V measurement when the sensor reaches the gain layer depletion. Moreover, the thickness of the sensor has been determined by using its correlation with capacitance. Figure 3.14 shows the depletion width as a function of the voltage. As expected, at 30 V the device starts to deplete rapidly, achieving a value of 49 µm at full depletion voltage. Nevertheless, the device reaches saturation At 400 V (not displayed in the graph), where the depleted thickness is 51 µm. This happens due to the diffusion of impurities from the low-resistivity handle wafer to the high-resistivity epitaxial wafer, which creates a moderately p-doped region at the end of the epitaxial wafer.

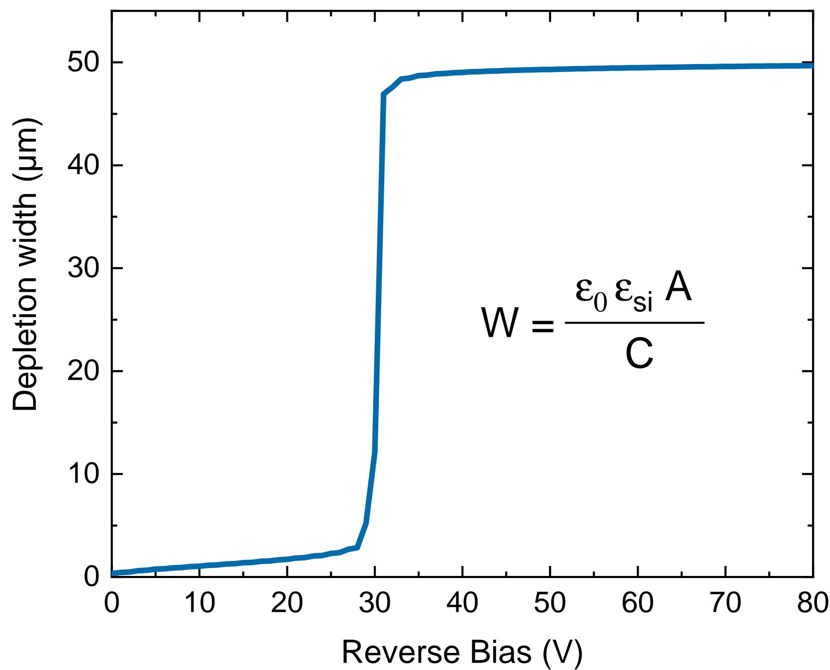

Figure 3.14: Depletion width as a function of the applied voltage extracted from the C-V measurement in epitaxial wafers (6LG3).

Figure 3.15 shows the simulated profile of the resulting multi-layer structure, using the extracted doping concentration and assuming a thickness of 55 µm. As it can be observed, at the epitaxial/handle wafers junction there is a significant boron diffusion and the LGAD is not able to deplete more than 51 µm since the doping concentration is very high up to this value. Therefore, 4 µm of the active substrate is lost during the thermal steps of the fabrication process. In conclusion, the active substrate of the sensors is 51 µm thick, but it is also necessary to take into account that these values are obtained by C-V measurements, which are very sensitive to the measurement itself. Therefore, the values of the thickness and the doping concentration may vary in the whole production.

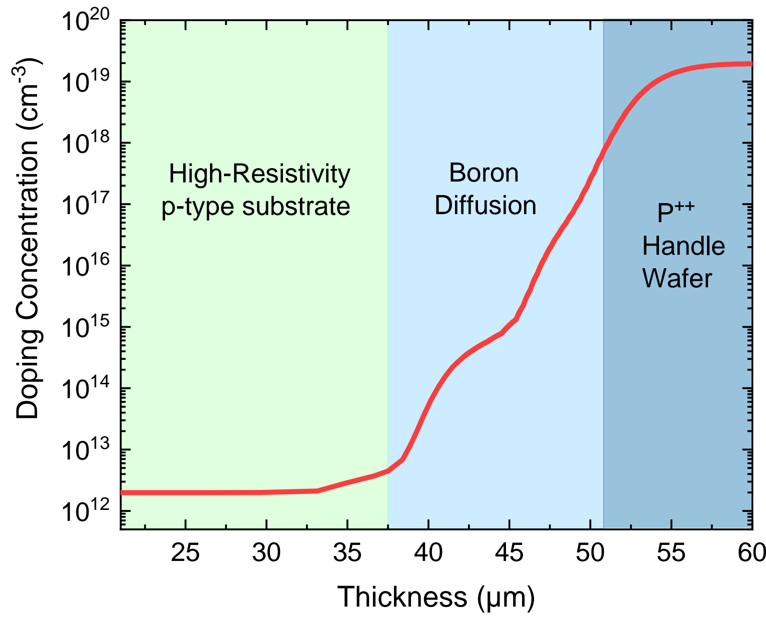

Figure 3.15: Simulated doping profile at the epitaxial-handle wafer junction, using the extracted value of the doping concentration.

Gain and timing measurements

TCT measurements using an IR laser have been performed in 3.3x3.3 mm^2 LGADs to determine the gain at room and low temperatures. High-dose wafers from 6LG1 have been characterized, as depicted in figure 3.16. The sensors present a gain between 3-14, where there is some dispersion between them due to a non-uniform gain layer.

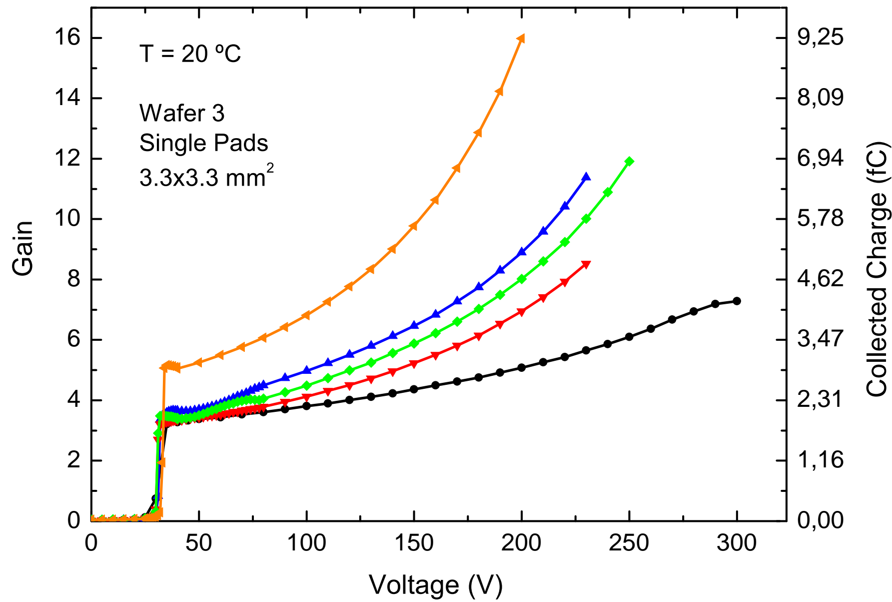

Figure 3.16: Gain measurements for the 3.3x3.3 mm^2 LGADs from wafer 3 of the 6LG1.

In addition, LGADs from 6LG3 are also characterized for different boron doses, as can be observed in figure 3.17. Experimental gain is the target (low gain) and the

sensors are able to reach 15 fC at low temperatures. It is also clear that gain is higher at low temperatures in accordance with the lower no gain before full depletion, as expected.

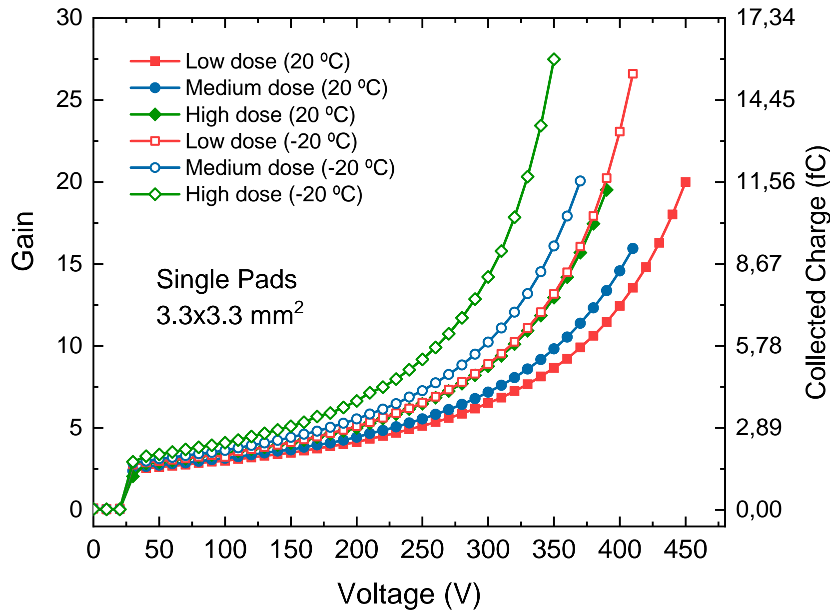

Figure 3.17: Gain measurements for different boron doses at room and low temperature for the 3.3x3.3 mm^2 LGADs from 6LG3.

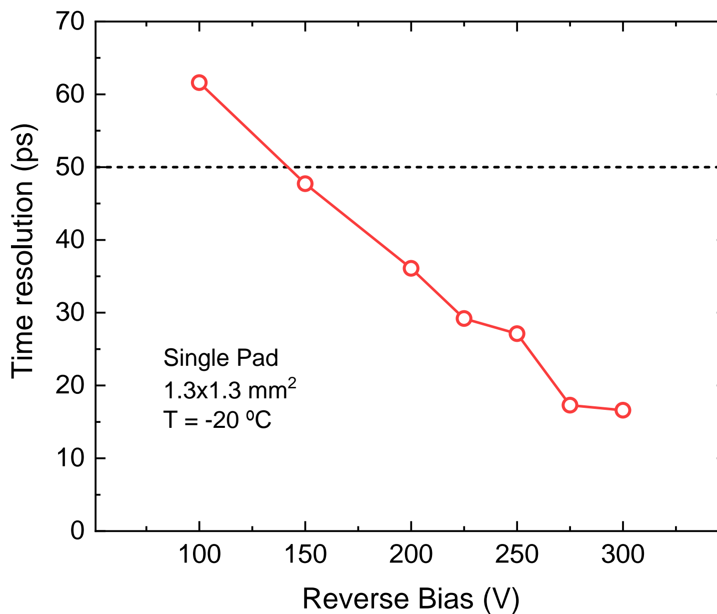

Figure 3.18: Time resolution as a function of applied voltage for the highest dose from 6LG3.

Some conclusions can be extracted when comparing the gain measurements using different wafers. While in SOI wafers the gain behavior is almost linear, using epitaxial wafers requires a higher voltage to achieve the desired gain. In this sense, epitaxial wafers must work closer to the breakdown voltage. For instance, at 200 V the epitaxial

wafers at room temperature are not able to overpass a gain of 5, while in SOI wafers a gain of 7.5 is reached.

Finally, the time resolution of the LGAD sensors from 6LG3 has also been measured, following the technique described in [70]. In figure 3.18 one can see how time resolution is reduced with the operating voltage since the gain is increased. ATLAS and CMS experiments require a time resolution as low as 50 ps for non-irradiated LGAD sensors and LGAD sensors from the 6LG3 generation achieve this value far from the breakdown voltage, providing a time resolution of 20 ps, which is an excellent performance.

3.5.2 Characterization of irradiated sensors

LGAD sensors with the highest boron dose have been neutron-irradiated in order to test the damage introduced by the radiation at different fluences. The final goal is to develop thin LGADs in 150 mm wafers for the HL-LHC. Therefore, the characterization of irradiated sensors will be a reference for future LGAD productions. Figure 3.19 shows the I-V measurements on neutron-irradiated 1.3x1.3 mm^2 single pad LGAD sensors at -20 ºC. The current is lower than 1 µA until the breakdown voltage is reached for all the fluences. As expected, leakage current increases with fluence.

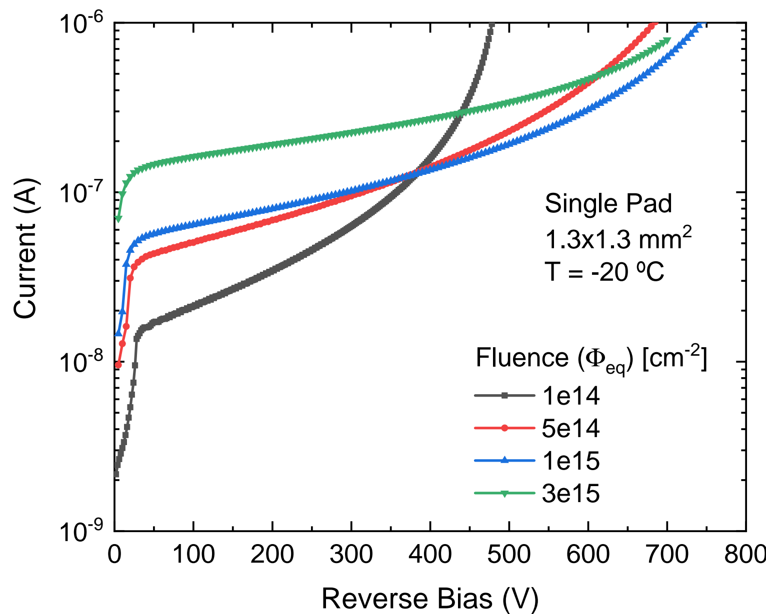

Figure 3.19: I-V measurement of neutron-irradiated 1.3x1.3 mm^2 single pad LGADs at -20 ºC from 6LG3.

Gain measurements

TCT measurements with an IR laser have been performed on the neutron-irradiated LGAD sensors. Figure 3.20 shows the gain and the collected charge at -20 ºC and the limits of CMS and ATLAS are also included. As expected, gain (and collected charge)

decreases with the fluence due to the acceptor removal phenomenon, which entails the deactivation of the acceptors in the multiplication layer. This effect, already mentioned in chapter 1, is going to be studied further. Each experiment requires collected charge values in different temperature and fluence conditions, therefore the results cannot be directly correlated. Nevertheless, it is clear that the performance of the LGAD sensors is not compatible with the irradiation conditions of the HL-LHC (neither ALTAS nor CMS) since they are not able to reach the desired collected charge. As a consequence, the boron dose of the multiplication layer must be increased in future LGAD productions in order to reach the desired performance after irradiation.

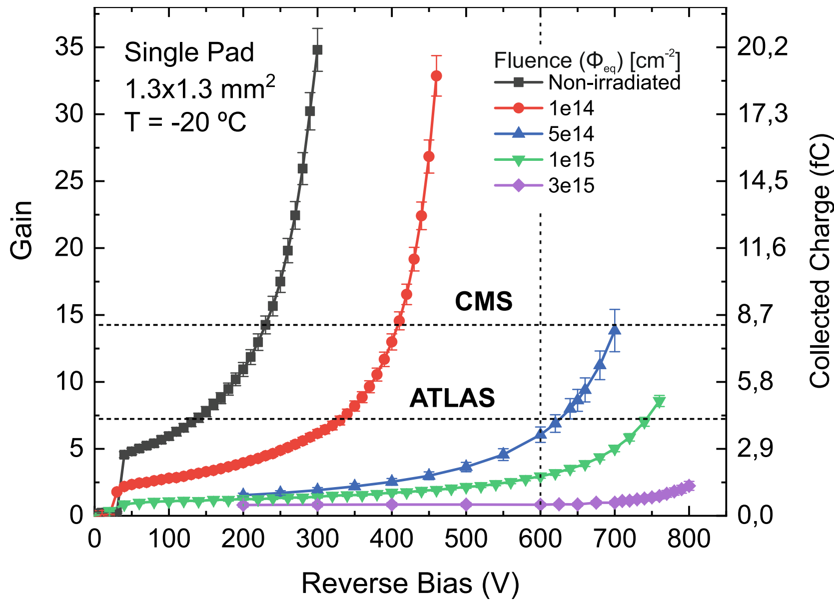

Figure 3.20: TCT measurement of neutron-irradiated 1.3x1.3 mm^2 single pad LGADs at -20 ºC.

In addition, the collected charge has been calculated with an Sr90 source measurement, in the same way as in AIDA2020 [78, 77]. The measurements are performed at -30 ºC, which is the working point for the HGTD. Figure 3.21 shows the charge collected by neutron-irradiated LGAD sensors at -30 ºC using an Sr90 source. The LGAD sensors are irradiated up to a fluence of $1 \cdot 10^{15}$ cm^{-2}. The results are similar to those obtained in the TCT measurements and are important to mention that the Sr90 technique leads to an extremely high error in the measurements. The minimum collected charge required by the CMS specifications is achieved (within the error) at more than 750 V. However, at 600 V (the maximum voltage allowed at CMS) the collected charge is below the requirements.

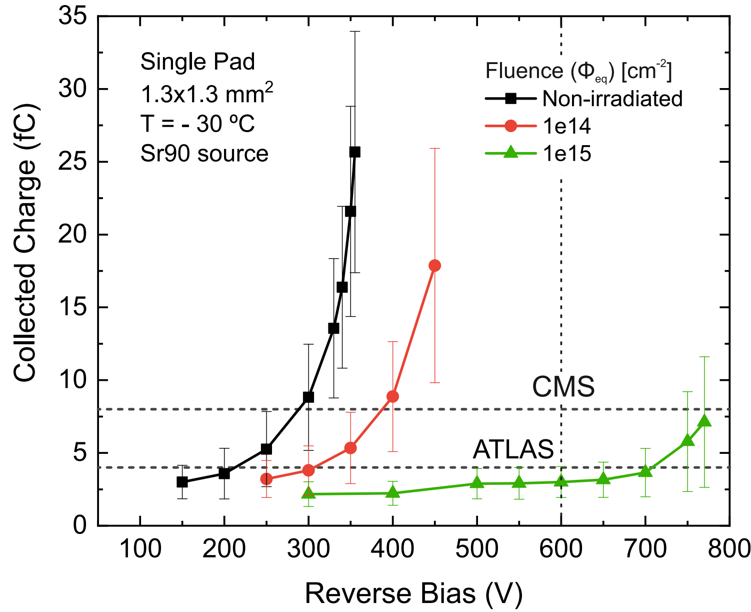

Figure 3.21: Sr90 measurement of neutron-irradiated 1.3x1.3 mm^2 single pad LGADs at -20 ºC.

Acceptor removal studies

Acceptor removal has been studied in LGAD sensors of the 6LG3 fabrication process. In this case, the gain layer depletion is calculated using TCT measurements. Once the full depletion is reached, LGAD sensors start to collect charge. Figure 3.22 shows the collected charge (normalized) for neutron-irradiated LGAD sensors. As expected, depletion voltage reduces with neutron fluence. A linear fit is applied in each curve to determine the gain layer depletion and, for instance, at a fluence of $5 \cdot 10^{15}$ cm^{-2}, there is no gain since at 0 V the LGAD sensor starts to collect charge. Using these values, we have been able to model the gain layer depletion as a function of the neutron fluence, as depicted in figure 3.23. From this data and using equation 1.18 the constant value found is $c_A = 9.9 \cdot 10^{-16}$ cm^2, which agrees with the value found in the AIDA2020 LGAD sensors. Therefore, the reduction of V_{GL} has the same tendency in both 100 and 150-mm wafers.

Nevertheless, as already mentioned in chapter 2, some studies report an increase in the radiation hardness of multiplication layers enriched with carbon [83, 84, 85, 86]. The necessity to improve the radiation hardness of irradiated LGADs is independent on the wafer diameter. Hence, future developments of LGADs in 150 mm must include proposals and solutions to overcome this problem.

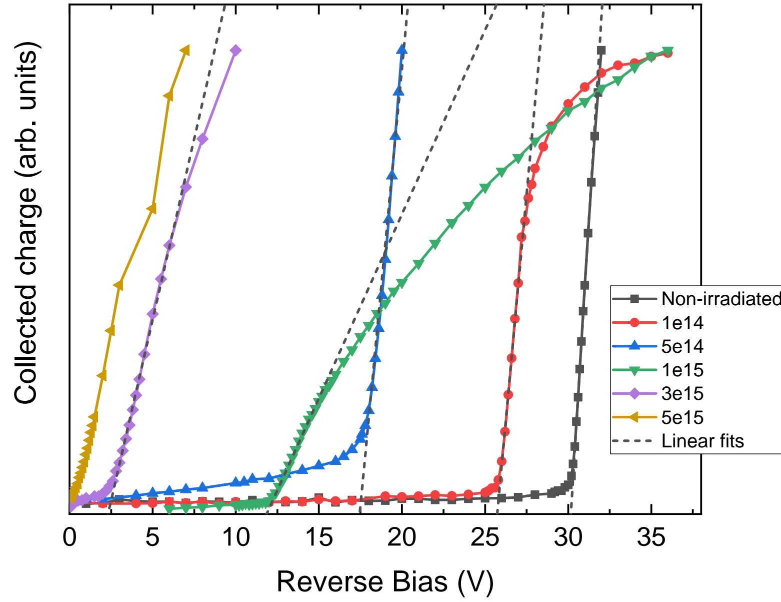

Figure 3.22: Normalized collected charge as a function of applied bias for neutron-irradiated LGADs.

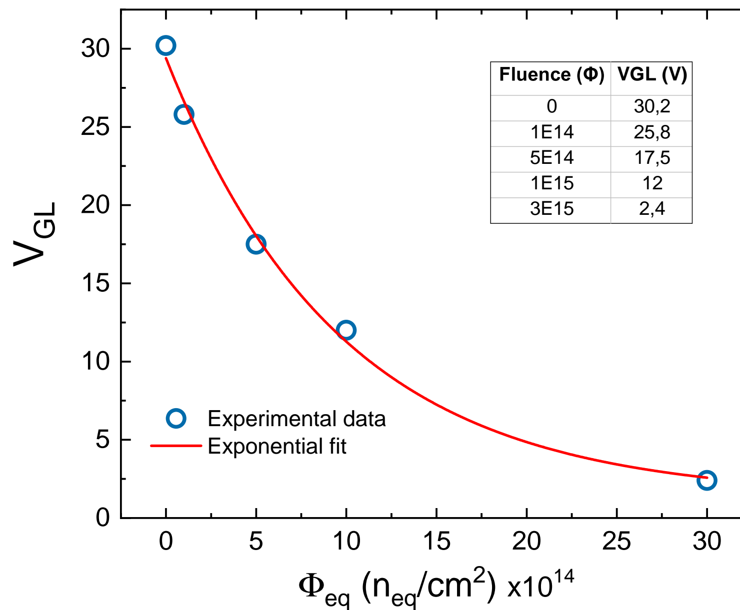

Fluence (Φ)	VGL (V)
0	30,2
1E14	25,8
5E14	17,5
1E15	12
3E15	2,4

Figure 3.23: Gain layer depletion as a function of neutron fluence.

Timing measurements

Timing measurements have been performed at IMB-CNM and IFAE laboratories on neutron-irradiated LGAD sensors at fluences of $4 \cdot 10^{14}$ cm^{-2} and $1 \cdot 10^{15}$ cm^{-2}. Figure 3.24 shows the time resolution for irradiated LGAD sensors at -20 ºC (measured at IMB-CNM). At a fluence of $1 \cdot 10^{14}$ cm^{-2}, LGAD sensors exhibit a time resolution of 20 ps. Nevertheless, at a fluence of $1 \cdot 10^{15}$ cm^{-2}, LGAD sensors can only reach 100 ps, which is far from the time resolution required at the CMS specifications. Timing measurements have been repeated using the IFAE setup [78] at -30 ºC, as shown in

figure 3.25. The lower temperature enhances the performance and a similar behavior is obtained for the non-irradiated and the low-fluence irradiated LGAD sensors. Nevertheless, for the highest irradiated LGAD sensors, there are huge differences. The IFAE measurements show a time resolution of 50 ps in the entire voltage regime (> 500 V). However, the performance differences are basically due to the different setups used in the measurements and an exhaustive comprehension of both measurements must be done.

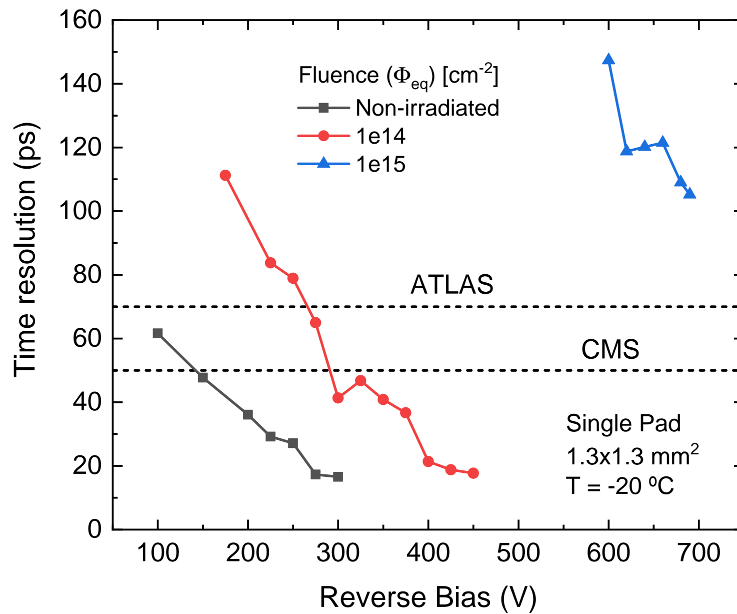

Figure 3.24: Time resolution as a function of applied bias for neutron-irradiated LGADs measured at IMB-CNM laboratories.

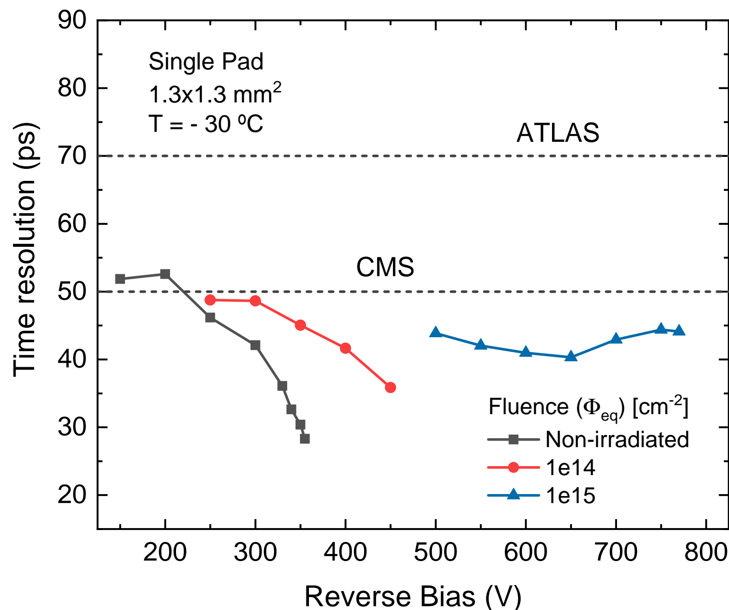

Figure 3.25: Time resolution as a function of applied bias for neutron-irradiated LGADs measured at IFAE laboratories [78].

3.5.3 Summary and conclusions

Non-irradiated sensors

We have characterized non-irradiated LGAD sensors from 6LG1 and 6LG3, where I-V, C-V, gain, and timing measurements have been performed. Both types of wafers present a very low leakage current, although epitaxial wafers offer the best performance in this sense. Moreover, the breakdown voltage is higher in epitaxial wafers and this is observed in C-V measurements due to a higher V_{GL} in LGADs from 6LG1. However, both technologies provide enough room to operate the sensor before irradiation. In addition, epitaxial wafers show a good yield at 100 V.

TCT measurements using an IR laser show a different behavior of gain, depending on the type of wafer used. Since epitaxial wafers provide a higher V_{BD}, the gain achieved is higher, while SOI wafers are able to reach a lower gain. Nevertheless, the maximum gain in epitaxial wafers is much closer to breakdown than in SOI wafers, where we observe a linear gain. Therefore, SOI wafers can be operated with a higher gain in the same working voltage. Furthermore, epitaxial wafers provide a time resolution down to 20 ps at 300 V, which is an excellent result taking into account the requirements of ATLAS and CMS.

Irradiated sensors

LGADs using 150 mm wafers provide a good performance before irradiation in terms of leakage current, breakdown gain, and timing. After irradiation, the electrical performance of the sensors is still good, providing low leakage currents and high breakdowns. In contrast, gain measurements show that the charge collected is not enough at high fluences ($> 1 \cdot 10^{15}$ cm^{-2}), and gain layer is completely removed at $5 \cdot 10^{15}$ cm^{-2}. Therefore, in the future optimization of LGADs in 150 mm technology, the boron dose of the gain layer has to be increased in order to collect a higher amount of charge. The timing performance of the non-irradiated and low-irradiated sensors is excellent. At high fluence, there are discrepancies between results obtained with different experimental setups, where at IMB-CNM labs time resolutions lower than 100 ps cannot be measured. Nevertheless, at IFAE labs, time resolutions lower than 50 ps have been measured.

3.6 ATLAS-CMS Common Run

In order to use LGAD sensors fabricated in 150 mm wafers at the HL-LHC, the ATLAS-CMS Common Run has been developed. In this fabrication, both 6LG2 and 6LG3 technologies are going to be used. The design of the mask set is shared between ATLAS and CMS to have different designs in the same wafer and is described in the next subsections. The gain layer parameters have to be optimized to reach the requirements of ATLAS and CMS experiments of the HC-LHC, taking the 6LG3

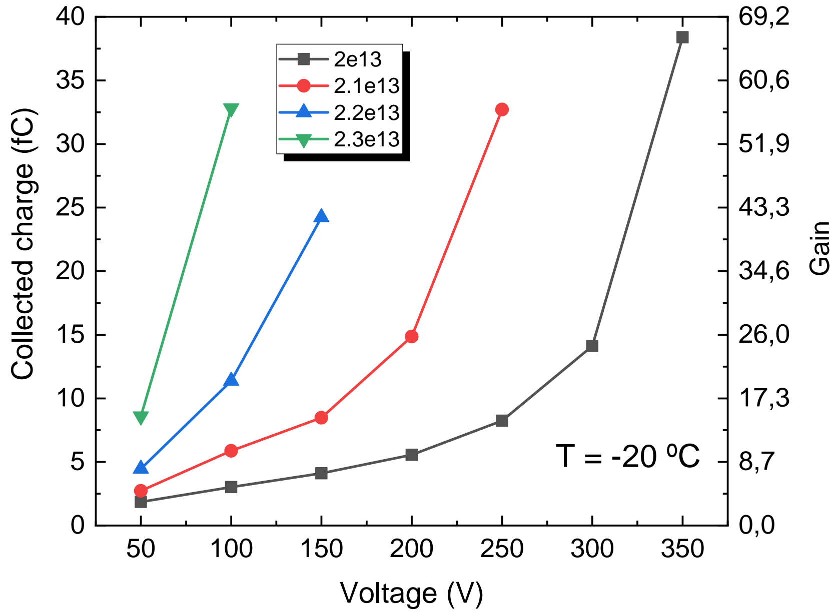

Figure 3.26: Simulated collected charge as a function of boron dose at -20 ºC for 50 µm epitaxial LGADs.

results as a reference. In the next subsections, the optimization of the sensors to reach the requirements of the Market Survey is described, using two different 150 mm substrates: the same epitaxial substrates as in 6LG3 generation and Si-Si 50 µm high-resistivity (> 1 k$\Omega \cdot$ cm) 50 µm substrates (6LG2).

3.6.1 Optimization of the sensors for the HL-LHC

As already stated, taking into account the results obtained using the 6LG3, the boron implantation dose has to be increased, while maintaining an optimal trade-off between gain and breakdown voltage before and after irradiation. 1D TCAD simulations have been performed to obtain the collected charge of the sensors by increasing the boron implantation dose and fitting the simulator to the available experimental results, such as the doping concentration and wafer thickness. As we observed a high non-uniformity in the boron profile entails a variation in the collected charge. Figure 3.26 shows the simulated collected charge and gain as a function of the applied reverse bias. As expected, the collected charge increases with the boron implantation dose, but the highest dose cannot support more than 100 V at -20 ºC. Therefore, the maximum boron implantation dose is $2.3 \cdot 10^{13}$ cm^{-2}. Hence, boron implantation doses between $1.7 - 2.2 \cdot 10^{13}$ cm^{-2} are established to have a wide range of operations.

Optimization for irradiated sensors

The boron implantation dose to create the gain layer is directly correlated with the collected charge. As aforementioned, the trade-off between gain and breakdown voltage before and after irradiation has to be maintained, but the sensors have to be operative in high irradiation conditions. The use of carbon-enriched gain layers has been

investigated during the last few years in the RD50 community [34, 83, 84, 85, 86]. It has been demonstrated that the acceptor removal rate is lower in carbonated LGAD sensors and, therefore, the performance at high fluences is enhanced. However, at low fluences and before irradiation, the performance has no difference and there is a higher leakage current before irradiation in carbonated LGADs. For instance, this issue has been taken into account in the Market Survey for CMS, and higher leakage currents before irradiation would be accepted.

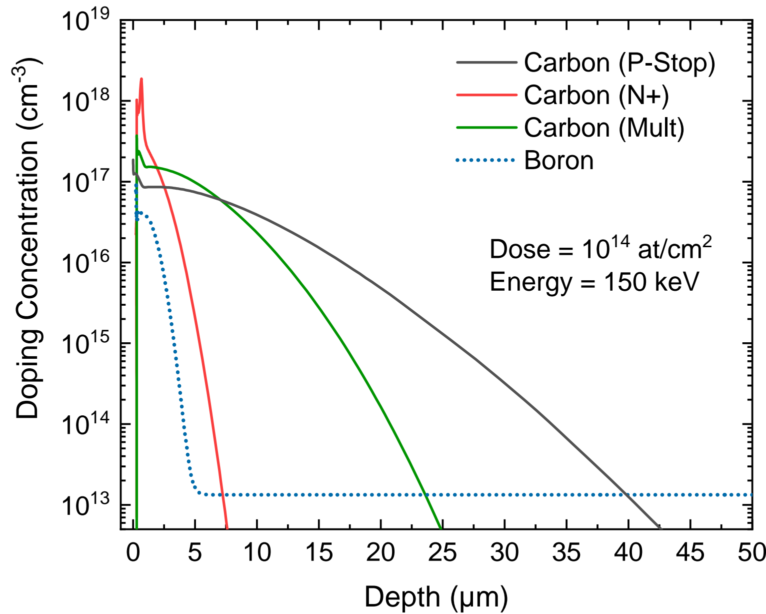

Figure 3.27: Simulated doping profiles for carbonated LGAD sensors.

At IMB-CNM, carbon was introduced in LGAD sensors to enhance the performance after irradiation, but the obtained performance of the sensor was not as expected [87]. Carbon was implanted at the beginning of the fabrication process and now we assume that after all the thermal budget carbon diffused.

In this sense, TCAD simulations have been carried out to study the carbon profiles during the LGAD fabrication steps, as shown in figure 3.27, analyzing three different scenarios. The first scenario accounts for carbon implantation at the beginning of the fabrication process, before the p-stop diffusion. This was the method used in the first carbonated LGAD sensors fabricated at IMB-CNM. In the second scenario, carbon is implanted with the multiplication layer, and, in the last one, with the n^+ diffusion. Obviously, the later carbon is implanted, the less is diffused, as shown in figure 3.27, where the multiplication layer profile is also included. As expected, carbon is less diffused when it is implanted with the n^+ diffusion. For the ATLAS-CMS Common Run, carbon will be diffused with the multiplication layer since it is the easiest way to proceed, and we expect a proper performance of the sensors since it will not be completely removed.

3.6.2 Photolithographic mask designs

The new mask set includes thin LGAD sensors for ATLAS and CMS detectors and is divided into two sections, corresponding to each experiment, with different devices and specifications. Figure 3.28 shows the mask design, with identical design rules to in previous thin LGAD generations. Figure 3.29 shows an example of a 2x2 array with standard JTE, p-stop, and n-type collector ring structures. The main parameters for the sensors located in ATLAS and CMS side of the mask CNM1023 are listed respectively in tables 3.4 and 3.5, including pad and array patterns. The edge distance corresponds to the distance between the collector ring and the edge of the sensor, while the IP distance is the same as in the AIDA2020 sensors, using 37, 47, and 57 µm.

This mask set is going to provide a large number of possible scenarios in terms of LGAD designs. Several single-pad LGADs are located throughout the wafer to carry out basic IV, CV, gain, and timing measurements before and after irradiation. Furthermore, these measurements are planned for pixelated sensors using different areas to study their behavior in terms of uniformity of the gain layer. In addition, big-area pixelated LGADs are designed to probe the feasibility of large LGADs, to meet the HL-LHC requirements.

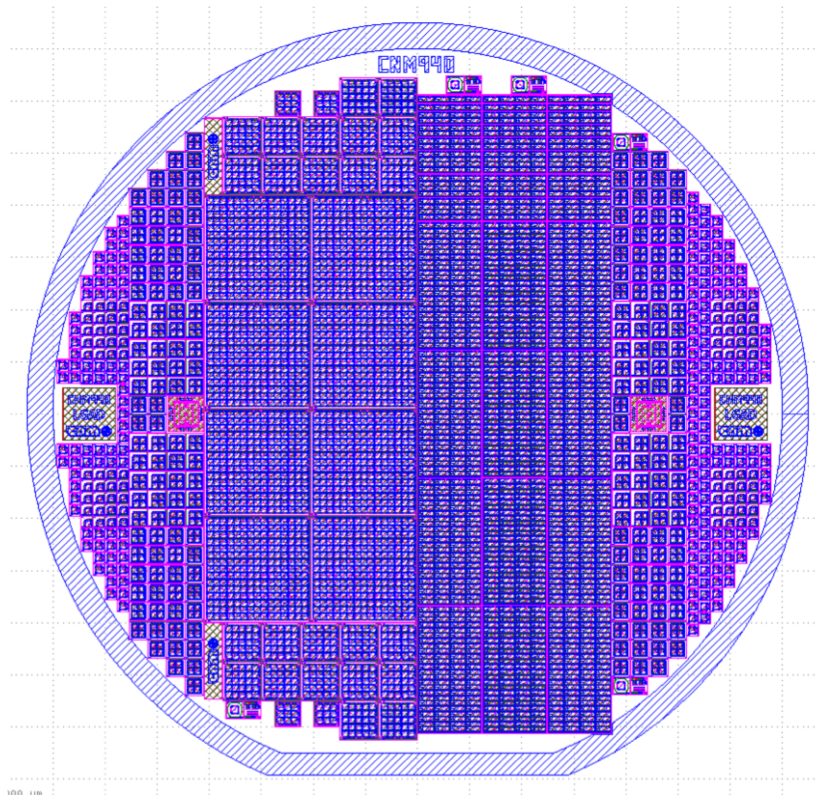

Figure 3.28: CNM1023 mask design with ATLAS and CMS sensors located at the left and right sides, respectively.

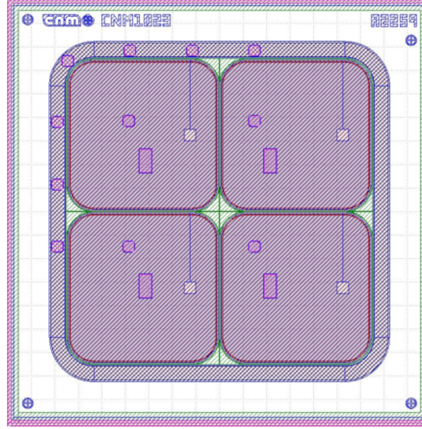

Figure 3.29: LGAD 2x2 array from the CNM1023 mask.

Type	Edge (µm)	IP Distance (µm)	Total devices
Single Pad	200; 300; 500	47	115
2x2 Arrays	200; 300; 500	37; 47; 57	104
3x3 Arrays	500	47	4
5x5 Arrays	300; 500	37; 47	24
15x15 Arrays	500	47	4
15x20 Arrays	500	47	2

Table 3.4: Parameters of the devices located in the ATLAS side of the CNM1023 mask.

Type	Edge (µm)	IP Distance (µm)	Total devices
Single Pad		47	126
2x2 Arrays		37; 47; 57	74
5x5 Arrays	500	47	58
16x16 Arrays		47	2
16x32 Arrays		47	1

Table 3.5: Parameters of the devices located in the CMS side of the CNM1023 mask.

3.6.3 Fabrication of the sensors

Upon closing this Ph.D. thesis, the ATLAS-CMS Common Run has been fabricated using 6LG3 technology, hence using epitaxial wafers. The use of Si-Si wafers is now considered since these wafers are at this moment available at IMB-CNM.

At the same time, in the IMB-CNM clean room facilities, the furnaces have been replaced, leading to more modern equipment which will entail a better uniformity of the multiplication layer. In this sense, an experimental calibration of the thermal processes needs to be carried out to assure the proper diffusion of the multiplication

layer. The choice of the multiplication layer parameters is based on the previous optimization, to meet the requirements of ATLAS and CMS, and are listed in table 3.6. There are multiple configurations for the formation of the gain layer, and some of them will be carbonated to study their radiation hardness. The energy for the boron implant is 100 keV and for carbon 150 keV. In addition, different dry oxidation times (DOT) for the multiplication layer are considered to calibrate the processes of the furnaces.

Wafer	**Boron Dose**	**Carbon Dose**	**DOT (min)**
1	1.7	-	
2	1.8	-	30
3	1.9	-	
4	2.0	-	
5	2.1	-	180
6	2.2	-	
7		5	30
8	1.9	10	180
9		-	90
10		-	180

Table 3.6: Boron and carbon doses (at/cm^2 x10^{13}) and DOTs used in the ATLAS-CMS Common Run.

3.6.4 Characterization of the LGAD sensors

A first characterization of the fabricated sensors has been performed [88]. The multiple LGAD structures integrated into the ATLAS-CMS Common Run have been electrically tested, and the yields obtained are depicted in table 3.7, where good sensors must exhibit a breakdown voltage of 50 V over the depletion of the gain layer. Due to a non-uniform gain layer, the yield decreases with size, as expected. However, the performance in terms of yield of this fabrication is outstanding, and some big-area pixelated LGADs can be operated. In addition, the yield decreases for higher doped multiplication layers, where a higher gain is expected.

In order to understand the influence of carbon in the sensors, we have compared two identical wafers, with the exception of the carbon implant. Figure 3.30 shows the I-V measurements for different LGAD structures from a carbonated wafer (top) and a non-carbonated wafer (bottom). As already stated, carbon induces a slightly higher leakage current in the measurements, although the values obtained are excellent. In addition, the carbonated 16x16 LGAD is able to be operated, unlike the non-carbonated wafer, where any 16x16 LGAD meets the requirements.

Wafer	16x32 / 15x30	16x16 / 15x15	5x5	2x2
1	0% / 50%	50% / 75%	100% (20/20)	-
2	100% / 50%	100% / 50%	75% (15/20)	-
3	100% / 50%	100% / 75%	90% (18/20)	-
4	0% / 0%	0% / 25%	80% (16/20)	-
5	0% / 0%	0% / 0%	50% (10/20)	95% (19/20)
6	0% / 0%	0% / 0%	5% (1/20)	25% (5/20)
7	0% / 100%	100% / 100%	90% (18/20)	-
8	0% / 50%	50% / 50%	77% (58/75)	93% (38/41)
9	0% / 0%	100% / 50%	90% (18/20)	-
10	0% / 50%	0% / 50%	74% (53/74)	93% (38/41)

Table 3.7: Yield for different LGAD structures integrated into the ATLAS-CMS Common Run.

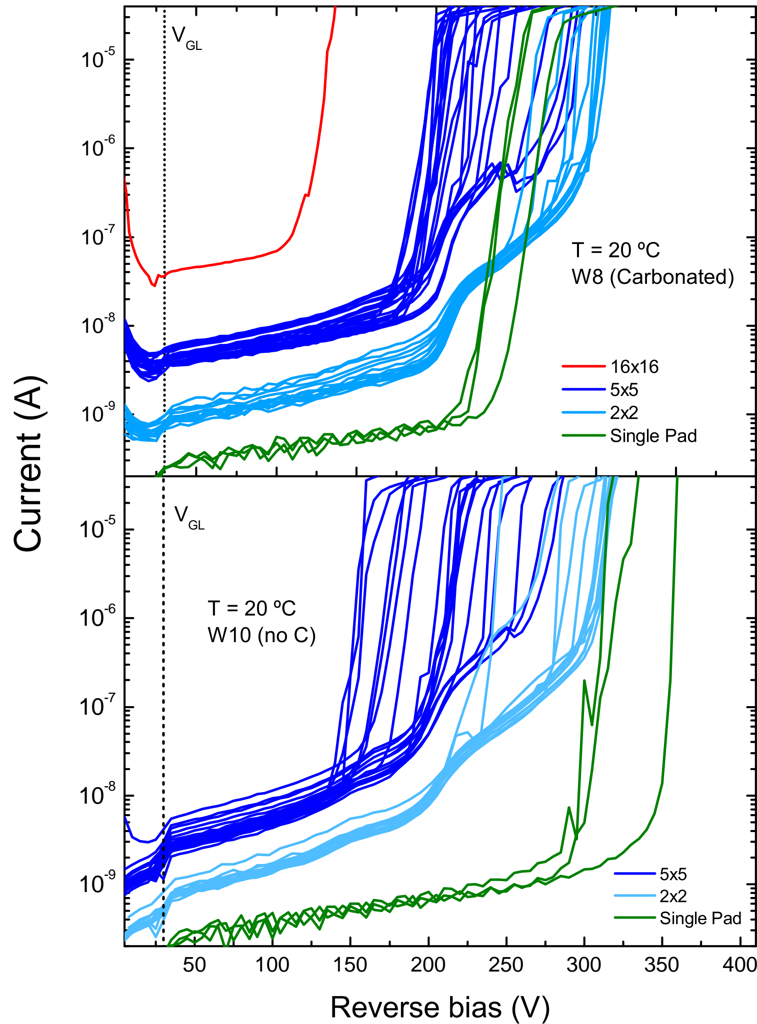

Figure 3.30: I-V measurements for different LGAD structures integrated into the ATLAS-CMS Common Run, from wafer 8 (top) and wafer 10 (bottom). [88]

The higher yield in the carbonated wafer has been studied by C-V measurements, as shown in figure 3.31. Some LGADs integrated into different positions through the wafer have been measured, in order to determine if there is a variation of V_{GL}. LGADs located on the left side of the wafer have a lower V_{GL} than the ones on the right side, for the non-carbonated wafers. However, all the LGADs integrated into the carbonated wafer provides the same V_{GL}, independently of the location on the wafer. Therefore, carbon induces a uniformity in the multiplication layer, which is the reason for the higher yield in big-area LGADs. This phenomenon must be studied in future developments to optimize it for the fabrication of big-area LGADs.

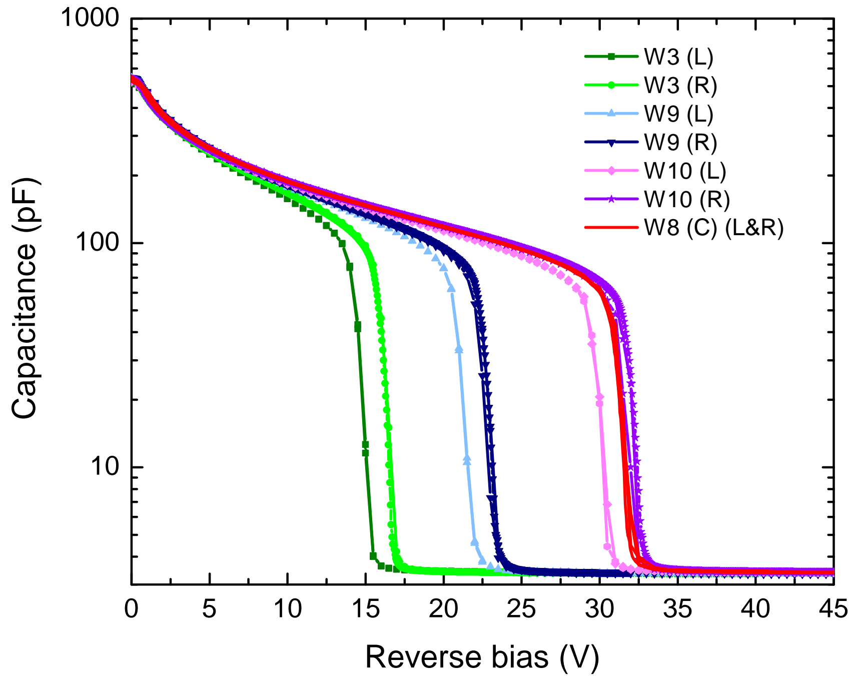

Figure 3.31: C-V measurements for LGADs integrated into different positions through the wafer, from ATLAS-CMS Common Run [88].

In addition to the electrical measurements, some equivalent carbonated and non-carbonated LGADs have been irradiated to measure their acceptor-removal constant [89, 90]. As already stated in previous chapters, the c_A is related to the radiation hardness of LGADs, where the aim is to obtain the lowest possible value. In this sense, the target for the use of LGADs in harsh radiation environments has been set at $1.5 \cdot 10^{-16}$ cm^2. Table 3.8 shows the values obtained for the c_A, using C-V and I-V measurements to obtain the V_{GL}, where there is an important difference between both methods. However, there is a huge decrease of c_A for carbonated sensors and the lowest value obtained is close to the desired target. Therefore, the use of carbon to mitigate the radiation effects in the multiplication layer has been demonstrated, and it is along the same line as other LGAD manufacturers. Figure 3.32 shows the c_A, calculated using the I-V, for different LGADs from various fabrications and manufacturers [89]. The use of carbon in the LGAD fabrication process entails a clear

advantage for radiation environments since there is a substantial decrease in c_A, and some of them can meet the desired target.

Wafer	c_A (CV)	c_A (IV)
8	4.95 ± 0.06	2.4 ± 0.4
10	8.25 ± 0.08	6.4 ± 0.5

Table 3.8: Acceptor removal constant (10^{-16} cm^2) for carbonated and non-carbonated LGADs from ATLAS-CMS Common Run, using CV and IV measurements [89, 90]

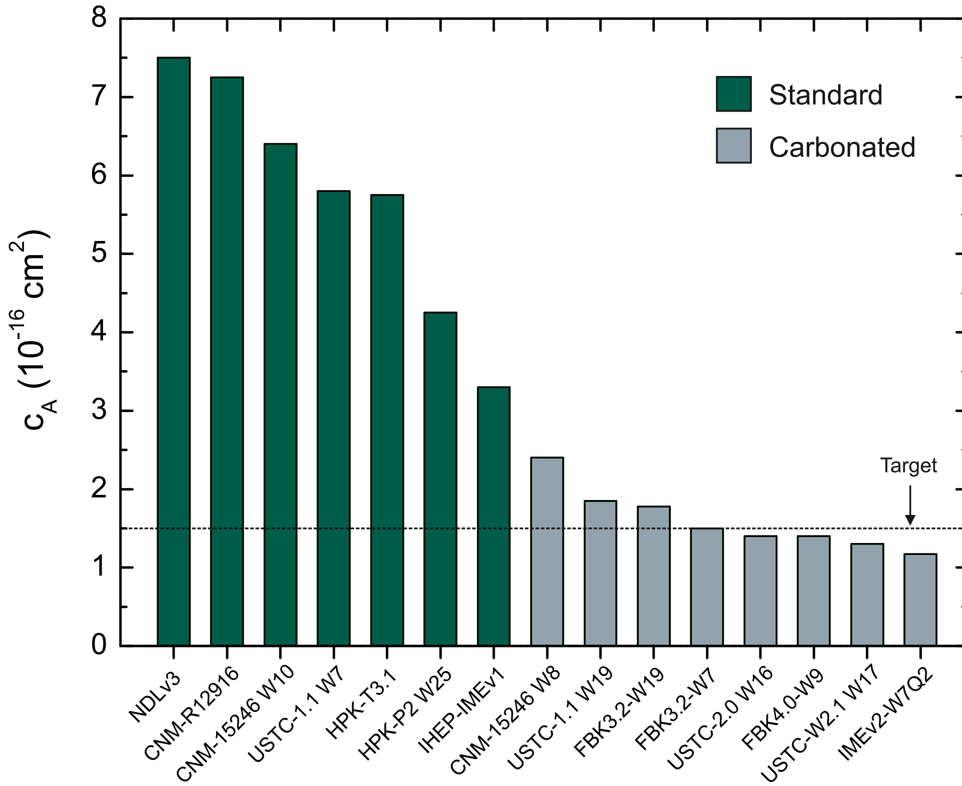

Figure 3.32: Acceptor removal constant for different LGAD fabrications. Adapted from [89].

3.6.5 Summary and conclusions

The ATLAS-CMS Common Run is going to establish a new LGAD production to meet the requirements of both ATLAS and CMS timing detectors using 150 mm wafers. It is planned to use both 6LG2 and 6LG3, using Si-Si and epitaxial wafers, respectively. By using the exhaustive characterization in 6LG3 LGADs, the dose and energy for the boron diffusion are optimized. Furthermore, the multiplication layer is enriched with carbon to enhance the radiation hardness of the sensors, including an additional optimization of the technological parameters to avoid premature carbon diffusion.

Different LGAD designs have been envisaged using a new mask, in order to study the performance of LGADs. Single-pad LGADs will be used to test the electrical performance, gain, and timing before and after irradiation, as well as different configurations of arrays. Big-area pixelated sensors should demonstrate the viability to develop large LGAD sensors without altering the electrical performance.

Upon doing this Ph.D. thesis, the ATLAS-CMS Common Run has been fabricated using 6LG3 technology and a first characterization has been carried out. Excellent performance is achieved, where the LGADs exhibit low leakage currents and a proper operating range due to a high breakdown voltage. In addition, we found a high yield for different LGAD structures, including big-area pixelated LGADs. Furthermore, the use of carbon has entitled a higher uniformity in the formation of the gain layer, which implies a higher yield in the carbonated wafer compared to the non-carbonated one. This behavior has to be taken into account and well-studied for future LGAD fabrications.

Irradiated LGADs have been studied, whereas carbonated ones offer better radiation hardness. Some differences appear when obtaining the acceptor removal constant either with I-V or C-V measurements, and this issue must be solved in the future in order to set a common procedure. Nevertheless, it is demonstrated that carbon helps to reduce this constant and brings it closer to the desired target. An exhaustive characterization of irradiated LGADs must be envisaged to study if they satisfy the requirements of ATLAS and CMS, in order to use these sensors in the future HL-LHC.

Chapter 4

Inverse LGAD for X-Ray Applications

The development of iLGAD sensors for X-Ray applications is fully described in this chapter. The extensive optimization of the periphery design to allow it to support surface damage using TCAD tools is described, as well as the mask design and the full fabrication. Furthermore, this chapter covers the characterization of the fabricated sensors and irradiation testing to probe the optimization followed during the design.

4.1 Introduction

First Inverse LGAD (iLGAD) generation (iLG1) sensors were successfully fabricated by IMB-CNM [38, 39, 40], where the multiplication region remains unsegmented allowing a 100 % fill factor and hence solving the fill factor issue. Even though iLGADs were first suggested to be used in HEP applications, they can be a great solution for synchrotrons since LGAD sensors have been already studied for X-Ray applications [91, 92, 93].

Based on the iLG1, we have developed the second generation (iLG2) with a periphery optimized against X-Ray irradiations. In this chapter, the optimization to reach a usable iLGAD for X-Ray detection and the mask used for the fabrication are described, together with the fabrication process. Finally, the results of the electrical characterization of un-irradiated and irradiated sensors are reported.

4.1.1 First iLGAD generation (iLG1)

The cross-section of the first iLGAD generation designed and fabricated at IMB-CNM is shown in figure 4.1. The core region corresponds to the gain region, where all the pixels (or strips) are located. The multiplication layers for the iLGAD are the same as in LGAD counterparts since there is no difference in terms of gain. Contrary to LGADs, iLGADs are double-side structures, since the ohmic side is not a continuous p^+ diffusion. The multiplication side periphery, where the n^+/p layers are located, uses the same protection strategy as that used in the standard LGAD designs: a JTE and a guard ring diffusions with a p-stop in the middle to avoid a possible inversion of this area due to the irradiation, and a channel stopper at the end of the detector.

The channel stopper is introduced to avoid the depletion region to reach the lateral side of individual chips, short-circuiting the top, and bottom sides. On the ohmic side, a collector ring is also diffused.

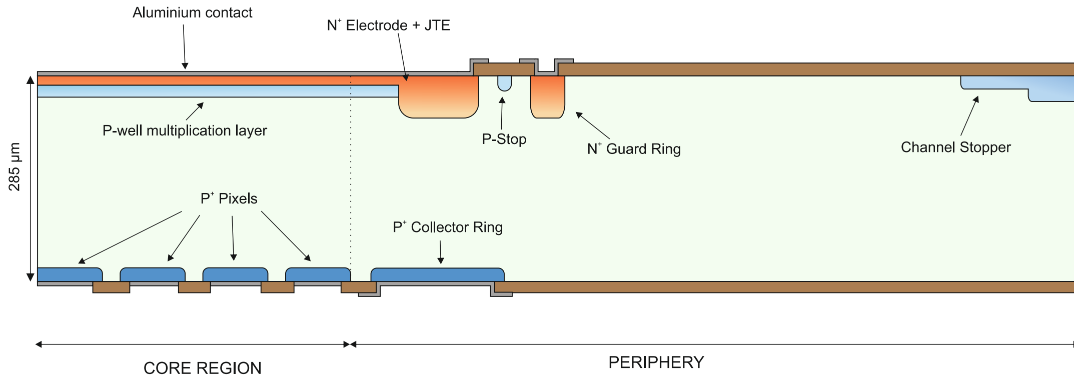

Figure 4.1: Cross-section of the first iLGAD generation fabricated at IMB-CNM

The optimization, fabrication, and characterization of the first iLGAD generation is fully described in [41], and it showed excellent tracking capabilities in HEP experiments [38, 40]. Figure 4.2 shows the result of a test beam in strip LGAD and iLGAD detectors. In the LGAD case, two peaks are observed, corresponding to the non-gain (around 24 ke) and the gain regions (77 ke). In the iLGAD case, only one peak is present (75 ke) due to the 100 % fill factor [40].

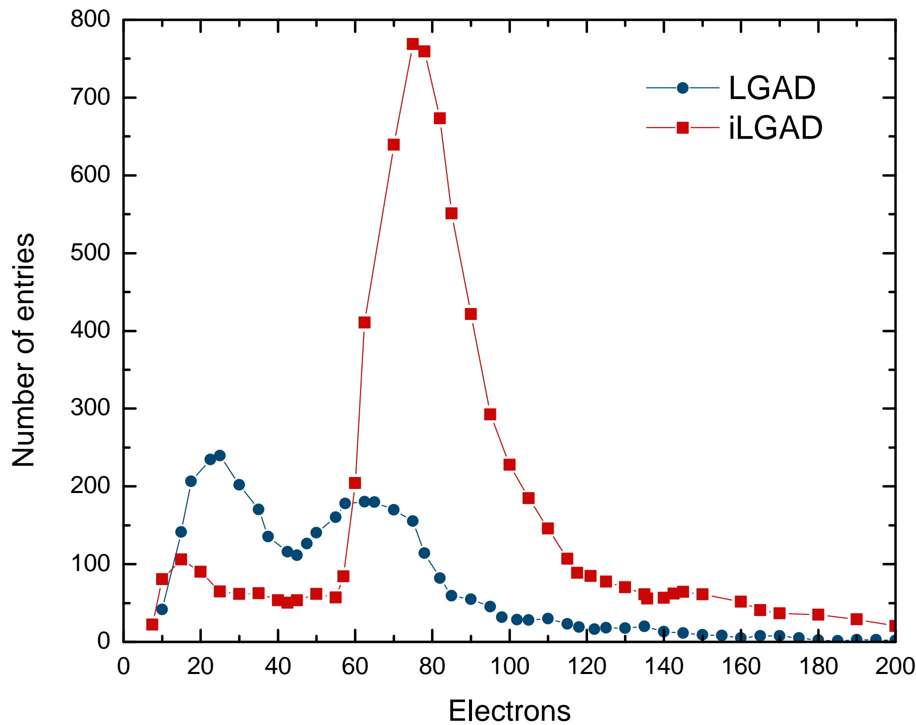

Figure 4.2: Charge distribution measured during a test beam for strip LGAD and iLGAD detectors.

4.2 Optimization of the iLGAD detectors

4.2.1 Periphery optimization for X-Ray applications

We have optimized the periphery of the iLG1 to develop a new iLGAD generation for X-Ray applications. Since the multiplication region is the same for LGAD and iLGAD structures, we have only optimized the periphery of the detector to make it suitable for synchrotron applications. The first iLGAD generation was not designed taking into consideration a high charge concentration in the Si-SiO_2 interface, since those detectors were not oriented for X-Ray applications, and hence no surface damage was expected. In order to study the damage created in the detector during X-Ray irradiations, we have simulated the iLGAD structure introducing a certain oxide charge density (N_{ox}) at the Si-SiO_2 interface, using a reference value of N_{ox} = 10^{12} cm^{-2}, which corresponds to Φ = 10 MRad [59]. The most critical effect as a consequence of the N_{ox} is the degradation of the voltage capability, clearly shown in figure 4.3. One can observe that breakdown voltage is decreasing greatly when the charge increases. Thus, the effectiveness is drastically reduced in a harsh X-Ray radiation environment.

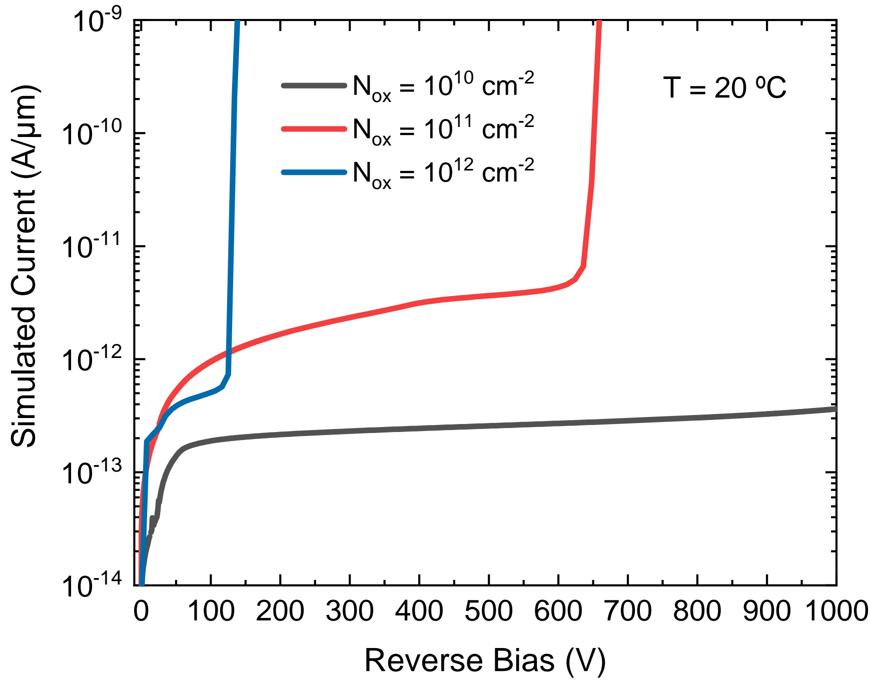

Figure 4.3: I-V simulation of iLGAD structures with different Nox concentrations. Breakdown voltage is reduced by increasing Nox.

Multiplication side optimization

Due to surface damage, electrons are accumulated in the oxide-silicon interface creating an n-doped layer, which lowering the electrical performance of the device since it creates a high electric field at the edge of the channel stopper (p-type diffusion). In this situation, the electric field peak is higher than the electric field value created

at the multiplication region. Hence, this peak has to be reduced to increase the robustness of the device, thus we have introduced five floating guard rings with their respective p-stop diffusions between them and two p-stop diffusions between the last floating guard ring and the channel stopper. A breakdown voltage increase of 50 V is obtained using this strategy, which is less than expected. It would be possible to use a multi-ring structure with more than five floating guard rings, but the periphery would consume too much area, not compatible with radiation detectors, where the area in which particles are not detected, also called dead area, has to be minimized. Ideally, these structures should be slim-edge, i.e. without any periphery. Therefore, we need to find a trade-off between performance and extension of the peripheral zone. Figure 4.4 shows the electric field distribution along the termination length in the Si-SiO_2 interface (y = 0.1 µm) at 600 V. This strategy enables the detector to lower the electric field peak down the desired threshold, which is the n^+/p junction peak.

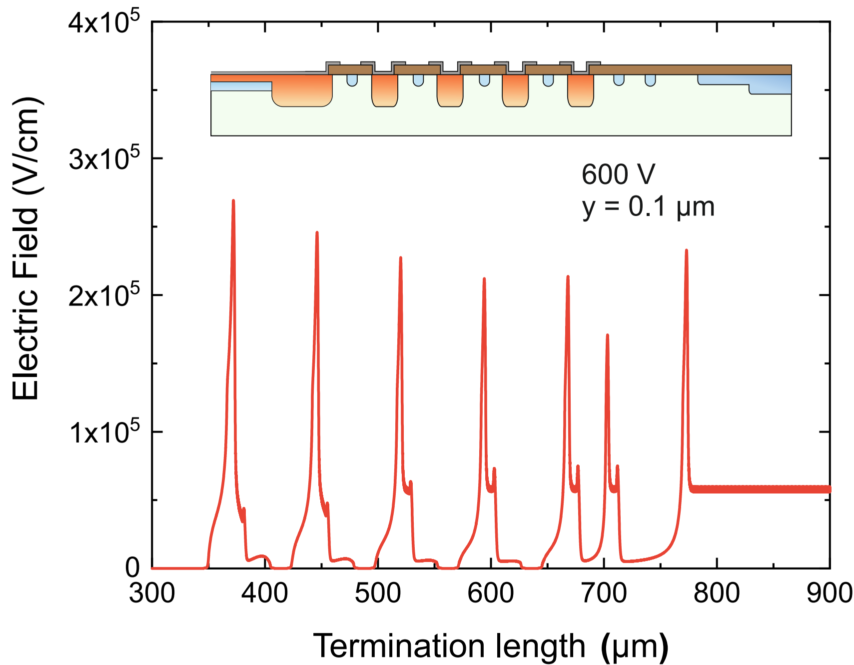

Figure 4.4: Electric field cut at 0.1 µm along the periphery in the multiplication side at 600 V.

Ohmic side optimization

In order to improve the breakdown voltage capability, we have also optimized the ohmic side of the device. We have considered three different approaches for the p^+ pixels before including a multi-ring structure, as shown in figure 4.5. The initial breakdown voltage is 350 V (with only the collector ring). By adding p^+ diffusions, the breakdown voltage is increased up to 500 V for the multi-ring structure (c). P-type pixels and the collector ring at the ohmic side are high-doped diffusions. Hence, the electric field created due to the conductive layer is higher than the electric field peak at the main junction. This behavior can be observed in figure 4.6, which shows the electric field distribution along the length of the sensor. We found that the

optimization of the ohmic side of the sensor is relevant for this application since these high electric fields must be considered. Nevertheless, by using the multi-ring strategy, we have been able to lower the peaks and achieve a breakdown voltage of 500 V, as shown in figure 4.7. Hence, we have increased the breakdown voltage up to four times in harsh X-Ray environments, widening the operation voltage regime. Figure 4.8 shows the final design proposed for the second iLGAD generation (iLG2).

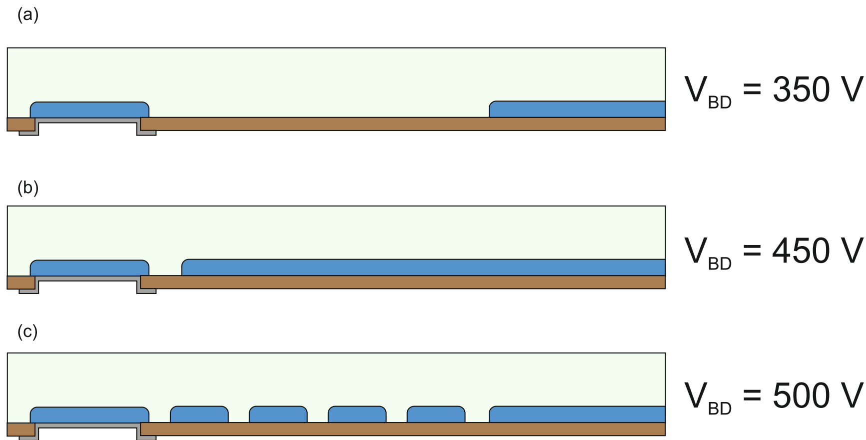

Figure 4.5: Different configurations of the p^+ diffusions at the ohmic side. Multi-ring structure gives the highest breakdown voltage and this is going to be the final design.

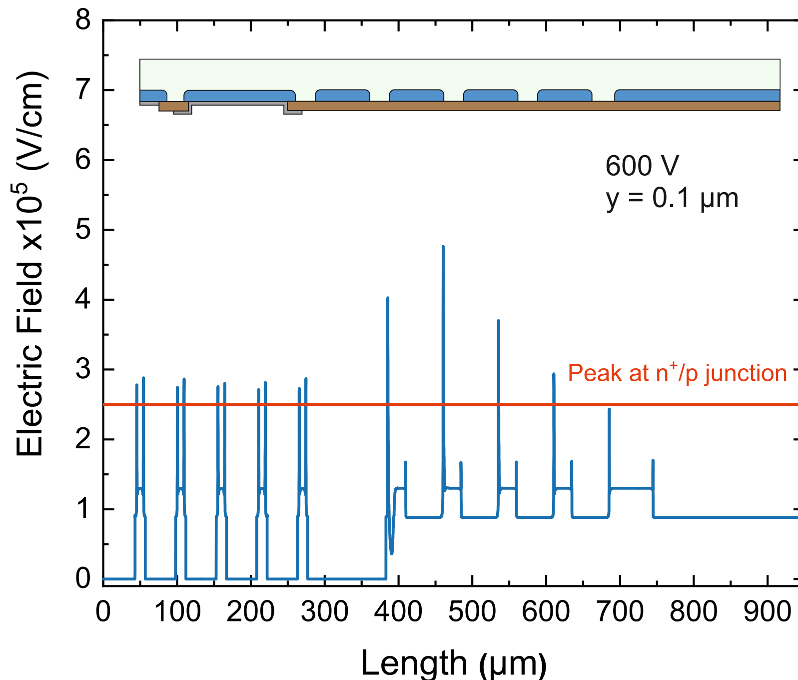

Figure 4.6: Electric field cut at 0.1 µm along the periphery in the ohmic side at 600 V.

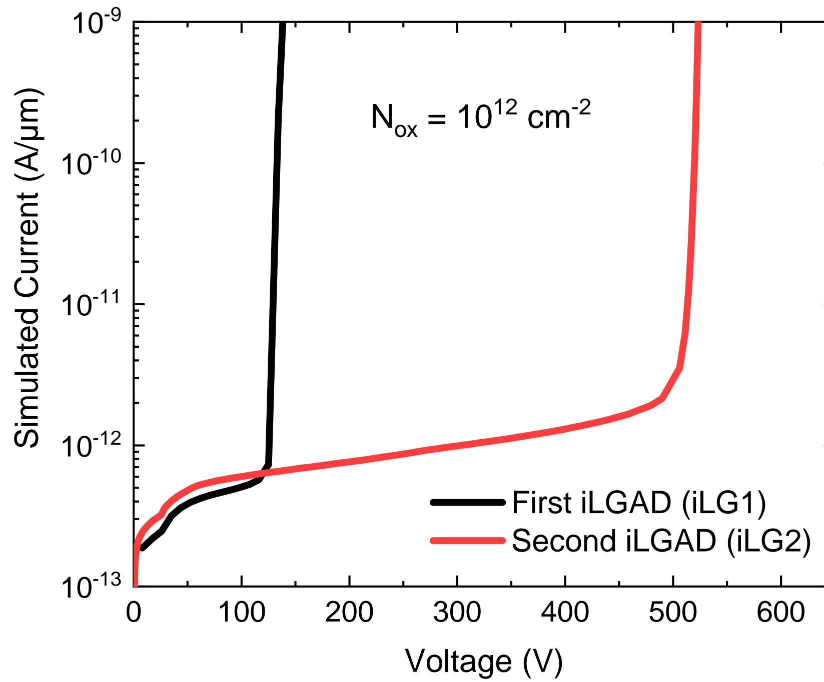

Figure 4.7: I-V simulation of iLGAD structures with Nox = 1012 cm-2.

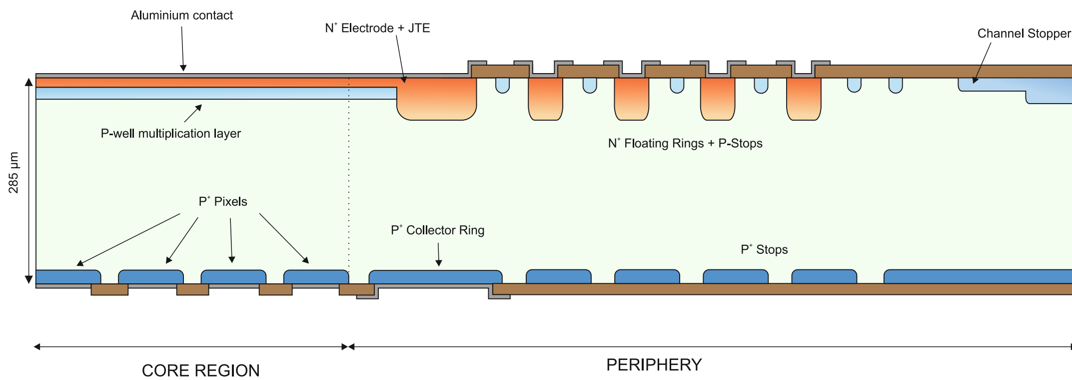

Figure 4.8: Final design of the second iLGAD generation

4.3 Photolithographic mask designs

Once the second generation of the iLGAD is optimized, we have designed the photolithographic mask set (CNM953) needed for its silicon integration, consisting of 12 photolithographic levels, depicted in table 4.1. It is described the mask level, the description, the alignment, and the insolation side (multiplication or ohmic side).

Mask level	Level description	Alignment	Insolation side
P-Stop	P-Stop Diffusion	Flat	Multiplication
JTE	JTE Diffusion	P-Stop	Multiplication
Multiplication	Multiplication Layer	JTE	Multiplication
NPlus	N+ Diffusion	Multiplication	Multiplication
Back-PPlus	P+ Diffusion	NPlus	Ohmic
Contact	Contact Opening	NPlus	Multiplication
Back-Contact	Contact Opening	Back-PPlus	Ohmic
Metal	Metallization	NPlus	Multiplication
Back-Metal	Metallization	Back-PPlus	Ohmic
Back-Metal2	Temporary Metal	Back-Metal	Ohmic
Pass	Passivation	Metal	Multiplication
Back-Pass	Passivation	Back-Metal	Ohmic

Table 4.1: Mask levels for the 12 photolithographic steps in the iLG2

The mask levels described in table 4.1 are illustrated in figure 4.9. It is clear that there is an added complexity due to the segmentation of the ohmic side, which must be passivated and metalized. Different ASIC designs are integrated in the CNM953 mask, which parameters are described in table 4.2. Medipix3 is a CMOS pixel detector that acts as a camera taking images based on the number of particles hitting the pixels [37], while JUNGFRAU is a 2D pixel detector for photon science applications at free electron lasers (FEL) and synchrotron light sources [94]. The use of these ASIC designs is considered since the development of this fabrication aims to detect X-Rays. In addition, we designed strip iLGADs to compare their performance with the previous iLG1.

Big-area iLGADs are used to test the uniformity of the gain layer, which is a key measurement in the development of LGADs. As already stated in previous chapters, the non-uniformity of the gain layer may lead to a premature breakdown in large detectors. Therefore, we consider small-area detectors to test the quality of the fabrication by removing this effect. In that sense, pixelated and pad iLGADs are included. Moreover, as the periphery is the same for big and small detectors, we are going to be able to measure the influence of the new periphery design against X-Ray irradiations. Some of these structures are illustrated in figure 4.10. Finally, structures such as PiN detectors and Metal-Oxide-Semiconductor (MOS) capacitors are designed to test the electrical performance and the quality of the thermal oxides, respectively. Figure 2.14 shows the mask design used in the iLG2.

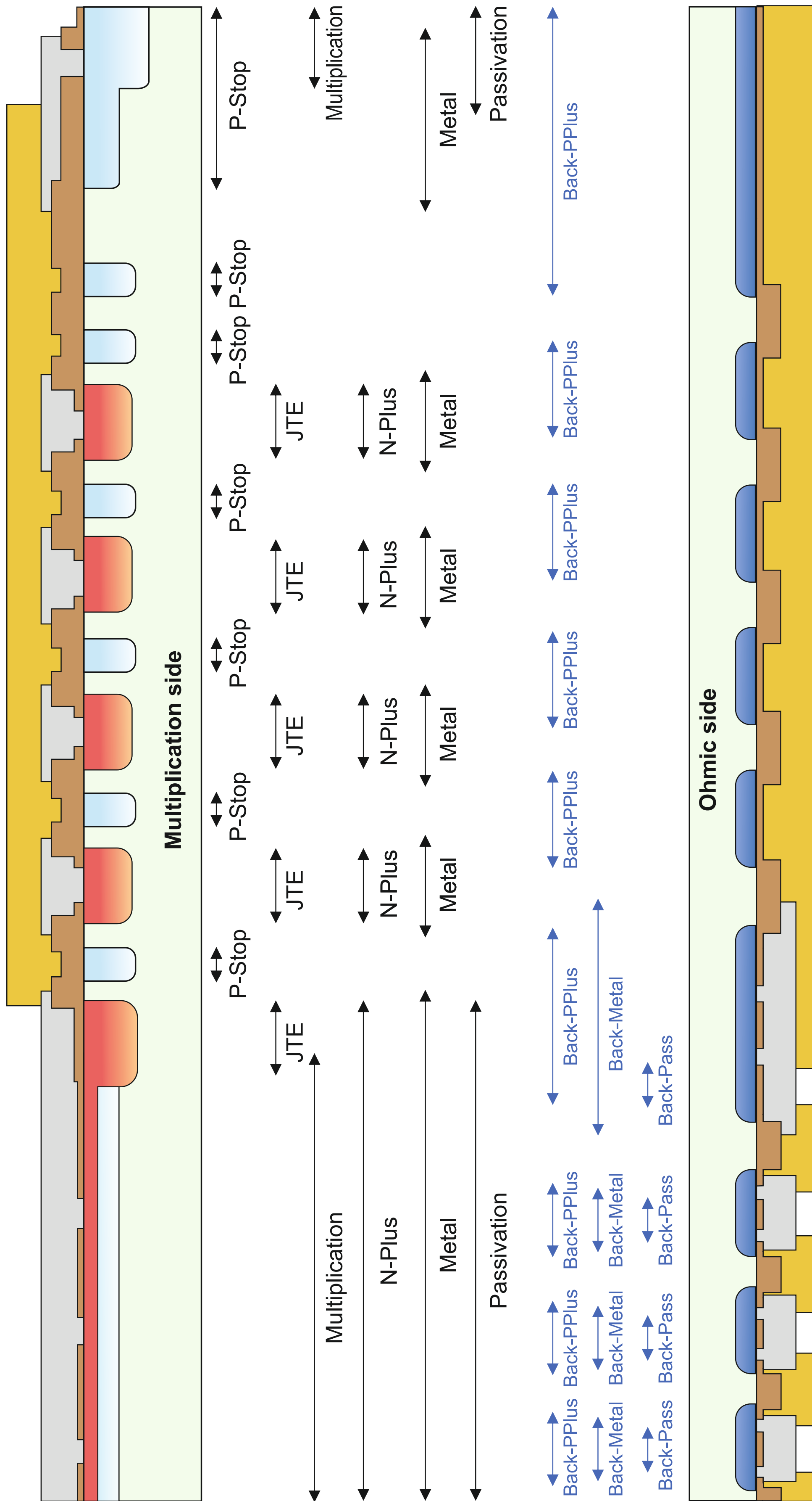

Figure 4.9: CNM953 mask levels sketch.

iLGAD Design	Pitch (μm)	Pixels/Strips	Area
Medipix3	55	256x256	1.56x1.56 cm^2
JUNGRFAU	75	256x256	1.97x1.97 cm^2
Strip iLGAD	110	73 Strips	1x1 cm^2
Small iLGAD	55	10x10	2337x2337 μm^2
Pad iLGAD	-	-	2337x2337 μm^2

Table 4.2: Design parameters of the different iLGAD detectors included in the mask CNM953.

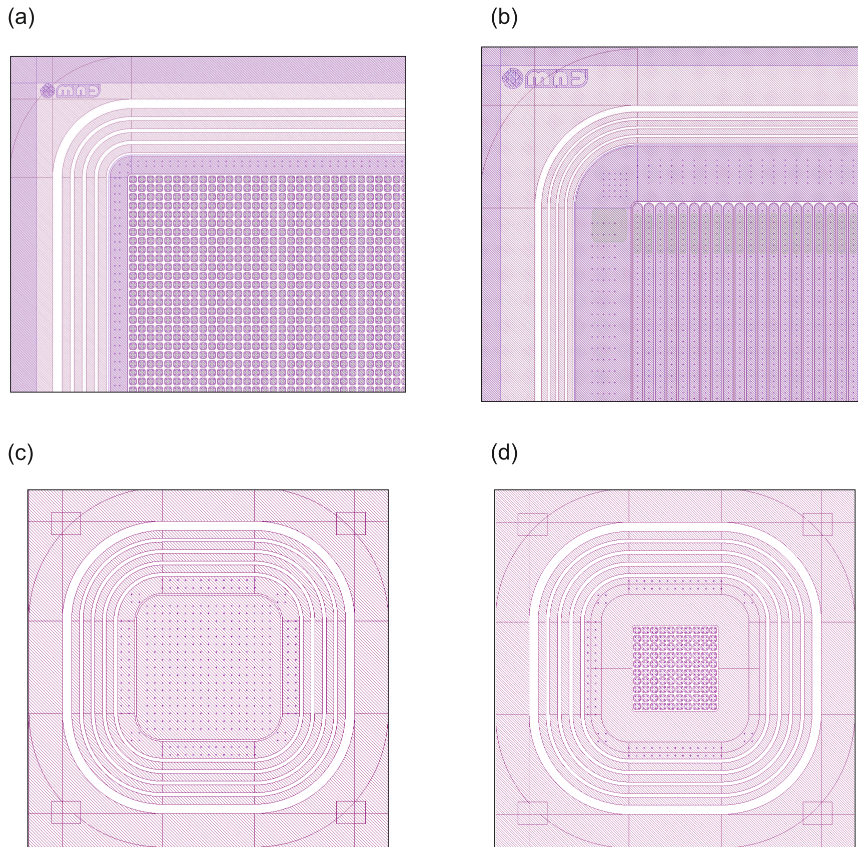

Figure 4.10: Different iLGAD designs included in the mask CNM953: (a) Medipix3, (b) Strip iLGAD, (c) Pad iLGAD, and (d) 10x10 iLGAD.

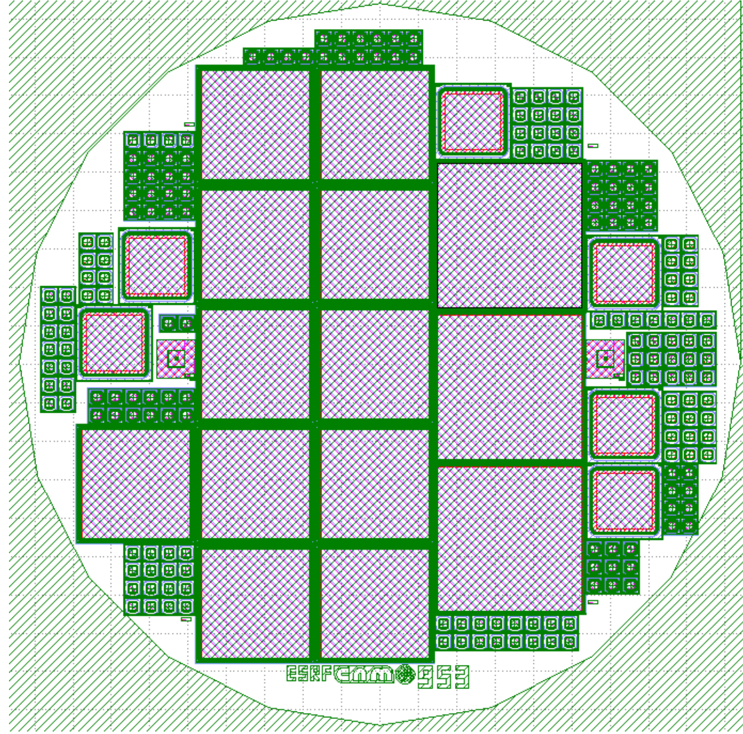

Figure 4.11: Design of the CNM953 mask used in the development of the iLG2.

4.4 Fabrication of the iLG2

The iLG2 production has been fabricated at the IMB-CNM clean room. The whole fabrication process consists of 150 steps, including the twelve photolithographic steps. The process flow is the same as previous LGAD productions, however, some additional considerations must be taken into account. First, we had to decide on the wafer characteristics. Since this is a production for X-Ray detection we need thicker substrates in comparison with LGAD for timing applications, in order to collect all the charge deposited (Figure 1.6). Therefore, we decided to implement the run in 285 µm thick, high resistivity (> 10 k$\Omega \cdot$ cm) p-type wafers, taking advantage that they have been already used in previous LGAD productions. In addition, we have used n-type test wafers to control the resistivity of the boron implant, as usual in LGAD fabrications.

Wafer	**Description**
1,2	Process PiN wafers
3-8	Process iLGAD wafers
9-11	Test iLGAD wafers

Table 4.3: Main characteristics of the wafers used in the production and their description.

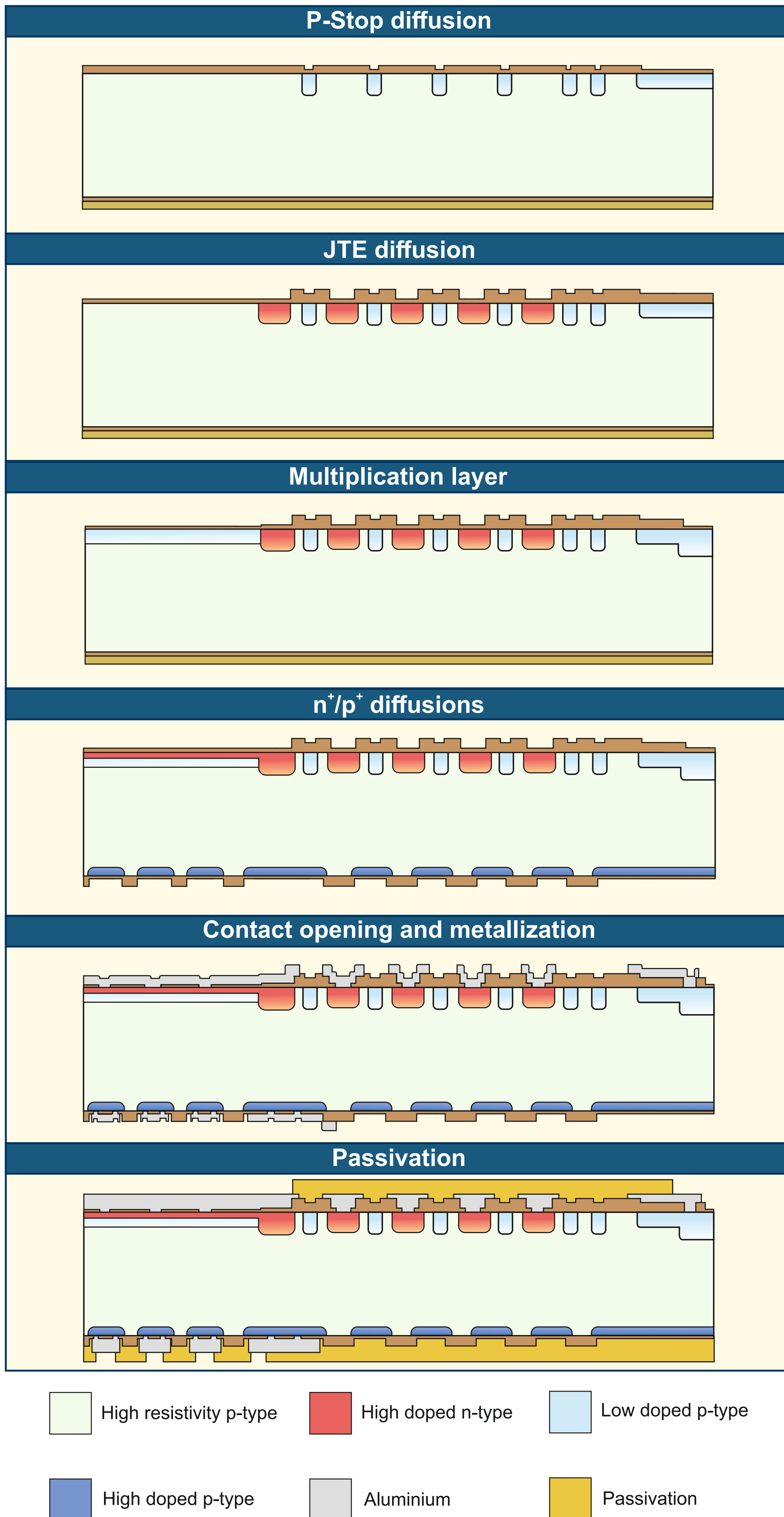

Figure 4.12: Fabrication process for the iLG2.

Table 4.3 shows the total number of wafers and their description. In total, the run consists of 11 wafers, including two PiN wafers to evaluate the quality of the fabrication process and the yield of the big-area diodes without gain. Figure 4.12 shows the fabrication process for the iLG2. It is important to mention that the main difference between this fabrication and standard LGAD productions is that this is a double-sided fabrication. Therefore, the ohmic side of the detector is also processed. Since it is a double-side process, an 1800 Å LPCVD (Low Chemically Vapor Deposition) nitride (Si_3N_4) is deposited at the ohmic side, in order to protect it during the process.

4.4.1 Multiplication layer

The formation of the multiplication layer is the most critical step of the iLGAD process technology. Small variations in dose and energy will produce huge variations in terms of breakdown voltage and leakage current, as shown in previous chapters. Therefore, an exhaustive control of the clean room parameters is mandatory for the iLGAD as well. To study the sheet resistance of the boron implant, we have used n-type test wafers, like in LGAD fabrications. Figure 4.13 shows the sheet resistance values for the iLG2 and some LGAD previous fabrications. We have used the same boron parameters as the AIDAv2 sensors: an energy of 100 keV and a boron dose of $1.8 \cdot 10^{13}$ cm^{-2}.

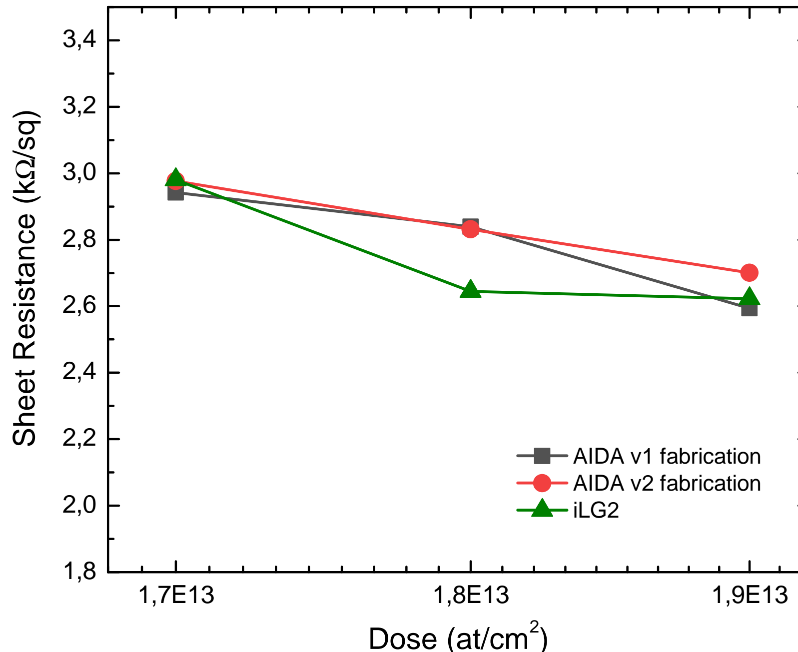

Figure 4.13: Average sheet resistance as a function of the boron dose for two LGAD productions and the iLG2 production.

As it can be seen, for this particular case we got a low sheet resistance (more doped) boron multiplication layer in comparison with the previous LGAD fabrications. Therefore, we can expect to have a higher gain, which is going to be tested

during the gain measurements. This value is measured in one test wafer, however, different values can be obtained in processed wafers since we use this method to extract an approximation. The simulated value for this medium dose is 2890 Ω/sq, which is higher than the measured. It is important to mention that the experimental value is the mean value of the 49 points measured. As already seen in previous LGAD chapters, there is a non-uniformity of sheet resistance in the wafer. Figure 4.14 shows the sheet resistance map created with the 49 points measured in the wafer. This map exhibits a non-uniform resistivity of the gain layer across the wafer with the central region of the wafer less doped than the external area. Therefore, we expect a high dispersion in terms of the electrical performance of the devices, since these variations can lead to huge changes in the profiles.

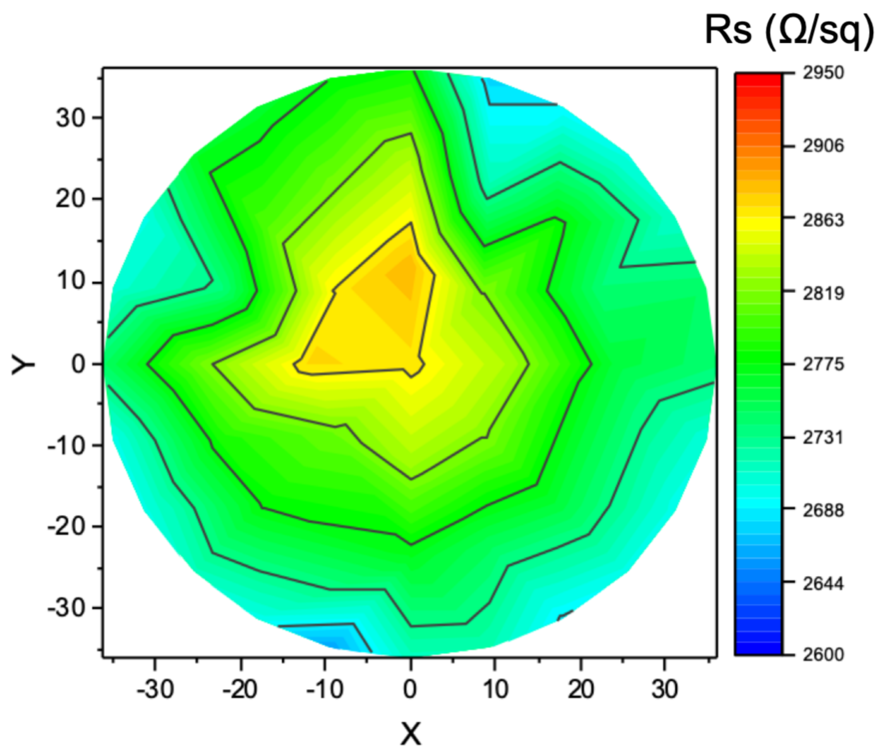

Figure 4.14: Sheet resistance wafer map for the medium dose in the iLG2.

Once the formation of the multiplication region is completed, we checked the oxide thickness in each region of the detector by ellipsometry. Table 4.4 shows the measured and the simulated oxide thickness values for each region, where a high consistency between experimental and simulated values is achieved. Figure 4.15 shows a microscope image of the periphery of an iLGAD sensor where it can be seen the different oxide thicknesses, which corresponds to different colors.

Region	Experimental thickness (Å)	Simulated thickness (Å)
Field oxide	12986 ± 28	13000
P-Stop	10044 ± 14	10000
JTE	5668 ± 3	5600
Multiplication	5488 ± 4	5500

Table 4.4: Experimental and simulated oxide thickness of the different regions in the detector

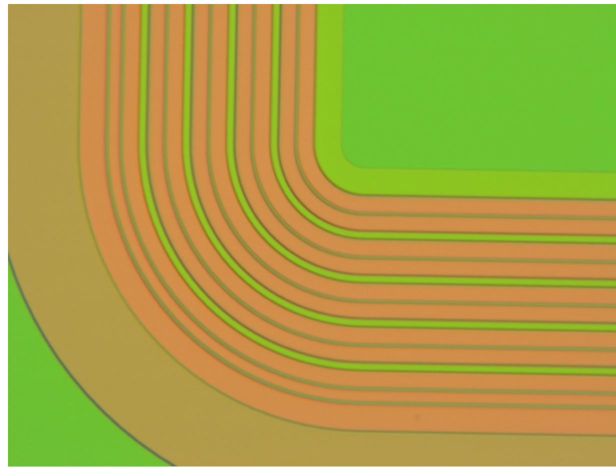

Figure 4.15: Detailed view of the iLGAD periphery after the multiplication diffusion

4.4.2 End of the process

Figures 4.16 and 4.17 shows a general and detailed views of one fabricated wafer on both sides. Also, we can see zooms views in the Medipix3 pixelated area (a,b), strips (c) and rings at the multiplication side (d).

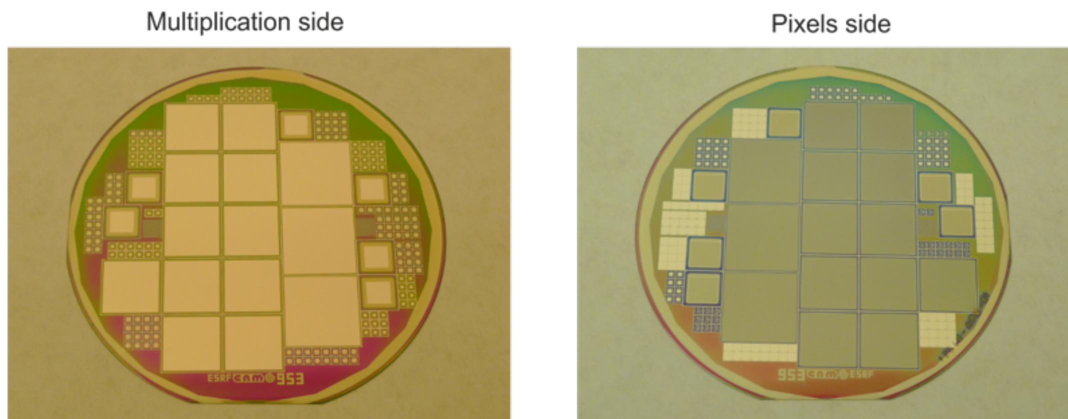

Figure 4.16: Images of a fabricated wafer at the multiplication and ohmic sides.

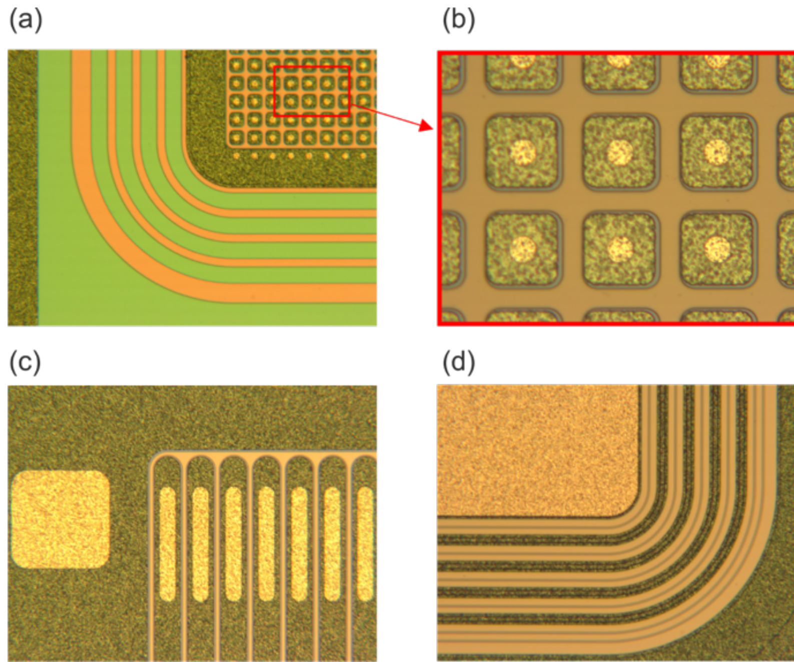

Figure 4.17: Detailed views of the iLGAD at the end of the process. (a) Medipix3 design iLGAD at the ohmic side. (b) Zoom of the 45-µm pixel size. (c) Strip iLGAD at the ohmic side (d) Floating n^+ rings at the multiplication side.

4.5 Characterization of the fabricated sensors

The fabricated sensors have been fully characterized. We have carried out an electrical characterization of the different designs in order to extract the main parameters of the sensors before irradiation. Pad LGAD sensors have been used to make gain measurements, since the multiplication region is the same for iLGADs and LGADs, and they are easier to characterize due to the non-segmented electrodes. Finally, we have performed an X-Ray irradiation of an iLGAD of the iLG2 production and another one from the iLG1, in order to compare their performances.

4.5.1 Electrical characterization

Pad LGAD structures

In order to test the quality of the process technology, we have performed an electrical characterization on pad LGAD structures. Figure 4.18 shows the I-V curves of some LGADs at room temperature in the same region of the wafer and a PiN diode to compare the leakage current. We expected to have a breakdown voltage higher than 500 V and a leakage current of 1 nA. As it can be seen, the breakdown voltage ranges from 300 to 400 V and the leakage current is 10 nA. Therefore, the performance of the detectors is worst than expected. Nevertheless, it can be related to the gain (due to the lower sheet resistance observed) since a higher gain than expected will lead to a lower breakdown and a higher current. It is clear that from 40 V there is an

increase in the current of one order of magnitude, which is the depletion of the gain layer.

In order to determine the depletion voltage of the gain layer, we performed C-V measurements on LGAD sensors at room temperature, shown in figure 4.19. The gain layer depletion occurs at 38 V, which is also higher than expected, which can be related to the lower sheet resistance observed during the fabrication. Therefore, we expect to have a higher gain in this production. Finally, V_{FD} is reached at 70 V, which implies an operating voltage from 70 to 300-400 V.

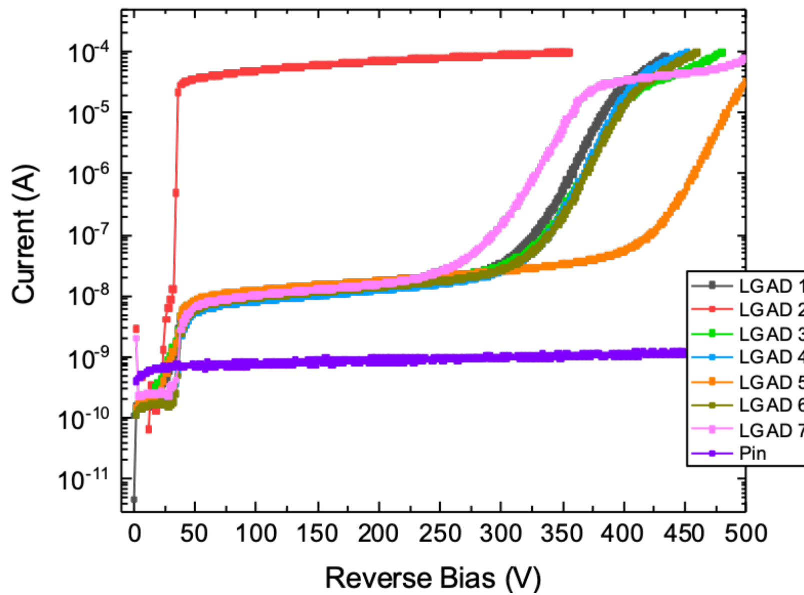

Figure 4.18: I-V measurement of pad LGAD structures at room temperature.

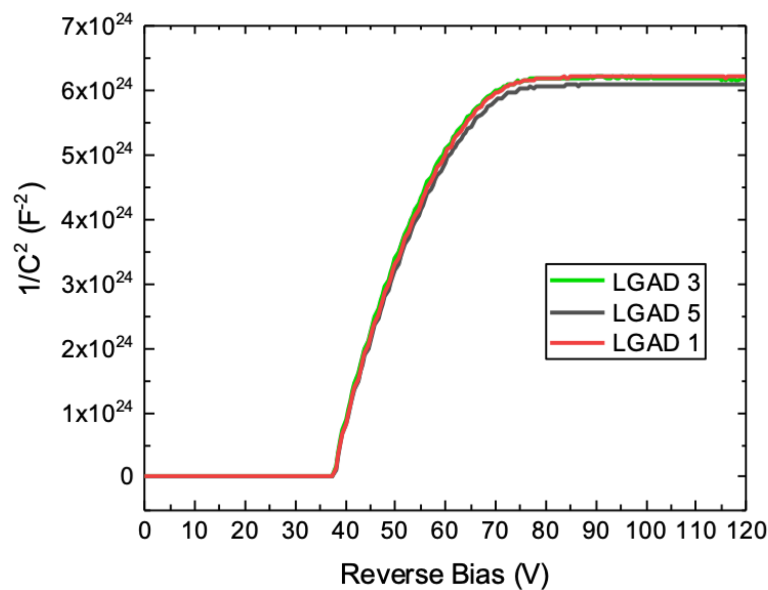

Figure 4.19: C-V measurement of pad LGAD structures at room temperature.

Inverse LGAD structures

Once the LGAD structures are characterized, we performed the same measurements on the iLGAD sensors. First, we have characterized the PiN wafer, where figure 4.20 shows the current density for all the designs. As one can observe, all the designs have a similar current density in the range of 10^{-7} A/cm^2, which is the expected value. This measurement proves that there is any problem with the design of the segmented ohmic contacts and the periphery since it does not appear a shortcut in the measurement and the optimized periphery does not interfere with the I-V measurements.

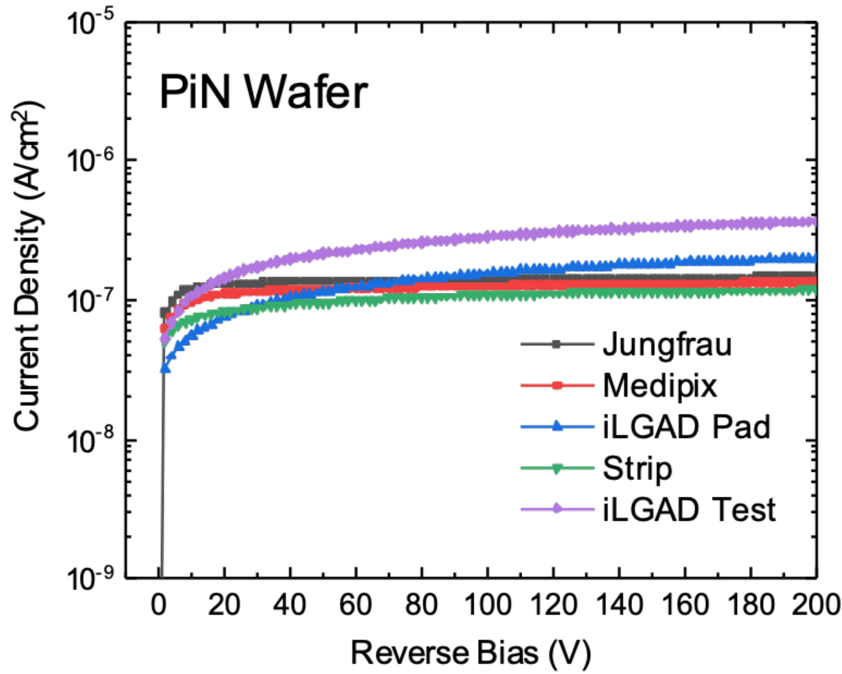

Figure 4.20: Current density at room temperature of each iLGAD design in the non-gain wafer.

In the wafer with multiplication, we expect to have similar behavior. Figure 4.21 shows the I-V measurement for the different iLGAD designs. The iLGAD pad and small-area pixelated detectors have the same performances as the standard LGAD structures. On the contrary, we are obtaining a premature breakdown in the big-area detectors. We attribute this low breakdown to a problem in the periphery design or a non-uniformity in the gain layer in big-area detectors. The first assumption can be discarded due to the PiN wafer measurements since we are not observing this low breakdown when the multiplication region is not present. Therefore, we consider that the low breakdown is devoted to the presence of the multiplication region.

Thanks to the previous manufacturing processes, we know that we have a high non-uniformity in the boron implant process, which can lead to huge differences in terms of doping concentration in big-area detectors (that are not so evident in small sensors), creating a non-uniform multiplication layer that can induce drastic reductions in its breakdown voltage, that can lead to a premature breakdown, especially in big-area

detectors. This is the main challenge for big-area LGAD and iLGAD productions and needs to be solved in future fabrications.

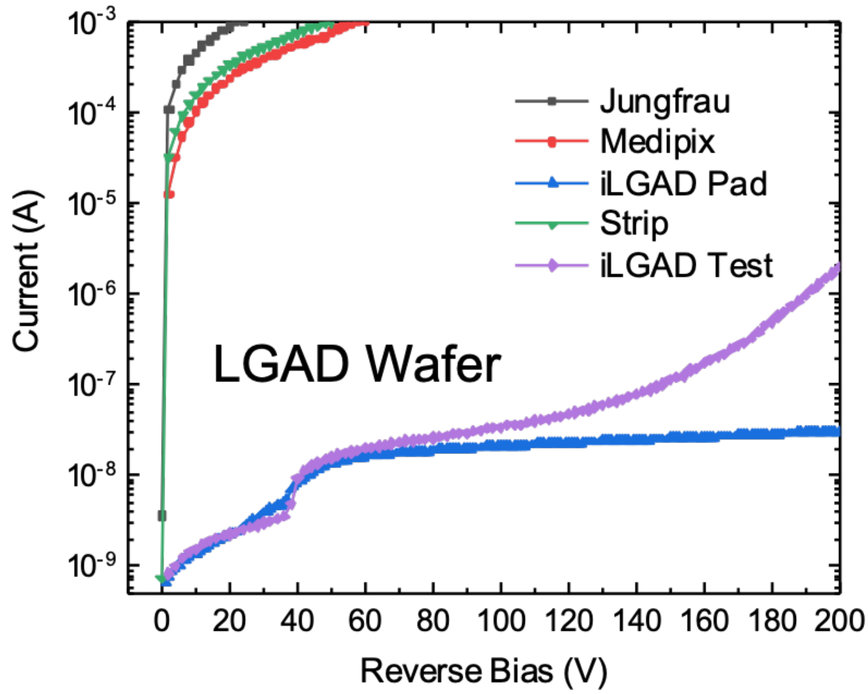

Figure 4.21: I-V at room temperature of each iLGAD design.

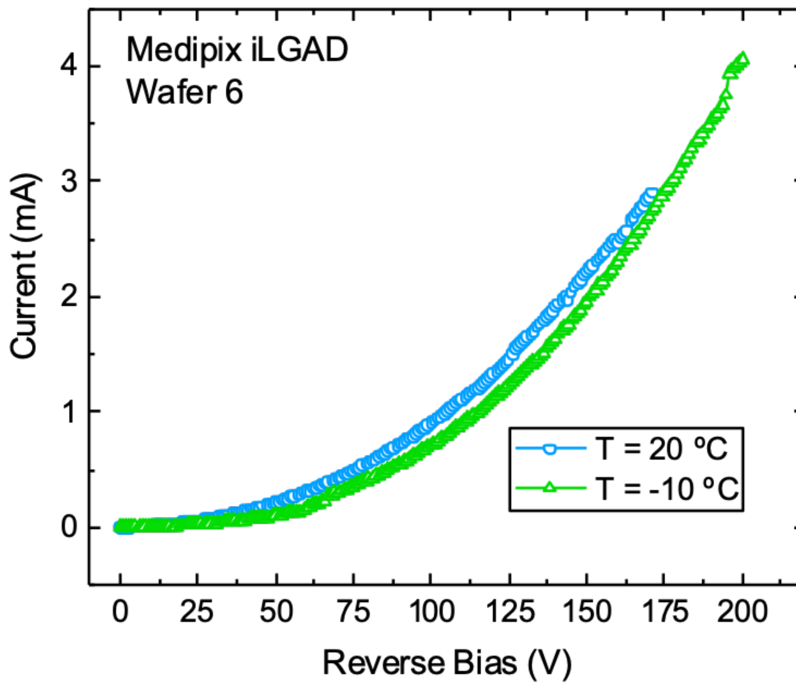

Figure 4.22: I-V measurement of the Medipix3 iLGAD at different temperatures.

In order to reinforce this hypothesis, we performed the I-V measurements at low temperatures in order to see if this current is a high leakage current due to the

high gain. Figure 4.22 shows the I-V measurement of a Medipix3 iLGAD at room temperature and at -10 ºC. If there is a high current due to a high gain, the leakage current should be reduced, but we are not seeing this behavior. Therefore, the sensors are under breakdown since the beginning of the measurement.

Therefore, we are not able to determine the actual reason for the big-area iLGADs performance. Further studies must be envisaged in future developments to clarify this effect and try to avoid it. Different area sensors can be designed in order to see their deterioration, as well as wider multiplication layer doses. Moreover, some solutions to achieve a higher uniformity as a deeper implant may be considered.

MOS capacitors

We have included MOS capacitors to extract the oxide charges before irradiation by C-V measurements, which is an important parameter in X-Ray detectors. Figure 4.23 shows the C-V measurement of a MOS capacitor at 10 kHz and a cross-section of the MOS capacitor structure. Here, we do not have the n^+ and multiplication layers. From the C-V measurement, we can determine an oxide capacitance (C_{ox}) of 27.5 pF, which is similar to the 28.8 pF calculated theoretically. Therefore, there is an agreement between experiment and theory. Flat-band voltage (V_{FB}) can be calculated by the intersection of the capacitance with the flat-band capacitance value (C_{FB}).

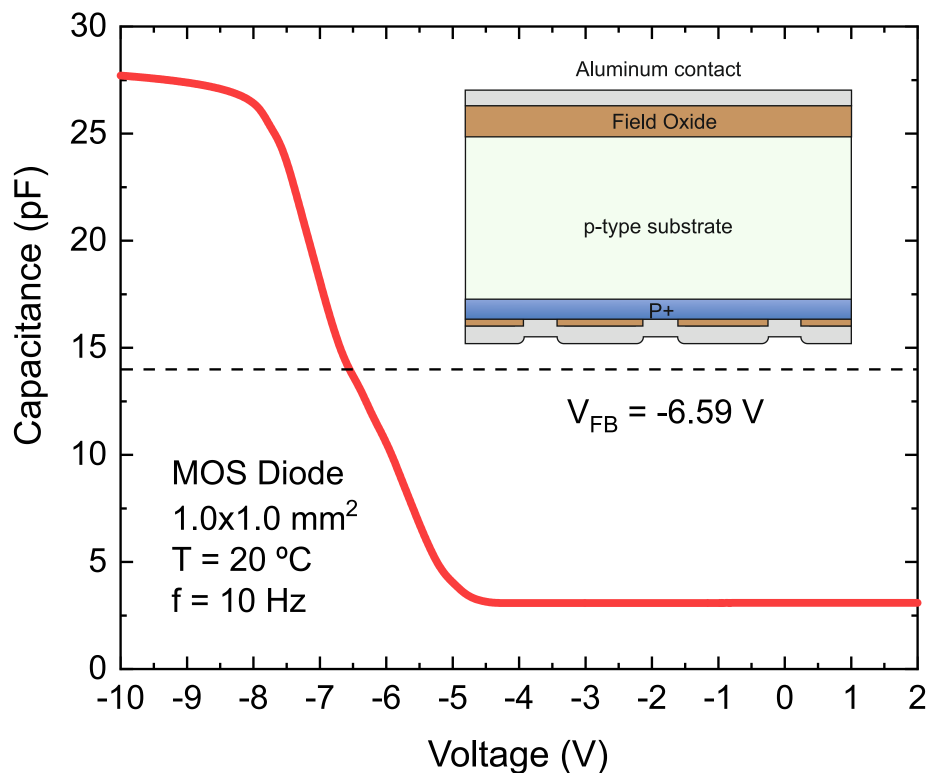

Figure 4.23: C-V measurement of a MOS capacitor at room temperature and 10 kHz.

C_{FB} is defined by [95]:

$$C_{FB} = \frac{C_{ox}(\epsilon_{Si}A/L_D)}{C_{ox} + C_{ox}(\epsilon_{Si}A/L_D)} \tag{4.1}$$

$$L_D = \sqrt{\frac{\epsilon Si k_B T}{q^2 N_B}} \tag{4.2}$$

Where L_B is the Debye length and k_B is the Boltzmann's constant. Using equation (2), L_B is 4.04 µm. Then, C_{FB} is calculated with equation 4.1 resulting to be 14.1 pF, which is the dashed line represented in figure 4.23, and the flat-band voltage is -6.59 V.

Oxide charge is determined by solving:

$$Q_{ox} = -C_{ox}\Delta V_{FB} \tag{4.3}$$

where ΔV_{FB} is the difference between the experimental and the theoretical flat-band voltage values. Therefore, to determine the Q_{ox}, we must calculate the theoretical flat-band voltage. Assuming an ideal MOS with no oxide charges:

$$V_{FB} = \phi_{MS} = \phi_M - \phi_S \tag{4.4}$$

where ϕ_M and ϕ_S are the metal and semiconductor work functions, respectively.

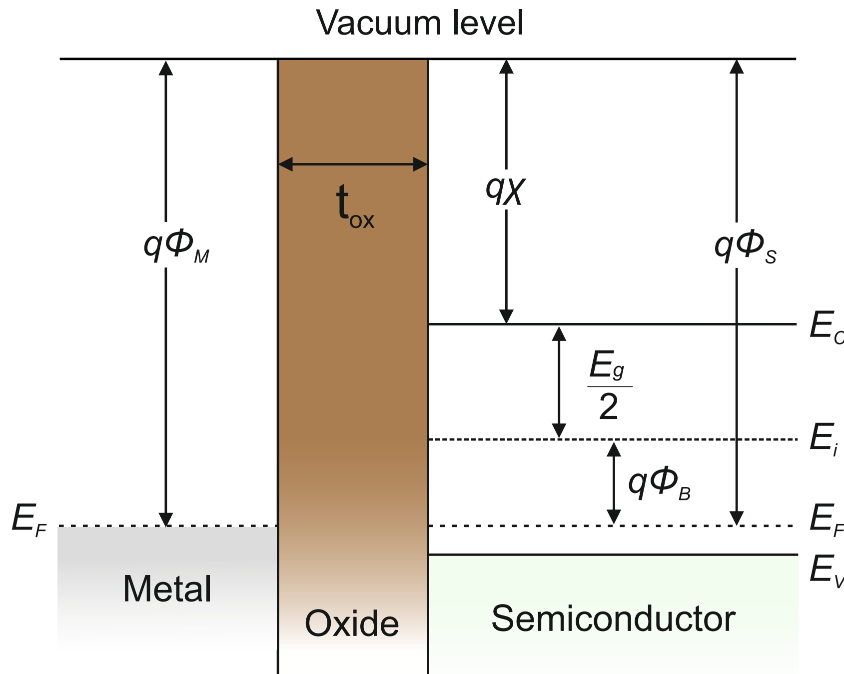

Figure 4.24: Energy band diagram of an ideal MOS structure at thermal equilibrium.

Figure 4.24 shows the energy bands of a typical MOS at thermal equilibrium. From this diagram, equation 4.4 is rewritten as:

$$V_{FB} = \phi_M - (q\chi + \frac{E_g}{2} + \phi_B) \tag{4.5}$$

$$\phi_B = \frac{k_B T}{q} \ln \frac{N_B}{Ni} \tag{4.6}$$

where $q\chi$ is the silicon electron affinity and ϕ_B is the energy difference between the Fermi level (E_F) and the intrinsic Fermi level (E_i). By using equations 4.5 and the theoretical flat-band voltage obtained is -0.58 V. Then, using equation 4.3 we have determined that $Q_{ox} = 10^{11}$ cm^{-2}, which is the expected value for a standard fabrication process.

Moreover, we have carried out TCAD simulations to compare them with the experimental measurements. Figure 4.25 shows the C-V simulation of a MOS structure using different oxide charges. Flat-band voltage is determined in the graph in the same way as figure 4.23, by solving equation 4.1 to find flat-band capacitance. We found a value of -6.1 V, which is a similar value to the experimental measurement. Therefore, the oxide charge in the SiO_2 has to be into consideration since it plays an important role in the performance of the sensor.

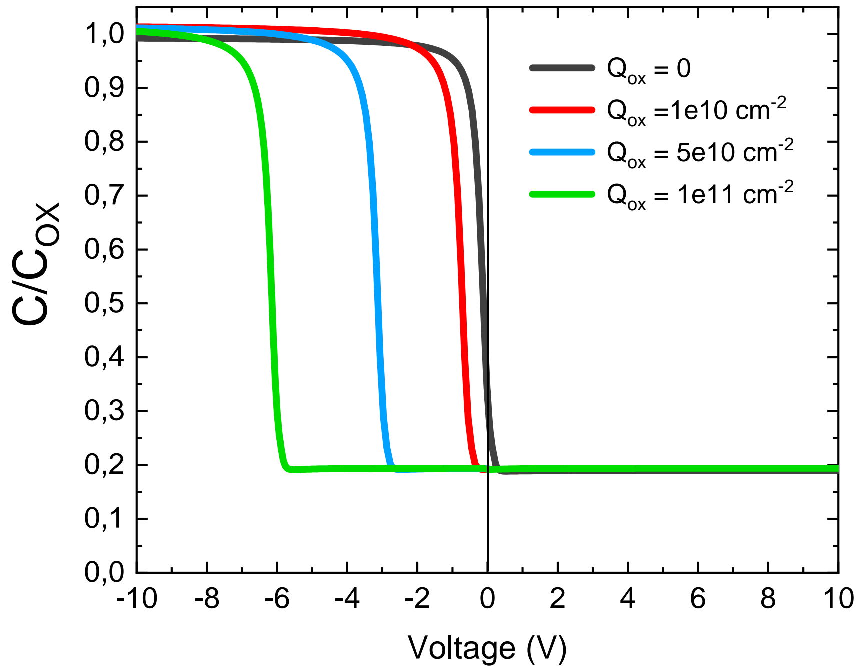

Figure 4.25: C-V simulation of a MOS capacitor at room temperature and 10 kHz.

4.5.2 Gain measurements

In order to obtain the gain of the produced sensors, we have carried out TCT measurements in a small-area iLGAD sensor (10x10 array). Figure 4.26 shows the collected

charge of the iLGAD and the PiN sensors and the gain of the LGAD, which is obtained by diving the iLGAD collected charge by the PiN charge. The expected gain is 3-4 at 200 V, which is three times lower than the measured. We obtained values from 12 to 24 at the operating voltage regime. From 360 V, auto-triggering appeared. This higher gain leads to a reduction in the breakdown voltage and an increase in leakage current and gain layer depletion. This result is in agreement with previous measurements since we expected a higher gain due to the higher V_{GL} and lower V_{BD}.

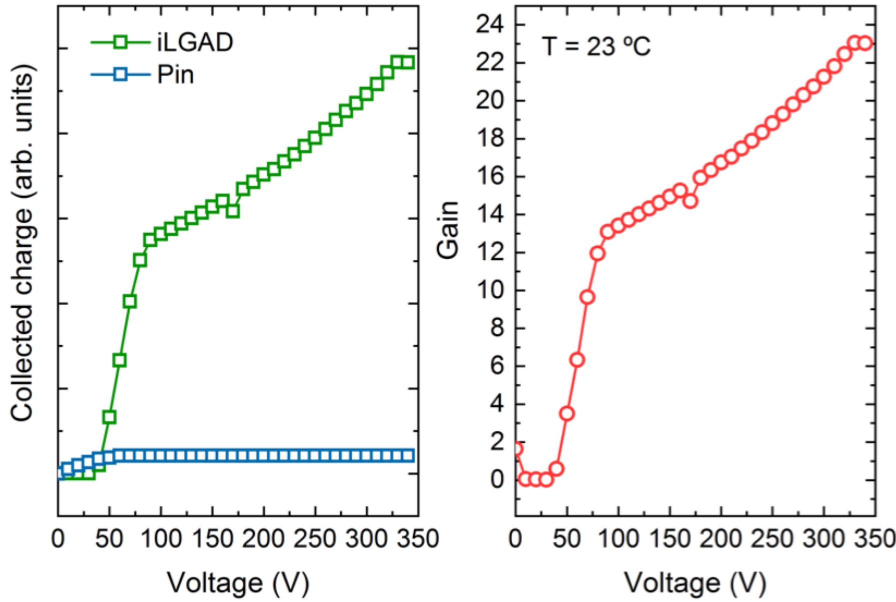

Figure 4.26: Left) Collected charge of the iLGAD sensor and the PiN diode. (Right) Gain of the iLGAD sensor at room temperature using the IR laser.

4.5.3 Irradiated measurements

The iLGAD sensors are proposed for X-Ray detection with an optimized periphery. In order to test this radiation-resistant periphery, we have irradiated a pixelated iLGAD with an active area of 1x1 mm^2 (10x10 array) from the iLG2. Furthermore, a strip iLGAD (8x8 mm^2) from the first iLGAD run (iLG1) has also been irradiated. Both samples are irradiated at a fluence of $\Phi = 10$ MRad with a dose rate of 1.8 MRad/h. Figure 4.27 shows the I-V measurements (current density) of both irradiated and unirradiated samples, done in identical conditions. The probes are contacting the multiplication region, while the segmentation is contacting the chuck of the probe station. In this sense, the collector ring of the iLGAD corresponding to the iLG2 is not acting, which entails a higher current density. Moreover, we had problems with contacting the pixels, as we can observe in the unirradiated measurements, where it is not contact up to 125 V. In the iLG2 sensor there is a slight increase of leakage current but the breakdown voltage remains the same. On the other hand, for the

iLG1 sensor, the breakdown voltage is reduced to 50 V, making it useless for X-Ray applications.

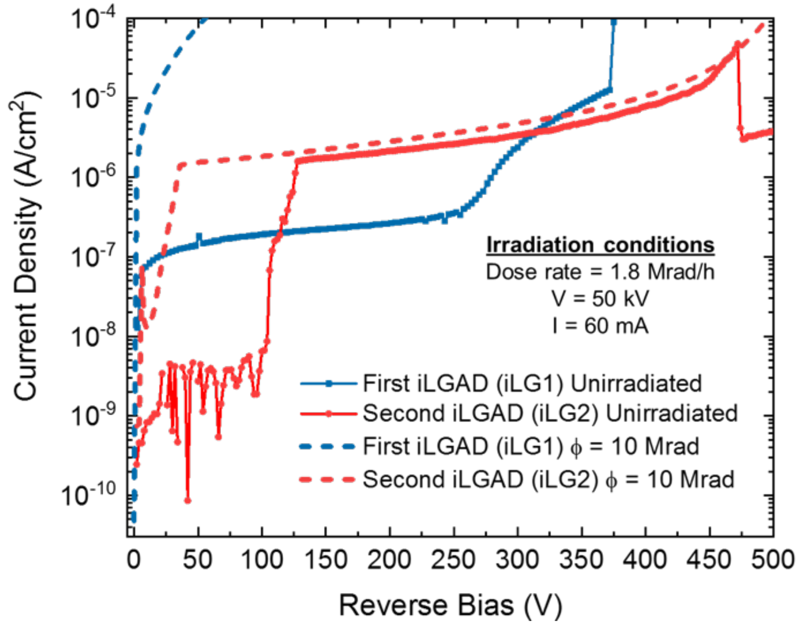

Figure 4.27: Current density of unirradiated and $\Phi = 10$ MRad irradiated iLGAD samples from the iLG1 and iLG2 runs. There

Therefore, the optimization of the periphery allows the iLGAD from iLG2 to withstand a higher breakdown voltage than the iLG1 ones. In this sense, the multi-ring design of the multiplication region and the omhic side of the sensor has played a crucial role in this measurement. Nevertheless, further measurements should be considered to irradiate these sensors using a higher fluence to determine its threshold in terms of applicability.

4.6 Summary and conclusions

We have developed an iLGAD sensor for X-Ray applications. First, we have described the main advantage over the LGAD technology, which is the 100 % fill factor. In order to use this structure for X-Ray detection, we have designed a suitable periphery by means of TCAD tools. We have shown the limitations of the first generation against X-Ray irradiations and then the periphery has been modified to achieve a higher operability voltage. We have described the importance to optimize the ohmic side of the sensor, which was not investigated in the first generation since there are high electric field peaks at the curvature of the p^+ diffusions.

The sensors have been fabricated in the IMB-CNM clean room and have been electrically characterized. Pad-like iLGADs show a lower breakdown voltage and a higher leakage current than expected and we attribute this performance to the gain. We obtained a gain between 12-24, which is slightly higher than the obtained by simulation. C-V measurements have been performed to obtain the V_{GL} and V_{FD} of the sensor, in

order to know the operability range. The main characteristics of each structure are depicted in table 4.5. Small-area (pad and pixelated) iLGADs show a good electrical performance, as well as small-area PiN diodes. For the big-area structures, the PiN diodes have an excellent performance, while the iLGADs exhibit a low breakdown voltage. We attribute this to the formation of the gain layer, although no clear statements are considered. In addition, C-V measurements have been carried out in MOS capacitors to extract the oxide charge of a non-irradiated sensor, which results are expected.

Structure	$\mathbf{V_{VBD}}$	$\mathbf{V_{FD}}$	$\mathbf{V_{GL}}$	$\mathbf{I_{leak}}$ **(@20 ºC)**	**Gain**	**Operating Range**
Small-area iLGAD	350-450 V	70 V	38 V	10 nA	12-24	300-350 V
Big-area iLGAD	<20 V	-	-	0.1-1 mA	12-24	-
Small-area PiN	>600 V	3 V	-	1-5 nA	-	>600 V
Big-area PiN	>200 V	3 V	-	1-10 µA	-	>200 V

Table 4.5: Electrical characteristics of the different produced structures in the iLG2 generation.

Finally, we have carried out an irradiation measurement in the produced sensors in order to test the new periphery design. We have compared the I-V behavior of the sensor with the first iLGAD generation. The optimized design is able to withstand the same voltage before and after irradiation, while the sensor corresponding to the first iLGAD generation cannot be used more than the V_{FD}, making it unusable for X-Ray applications.

Chapter 5

Trench iLGAD for 4D Tracking Applications

In this chapter, the use of thin iLGAD sensors for 4D tracking applications is presented, taking benefit of their 100% fill factor and the better performance of thin sensors for timing applications. A novel periphery design using vertical trenches is also illustrated, as well as the optimization of the sensor by means of TCAD simulations. Moreover, the first fabrication proposal for these sensors is reported.

5.1 Introduction

New LGAD structures designed to overcome the main LGAD challenges are described and optimized in previous chapters, including the iLGAD to enhance the fill factor problem. The basic iLGAD structure is achieved by segmenting the p^+ electrode allowing an unsegmented n^+/p junction, where the multiplication takes place. As a consequence, holes are multiplied and collected at the pixelated electrodes. The second iLGAD generation (iLG2), designed to be used in X-Ray applications, includes a specific peripheral region and a substrate thickness in the range of 300 µm.

As aforementioned in previous chapters, the 4D tracking paradigm requires both high tracking precision and low time resolution. The tracking resolution is achieved with the basic iLGAD design with a 100% fill factor and a pixelated design at the p^+ electrodes, as detailed in chapter 4. Time resolution is directly related to the sensor thickness and, therefore, the iLGAD time resolution can only be reduced by shrinking the amount of depleted substrate. Figure 5.1 shows simulated transient current curves of 50 and 285 µm thick iLGADs at an operating voltage of 300 V. A MIP particle is forced to pass through both detectors to determine the corresponding particle detection time. At a given voltage, the electric field of the thinner detector is increased, helping to reach the hole drift velocity saturation. Assuming similar saturation velocity for holes and electrons (high electric field) [10], the time resolution performance of thin iLGADs is comparable with that of the previously fabricated thin LGADs. However, pixelated LGADs do not provide the desired 100% fill factor, and, for this reason, thin iLGADs fulfill the essential requirements to build 4D tracking detectors.

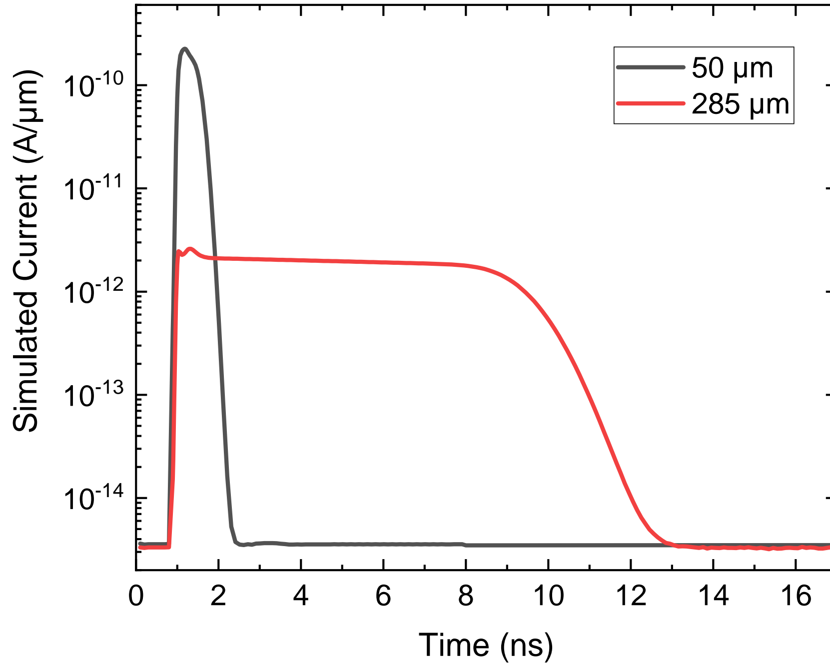

Figure 5.1: Simulated I-t curve for 50 and 285 m thick iLGADs at 300 V, obtained from a MIP simulation

An improved third iLGAD generation (iLG3) has been proposed at IMB-CNM based on trench technology: the Trench iLGAD [46]. The iLG3 includes a novel periphery design to assure the proper performance of the sensor and to reduce the complexity of the process technology and the number of fabrication steps. The following sections are devoted to describing the Trench iLGAD concept, including the optimization of the periphery, a full description of the mask set, and the process technology for the fabrication of Trench iLGADs at the IMB-CNM clean room.

5.2 Trench iLGAD design

5.2.1 Concept and structure design

The cross-section of the Trench iLGAD sensor is shown in Figure 5.2 with the proposed novel periphery design. The standard diffusions implemented in previous LGAD structures are superseded by 8 µm wide trenches, which are used to properly isolate the active area of the sensor. The trenches are filled with oxide and non-doped polysilicon, and the outermost trench is thought to protect the edge of the sensor after the dicing process. The trenches must be deep enough to reach the handle wafer to avoid an electrical connection between the active detection volume and the detector edge, where undesired leakage currents can be created. The multiplication layer is placed over an N-type low resistivity handle wafer ($\sim$ 300 µm), creating the desired unsegmented n^+/p junction, and the p-type multiplication layer can be obtained either by implantation and diffusion or epitaxial growth. On top of the multiplication layer, a high-resistivity p-type substrate (50 µm thick) is used to

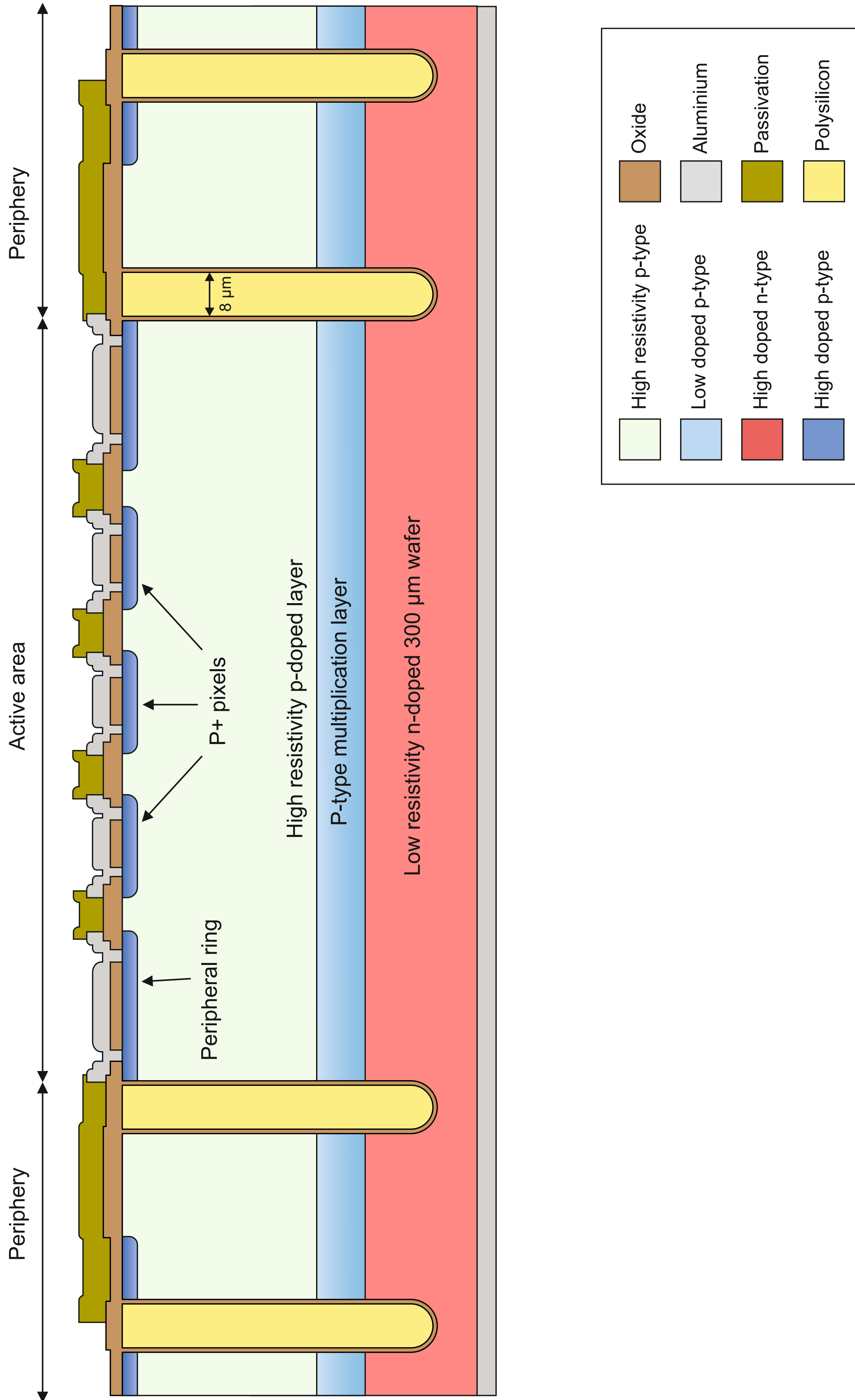

Figure 5.2: Cross-section of the Trench iLGAD sensor.

sustain the operating reverse voltage. Finally, the p^+ electrodes are implanted at the top of the sensor. A peripheral p-type ring is diffused at the edge of the active area to collect possible injected currents generated at the periphery of the sensor. In contrast with previous LGADs, there is no need to save space in the periphery to assure a good electrical performance, leading to an intrinsic slim-edge design. Moreover, in the iLG3 generation only the ohmic side of the sensor requires photolithography steps to create the Trench iLGAD and the first photolithographic steps, used to create the p-stop and JTE diffusions in previous LGAD designs, are skipped.

5.2.2 Periphery optimization

Although the periphery of the Trench iLGAD is more simple than all the previous designs, an optimization of the trenches has to be done, considering that trenches are created using the 3D detectors technology of the IMB-CNM clean room [96] where a Deep Reactive Ion Etching (DRIE) process is used to create trenches with a width of 8-10 µm. TCAD simulations of the Trench iLGAD have been carried out, varying the main parameters of the trenches.

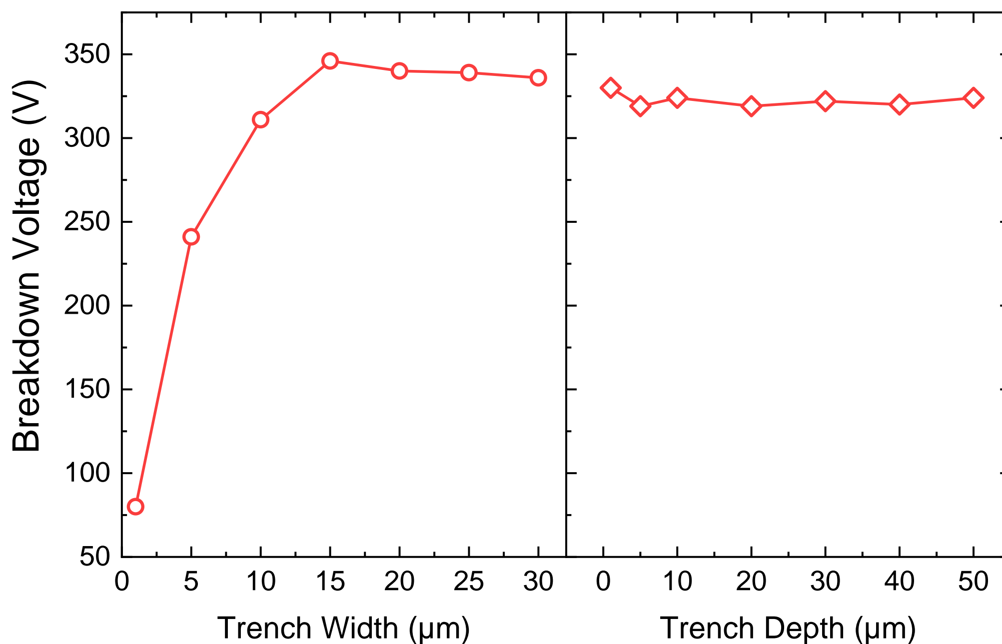

Figure 5.3: Simulated breakdown voltage as a function of the trench width and depth.

Figure 5.3 shows the simulated breakdown voltage as a function of the trench design. The voltage capability increases with the trench width until saturation is reached at a trench width of 15 µm. For 8-10 µm wide trenches, the breakdown voltage reaches a $\sim$ 85% of the maximum voltage capability, high enough for the Trench iLGAD sensor. The trench depth is also critical for the Trench iLGAD performance, but in any case, the trench has to reach the n-type handle wafer (in the range of 60 µm), in order to isolate completely the active area and to avoid the main junction to extend until the edge of the detector chip (floating p-n junctions at the dicing path are not

allowed due to reliability issues). TCAD simulations varying the trench depth have been carried out with a constant trench width of 10 µm, showing no dependence of the voltage capability on the trench depth. The last relevant design issue related to the peripheral ring, as plotted on the Trench iLGAD structure in figure 5.2, is the p-type peripheral ring in contact with the trenches to avoid having an electric field peak at the edge of the diffusion. Figure 5.4 shows the simulated breakdown voltage as a function of the distance between the trench and the peripheral ring, being zero the ideal distance, which is the value implemented in the proposed design. As expected, if the peripheral ring is not in touch with the trench, more than 100 V is lost in terms of breakdown voltage.

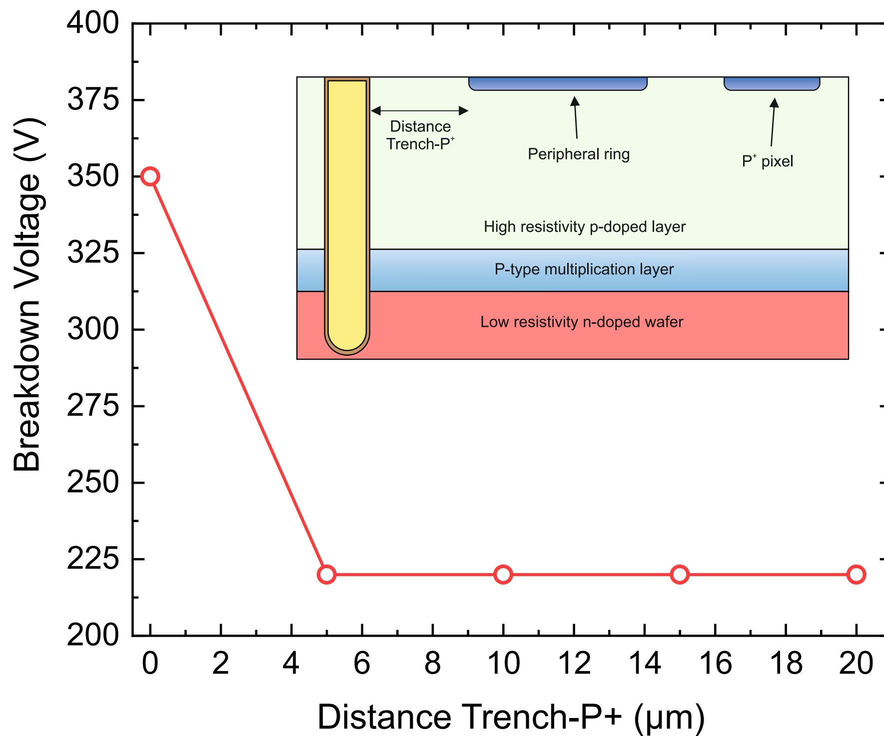

Figure 5.4: Simulated breakdown voltage as a function of the distance between the trench and the peripheral ring

Figure 5.5 shows the electrostatic potential and the absolute electric field for structures with no distance and with 10 µm between the trench and the peripheral ring. As observed in (a), the active area is properly isolated while in (b) there is a voltage gradient between the peripheral ring and the trench. This voltage gradient may cause an electric field peak at the edge of the peripheral ring due to punch-through. In the design with no space between the peripheral ring and the trench, the voltage gradient is confined to the trench. The highest electric field in (c) is located inside the trench and the oxide, therefore the sensor is able to sustain higher reverse voltage. On the contrary, in (d), a high electric field appears at the edge of the peripheral ring. Therefore, we consider using the option with no distance between the trench and the peripheral ring.

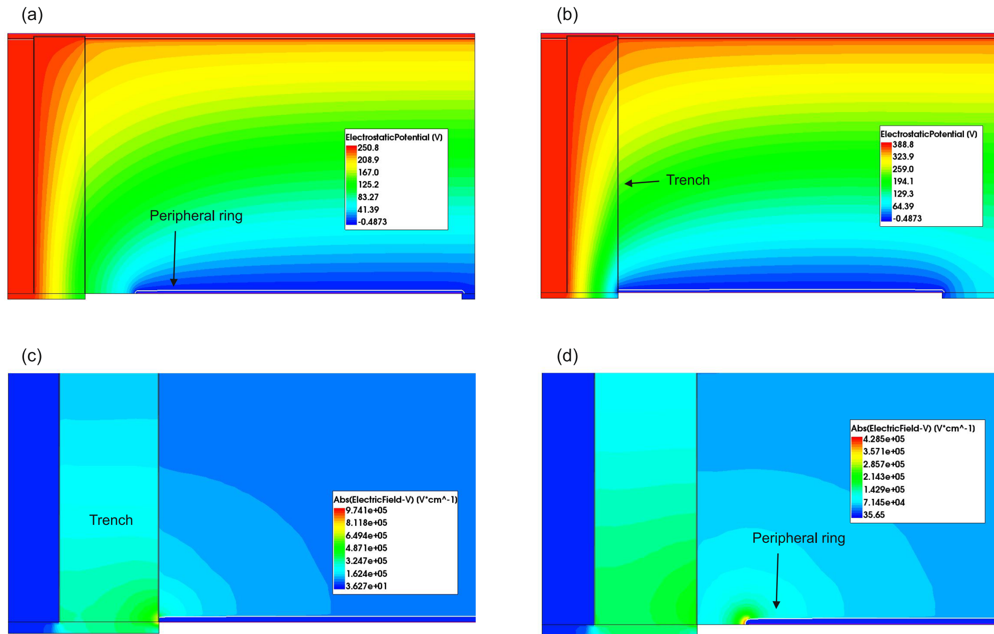

Figure 5.5: Simulated voltage and electric field distribution at the breakdown as a function of the distance between the trench and the peripheral ring. (a) Voltage distribution with 10 µm distance, (b) Voltage distribution without distance, (c) Electric field distribution without distance, and (d) Electric field distribution with a 10 µm distance.

5.3 Fabrication of the third iLGAD generation

In this section, the process technology for the fabrication of the first Trench iLGAD prototypes, corresponding to the third iLGAD generation (iLG3) is described.

5.3.1 Type of wafer selection

The first challenge of the iLG3 design is the formation of the n^+/p junction. In previous thin LGAD designs, the high-resistivity substrate was in contact with the low-resistivity handle wafer, which acts as p^+ electrode, and dopant diffusion from the highly doped handle wafer towards the extremely low doped active substrate has been observed during high-temperature process steps due to the high doping gradient. In the iLG3 design, the handle wafer acts as a n^+ electrode, and the p-type multiplication layer must be in contact with the handle wafer. This can be achieved with two different technological approaches: using Si-Si bonded wafers, in a similar way to thin LGAD fabrication or growing two epitaxial layers on top of the handle wafer, one for the multiplication layer and the other as the active substrate.

Trench iLGAD in Si-Si wafers

The desired Si-Si wafers suitable for the development of trench iLGADs are obtained by performing the following processes. First, the multiplication layer is implanted at

the IMB-CNM through a thin screen oxide, to avoid excessive surface damage, in a high-resistivity p-type 285 µm wafer. Then, wafers are sent to IceMOS to perform the Si-Si bonding process with a low-resistivity n-type wafer. After the bonding process, p-type wafers, which are the active substrate, are thinned down to 50 µm and sent back to IMB-CNM to start the fabrication process. As in any LGAD-based detector, the boron implantation parameters of the multiplication layer have to be optimized in the iLG3 structure. If the standard LGAD values for the energy and dose of the multiplication layer are selected, the gain will not be the expected, since the Si-Si bonding process includes a thermal annealing of 60 minutes at 1200 ºC which enhances the Boron diffusion. Figure 5.6 shows the simulated profiles using different technological parameters, listed in table 5.1, and a sketch of the process to obtain the Si-Si wafers. The technological parameters have been studied to obtain a similar profile after the multiplication, as in the standard LGAD, which provides the expected gain and breakdown voltage values.

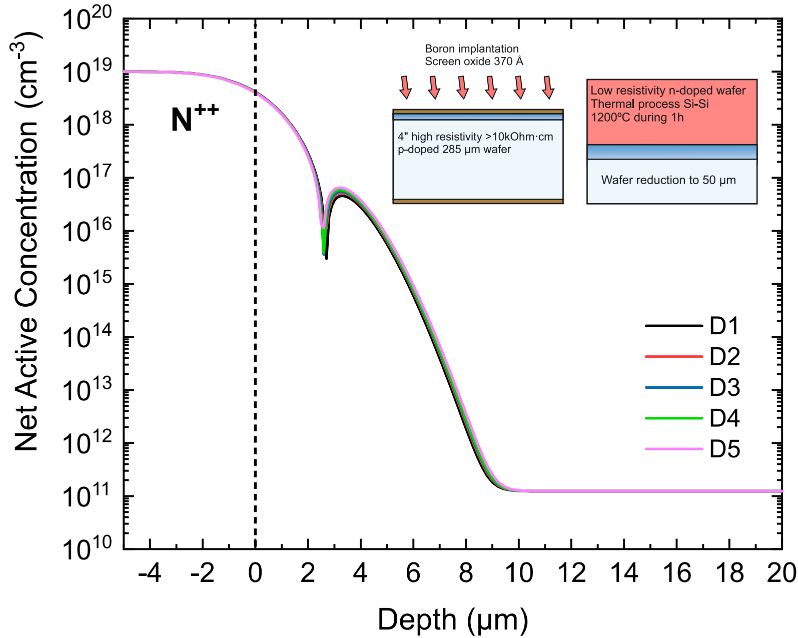

Figure 5.6: Simulated net doping profiles after the Si-Si bonding process for the Trench iLGAD.

Wafer	Energy (keV)	Boron dose (at/cm^2)	Comments
1-5	150	$3.7 \cdot 10^{14}$	D1
6-10	150	$3.9 \cdot 10^{14}$	D2
11-15	150	$4.0 \cdot 10^{14}$	D3
16-20	150	$4.1 \cdot 10^{14}$	D4
21-15	150	$4.3 \cdot 10^{14}$	D5
26-30	-	-	PiN

Table 5.1: Boron parameters for the multiplication layer of Si-Si wafers for the iLG3.

Trench iLGAD in epitaxial wafers

As already stated, Trench iLGADs can be fabricated on epitaxial wafers. First, an epitaxial p-type multiplication layer is grown on top of the n-type handle wafer and a subsequent high-resistivity p-type layer, is also grown over the multiplication, creating the desired $n^+/p/p^+$ junction. The epitaxial wafers provide better control of the gain layer, due to the inherent better knowledge of the real amount of charge introduced during the epitaxial growth. Nevertheless, it is important to assure that the resistivity of the gain layer will not degrade the desired performance.

Table 5.2 shows the main parameters of the three layers of the iLG3 structure. The multiplication layer has a thickness of 3 µm with a resistivity in the range of 0.39-0.53 $\Omega \cdot$ cm. In order to determine if these parameters are suitable for the iLG3 fabrication, 1D technological simulations have been performed.

Parameter	Handle Wafer	Multiplication Layer	Substrate
Conductivity Type	n-type	p-type	p-type
Dopant	As	B	B
Thickness (µm)	460 ± 20	**3 ± 0.3**	50 ± 5
Resistivity ($\Omega \cdot$ cm)	0.0015 - 0.005	**0.39 - 0.53**	-

Table 5.2: Parameters for the handle wafer, multiplication layer, and active substrate in the epitaxial Trench iLGAD.

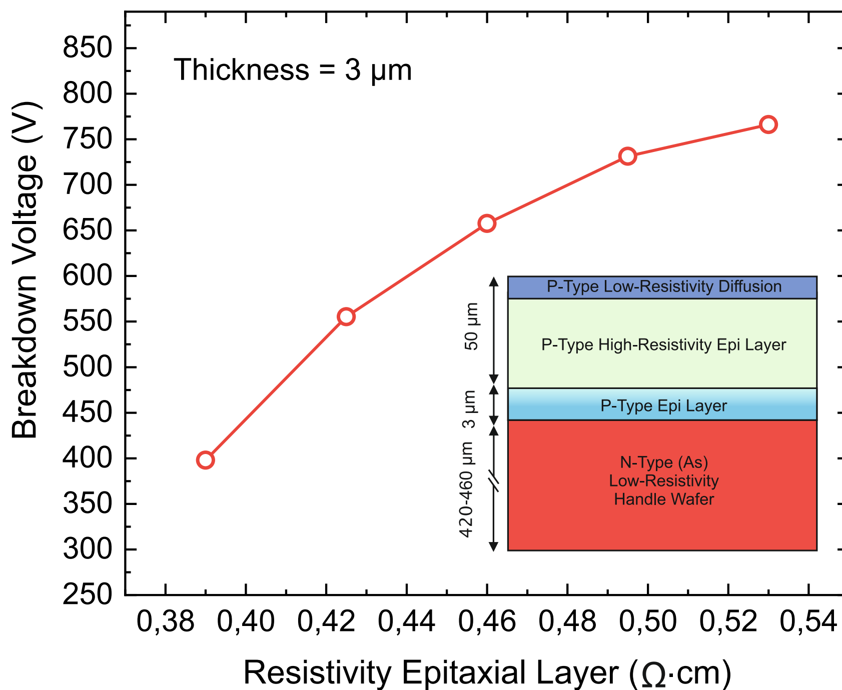

Figure 5.7: Breakdown voltage as a function of the resistivity of the epitaxial gain layer in Trench iLGAD.

Figure 5.7 shows the breakdown voltage as a function of the resistivity of the gain layer, using the parameters listed in table 5.2, and also the cross-section of the epitaxial Trench iLGAD. It can be inferred that there is a huge difference in terms of breakdown voltage depending on the selected resistivity. Nevertheless, the device will be operative in the entire resistivity range. As expected, the higher the resistivity, the higher the breakdown voltage, with the subsequent gain degradation. However, the lower gain in the high-resistivity regime can be compensated by applying a higher reverse voltage in the detector.

5.3.2 Fabrication process

Once the initial wafer type is selected, the complete iLG3 process technology can be set up, detailed in figure 5.9, considering that the multiplication region is already created, saving three photolithographic steps in comparison with the standard thin LGAD technology.

The first step is the field oxide growth with a thickness less than the standard 8000 Å since the multiplication layer does not have to be diffused at high temperatures. Therefore, a screen oxide of 190 Å is grown at a low temperature (900 ºC) to protect the silicon surface during the implantation and drive-in of the p^+ electrodes. Then, trenches are formed with a DRIE process with a depth determined by the time consumed during the DRIE process. Figure 5.8 shows the dependence of the trench depth with the DRIE duration. Assuming that the trench depth is in the range of 60 µm, a minimum of 30 min DRIE etch is needed to be sure that the trench reaches the handle wafer (the final time value will be fixed from trials on test wafers). After the DRIE process, a 1-µm oxide is grown at 950 ºC and the trenches are filled with polysilicon. Finally, the contacts are metalized with 1.5 µm thick aluminum and the sensor is passivated on the ohmic side with 4000 Å oxide + 7000 Å nitride.

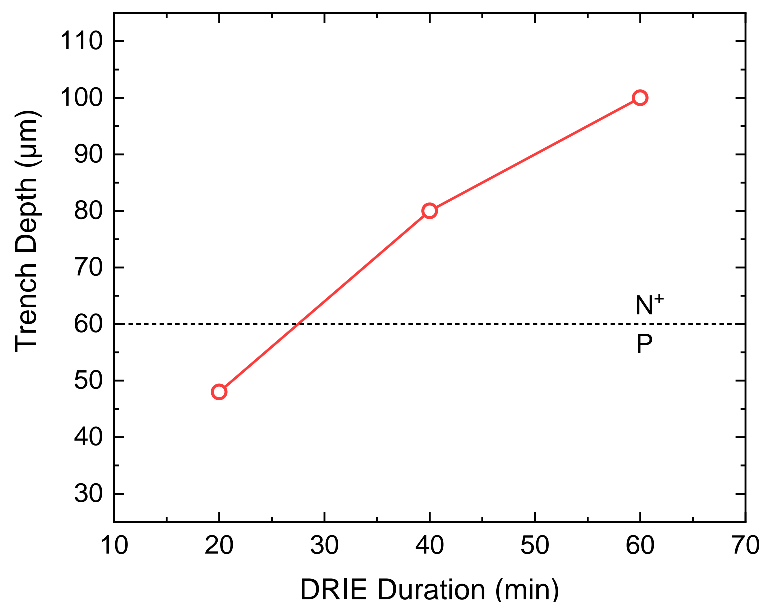

Figure 5.8: Trench depth as a function of DRIE process duration.

5.4 Photolithographic mask designs

A specific mask set for the Trench iLGAD sensor has been designed, named CNM1086. Figure 5.12 shows a cross-section of the main photolithographic levels in the ohmic side of the sensor and table 5.3 resumes the photolithographic levels of the mask, their description, and the alignment sequence. Figure 5.12 shows the complete CNM1086 mask layout, where different designs are included to have different area detectors in order to study the homogeneity of the gain layer and its influence on the electrical performance of the devices. In addition, different pixelated devices are designed, varying the pitch and the number of pixels, summarized in Table 5.4. Moreover, pad detectors are included to facilitate the measurements and the study of the periphery design, small pixelated detectors (3x3 arrays) are included to study the performance of the Trench iLGAD without using big-area sensors and, finally, MOS capacitors are included to test technological parameters.

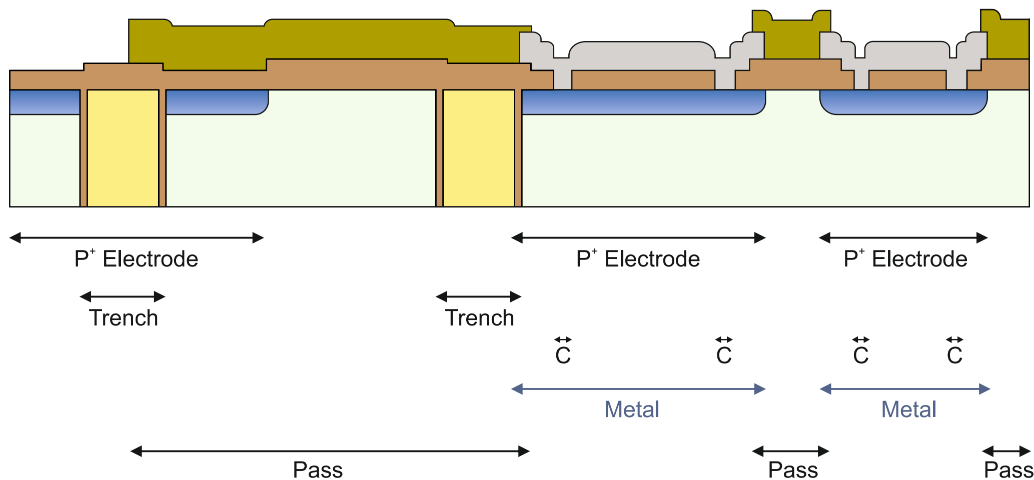

Figure 5.10: Cross-section of the ohmic side of the CNM1086 mask.

Mask level	Level description	Alignment
P^+ Electrode	P^+ Pixels	Flat
Trench	Trenches	P^+ Electrode
C	Contacts	Trench
Metal	Metallization	Trench
Pass	Passivation	Metal

Table 5.3: Ohmic side mask level description of the CNM1086 mask set

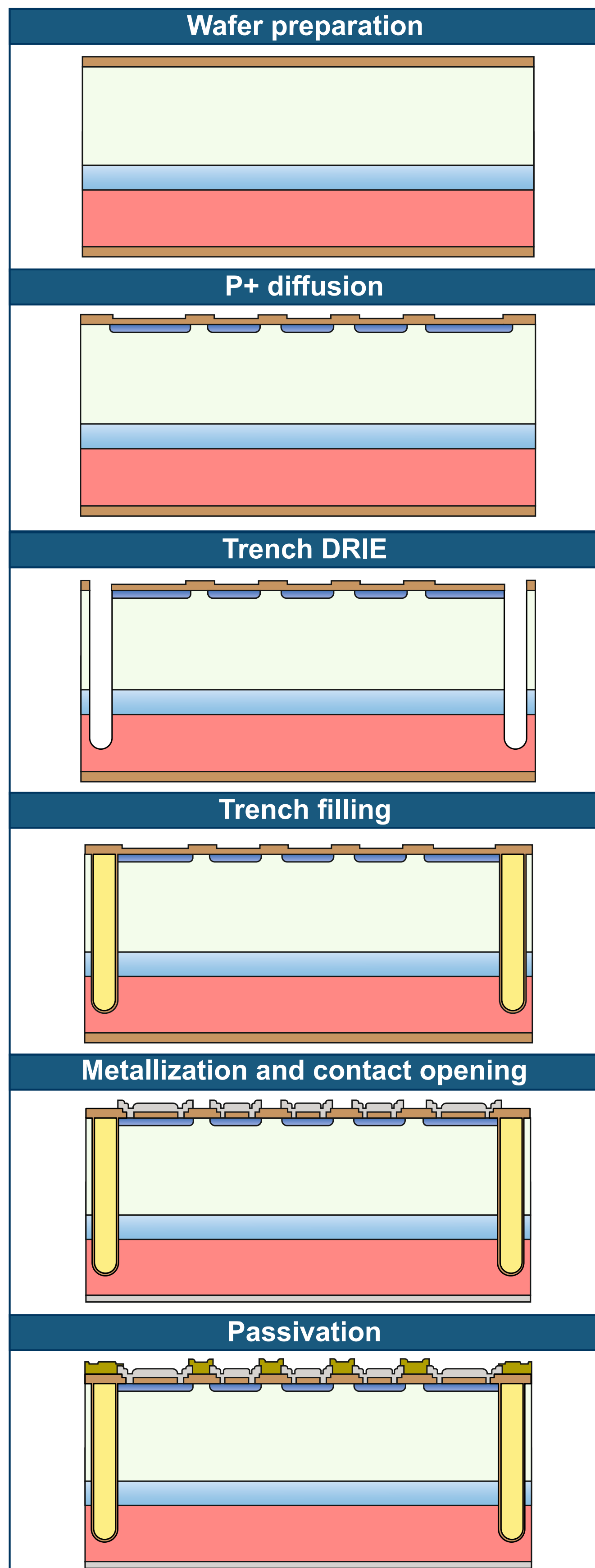

Figure 5.9: Fabrication steps in the Trench iLGAD (iLG3).

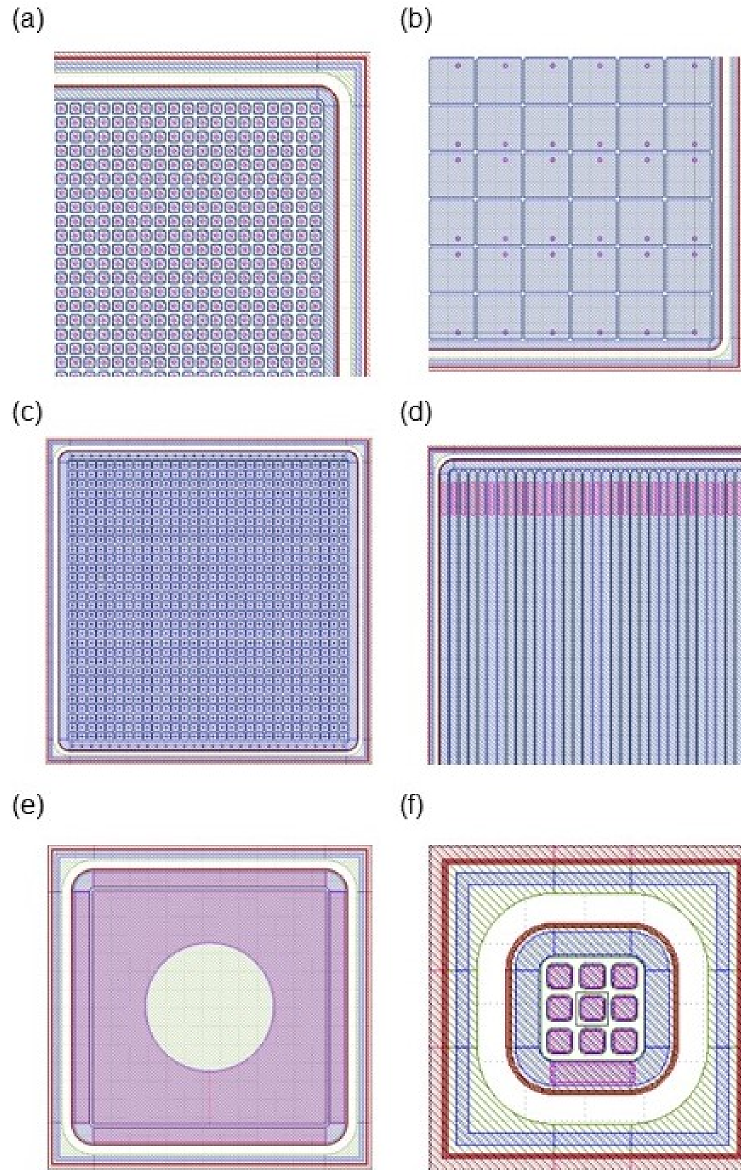

Figure 5.11: Design of the different structures included in the CNM1086 mask set: (a) Timepix3, (b) TDCPix, (c) UZH-PSI, (d) iStrip, (e) Pad Trench LGAD and (f) 3x3 Trench iLGAD.

Sensor	Pitch (µm)	Pixels/Strips
Timepix3	55x55	256x256
TDCPix	300x300	44x45
UZH-PSI	100x100	30x30
iStrip	100x100	75

Table 5.4: Design parameters of the different pixelated structures included in the CNM1086 mask set.

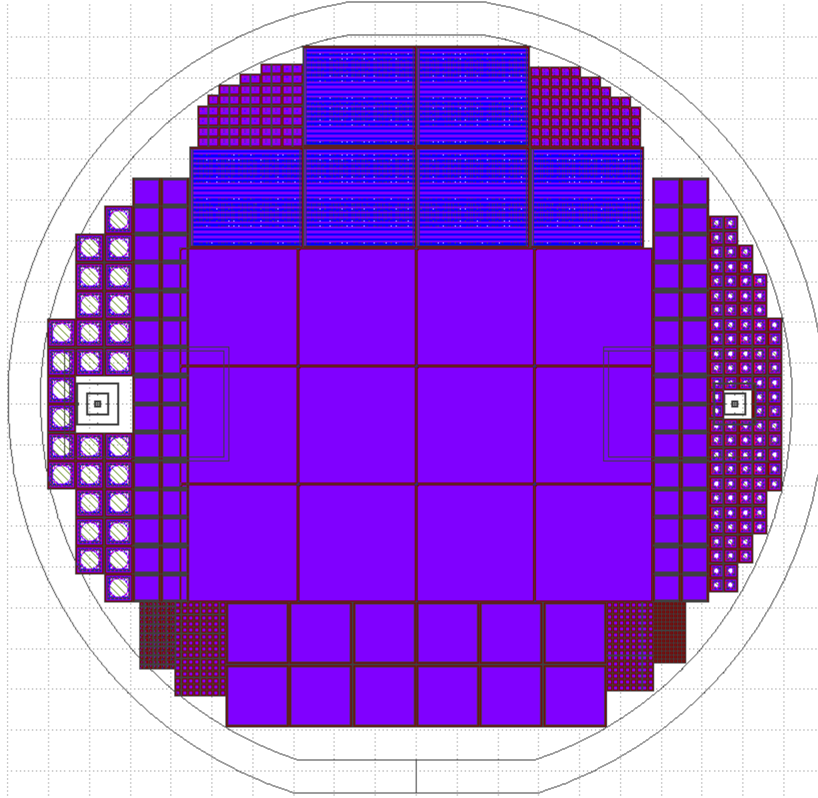

Figure 5.12: Full view of the CNM1086 mask set.

5.5 Conclusions and future work

In this chapter, a new thin iLGAD sensor for 4D tracking applications is analyzed, based on trench technology to isolate the active area of the sensor and to reduce the periphery length. A 50-µm iLGAD provides the desired time resolution and track precision and the trench technology provides several advantages over the standard planar iLGAD structure, after an accurate optimization of the periphery.

Two different wafer types can be used for the fabrication of the Trench iLGAD, based on Si-Si and epitaxial technologies. Both wafer types have been optimized to reach the desired performance in terms of breakdown voltage and gain. The process technology, including the optimization of the trenches to reach the expected depth, has been set up. Finally, the mask set has been designed with different sensor patterns, including pixelated, pad, and technological test structures.

At the time of closing the Ph.D., the fabrication of the Trench iLGAD is ongoing. Once the fabrication is completed, the wafers will be exhaustively characterized, including a detailed study on the gain layer homogeneity, as well as on the most relevant electrical parameters. TCT measurements are also planned to optimize the trade-off between gain and breakdown voltage and a comparison of detection performances in each wafer technology is also intended. Finally, the best-performing detectors will be sent to an irradiation campaign to study the radiation resistance.

Chapter 6

Development of LGAD sensors in n-type substrates

The description of the first n-type LGAD sensor is presented in this chapter, including the optimization for n-type substrates, the fabrication, and the first electrical testings. In addition, this sensor will act as the baseline for a new n-type sensor used to detect low-energy particles.

6.1 Introduction

The development of LGAD sensors at IMB-CNM has been produced using high-resistivity p-type substrates. As aforementioned, detectors must work in full depletion to be able to collect the electron-hole pairs created, thus, high-resistivity substrates are useful to reach low full depletion voltage values. Chapter 1 has described the radiation effects on silicon detectors like the substrate inversion mechanism in n-type substrates for HEP applications, which is the reason why we have based the development of LGADs in p-type substrates. Nevertheless, for X-Ray applications, we expect only surface damage using n-type substrates.

However, the development of LGADs using n-type substrates is mainly devoted to their use to detect low-energy particles. The nLGAD, which is based on the standard p-type LGAD, has been developed and produced by IMB-CNM to improve the efficiency of standard LGADs when detecting low-energy particles [97, 98]. In this chapter, we present the first approximation of developing the nLGAD detector, produced using an existing mask set of previous LGAD fabrications. Furthermore, the optimization, fabrication, and the first characterizations are described.

In addition, we report the Proton Low Gain Avalanche Detector (pLGAD), which is a novel structure to detect low-energy particles, based on the nLGAD design. Here, the multiplication region is modified by adding an extra p-type diffusion and using a shallow p^+ diffusion to enhance the collection of low-energy particles such as 15 keV protons [99].

6.2 The nLGAD detector

The nLGAD sensor is based on the standard LGAD technology. In this case, as we are going to use n-type substrates, there is an inversion of dopants in all layers, including substrate, multiplication, and electrodes. Figure 6.1 (top) shows a cross-section of the nLGAD sensor. In this case, the electric field peak is located at the p^+/n junction.

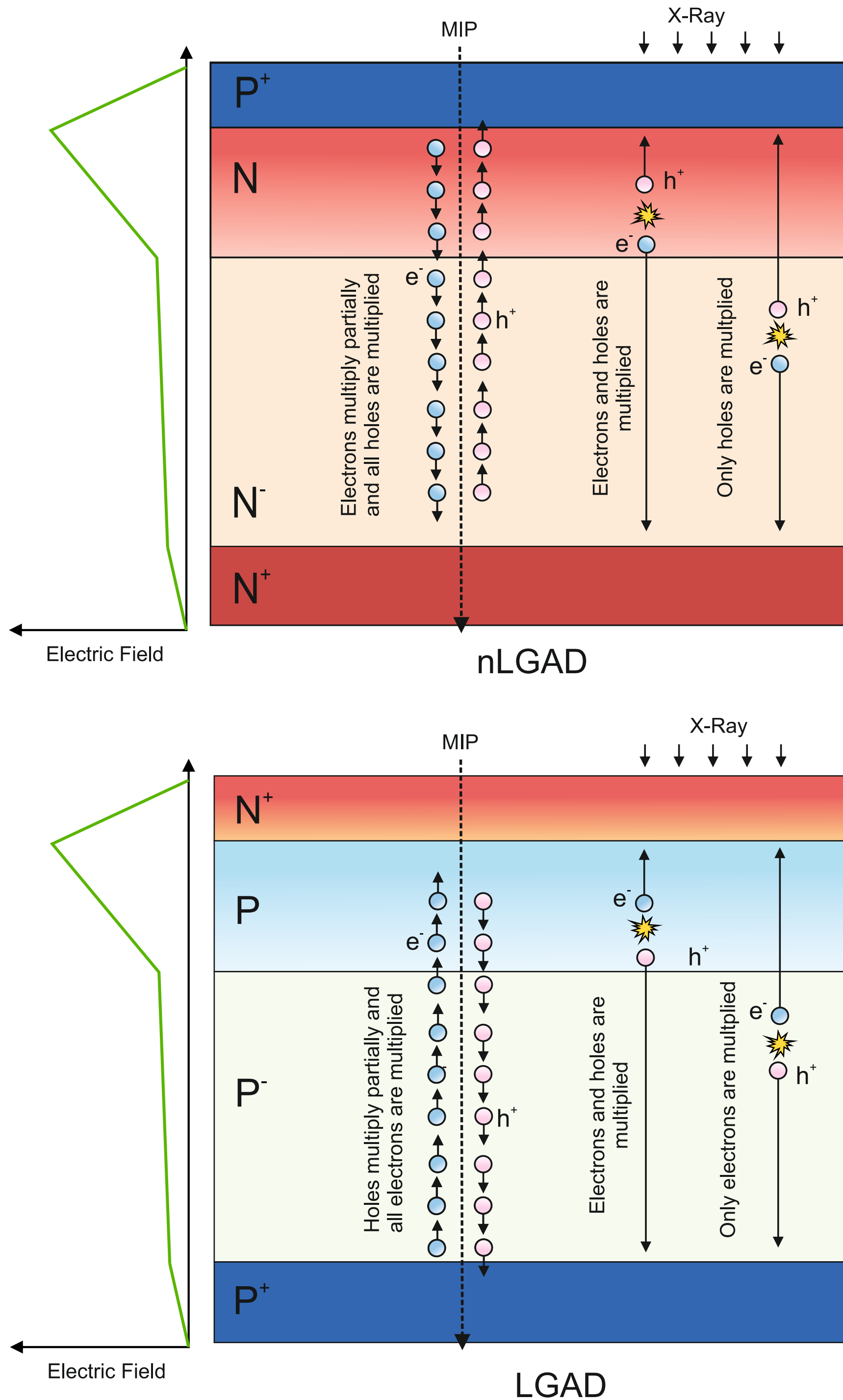

Figure 6.1: Different charge deposition scenarios using p-type and n-type substrate LGADs.

This design is going to be the baseline for future developments of LGADs using n-type substrates, which are focused on the detection of low-energy particles. In this sense, is crucial to understand the differences between using p-type or n-type LGADs in the detection of charged or low-energy particles. Figure 6.1 shows a schematic view of different scenarios using the standard p-type LGAD or the nLGAD when detecting charged particles or X-Rays with different energy.

A MIP going through a detector is the standard scenario described in previous chapters, where a charged particle creates electron-hole pairs in the entire volume of the sensor. In the standard p-type LGAD, most of the electrons collected by the n^+ go through the high electric field region leading to a multiplication of the signal. Due to avalanche multiplication, some holes will be also multiplied. On the other hand, detecting charged particles in the nLGAD leads to a low gain since the multiplication is mainly led by holes. Therefore, the gain will be higher in standard LGADs when detecting charged particles.

The absorption length of X-Rays depends on the incident energy (see figure 1.6), hence low-energy X-Rays deposit all the charge in the first microns of silicon. In standard LGADs, the electrons are promptly collected by the n^+ electrode, and the multiplication mechanism is mainly led by holes going through the electric field region. Therefore, since the impact ionization coefficient of electrons is higher than holes [100], the gain of standard p-type LGADs when detecting low-energy particles will be low. In the case of the nLGAD, electrons created by the low-energy particle go through the electric field region since they are collected by the n^+ diffusion, leading to a higher gain than the obtained with standard p-type LGADs. Therefore, the nLGAD detector is more suitable when detecting low-energy particles.

The last case of study is the detection of medium-energy X-Rays, where the charge is deposited in the active substrate. Here, in standard LGADs only electrons are multiplied since holes are directly collected by the p^+ diffusion. On the contrary, in nLGADs only holes are multiplied, leading to a lower gain rather than in standard LGADs. In this situation, the use of p-type LGADs turns out to be more optimal.

6.2.1 Optimization and design of the nLGAD detector

Since the nLGAD is based on the LGAD structure, there is no substantial difference in relation to detector design. Nevertheless, due to the different diffusion processes in B and P, the technological parameters of the main diffusions must be optimized to reach the desired performance. Therefore, TCAD simulations have been carried out to assure the desired characteristics. Since it is the first prototype, the expected performance is a good V_{BD}-Gain trade-off. Here, we are not assuming harsh irradiation conditions. We have tuned the technological parameters using the same thermal processes as in a standard LGAD. Figure 6.2 shows the simulated profile for an nLGAD detector using a low dose. We found a similar structure as in standard LGAD sensors, with slight differences in the thickness of the layers. This structure has been

electrically simulated, as depicted in figure 6.3. Here, we can observe the simulated C-V and I-V measurements. It is clear that the multiplication layer is fully depleted at $\sim$ 30 V and the sensor has a low leakage current of up to 1 kV. Therefore, we expect to have a high operating regime.

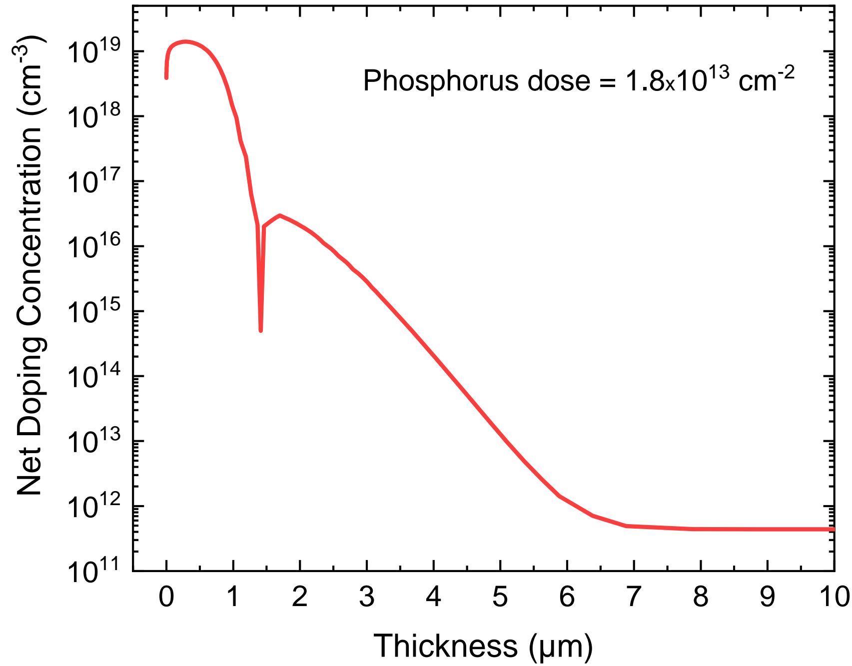

Figure 6.2: nLGAD simulated doping profile using a low dose.

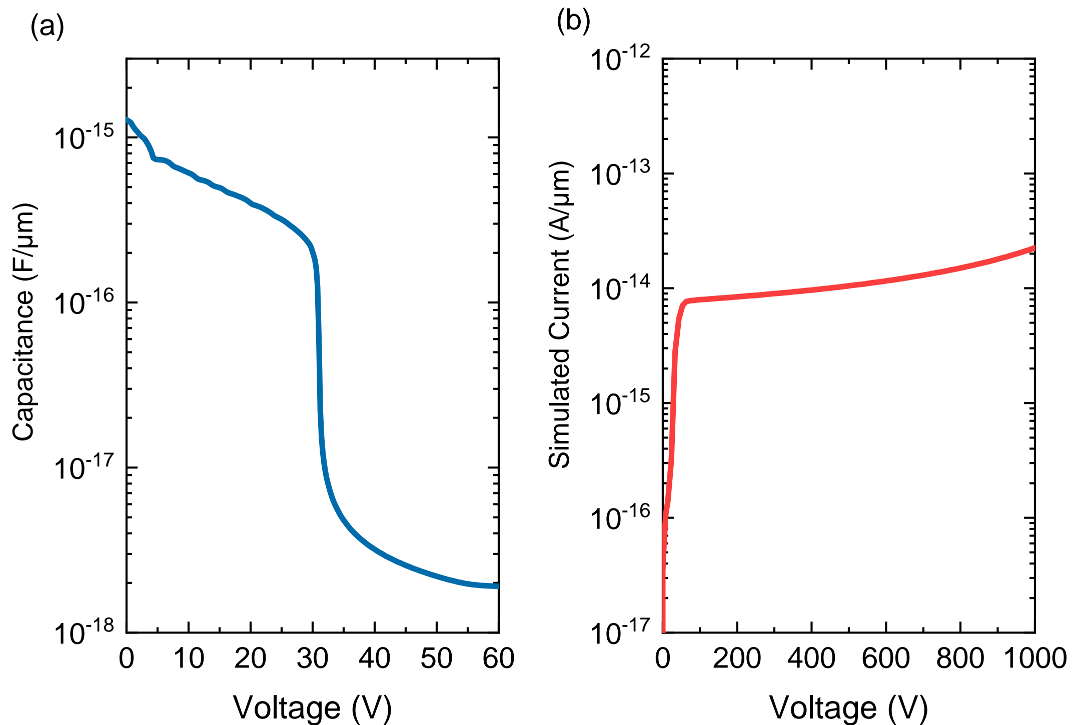

Figure 6.3: (a) C-V and (b) I-V 1D simulations of the nLGAD structure using a low dose.

We have been able to design an nLGAD sensor with a low leakage current and a high breakdown voltage. Moreover, we performed gain simulations to study the gain of the detectors and their trade-off with breakdown voltage. The sensor is illuminated with an infrared laser at 200 V. Figure 6.4 shows the V_{BD}-Gain trade-off at room temperature, setting the gain at 200 V, as a function of the n-type multiplication layer dose. As it can be observed, there is a huge decrease in terms of breakdown voltage (> 1 kV) with a slight increase in the dose ($\sim 5\%$). As expected, the gain is higher as we increase the multiplication layer dose, and it can be increased by applying higher voltages.

It is clear that there is less room to fabricate nLGAD detectors in comparison with p-type LGADs. Therefore, the uniformity of the gain layer must be controlled with even higher precision. Moreover, as already mentioned in previous chapters, some solutions like a deeper implant can be envisaged to overcome this issue in future developments of nLGAD detectors.

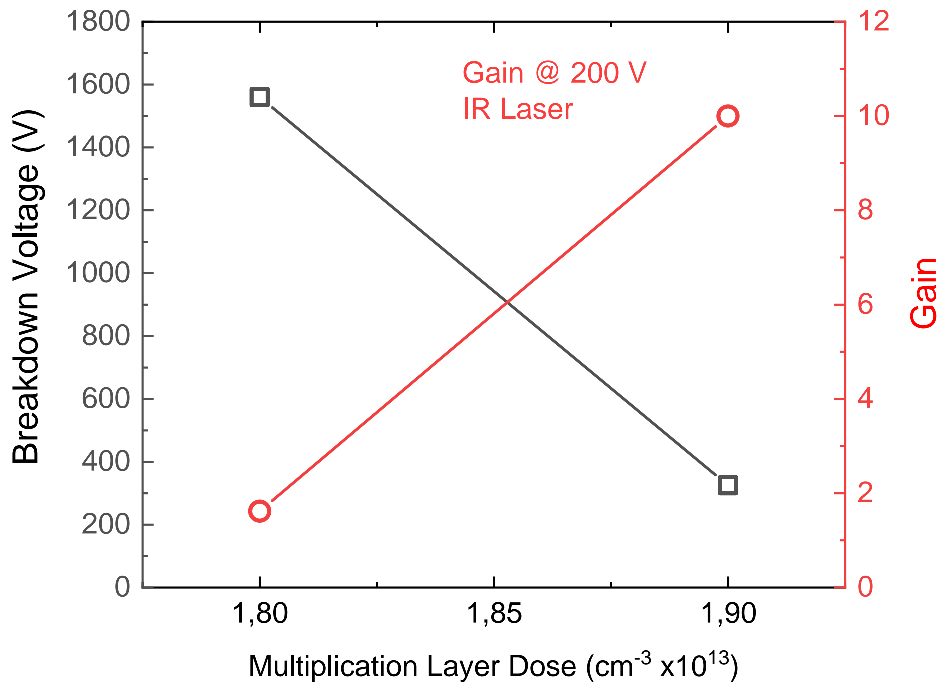

Figure 6.4: Breakdown voltage and gain trade-off for the nLGAD device using an IR laser.

Photolithographic mask designs

We have used an existing LGAD mask set [62] for the development of nLGAD sensors, which consists of 5.2x5.2 mm^2 pad detectors, thus without pixelating the n^+ electrode. Figure 6.5 shows the mask design used and the design of one pad nLGAD detector. As usual, this sensor has the standard collector ring (p-type), JTE diffusion (p-type), n-stop, and an n-type channel stopper at the edge of the periphery. We consider this a simpler solution in order to understand the behavior of n-type LGAD sensors since

it is the first nLGAD development. Further developments of nLGADs will consider pixelated structures.

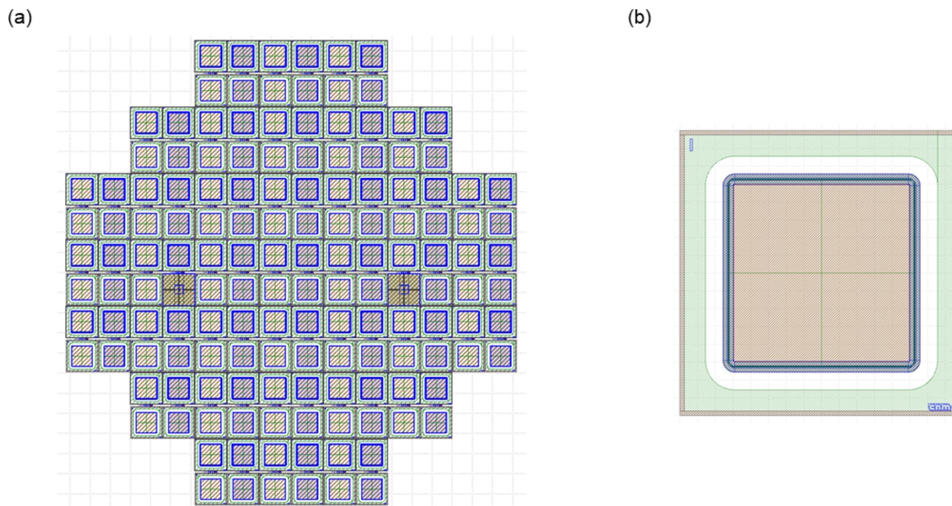

Figure 6.5: (a) Mask used in the development of nLGAD sensors. (b) Pad design of the nLGAD sensor.

6.2.2 Fabrication process

The nLGAD sensors have been fabricated in the IMB-CNM clean room using 100 mm high resistivity (> 10 kΩ·cm) 277 µm wafers. One wafer is devoted to PiN detectors in order to study the quality of the production and to use them for gain measurements. Different doses for the n-type multiplication layer are considered. Figure 6.6 shows the whole process for the fabrication of nLGAD detectors. As one can observe, the process follows the standard photolithographic steps as described in previous chapters for p-type LGADs, with the difference being the inversion of the dopants.

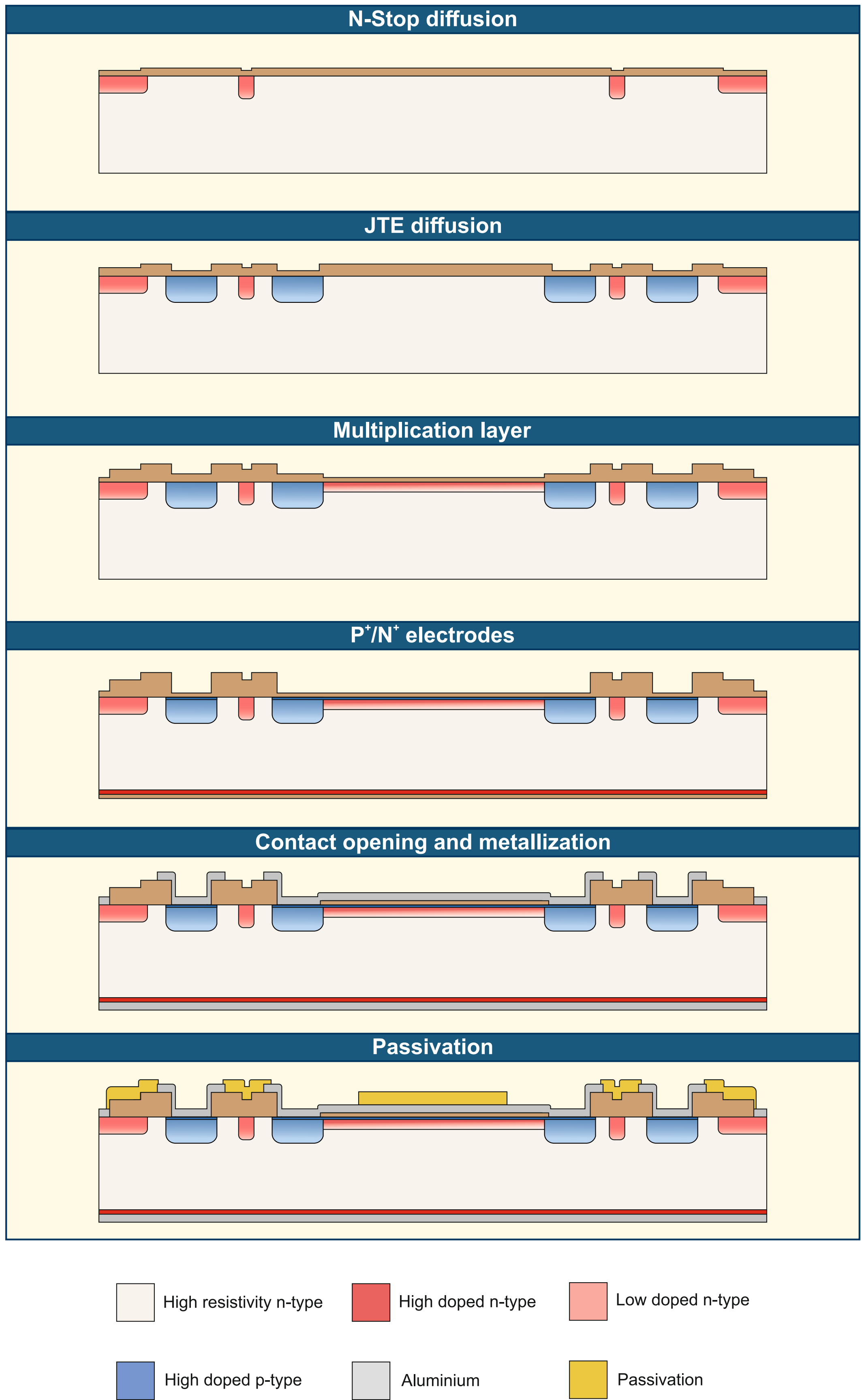

Figure 6.6: Sketch of the nLGAD fabrication process.

6.2.3 Characterization of the detectors

A first characterization of the produced detectors has been carried out. Lowest-dose nLGAD and PiN wafers are tested to study the electrical performance of the detectors, as well as gain measurements.

Electrical characterization

Figure 6.7 shows the I-V measurements on low-doped nLGAD sensors at room temperature. The leakage current measured at room temperature is higher than the obtained using standard p-type LGADs. Even though the higher area, the current density is still ~ 8 higher than the one measured in previous LGAD fabrications. In addition, the breakdown voltage is lower than expected and the sensors work up to 150-200 V. This can be related to a higher doping concentration of the gain layer than expected, and this suggestion can be probed using C-V measurements, depicted in figure 6.8. The sensor is fully depleted at ~ 30 V, which is the expected value in the simulations. There is a high consistency between samples in the full depletion value. Therefore, we cannot attribute the differences in terms of breakdown voltage to the gain layer.

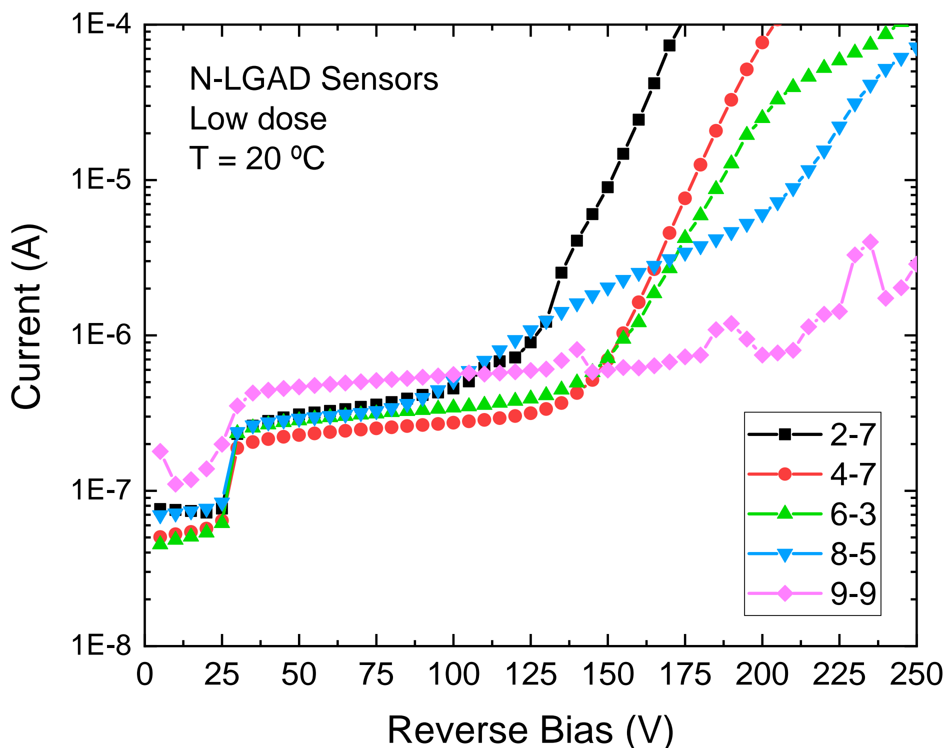

Figure 6.7: I-V measurements of low-dose nLGAD sensors at room temperature.

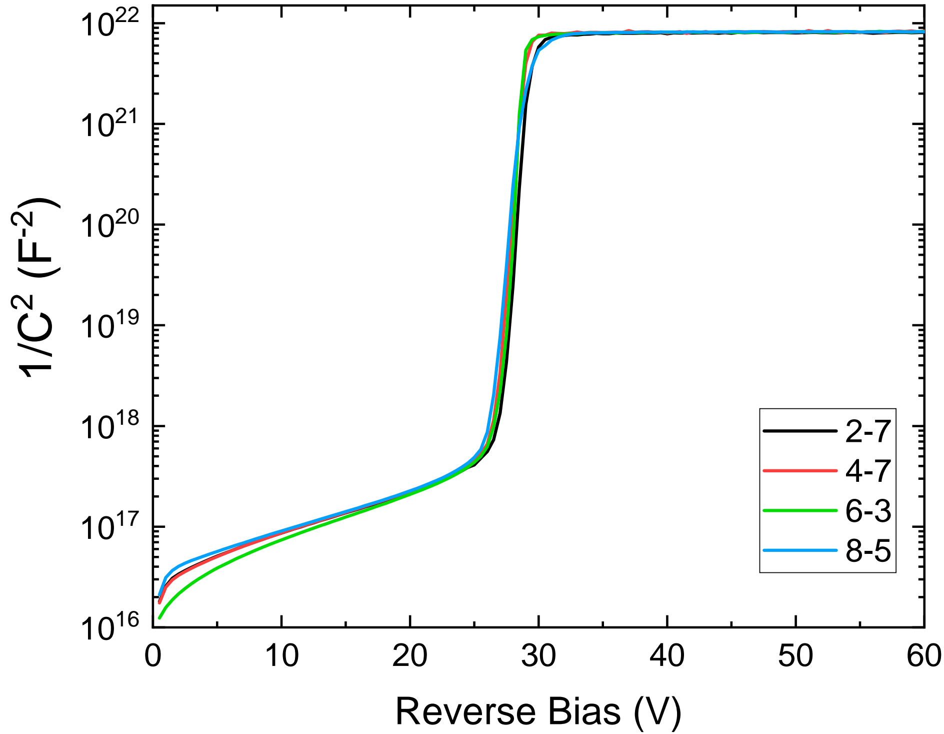

Figure 6.8: C-V measurements of low-dose nLGAD sensors at room temperature.

In order to contrast these results, the same measurements have been carried out for PiN detectors. Figure 6.9 shows the I-V and C-V measurements of n-type PiN detectors. These detectors present a lower leakage current than nLGADs due to the lack of gain, but the current is still higher than standard p-type PiNs. On the other hand, the breakdown is reached at a similar range, and, therefore, we assume that the lower breakdown voltage is not provoked by the gain layer. Future developments must solve this issue by optimizing the periphery of the sensors, which may be the reason for the high current and low breakdown voltage. In addition, using the C-V measurements and equation 2.1 we are able to extract the substrate resistivity, which is $\sim$ 12 kΩ·cm.

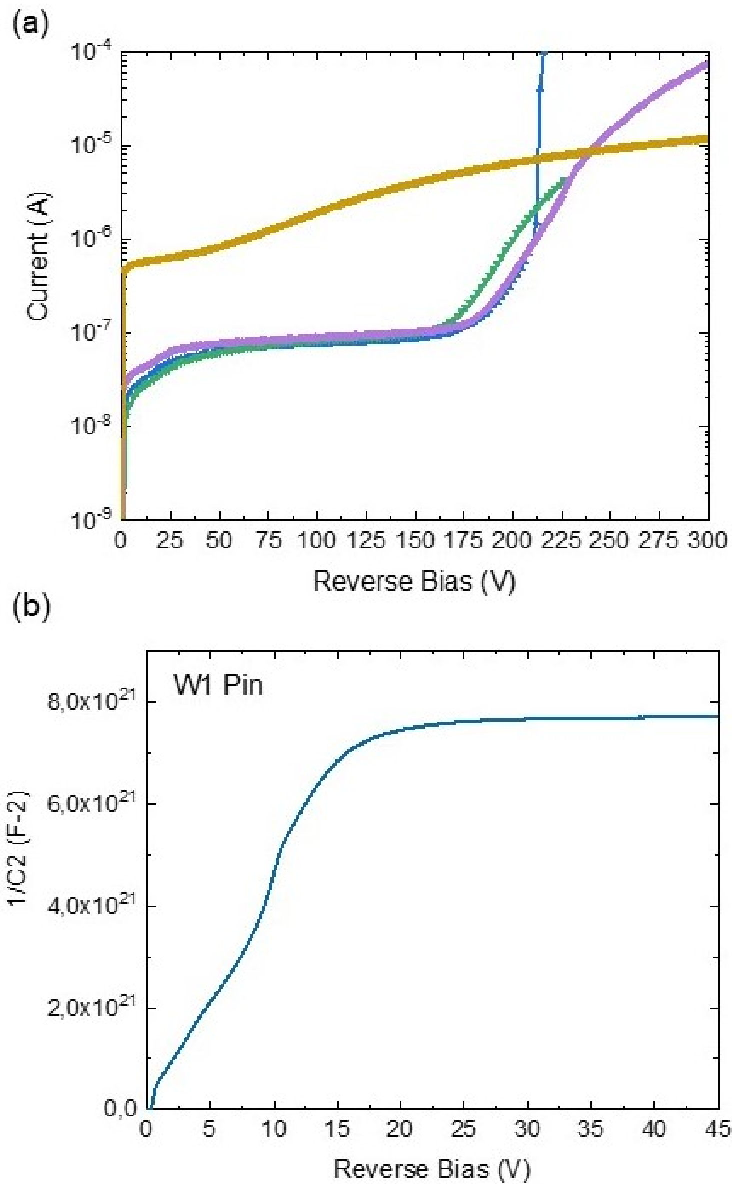

Figure 6.9: (a) I-V and (b) C-V measurements of n-type PiN sensors at room temperature.

Gain measurements

The nLGAD sensors have been irradiated using different wavelength lasers, which will generate electron-hole pairs in different depths of the sensor. In addition, they have been irradiated using 15 keV X-Rays, which will deposit the charge around $\sim$ 300 µm (figure 1.6). This study [98] has been performed to understand the behavior of nLGADs and demonstrate the higher gain using low-penetrating particles. Figure 6.10 shows the gain at room temperature and 100 V for nLGADs using different wavelengths. As absorption length increases, the gain is reduced, due to the transition to a multiplication lead by holes. Therefore, this study demonstrates the use of nLGADs for low-energy particles. Nevertheless, the detectors were not able to detect ultraviolet (UV) light of 369 nm, due to the low absorption length that prevents the

charge to be collected. This issue remarks on the necessity to optimize the entrance window of the sensor, making a shallow p^+ diffusion.

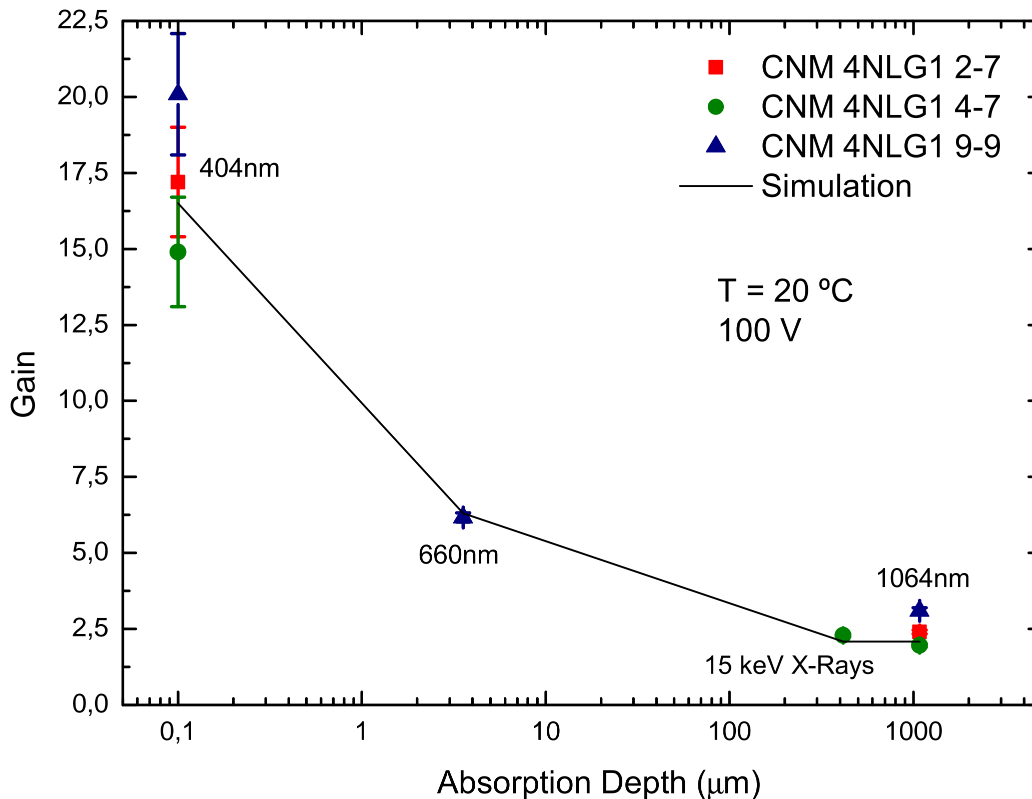

Figure 6.10: Gain as a function of the absorption length for nLGAD detectors, using different low-penetrating particle sources [98].

6.2.4 Conclusions

We have successfully developed the first generation of nLGAD sensors. We have described the optimization of the sensors, the fabrication, and the first characterization of the lowest-doped detectors.

The optimization of the multiplication region highlights the importance of a very uniform gain layer, due to a huge reduction of breakdown voltage increasing the phosphorous dose. We found a suitable trade-off between gain and breakdown voltage, but future fabrications may consider the use of an alternative solution for the multiplication layer diffusion. For instance, the use of a deeper implant could be ideal to lower the phosphorous peak and have a more uniform gain layer due to the reduction of thermal processes, as already stated in chapter 2.

The electrical characterization exposes a non-ideal behavior since the leakage current is higher and the breakdown voltage is lower than expected by simulations and with respect to previous LGAD fabrications. Nevertheless, this seems not to be related to the doping of the gain layer since the C-V and gain measurements agree with simulations. Therefore, we correlate the poor electrical behavior with a non-optimized periphery which must be studied in future developments.

Finally, the gain of the nLGAD detectors has been evaluated using sources with different penetration depths in silicon. In this sense, it is proven that in nLGADs gain increases with low-penetrating particles, such as 440 nm lasers. This study opens the possibility to develop optimized nLGAD detectors that are able to detect even less penetrating depth particles.

6.3 Proton Low Gain Avalanche Detector (pLGAD)

The nLGAD detector has been developed to explore the use of n-type substrates in LGAD sensors, in order to act as the baseline of future developments of low-penetrating particles, as well as the use of LGADs for X-Ray applications. As already described, the nLGAD is capable to detect and amplify the signal produced by $\sim$ 400 nm penetrating particles. Nevertheless, to detect even lower penetrating depths, this sensor must be optimized.

In this sense, we have proposed the so-called Proton Low Gain Avalanche Detector (pLGAD) [99, 97]. This sensor has been designed for the NoMoS (Neutron decay prOducts MOmentum Spectrometer) measurement concept, which aims to detect 15 keV protons [101]. The optimization of the multiplication region must take into account the low penetration of the protons, which is expected at $\sim$ 250 nm [102]. Figure 6.11 shows a cross-section of the pLGAD concept, where a shallow electrode (p^+ electrode) is diffused on top of the device with a depth of less than 100 nm. A p-type collection layer of 1 µm is diffused underneath the p^+ electrode to absorb all the energy deposited by the proton. In order to get a multiplied pulse of the collected charge, an n-type multiplication layer is diffused below the p-type collector layer, leading to a final triple diffusion profile. Hence, a high electric field ($> 3 \cdot 10^5$ V/cm) is created at the p/n junction, where the created electron-hole pairs (e^-/h^+) will be multiplied.

The behavior of this sensor when particles go through it is similar as the nLGAD, with the exception of very low-penetrating particles, such as the forenamed 15 keV protons. In this case, charge will be deposited on the p-type collection layer and holes will be fastly collected and any multiplication is expected. On the other hand, all the electrons will be multiplied since they will pass through the high-electric region, leading to a multiplication of the signal.
Among other detection technologies, Silicon Drift Detectors (SSDs) and Depleted Field Effect Transistors (DEPFETs) have been proposed for low-energy particle detection, which provide different advantages over traditional silicon technologies. The pLGAD structure expects to match the performance of both technologies and, at the same time, simplify the characterization [103]. It is able to work at room temperature, using commercial readout systems (planar sensor) and it can be operated by applying one supply voltage. Moreover, since it is a planar fabrication, the overall cost of the process can be greatly reduced. Finally, the pLGAD has a high time resolution, as shown in the performance of LGADs for HEP. Despite the pLGAD expects to detect

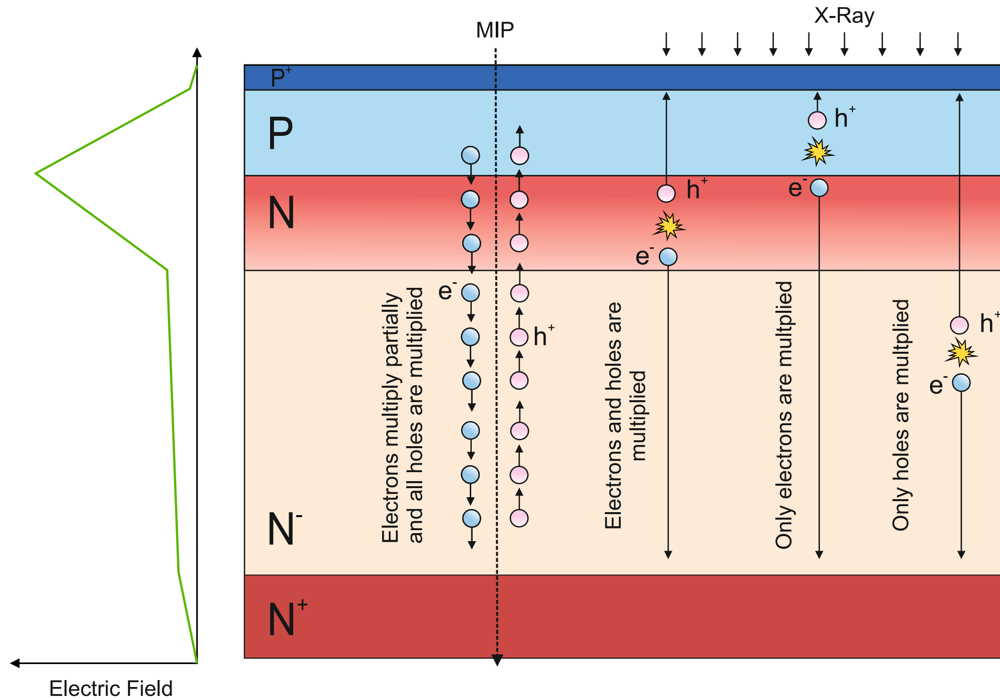

Figure 6.11: Cross-section of the pLGAD structure.

15 keV protons, it can be operated to detect any low-penetrating particle in the range of ∼ 1 µm.

The following sections are going to describe the pLGAD electrical and technological simulations, the design of the device termination using an existing LGAD mask set, and the simulation of a signal pulse shape created by low energy (15 keV) protons.

6.3.1 Optimization of the pLGAD sensor

An initial 1D simulation is performed in order to optimize the trade-off between breakdown voltage and gain, introducing the charge created by the irradiation of a low penetrating particle. Technological simulations have also been carried out to obtain the most relevant fabrication parameters, necessary to set the doping concentration profile in the 1D structure. Then, a 2D simulation has been done to study the edge termination of the device and a first 2D pLGAD prototype is proposed, based on the standard LGAD termination design.

Multiplication region optimization

In order to analyze the trade-off between V_{BD} and gain, the doping profiles of the structure have to be optimized, targeting a $V_{BD} > 500$ V and a gain of 10 at 200 V. There are different parameters involved in the control of V_{BD} and gain values. The substrate doping concentration has been fixed to $5{\cdot}10^{11}$ cm^{-3}, which is a standard value for high resistivity n-type wafers used in radiation detector applications. Then, the doping concentration peaks of the p and n-type diffusions and their thickness have been optimized.

Figure 6.12 shows the obtained doping concentration profile of the structure at the multiplication region, where the $p^+/p/n$ structure is created. It can be clearly seen that the doping concentration peak of the p/n diffusions is in the same range, in order to obtain the desired electric field profile and the subsequent multiplication effect. The triple diffusion region is diffused 4 µm and the p^+ electrode is obtained by using a BF_2 implantation since the conventional boron implantation cannot provide the desired shallow junction.

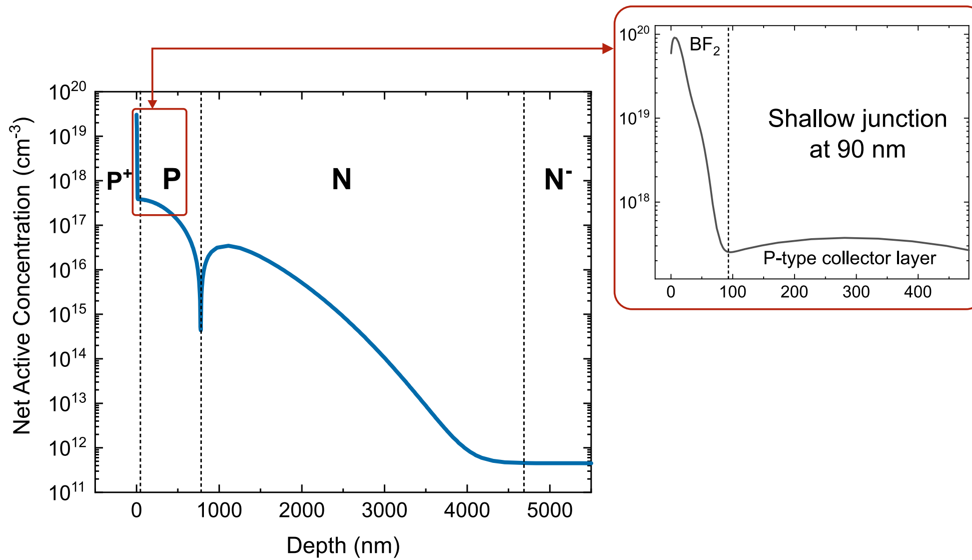

Figure 6.12: Optimised net doping concentration of the $p^+/p/n$ region for a pLGAD sensor.

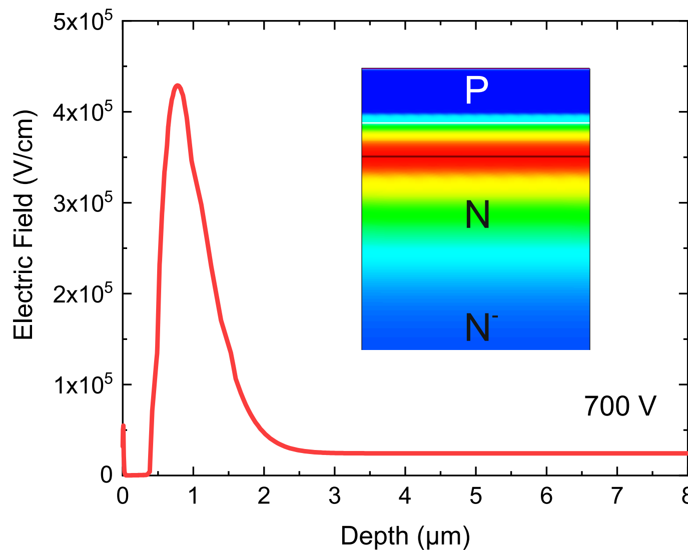

Figure 6.13: Electric field distribution along the depth of the multiplication region at 700 V.

Once the whole 1D structure is already created, electrical simulations are performed. The structure with the doping profile shown in figure 6.12 has a $V_{BD} = 700$ V and the electric field along the depth of the multiplication region at 700 V is plotted in figure

6.13, with an electric field peak of $4.3 \cdot 10^5$ V/cm. As expected, there is a high peak at the junction between the p/n layers enabling that the charge generated before 1 µm depth will be multiplied.

The gain of different pLGAD structures has to be calculated. In this sense, gain simulations have been performed by irradiating with low penetrating protons of 15 keV, assuming that each proton deposits 2000 (e^-/h^+) pairs at 250 nm depth, so all the charge is collected at the p-layer. Figure 6.14 shows a transient simulation of a PiN diode (without the n-type multiplication layer) and two pLGADs with different doses for the n-type multiplication layer, all of them biased at a reverse voltage of 200 V. It is worth mentioning that the peak doping concentration of the p-type collector layer is set to $5 \cdot 10^{17}$ cm^{-3} for all the structures. The total current is integrated during 30 ns when a particle penetrates the p^+ electrode and deposits all the charge at t = 1 ns.

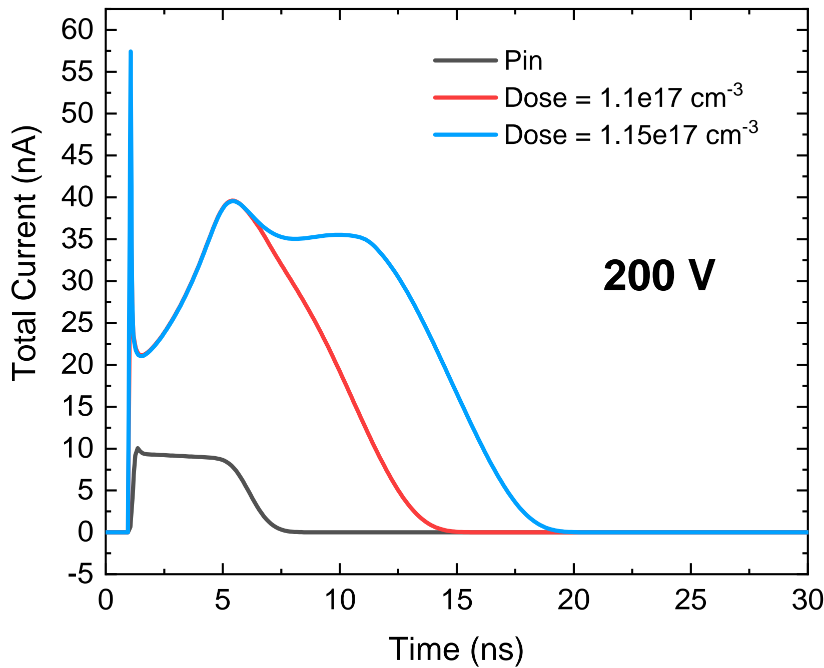

Figure 6.14: Transient simulation of PiN and pLGAD structures biased at 200 V, irradiated with a 15 keV proton.

Figure 6.15 shows the trade-off between V_{BD} and gain as a function of the n-type multiplication layer doping concentration. In the case of the pLGAD structure with a peak doping concentration in the n-type layer of $1.15 \cdot 10^{17}$ cm^{-3}, the desired gain of 10 at 200 V is obtained. If a higher gain is needed, the breakdown voltage capability will be considerably degraded due to the increase of the n-type layer peak doping concentration. On the contrary, if the peak doping concentration of the n-type layer is reduced, the gain will be also reduced, reaching a value of 6 at $1.1 \cdot 10^{17}$ cm^{-3}. Thus, there is a narrow window in the n-type peak doping profile for proper operation of the pLGAD structure, in a similar way to what is observed in the nLGAD detector.

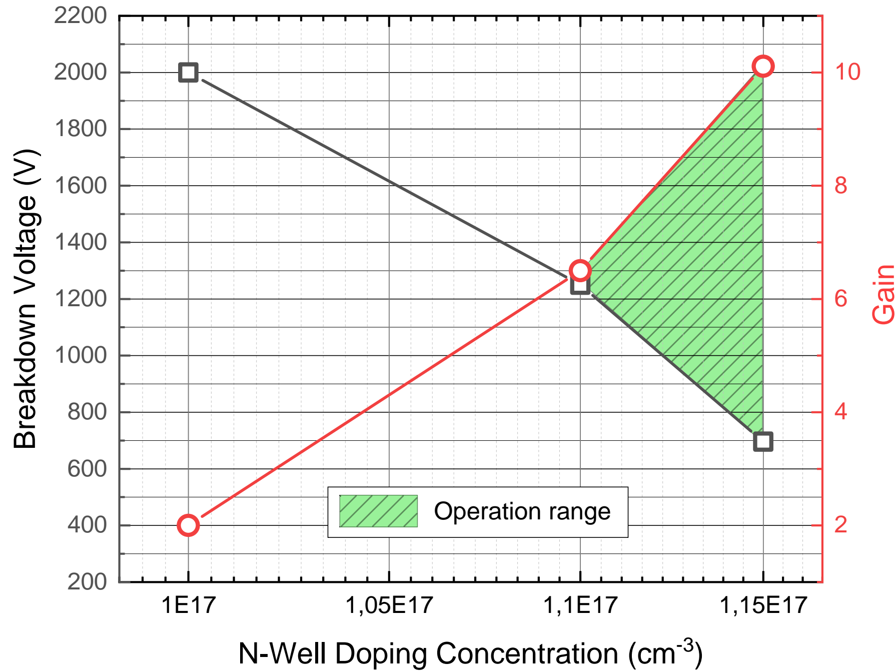

Figure 6.15: Breakdown voltage and gain trade-off as a function of the peak doping concentration of the n-type multiplication layer.

Small variations in the implantation dose of the n-type multiplication layer can lead to huge differences in terms of breakdown voltage and gain.

Periphery optimization

To study the feasibility of the pLGAD structure, a first design approach is proposed, based on a mask set used in previous LGAD fabrications. This mask set was designed with the standard termination structures already described in previous chapters, shown in figure 6.16.

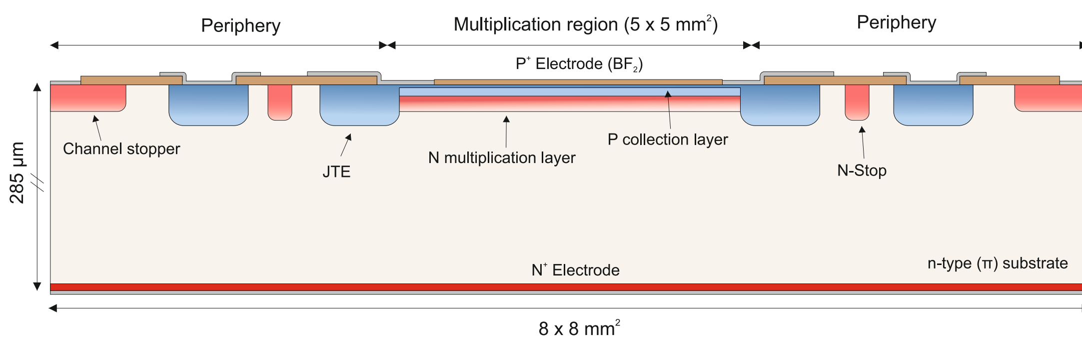

Figure 6.16: Cross-section of the pLGAD design, including the periphery and the active area.

Numerical 2D simulations have been performed where the pLGAD structure has the geometrical dimensions drawn in the existing LGAD mask. Therefore, the efficiency of the periphery design can be estimated. Figure 6.17 shows the electrostatic potential distribution in all the structures, at the breakdown voltage value (1000 V in this case).

The high voltage is applied at the n+ electrode, while the collector ring and the n/p junction remain at 0 V.

Figure 6.18 shows the electric field distribution along the structure, close to the surface. The optimal case is to have the highest electric field peak at the n/p junction and avoid higher peaks at the periphery of the device, which can lead to instabilities and premature breakdown. We can see that the higher peak corresponds to the n/p junction, as expected, with secondary high peaks at the end of the junctions. Nevertheless, these peaks are smaller than the multiplication peak.

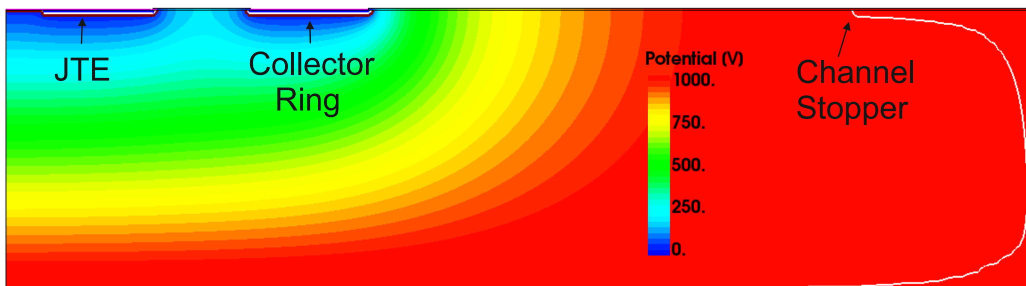

Figure 6.17: Cross-section of the pLGAD design, including the periphery and the active area.

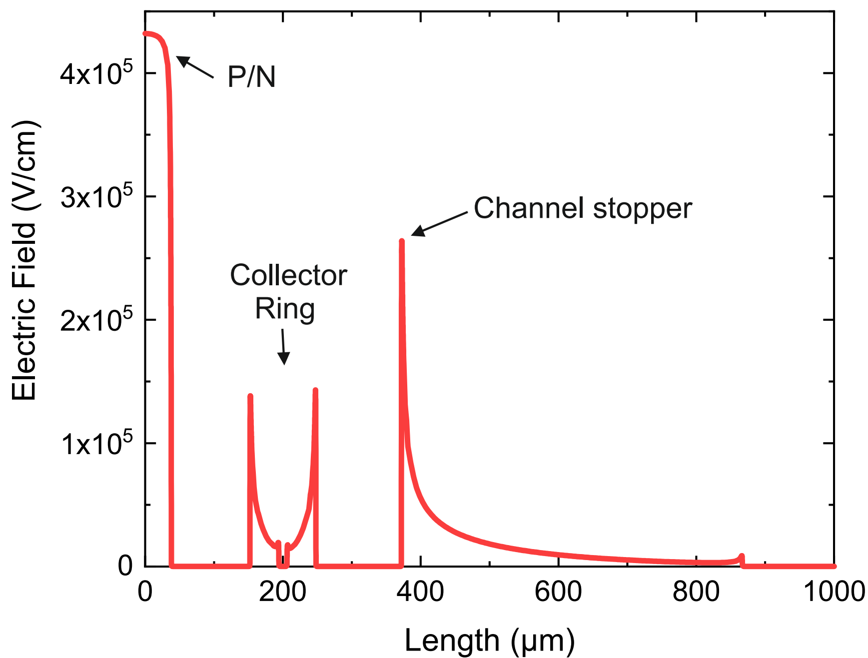

Figure 6.18: Cross-section of the pLGAD design, including the periphery and the active area.

6.3.2 Conclusions

We have proposed the pLGAD sensor to detect low-energy particles, targeting the detection of 15 keV protons and basing the design on the nLGAD technology developed by IMB-CNM.

We have fully described the design of the sensor, including the optimization of the multiplication region and a first termination design. Moreover, we performed gain simulations by introducing the amount of charge produced by 15 keV protons, where a gain of 10 at 200 V, is obtained. Nevertheless, the performance is greatly sensitive to the technological parameters of the multiplication layer, and, therefore, we must have huge control over them during the fabrication. Moreover, different gain layer configurations can be studied to obtain a better V_{BD}-Gain trade-off, taking advantage of the technological progress in the LGAD technology.

At the time of closing the Ph.D. thesis, the pLGAD concept has been proven and patented [104], while the fabrication of this sensor is ready to start. Afterward, this fabrication will be characterized electrically and the gain will be evaluated using different penetrating depth sources.

Conclusions and Future Work

This thesis covers the development of LGAD and iLGAD detectors for their use in HEP and synchrotron applications. The most important conclusions that can be drawn are detailed below, in addition to the current status of each development and further work needed in the future.

Development of thin LGAD sensors on behalf of the AIDA2020 project.

- The whole development of LGADs in Si-Si wafers for timing applications is fully described, including the design and optimization of the sensors, the fabrication process, and the characterization of both AIDAv1 and AIDAv2 fabrications.
- AIDAv1 sensors exhibit a high leakage current, which has been evaluated using TCAD simulations and thermographic measurements to determine that a misalignment in the n^+ diffusion is responsible for it. In addition, the timing performance of 35 µm thick wafers does not justify the necessity to use thinner wafers than 50 µm.
- AIDAv2 sensors, with the corrected mask and using only 50 µm, have been produced and fully characterized, showing an outstanding performance in terms of leakage current but with a lower breakdown voltage than expected. Increasing the area of the sensors results in to decrease in the breakdown voltage, and future developments must consider increasing the uniformity of the multiplication layer.
- AIDAv2 LGADs meet all the CMS specifications to be used in the ETL, with the exception of the low breakdown voltage before irradiation. On the other hand, the ATLAS requirements are accomplished as well, but the collected charge is achieved at a higher voltage than the required. In addition, the breakdown voltage specification before irradiation is not fulfilled.
- Future developments of thin LGADs must consider achieving a better trade-off between breakdown voltage and gain before and after irradiation, by optimizing the multiplication region. Carbon-enriched and deeper implants may be considered to overcome this issue in the next thin LGAD fabrications.

LGADs for timing applications using 150 mm wafers

- Due to the necessity of higher silicon wafers in the microelectronics industry, we produced LGAD sensors using different types of 150 mm silicon wafers. For timing applications, 50 µm thick wafers are required, where SOI and epitaxial are the ones used due to the lack of Si-Si wafers.

- Produced sensors exhibit a good electrical performance before irradiation using SOI and epitaxial wafers, even though the last ones offer a lower leakage current and higher breakdown voltage. Both types of wafers show the expected low gain, but epitaxial wafers need to be applied at a voltage closer to breakdown.

- Irradiated LGADs from 6LG3 exhibit a huge decrease of gain in terms of neutron fluence, resulting in a not enough collected charge at the required fluences for both ATLAS and CMS. Timing performance is excellent before and after irradiation, despite the discrepancies between IMB-CNM and IFAE laboratories.

- The ATLAS-CMS Common Run is optimized and fabricated using epitaxial wafers, but Si-Si wafers are expected to be used in the next fabrications. This fabrication considers carbon-enriched multiplication layers to overcome the issue of the fast decrease in gain observed during neutron irradiations. In addition, different pixelated structures are designed to study the uniformity of the gain layer with respect to the area.

- Upon closing this thesis, a first characterization of the ATLAS-CMS Common Run has been carried out, obtaining an excellent performance before irradiation. There is a high yield even for big-area pixelated structures. The use of carbon in the multiplication layer leads to a higher uniformity, and this behavior must be explored in new fabrications since it is a clear advantage.

- Some LGADs have been irradiated, obtaining a better radiation hardness in carbonated wafers. There are some discrepancies when obtaining the acceptor-removal constant, but it is lower using carbon, as other LGAD manufacturers stated.

- The ATLAS-CMS Common Run must be fully characterized, including an exhaustive irradiation campaign to study the performance of these sensors against radiation. In addition, this fabrication will be the baseline for future carbonated LGADs, where proper optimization must be envisaged.

Development of iLGADs for X-Ray applications

- The periphery of the iLG1 has been optimized and re-designed in order to enhance its performance under X-Ray irradiations. In this sense, we have developed the iLG2, which uses a multi-ring structure on both sides of the sensor to be able to support higher voltages when surface damage is expected.

- Produced sensors exhibit a higher gain than expected that resulting in a higher leakage current and lower breakdown voltage. However, pad LGADs maintain a good trade-off between breakdown voltage and gain. On the other hand, high-area pixelated structures are not able to be operated due to a premature breakdown caused by the gain layer formation, which needs to be studied in future developments.

- The optimized iLGAD sensor is able to support a higher voltage than the one from the iLG1 during X-Ray irradiation, thus highlighting the importance of the periphery design.

- This fabrication has to be the baseline for future developments of iLGADs for X-Ray applications. Irradiations using different X-Ray sources must be considered to understand the limits of the sensor. In addition, the poor performance of big-area sensors needs to be reviewed and fully understood. Carbon must be considered in the multiplication layer due to the promising results obtained in the ATLAS-CMS Common Run.

Thin iLGADs for timing applications

- Thin (50 µm) iLGADs have been proposed for 4D tracking applications, using trenches to isolate the active area of the sensor reducing the periphery length, and avoiding fabrication steps.

- It is described the fabrication process, as well as the optimization of the trenches to assure good electrical performance. In addition, Si-Si and epitaxial wafers are proposed to develop this sensor. A new mask set has been designed including different pixelated structures and different pad sizes to test the uniformity of the gain layer.

- The first Trench iLGAD fabrication is ready to start, and a subsequent full characterization is expected to study the main electrical characteristics and the gain, before and after irradiation.

Development of LGADs using n-type substrates

- The first LGAD using n-type substrates has been proposed, optimized, and fabricated. This sensor can be used to collect electrons in X-Ray applications, and also for detecting low-energy particles.

- The nLGAD has been optimized to reach the desired performance in terms of leakage current, breakdown voltage, and gain. It has been fabricated using standard n-type wafers and an existing mask set.

- The first electrical measurements show a higher leakage current and low breakdown voltage than expected by simulation. We do not attribute this issue to a higher doping concentration since C-V and gain measurements, which are

related to the gain layer, exhibit the anticipated performance. Therefore, future developments must include an optimization of the nLGAD periphery to improve electrical performance. In addition, the use of the nLGAD in detecting low-energy particles has been proven by studying the gain using different absorption length sources. The gain increases as absorption length decrease until a threshold of 369 nm.

- In order to enhance the efficiency when detecting low-energy particles, we proposed the pLGAD sensor, which includes a new multiplication region composed of three diffusions. Here, a shallow junction and a p-type collector layer are included to collect the charge of sub-micron penetrating particles like 15 keV protons. The optimization of the multiplication region is described, as well as the first proposal to develop pLGADs using standard fabrication processes and mask set designs.
- The first pLGAD fabrication is ready to start, and a full characterization needs to be envisaged to probe the electrical performance of the sensor. Furthermore, different absorption length sources have to be used to study the capacity of the pLGAD to detect low-energy particles.

Scientific Contributions

Scientific publications

- Carulla, M., Doblas, A., Flores, D., Galloway, Z., Hidalgo, S., Kramberger, G., ... and Zhao, Y. (2019). 50 μm thin Low Gain Avalanche Detectors (LGAD) for timing applications. *Nuclear Instruments and Methods in Physics Research Section A: Accelerators, Spectrometers, Detectors, and Associated Equipment*, 924, 373-379.

- Doblas, A., Flores, D., Hidalgo, S., Pellegrini, G., Quirion, D., and Vila, I. (2021, June). Technology Developments on iLGAD Sensors at IMB-CNM. In 2021 13th Spanish Conference on Electron Devices (CDE) (pp. 132-136). IEEE.

- Doblas, A., Khalid, W., Flores, D., Hidalgo, S., Pellegrini, G., and Valentan, M. (2021, June). Proton Low Gain Avalanche Detector (pLGAD) for Low Energy Particles Detection. In 2021 13th Spanish Conference on Electron Devices (CDE) (pp. 137-140). IEEE.

- Khalid, W., Valentan, M., Doblas, A., Flores, D., Hidalgo, S., Konrad, G., ... and Villegas, J. (2022). First results for the pLGAD sensor for low-penetrating particles. *Nuclear Instruments and Methods in Physics Research Section A: Accelerators, Spectrometers, Detectors, and Associated Equipment*, 1040, 167220.

- Grieco, C., García, L. C., Doblas, A., Gkougkousis, E. L., Grinstein, S., Hidalgo, S., ... and Dominguez, J. V. (2022). Overview of CNM LGAD results: Boron Si-on-Si and epitaxial wafers. Journal of Instrumentation, 17(09), C09021.

- Doblas, A., Flores, D., Hidalgo, S., Moffat, N., Pellegrini, G., Quirion, D., Villegas, J., Maneuski, D., Ruat, M. and Fajardo, P. (2022). Inverse LGAD (iLGAD) Periphery Optimization for Surface Damage Irradiations. Submitted to *Sensors: Special Issue "Radiation Sensors and Detectors: Materials, Principles, and Applications"*.

- Currás, E., Doblas, A., Fernández, M., Flores, David., González, J., Hidalgo, S., Jaramillo, R., Moll, M., Navarrete, E., Pellegrini, G. and Vila, I. (2022) Timing performance and gain degradation after irradiation with protons and neutrons of Low Gain Avalanche Diodes based on a shallow and broad multiplication layer in a float-zone 35 μm and 50 μm thick silicon substrate. Submitted to *Nuclear Instruments and Methods in Physics Research Section A: Accelerators, Spectrometers, Detectors, and Associated Equipment.*

Scientific conferences and workshops

- Albert Doblas. *CNM activities on LGADs in the RD50 framework.* The 35th RD50 Workshop on Radiation Hard Semiconductor Devices (CERN, Switzerland). November 2019
- Albert Doblas. *Status of CNM LGAD Runs.* The 37th RD50 Workshop on Radiation Hard Semiconductor Devices (CERN, Online). November 2020
- Albert Doblas. *Technology Developments on Thin iLGAD Sensors for Pixelated Timing Detectors.* 16th Trento Workshop on Advanced Silicon Radiation Detectors (FBK, Online). February 2021
- Albert Doblas. *Technology Developments on Thin iLGAD Sensors for Pixelated Timing Detectors.* International Workshop on Future Linear Colliders, LCWS2021 (Online). March 2021
- Albert Doblas. *iLGAD Sensor for X-Ray Applications.* The 38th RD50 Workshop on Radiation Hard Semiconductor Devices (CERN, Online). June 2021

Bibliography

[1] Y Eisen and A Shor. CdTe and CdZnTe materials for room-temperature X-ray and gamma ray detectors. *Journal of crystal growth*, 184:1302–1312, 1998.

[2] Jose Millan, Philippe Godignon, Xavier Perpiñà, Amador Pérez-Tomás, and José Rebollo. A survey of wide bandgap power semiconductor devices. *IEEE Transactions on Power Electronics*, 29(5):2155–2163, 2013.

[3] PJ Sellin and J Vaitkus. New materials for radiation hard semiconductor dectectors. *Nuclear Instruments and Methods in Physics Research Section A: Accelerators, Spectrometers, Detectors and Associated Equipment*, 557(2):479–489, 2006.

[4] Ivana Capan. 4H-SiC Schottky Barrier Diodes as Radiation Detectors: A Review. *Electronics*, 11(4):532, 2022.

[5] James Paul Grant. *GaN radiation detectors for particle physics and synchrotron applications.* University of Glasgow (United Kingdom), 2007.

[6] R Szweda. GaN and SiC detectors for radiation and medicine. *III-Vs Review*, 18(7):40–41, 2005.

[7] Jinghui Wang, Padhraic Mulligan, Leonard Brillson, and Lei R Cao. Review of using gallium nitride for ionizing radiation detection. *Applied Physics Reviews*, 2(3):031102, 2015.

[8] Edoardo Bossini and Nicola Minafra. Diamond detectors for timing measurements in high energy physics. *Frontiers in Physics*, 8:248, 2020.

[9] Charles Kittel, Paul McEuen, and Paul McEuen. *Introduction to solid state physics*, volume 8. Wiley New York, 1996.

[10] B Jayant Baliga. *Fundamentals of power semiconductor devices.* Springer Science & Business Media, 2010.

[11] Gerhard Lutz et al. *Semiconductor radiation detectors.* Springer, 2007.

[12] G Pellegrini, M Chmeissani, M Maiorino, G Blanchot, J Garcia, M Lozano, R Martinez, C Puigdengoles, M Ullan, and P Casado. Performance limits of a 55 μm pixel CdTe detector. *IEEE transactions on nuclear science*, 53(1):361–366, 2006.

[13] Richard H Pehl, Richard C Cordi, and Fred S Goulding. High-purity germanium: Detector fabrication and performance. *IEEE Transactions on Nuclear Science*, 19(1):265–269, 1972.

[14] J Jakbek. Semiconductor pixel detectors and their applications in life sciences. *Journal of Instrumentation*, 4(03):P03013, 2009.

[15] A Datta, Z Zhong, and S Motakef. A new generation of direct X-ray detectors for medical and synchrotron imaging applications. *Scientific reports*, 10(1):1–10, 2020.

[16] CERN website. https://home.cern/science/experiments.

[17] Albert M Sirunyan, CMS collaboration, et al. Particle-flow reconstruction and global event description with the CMS detector. *JINST*, 12(10):P10003, 2017.

[18] N Cartiglia, M Baselga, G Dellacasa, S Ely, V Fadeyev, Z Galloway, S Garbolino, F Marchetto, S Martoiu, G Mazza, et al. Performance of ultra-fast silicon detectors. *Journal of instrumentation*, 9(02):C02001, 2014.

[19] ATLAS collaboration. Technical design report: a high-granularity timing detector for the ATLAS phase-ii upgrade. Technical report, CERN, 2020.

[20] CMS collaboration. A mip timing detector for the cms phase-2 upgrade e. Technical report, CERN, 2019.

[21] Hartmut FW Sadrozinski, Abraham Seiden, and Nicolò Cartiglia. 4D tracking with ultra-fast silicon detectors. *Reports on Progress in Physics*, 81(2):026101, 2017.

[22] ALBA website. https://www.albasynchrotron.es/en/accelerators.

[23] Alejandro Gutiérrez, José Ángel Martín-Gago, and Salvador Ferrer. La luz sincrotrón: una herramienta extraordinaria para la ciencia. *Apuntes de Ciencia y Tecnología*, 12:37–46, 2004.

[24] ESRF website. https://www.esrf.fr/about/upgrade.

[25] X-ray Detectors for Synchrotron Radiation Applications. 6th EIROforum school on Instrumentation (2019). https://indico.cern.ch/event/777129/contributions/3249497/attachments/1844115/3024882/2019.05_SR_X-rayDetectors.pdf.

[26] Donald F Swinehart. The beer-lambert law. *Journal of chemical education*, 39(7):333, 1962.

[27] National Institute of Standards and Technology (NIST). https://physics.nist.gov/PhysRefData/FFast/html/form.html.

[28] David Pennicard, Benoît Pirard, Oleg Tolbanov, and Krzysztof Iniewski. Semiconductor materials for x-ray detectors. *MRS Bulletin*, 42(6):445–450, 2017.

[29] Simon Ramo. Currents induced by electron motion. *Proceedings of the IRE*, 27(9):584–585, 1939.

[30] Marco Ferrero, Roberta Arcidiacono, Marco Mandurrino, Valentina Sola, and Nicolò Cartiglia. *An Introduction to Ultra-Fast Silicon Detectors*. CRC Press, 2021.

[31] Stefano Meroli, Daniele Passeri, and Leonello Servoli. Energy loss measurement for charged particles in very thin silicon layers. *Journal of Instrumentation*, 6(06):P06013, 2011.

[32] Joe C Campbell, Stephane Demiguel, Feng Ma, Ariane Beck, Xiangyi Guo, Shuling Wang, Xiaoguang Zheng, Xiaowei Li, Jeffrey D Beck, Michael A Kinch, et al. Correction to "recent advances in avalanche photodiodes". *IEEE Journal of Selected Topics in Quantum Electronics*, 10(6):1446–1447, 2004.

[33] Giulio Pellegrini, P Fernández-Martínez, M Baselga, C Fleta, D Flores, V Greco, S Hidalgo, I Mandić, G Kramberger, D Quirion, et al. Technology developments and first measurements of Low Gain Avalanche Detectors (LGAD) for high energy physics applications. *Nuclear Instruments and Methods in Physics Research Section A: Accelerators, Spectrometers, Detectors and Associated Equipment*, 765:12–16, 2014.

[34] M Ferrero, R Arcidiacono, M Barozzi, M Boscardin, N Cartiglia, GF Dalla Betta, Z Galloway, M Mandurrino, S Mazza, G Paternoster, et al. Radiation resistant LGAD design. *Nuclear Instruments and Methods in Physics Research Section A: Accelerators, Spectrometers, Detectors and Associated Equipment*, 919:16–26, 2019.

[35] HF-W Sadrozinski, A Anker, J Chen, V Fadeyev, P Freeman, Z Galloway, B Gruey, H Grabas, C John, Z Liang, et al. Ultra-fast silicon detectors (UFSD). *Nuclear Instruments and Methods in Physics Research Section A: Accelerators, Spectrometers, Detectors and Associated Equipment*, 831:18–23, 2016.

[36] G Kramberger, M Baselga, V Cindro, P Fernandez-Martinez, D Flores, Z Galloway, A Gorišek, V Greco, S Hidalgo, V Fadeyev, et al. Radiation

effects in Low Gain Avalanche Detectors after hadron irradiations. *Journal of Instrumentation*, 10(07):P07006, 2015.

[37] Medipix3 collaboration. https://medipix.web.cern.ch/medipix3.

[38] G Pellegrini, M Baselga, M Carulla, V Fadeyev, P Fernández-Martínez, M Fernández García, D Flores, Z Galloway, C Gallrapp, S Hidalgo, et al. Recent technological developments on LGAD and iLGAD detectors for tracking and timing applications. *Nuclear Instruments and Methods in Physics Research Section A: Accelerators, Spectrometers, Detectors and Associated Equipment*, 831:24–28, 2016.

[39] M Carulla, M Fernandez-Garcia, P Fernandez-Martinez, D Flores, J Gonzalez, S Hidalgo, R Jaramillo, A Merlos, FR Palomo, G Pellegrini, et al. Technology developments and first measurements on inverse Low Gain Avalanche Detector (iLGAD) for high energy physics applications. *Journal of Instrumentation*, 11(12):C12039, 2016.

[40] Esteban Currás, M Carulla, M Centis Vignali, J Duarte-Campderros, M Fernández, David Flores, A García, G Gómez, J González, Salvador Hidalgo, et al. Inverse Low Gain Avalanche Detectors (iLGADs) for precise tracking and timing applications. *Nuclear Instruments and Methods in Physics Research Section A: Accelerators, Spectrometers, Detectors and Associated Equipment*, 958:162545, 2020.

[41] M Carulla. *Thin LGAD timing detectors for the ATLAS experiment*. 2019.

[42] Artur Apresyan, Wei Chen, Gabriele D'Amen, Karri F Di Petrillo, Gabriele Giacomini, Ryan E Heller, Hakseong Lee, C-S Moon, and Alessandro Tricoli. Measurements of an AC-LGAD strip sensor with a 120 GeV proton beam. *Journal of Instrumentation*, 15(09):P09038, 2020.

[43] Gabriele Giacomini, Wei Chen, Gabriele D'Amen, and Alessandro Tricoli. Fabrication and performance of AC-coupled LGADs. *Journal of Instrumentation*, 14(09):P09004, 2019.

[44] Marco Mandurrino, R Arcidiacono, M Boscardin, N Cartiglia, GF Dalla Betta, M Ferrero, F Ficorella, L Pancheri, G Paternoster, F Siviero, et al. Demonstration of 200-, 100-, and 50 μm Pitch Resistive AC-Coupled Silicon Detectors (RSD) With 100% Fill-Factor for 4D Particle Tracking. *IEEE Electron Device Letters*, 40(11):1780–1783, 2019.

[45] G Paternoster, G Borghi, Maurizio Boscardin, Nicolo Cartiglia, Maricel Ferrero, F Ficorella, Federico Siviero, Alberto Gola, and Pierluigi Bellutti. Trench-isolated low gain avalanche diodes (ti-lgads). *IEEE Electron Device Letters*, 41(6):884–887, 2020.

[46] Albert Doblas, David Flores, Salvador Hidalgo, Giulio Pellegrini, David Quirion, and Iván Vila. Technology developments on ilgad sensors at imb-cnm. In *2021 13th Spanish Conference on Electron Devices (CDE)*, pages 132–136. IEEE, 2021.

[47] Sofía Otero Ugobono. Characterisation and optimisation of radiation-tolerant silicon sensors with intrinsic gain. 2018.

[48] Michael Moll et al. *Radiation damage in silicon particle detectors*. PhD thesis, PhD dissertation, Physics Dept., Univ. of Hamburg, Germany, 1999.

[49] Gunnar Lindström. Radiation damage in silicon detectors. *Nuclear Instruments and Methods in Physics Research Section A: Accelerators, Spectrometers, Detectors and Associated Equipment*, 512(1-2):30–43, 2003.

[50] Michael Moll. Displacement damage in silicon detectors for high energy physics. *IEEE Transactions on Nuclear Science*, 65(8):1561–1582, 2018.

[51] Z Galloway, V Fadeyev, P Freeman, E Gkougkousis, C Gee, B Gruey, CA Labitan, Z Luce, F McKinney-Martinez, HF-W Sadrozinski, et al. Properties of hpk ufsd after neutron irradiation up to 6e15 n/cm2. *Nuclear Instruments and Methods in Physics Research Section A: Accelerators, Spectrometers, Detectors and Associated Equipment*, 940:19–29, 2019.

[52] Carulla M. Cavallaro E. Cindro V. Flores D. Galloway Z. ... Zavrtanik M. Kramberger, G. Radiation hardness of gallium doped low gain avalanche detectors. *Nuclear Instruments and Methods in Physics Research Section A: Accelerators, Spectrometers, Detectors and Associated Equipment*, 898:53–59, 2018.

[53] Tao Yang, Yuhang Tan, Qing Liu, Suyu Xiao, Kai Liu, Jianyong Zhang, Ryuta Kiuchi, Mei Zhao, Xiyuan Zhang, Congcong Wang, et al. Time resolution of the 4H-SiC PIN detector. *Frontiers in Physics*, page 91, 2022.

[54] Tao Yang, Yuhang Tan, Congcong Wang, Xiyuan Zhang, and Xin Shi. Simulation of the 4H-SiC Low Gain Avalanche Diode. *arXiv preprint arXiv:2206.10191*, 2022.

[55] Jiaguo Zhang, Eckhart Fretwurst, Robert Klanner, Hanno Perrey, Ioana Pintilie, Thomas Poehlsen, and Joern Schwandt. Study of X-ray radiation damage in silicon sensors. *Journal of Instrumentation*, 6(11):C11013, 2011.

[56] Jiaguo Zhang, Eckhart Fretwurst, Robert Klanner, Ioana Pintilie, Joern Schwandt, and Monica Turcato. Investigation of X-ray induced radiation damage at the Si-SiO2 interface of silicon sensors for the european xfel. *Journal of instrumentation*, 7(12):C12012, 2012.

[57] Jiaguo Zhang, Eckhart Fretwurst, Heinz Graafsma, Robert Klanner, Ioannis Kopsalis, and Joern Schwandt. Study of x-ray radiation damage in the AGIPD sensor for the European XFEL. *Journal of Instrumentation*, 9(05):C05022, 2014.

[58] Joern Schwandt, Eckhart Fretwurst, Robert Klanner, and J Zhang. Design of the AGIPD sensor for the European XFEL. *Journal of Instrumentation*, 8(01):C01015, 2013.

[59] Joern Schwandt. Design of a radiation hard silicon pixel sensor for X-ray science. Technical report, Hamburg Univ.(Germany). Dept. Physik, 2014.

[60] Petra Riedler. *Radiation damage effects and performance of silicon strip detectors using LHC readout electronics.* PhD thesis, CERN, 1998.

[61] M Carulla, A Doblas, D Flores, Z Galloway, S Hidalgo, G Kramberger, Z Luce, I Mandic, S Mazza, A Merlos, et al. 50μm thin Low Gain Avalanche Detectors (LGAD) for timing applications. *Nuclear Instruments and Methods in Physics Research Section A: Accelerators, Spectrometers, Detectors and Associated Equipment*, 924:373–379, 2019.

[62] Pablo Fernández Martínez et al. *Diseño, fabricación y optimización de detectores con multiplicación (LGAD) para experimentos de física de altas energías.* Universitat Autònoma de Barcelona, 2014.

[63] Pablo Fernández-Martínez, David Flores, Salvador Hidalgo, Virginia Greco, Angel Merlos, Giulio Pellegrini, and David Quirion. Design and fabrication of an optimum peripheral region for low gain avalanche detectors. *Nuclear Instruments and Methods in Physics Research Section A: Accelerators, Spectrometers, Detectors and Associated Equipment*, 821:93–100, 2016.

[64] AIDA2020 project. https://aida2020.web.cern.ch/aida2020/.

[65] G Laštovička-Medin, G Kramberger, M Rebarz, J Andreasson, K Kropielnicki, T Laštovička, and J Kroll. A brief overview of the studies on the irreversible breakdown of lgad testing samples irradiated at the critical lhc-hl fluences. *Journal of Instrumentation*, 17(07):C07020, 2022.

[66] Gordana Laštovička-Medin, Mateusz Rebarz, Gregor Kramberger, Tomáš Laštovička, Jakob Andreasson, Martin Precek, Mauricio Rodriguez-Ramos, and Miloš Manojlovic. Studies of LGAD performance limitations,

single event burnout and gain suppression, with femtosecond-laser and ion beams. *Nuclear Instruments and Methods in Physics Research Section A: Accelerators, Spectrometers, Detectors and Associated Equipment*, 1041:167388, 2022.

[67] Synopsys Sentaurus. https://www.synopsys.com/.

[68] K Wu, M Zhao, T Yang, João Guimarães da Costa, Z Liang, and X Shi. Design of Low Gain Avalanche Detectors (LGAD) with 400 keV ion implantation energy for multiplication layer fabrication. *Nuclear Instruments and Methods in Physics Research Section A: Accelerators, Spectrometers, Detectors and Associated Equipment*, 984:164558, 2020.

[69] V Sola, M Costa, R Arcidiacono, N Cartiglia, M Tornago, MM Obertino, F Siviero, M Ferrero, M Mandurrino, and A Staiano. Characterisation of 50 μm thick lgad manufactured by fbk & hpk. Technical report, 2019.

[70] E. Currás, A. Doblas, M. Fernández, David. Flores, J. González, S. Hidalgo, R. Jaramillo, M. Moll, E. Navarrete, G. Pellegrini, and I Vila. Timing performance and gain degradation after irradiation with protons and neutrons of low gain avalanche diodes based on a shallow and broad multiplication layer in a float-zone 35 μm and 50 μm thick silicon substrate. Submitted to Nuclear Instruments and Methods in Physics Research Section A: Accelerators, Spectrometers, Detectors, and Associated Equipment, 2022.

[71] Sofía Otero Ugobono, Michael Moll, Salvador Hidalgo Villena, Christian Gallrapp, Giulio Pellegrini, Matteo Centis Vignali, Marcos Fernandez Garcia, Isidre Mateu, Ivan Vila, and Ana Ventura Barroso. Sissa: Multiplication onset and electric field properties of proton irradiated lgads. *PoS*, page 041, 2018.

[72] CR Crowell and SM Sze. Temperature dependence of avalanche multiplication in semiconductors. *Applied Physics Letters*, 9(6):242–244, 1966.

[73] P Mars. Temperature dependence of avalanche breakdown voltage temperature dependence of avalanche breakdown voltage in p—n junctions. *International Journal of Electronics*, 32(1):23–37, 1972.

[74] Tao Yang, Kewei Wu, Mei Zhao, Xuewei Jia, Yuhang Tan, Suyu Xiao, Kai Liu, Mengzhao Li, Yunyun Fan, Shuqi Li, et al. TCAD simulation and radiation damage modeling for low gain avalanche detector. *arXiv preprint arXiv:2106.15421*, 2021.

[75] V Eremin, N Strokan, E Verbitskaya, and Z Li. Development of transient current and charge techniques for the measurement of effective net

concentration of ionized charges (N_{eff}) in the space charge region of pn junction detectors. *Nuclear Instruments and Methods in Physics Research Section A: Accelerators, Spectrometers, Detectors and Associated Equipment*, 372(3):388–398, 1996.

[76] Institut de Física de Partícules (IFAE). https://www.ifae.es/.

[77] Chiara Grieco, L Castillo García, A Doblas Moreno, Evangelos Leonidas Gkougkousis, Sebastian Grinstein, Salvador Hidalgo, Neil Moffat, Giulio Pellegrini, and J Villegas Dominguez. Overview of CNM LGAD results: Boron Si-on-Si and epitaxial wafers. *Journal of Instrumentation*, 17(09):C09021, 2022.

[78] Chiara Grieco. Low gain avalanche detectors for the atlas high granularity timing detector. 2022.

[79] Santa Cruz Institute for Particle Physics (SCIPP). https://scipp.science.ucsc.edu/.

[80] Hamamatsu Photonics (HPK). https://www.hamamatsu.com/jp/en/index.html.

[81] Fondazione Bruno Kessler (FBK). https://www.fbk.eu/en/.

[82] R. Heller. Studies of LGAD mortality using the Fermilab Test Beam. In *38th RD50 Workshop (Online)*, 2021.

[83] Kewei Wu, Xuewei Jia, Tao Yang, Mengzhao Li, Wei Wang, Mei Zhao, Zhijun Liang, João Guimaraes da Costa, Yunyun Fan, Han Cui, et al. Design and testing of lgad sensor with shallow carbon implantation. *Nuclear Instruments and Methods in Physics Research Section A: Accelerators, Spectrometers, Detectors and Associated Equipment*, 1046:167697, 2023.

[84] Mengzhao Li, Yunyun Fan, Xuewei Jia, Han Cui, Zhijun Liang, Mei Zhao, Tao Yang, Kewei Wu, Shuqi Li, Chengjun Yu, et al. Effects of shallow carbon and deep N++ layer on the radiation hardness of IHEP-IME LGAD sensors. *IEEE Transactions on Nuclear Science*, 69(5):1098–1103, 2022.

[85] R Padilla, C Labitan, Z Galloway, C Gee, SM Mazza, F McKinney-Martinez, HF-W Sadrozinski, A Seiden, B Schumm, M Wilder, et al. Effect of deep gain layer and carbon infusion on lgad radiation hardness. *Journal of Instrumentation*, 15(10):P10003, 2020.

[86] SM Mazza, C Gee, Y Zhao, R Padilla, E Ryan, N Tournebise, B Darby, F McKinney-Martinez, HF-W Sadrozinski, A Seiden, et al. Tuning of gain layer doping concentration and carbon implantation effect on deep gain layer. *arXiv preprint arXiv:2201.08933*, 2022.

[87] Lucía Castillo García, Evangelos Leonidas Gkougkousis, Chiara Grieco, and Sebastian Grinstein. Characterization of Irradiated Boron, Carbon-Enriched and Gallium Si-on-Si Wafer Low Gain Avalanche Detectors. *Instruments*, 6(1):2, 2021.

[88] Jairo Villegas, Neil Moffat, Salvador Hidalgo, and Giulio Pellegrini. Measurements on last IMB-CNM LGADs production. In *40st RD50 Workshop (CERN)*, 2022.

[89] Anup Kumar, Cristian Quintana, Efren Navarrete, Ivan Vila, Javier González, Marcos Fernández, and Richard. Jaramillo. Radiation Tolerance Study of CNM-IMB Run 15246. In *41st RD50 Workshop (Sevilla, Spain)*, 2022.

[90] Kljun Ž. Howard, A. and G Kramberger. Radiation hardness of latest HPK and CNM runs. In *HGTD Week, June 2022*.

[91] N Moffat, R Bates, M Bullough, L Flores, D Maneuski, L Simon, N Tartoni, F Doherty, and J Ashby. Low Gain Avalanche Detectors (LGAD) for particle physics and synchrotron applications. *Journal of Instrumentation*, 13(03):C03014, 2018.

[92] Marie Andrä, Jiaguo Zhang, Anna Bergamaschi, Rebecca Barten, Camelia Borca, Giacomo Borghi, Maurizio Boscardin, Martin Brückner, Nicoló Cartiglia, Sabina Chiriotti, et al. Development of low-energy x-ray detectors using lgad sensors. *Journal of synchrotron radiation*, 26(4):1226–1237, 2019.

[93] Z Galloway, C Gee, S Mazza, H Ohldag, R Rodriguez, HF-W Sadrozinski, BA Schumm, A Seiden, W Wyatt, and Y Zhao. Use of “LGAD” ultra-fast silicon detectors for time-resolved low-keV X-ray science. *Nuclear Instruments and Methods in Physics Research Section A: Accelerators, Spectrometers, Detectors and Associated Equipment*, 923:5–7, 2019.

[94] Prototype characterization of the JUNGFRAU pixel detector for Swiss-FEL,.

[95] Dieter K Schroder. *Semiconductor material and device characterization.* John Wiley & Sons, 2015.

[96] Maria Manna. 3D Sensors for the ATLAS HL-LHC Pixel Upgrade and Future Colliders. 2021.

[97] Albert Doblas, Waleed Khalid, David Flores, Salvador Hidalgo, Giulio Pellegrini, and Manfred Valentan. Proton low gain avalanche detector (plgad) for low energy particles detection. In *2021 13th Spanish Conference on Electron Devices (CDE)*, pages 137–140. IEEE, 2021.

[98] Jairo Villegas, Oscar Ferrer, Neil Moffat, Salvador Hidalgo, and Giulio Pellegrini. Gain measurements on NLGAD detectors. In *41st RD50 Workshop (Sevilla, Spain)*, 2022.

[99] Waleed Khalid, Manfred Valentan, Albert Doblas, David Flores, Salvador Hidalgo, Gertrud Konrad, Johann Marton, Neil Moffat, Daniel Moser, Sebastian Onder, et al. First results for the pLGAD sensor for low-penetrating particles. *Nuclear Instruments and Methods in Physics Research Section A: Accelerators, Spectrometers, Detectors and Associated Equipment*, 1040:167220, 2022.

[100] R Van Overstraeten and H De Man. Measurement of the ionization rates in diffused silicon pn junctions. *Solid-State Electronics*, 13(5):583–608, 1970.

[101] Dirk Dubbers and Bastian Märkisch. Precise measurements of the decay of free neutrons. *Annual Review of Nuclear and Particle Science*, 71:139–163, 2021.

[102] Gerhard Hobler, Konstantin K Bourdelle, and Takeshi Akatsu. Random and channeling stopping power of h in si below 100 kev. *Nuclear Instruments and Methods in Physics Research Section B: Beam Interactions with Materials and Atoms*, 242(1-2):617–619, 2006.

[103] Waleed Khalid, Manfred Valentan, Sebastian Onder, Albert Doblas, Raluca Hidalgo, Salvador Jiglau, Daniel Moser, Giulio Pellegrini, Tosten Soldern, Johann Zmeskal, and Gertrud. Konrad. pLGAD: a new sensor concept for low-penetrating particles. In *15th Trento Workshop on Advanced Silicon Radiation Detectors*, 2020.

[104] Giulio Pellegrini, Salvador Hidalgo, David Flores, Waleed Khalid, and Manfred Valentan. Low-penetrating particles Low Gain Avalanche Detector, 2022. `https://patentscope.wipo.int/search/es/detail.jsf?docId=WO2022063852`.